# Utilisation of Green Solvents in Organic Photovoltaic Devices for Large-Scale Fabrication Process

**Author:** ***Ashkan Nikiyan***

**A thesis submitted in partial fulfilment of the requirement of Staffordshire University for the degree of Doctor of Philosophy**

**August 2023**

# *Abstract*

This dissertation presents innovative techniques for fabricating solution-processed bulk heterojunction solar cells, utilising eco-friendly green solvents by replacing conventional halogenated equivalent.

A key aspect of this study involves leveraging advanced Atomic Force Microscopy (AFM) phase analysis, and Raman mapping techniques. These approaches enabled a detailed examination of the constituent materials, resulting in a comprehensive three-dimensional profile of the electron donor and acceptor materials within the blend. Detailed analysis indicate that the acceptor material, $PC_{71}BM$[1], predominantly accumulates at the blended film's surface. Further investigations concerning donor/acceptor distribution throughout the bulk revealed a systematic reduction of $PC_{71}BM$, with an equilibrium of electron donor and acceptor presence approximately 50 nm below the film surface. These observations suggest a consistent relationship between $PC_{71}BM$ content and its distribution at various depths, exhibiting a funnel-like distribution pattern.

In further investigation, depth-specific electrical analyses offered valuable insights into fullerene migration's effects on device performance. While surface migration enhances charge collection at the cathode, could potentially impede exciton dissociation and disrupt charge carrier pathways due to reduced $PC_{71}BM$ concentration in the bulk. A higher $PC_{71}BM$ concentration at the film surface could potentially improve parameters like series resistance ($R_s$), parallel resistance ($R_{sh}$) and fill factor but could hinder charge carrier pathways.

Among the evaluated green solvents, 2-Methyl Anisole (2MA) demonstrated the most promising results, achieving higher power conversion efficiency (PCE) and closely matching the performance of the samples mixed with halogenated solvents (dissolved in ODCB:CB[2]) at a blend ratio of [1:2] for polymer/small organic molecule systems. Grazing

[1] [6,6]-Phenyl-C71-butyric acid methyl ester
[2] 1,2-dichlorobenzene /chlorobenzene

Incidence X-ray Diffraction (GIXRD) studies on pristine EFT[3] (electron donor material) and EFT:$PC_{71}BM$ donor/acceptor systems further indicated that 2MA affects the intensity of the peak associated with the $d_{100}$ plane of EFT molecules at lower 2θ values.

Beyond solvent optimisation, the current work reports on green solvent applications in passivation patterns for large-scale devices. Prototype samples utilising the EFT:$PC_{71}BM$ donor/acceptor system dissolved in 2MA were fabricated and analysed for their electrical parameters. The prototype cells' parallel configuration demonstrated the highest efficiency, achieving a PCE of 8.7-8.9% when utilising the selected green solvent, 2MA.

[3] Poly[4,8-bis(5-(2-ethylhexyl)thiophen-2-yl)benzo[1,2-b;4,5-b']dithiophene-2,6-diyl-alt-(4-(2-ethylhexyl)-3-fluorothieno[3,4-b]thiophene-)-2-carboxylate-2-6-diyl]

# *Acknowledgement*

Firstly, I would like to thank God for everything; by whose grace, He has guided, and supported me through from the beginning to the end of this programme.

I owe a huge debt of gratitude to my principal supervisor, Professor Torfeh. Sadat-Shafai, who gave me the opportunity of this programme and providing me the full scholarship. I deeply appreciate all of his invaluable assistance, teaching, leadership, encouragement, and inspiring enthusiasm during tough times, most importantly, not giving up on me. He has been patient with me and had believe in me. There was no one I could have asked for a greater mentor and supervisor. I am proud to say that I have learnt from the best.

I would like to express my appreciation to the technical staff and friends at the school of Digital, Technologies and Art, also the Science centre for providing generous help and supports in a variety of capacities.

I would like to thank Staffordshire University for offering me a scholarship, and the facilities, to conduct and complete my PhD and research.

I would also like to thank my family and relatives for providing me the strength to persevere through my PhD period.

And for my wife, I am also thankful for all her prayerful support and wonderful encouragement that she has given me throughout the time of my PhD, which has been involved in making this work a success.

# *Publications*

A journal publications list during this PhD program:

Nikiyan, A., Komilian, S., Sadat-Shafai, T., Techniques to Facilitate 3D Analysis of Self-Organized Nanostructure Mechanism in Polymer/Fullerene Bulk Heterojunction Device. *Adv. Mater. Technol.* 2021, 6, 2000999. https://doi.org/10.1002/admt.202000999

# *Content*

# *List of Figures*

# *List of Tables*

# *List of Equations*

$$E\,(eV) = hv = \frac{hc}{\lambda} \tag{2.1}$$

$$v\,(Hz) = \frac{c}{\lambda} \tag{2.2}$$

$$E\,(eV) = \frac{hc}{\lambda} \tag{2.3}$$

$$V_{oc} = \frac{1}{q}\left(HOMO_{Donor} - LUMO_{Acceptor}\right) - 0.3V \tag{2.4}$$

$$J = J_s\left[\exp\left(\frac{qV}{k_BT}\right) - 1\right] \tag{2.5}$$

$$J = J_s\left[\exp\left(\frac{qV}{k_BT}\right) - 1\right] - J_{sc} \tag{2.6}$$

$$V_{oc} = \frac{k_BT}{q}\ln\left(\frac{J_{sc}}{J_s} + 1\right) \tag{2.7}$$

$$P = IV \tag{2.8}$$

$$P_{max} = I_{mp}V_{mp} \tag{2.9}$$

$$PCE(\%) = \frac{P_{out}}{P_{in}} \times 100 \quad or \quad = FF \times \frac{J_{sc} \times V_{oc}}{P_{in}} \times 100 \tag{2.10}$$

$$FF = \frac{J_{max} \times V_{max}}{J_{sc} \times V_{oc}} \tag{2.11}$$

$$J = J_{sc} - J_s\left[\exp\left(\frac{q(V - JR_s)}{nk_BT}\right) - 1\right] - \frac{V - JR_s}{R_{sh}} \tag{2.12}$$

$$V_{oc} = \frac{nk_BT}{q}\ln\left(\frac{J_{sc}}{J_s} + 1\right) \tag{2.13}$$

$$I_{SC}(Total) = I_{SC}(Cell) \times n \tag{4.1}$$

$$V_{OC}(Total) = V_{oc}(Cell) \times m \tag{4.2}$$

$$d = k\omega^{\alpha} \tag{4.3}$$

$$E_{HOMO} = -e(\varphi_p^{ons} + 4.4) \tag{4.4}$$

$$E_{LUMO} = -e(\varphi_n^{ons} + 4.4) \tag{4.5}$$

$$E_{HOMO} = -e(\varphi_p^{ons} + 4.39) \quad (4.6)$$

$$E_{LUMO} = -e(\varphi_n^{ons} + 4.39) \quad (4.7)$$

$$A = \log (I_0/I) = -\log_{10} T \quad (4.8)$$

$$E\ (eV) = h.c / \lambda \quad (4.9)$$

$$R_s = \frac{\pi}{\ln (2)} \frac{\Delta V}{I} \quad (4.10)$$

$$\rho = R_s . t \quad (4.11)$$

# *List of Abbreviations*

| | |
|---|---|
| AFM | Atomic force microscopy |
| Al | Aluminum |
| BHJ | Bulk heterojunction |
| $C_{60}$ | Buckminsterfullerene |
| $CO_2$ | Carbon dioxide |
| D/A | Donor/Acceptor |
| EFT | PBDTTT-EFT molecule |
| $E_g$ | Energy band gap |
| eV | Electron Volt |
| FF | Fill Factor |
| FWHM | Full width at half maximum |
| GIXRD | Grazing Incidence X-ray Diffraction |
| HOMO | Highest occupied molecular orbital |
| ITO | Indium tin oxide |
| $J_{sc}$ | Short circuit current density |
| LCD | Liquid crystal displays |
| LUMO | Lowest unoccupied molecular orbital |
| OLED | Organic light-emitting diode |
| OFET | Organic field-effective transistor |
| OTFT | Organic thin-film transistors |
| OSC | Organic solar cell |
| $\phi$ | Work function |
| P3HT | Poly (3-hexylthiophene) |
| PCBM | [6, 6] phenyl-C61-butyric acid methyl ester |
| PCE | Power conversion efficiency |
| PL spectra | Photoluminescence spectra |
| PV | Photovoltaic |
| Si-based | Silicon-based |
| UV | Ultra-violet |
| $V_{oc}$ | Open circuit voltage |

# CHAPTER 1

# Introduction

*"Keep your face to the sun and you will never see the shadows …"*

***— Helen Keler, American author, activist and lecturer***

## 1.1 Introduction

Global concerns regarding the carbon footprint, escalating energy consumption, and increasing fossil fuel costs have become prominent topics in international market discussions (Electricity Production Data | World Electricity Statistics | Enerdata, 2021). At the heart of these discussions lies the urgent need to reduce carbon dioxide ($CO_2$) emissions, prompting a worldwide shift from environmentally harmful fossil fuels to cleaner, renewable energy alternatives. In this evolving landscape, solar photovoltaic (PV) power generation has emerged as a pivotal player, significantly influencing the global energy transition (Irena, 2019).

By 2100, scientific projections suggest that the global population could reach an estimated 9.5 billion people. This rapid population growth poses significant challenges to the environment, impacting food security, water availability, rapid urbanisation, and most critically, energy demand (Fox, 2013). In light of increasing concerns related to $CO_2$ emissions, global warming, and diminishing fossil fuel reserves, the need for secure and sustainable energy sources has become more urgent than ever. This has led to a growing consensus to transition from conventional energy production methods to cleaner and more sustainable alternatives, such as wind, geothermal, and solar energy.

In 2016, a landmark global initiative took place in Paris, where nations came together to address the climate crisis collaboratively. The Paris agreement is crucial accord aimed at reducing carbon emissions and accelerating the adoption of renewable energy sources to meet global energy demands. A seminal report by Sandia labs in 2006 provides valuable insights into the technical potential of renewable energy sources available globally, as summarized in Table 1.1 (Tsao, Lewis, and Crabtree Argonne, 2006). This report meticulously estimates the power generation capacities of various renewable energy sources, with a particular emphasis on solar electricity, based on 1.5 hours of sunshine.

Table 1.1- Global renewable energies available with technical powers calculated for Solar electricity, the theoretical value is at 1.5 hrs of sunshine (Electricity Production Data | World Electricity Statistics | Enerdata, 2021)

| Energy Resources | Theoretical Power (TW) | Technical Power (TW) | Extractable Power (TW) |
|---|---|---|---|
| Ocean Surface current | 8.1 | 2 | 0.012 |
| Ocean Tidal | 2.4 | 0.6 | 0.037 |
| Ocean Wave | 34 | 8.5 | 0.62 |
| Hydropower | 12 | 3.5 | 1.2 |
| Geothermal | 44 | 2.8 | 1.9 |
| Wind Power | 1,000 | 250 | 14 |
| Solar Electricity | 89,000 | 25,091 | 5,018 |

According to this report, solar energy exhibits an impressive theoretical potential of approximately 89,000 Terawatts within a 1.5-hour timeframe (Tsao, Lewis, and Crabtree Argonne, 2006). However, factors such as geographical location, atmospheric conditions, and conversion efficiencies inevitably reduce this potential to an estimated 25,091 Terawatts of technical solar power. Considering an average solar cell conversion efficiency of around 20%, the actual extractable power from the sun is approximately 5,018 Terawatts. To provide context, global electricity production and consumption in 2019 were approximately 27,000 and 23,000 Terawatts, respectively (Electricity Production Data | World Electricity Statistics | Enerdata, 2021).

Further supporting these findings, Figure 1.1 illustrates the annual growth in electricity production up to the end of 2019, highlighting the increasing contribution of renewable

energy sources. Notably, over 200 Gigawatts of new renewable power capacity was installed in 2019, maintaining an impressive average growth rate of over 8% in renewable power capacity over the preceding five years. This growth trajectory propelled solar PV power generation by 22%, reaching 720 Terawatt hours (TWh). As a result, solar PV's share in global electricity generation has risen to nearly 3%, surpassing bioenergy and establishing itself as the third-largest renewable electricity technology after hydropower and onshore wind (Solar PV – Analysis - IEA, 2021).

In many countries, both commercial and residential sectors are already benefiting from electricity generation costs that are lower than the variable portion of retail electricity prices. The increasing economic viability of distributed PV systems is poised to catalyse rapid expansion in the renewable energy sector in the coming decades, attracting substantial private investment (Solar PV – Analysis - IEA, 2021).

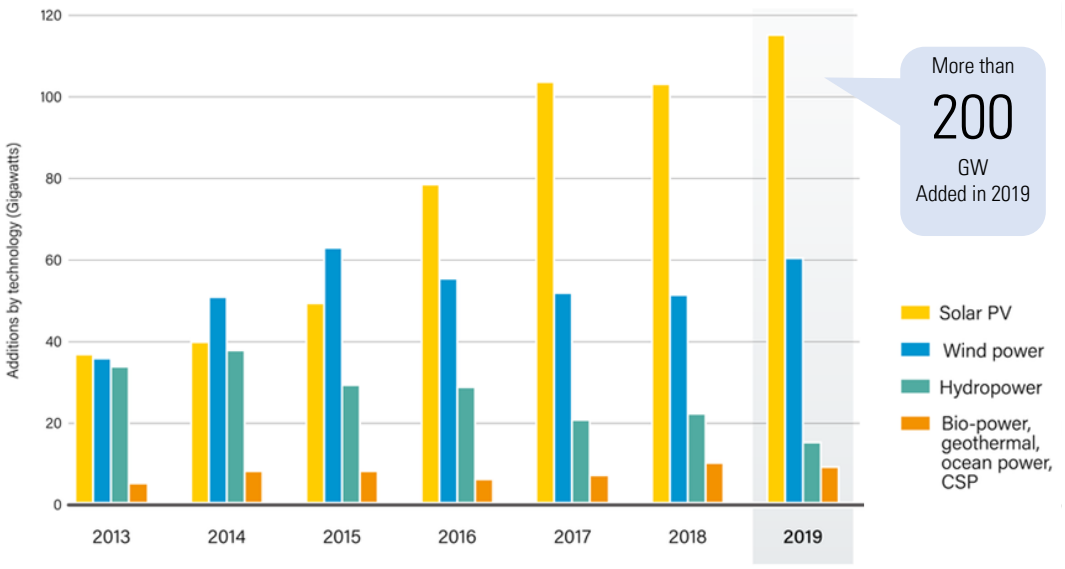


Figure 1.1 – Annual addition of Renewable Power capacity, by Technology and Total, 2013-2019 (Adopted from REN21 Renewable 2020 global status report (Hales, 2020))

Based on a report generated in 2019, as depicted in Figure 1.2, renewable energy sources accounted for an estimated 27.3% of global electricity generation by the end of the year. Hydropower remained the dominant renewable energy source, contributing 58% to this estimated generation share, followed by wind power (22%), solar PV (10%), and bio-power (8%).

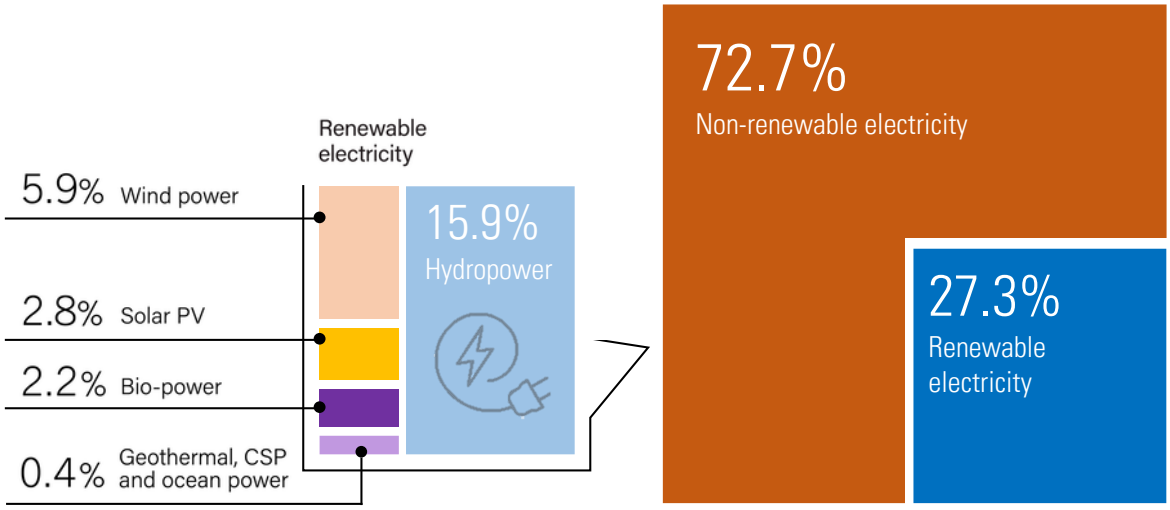


Figure 1.2 – Estimated Renewable Energy share of Global Electricity Production, End 2019 (Adopted from REN21 Renewable 2020 global status report (Hales, 2020))

Photovoltaic technology (PV) emerges as the most viable industry capable of converting sunlight into electrical energy, as evidenced by significant energy-related development initiatives. However, predicting the evolution of this rapidly expanding renewable energy sector, especially concerning changes in energy consumption patterns, presents considerable challenges (Deutsche Gesellschaft für Sonnenenergie., 2008).

## 1.2 Organic Solar Cells (OSCs)

Solar cells are typically classified into three main categories: Crystalline Silicon Solar Cells (Type I), Thin Film Technology Solar Cells (Type II), and Advanced Solar Cells (Type III). Each type has distinct characteristics, materials, manufacturing processes, and applications.

Type I solar cells are primarily composed of a single P-N junction diode, either fabricated from a single silicon crystal structure or from silicon fragments fused together to form a wafer (Schoder, 2018; Sendy, 2021). The power conversion efficiency (PCE) is a critical parameter for evaluating these cells. According to Shockley and H. Queissier, the maximum theoretical PCE for a single junction solar cell is approximately 33% (Shockley and

Queisser, 1961). In today's global market, these silicon-based solar cells typically achieve an average PCE ranging from 18% to 20% (Park, Lee, and Choi, 2015; Sendy, 2021). Solar cells utilising poly-crystalline silicon, a common material in Type I cells, often exhibit PCEs between 15% and 20% (Jay et al., 2014; Park, Lee, and Choi, 2015). While Type I solar cells offer high efficiency and a long lifespan, their production and manufacturing costs can be relatively high due to the complex manufacturing processes involved.

In contrast, type II solar cells were developed as a cost-effective alternative to Type I cells. These cells are primarily fabricated using materials like amorphous silicon, cadmium telluride (CdTe), and Copper indium gallium selenide (Cu [In, Ga] $Se_2$). Manufacturing techniques for Type II cells include thin-film technologies such as sputtering, plasma-enhanced chemical vapor deposition, and physical vapor deposition. Due to their non-crystalline structure and the presence of certain impurities, these cells generally exhibit lower PCEs compared to Type I cells. The highest recorded PCE for Thin Film Technology solar cells is between 21.1% and 23.3%, as certified by the National Renewable Energy Laboratory (NREL) in the USA (Records, 2015; NREL, 2021). Despite their lower efficiency in general, Type II solar cells offer several advantages, including easier manufacturing processes, faster production rates, and reduced material and manufacturing costs. These factors make them a competitive alternative to Type I cells, especially for large-scale solar installations where cost-effectiveness is crucial.

Type III solar cells represent the cutting-edge of solar cell technology and encompass a variety of innovative designs, including thin multi-junction cells, Dye-Sensitized Cells (DSCs), Organic Solar Cells (OSCs), and Perovskite cells. Multi-junction cells, such as those made from GaInP/GaAs/GaInNAs[4], have achieved the highest PCEs among all solar cell types, with a record efficiency of 44% (GREEN et al., 2012). These multi-layered cells are engineered to capture solar energy across a broad spectrum of wavelengths. Each semiconductor layer in a multi-junction cell has a unique energy band gap, allowing for optimal absorption of solar radiation. Theoretical calculations suggest that multi-junction solar cells could potentially achieve efficiencies as high as 66%. However, despite their impressive efficiency, the high production costs associated with these complex structures have limited their commercial applicability, making them primarily suitable for specialised

[4] Gallium indium phosphide/Gallium arsenide/Gallium Indium Nitride Arsenide

applications such as space missions where maximum efficiency is paramount (NREL Developing Improved Tech to Lower Costs for Multi-Junction Solar Cells, 2018).

Organic solar cells, also known as organic photovoltaics (OPVs), are a subcategory of Type III solar cells that have garnered significant attention due to their potential for low-cost, flexible, and lightweight solar energy solutions. OPVs are fabricated using organic materials, such as polymers or small organic molecules, which can be processed using low-cost printing techniques on flexible substrates. Although OPVs currently lag behind inorganic solar cells in terms of efficiency, ongoing research and development efforts aim to improve their performance and commercial viability (Spanggaard and Krebs, 2004).

## 1.3 The architecture of organic solar cells

Organic Solar Cells (OSCs) have evolved significantly over the years, with structure improvements categorised into three main types: single layer, bilayer, and bulk heterojunction (BHJ) as illustrated in Figure 1.3.

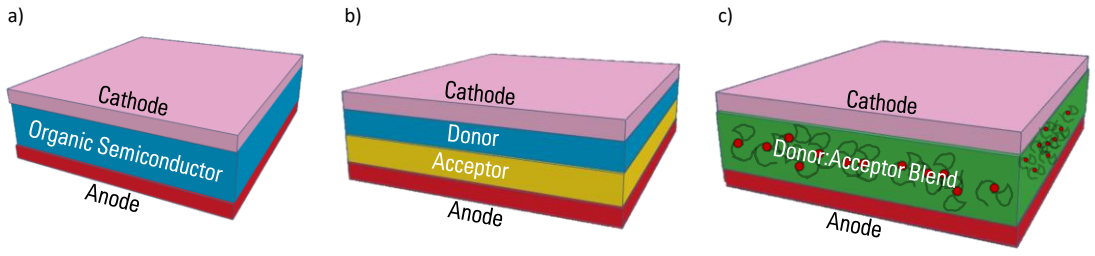


Figure 1.3- Main types of organic solar cells OSCs: a) single layer b) bilayer c) bulk heterojunction BHJ

Single layer organic solar cells are characterised by a simple architecture consisting of a layer of organic semiconductor sandwiched between two metallic conductors. The organic layer, also known as the active layer, plays a crucial role in light absorption and charge generation. The electric field necessary for charge separation is typically generated at the interface between the two metallic electrodes, which often consist of indium-tin-oxide (ITO) with a high work function and Aluminium (Al) with a low work function. When photons strike the solar cell, electrons are excited to the lowest unoccupied molecular orbital (LUMO), leaving behind a hole in the highest occupied molecular orbital (HOMO), thereby

forming an exciton. The potential energy difference between the two electrodes facilitates the separation of these excitonic electron-hole pairs. However, early single-layer OSCs faced challenges due to insufficient electric fields, leading to recombination of electrons and holes before reaching the electrodes. For instance, Tang et al. fabricated a sandwich configuration comprising Cr/Chlorophyll-a/Hg, achieving a marginal power conversion efficiency (PCE) of only 0.01% (Mao et al., 2017).

A significant breakthrough came in 1986 when Tang demonstrated that blending donor and acceptor materials could enhance the PCE of OSCs to around 1%. This discovery laid the groundwork for heterojunction OSCs, where the solar cells are structured based on a donor-acceptor architecture, including configurations such as dye/dye, polymer/dye, polymer/polymer, and polymer/fullerene blends (Spanggaard and Krebs, 2004).

Bilayer OSCs share similarities with single-layer devices but incorporate two distinct layers between the anode and cathode with differing electron affinities, generating an electric field potential at their interface. This enhanced electric field aids in exciton separation compared to single-layer OSCs. However, optimising the layer thicknesses to align with the exciton diffusion length, typically around 10 nm, remains challenging (Best Research-Cell Efficiency Chart | Photovoltaic Research | NREL, 2021). For example, a bilayer heterojunction solar cell consisting of copper phthalocyanine and perylene pigment achieved a PCE of 0.95% (Mao et al., 2017).

Bulk heterojunction (BHJ) OSCs have emerged as a promising solution to these challenges and are now widely adopted by researchers. BHJ OSCs feature a nanoscale blend of donor and acceptor materials within a single absorbing layer, replacing the two separate layers found in previous designs. The reduced thickness of this blended layer facilitates better exciton dissociation due to a larger interfacial area. Electrons and holes generated upon light absorption travel towards the respective acceptor and donor materials and are collected by the conducting electrodes. A BHJ OSC composed of poly(3-hexylthiophene) and methano-fullerene reported by Yang's group achieved a PCE of 4.2% (Mao et al., 2017).

Over the past two decades, BHJ OSCs have shown remarkable progress in achieving high PCEs (Preis et al., 2014). As depicted in Figure 1.4, the efficiency of various types of OSCs, represented in red, has significantly increased. Notably, OSCs based on conjugated polymers blended with fullerenes have demonstrated substantial advancements (Chen et al., 2009; Nelson, 2011; Zhao et al., 2015). Given this positive trajectory, the field of OSCs holds

considerable promise for further improvements through ongoing research (Scharber and Sariciftci, 2013).

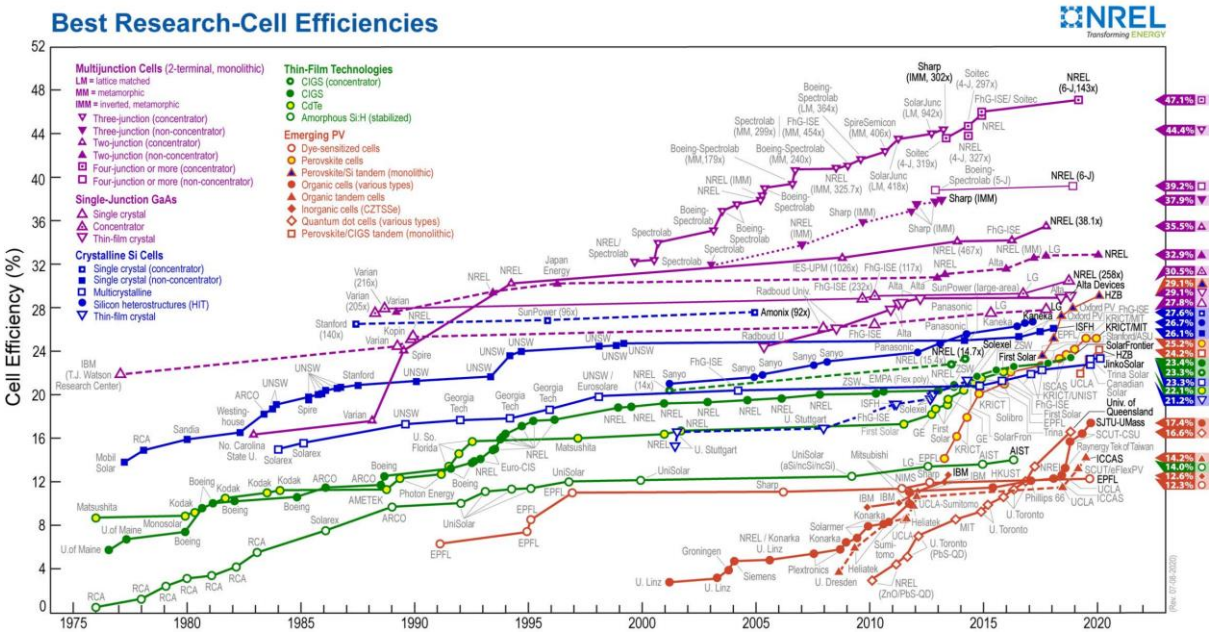


Figure 1.4- NREL Photovoltaic Efficiencies (NREL, 2021).

## 1.4 Challenges

As the quest for more efficient and cost-effective photovoltaic devices continues, researchers are exploring innovative approaches to solar cell manufacturing by transitioning from conventional inorganic materials to organic materials. Organic solar cells (OSCs) have garnered significant attention due to their inherent advantages, including flexibility, ease of low-cost fabrication, and lightweight properties, positioning them as potential competitors to traditional inorganic solar cells (Wallace C. H. Choy, 2013).

However, the adoption of OSCs is not without challenges. One of the most significant barriers to widespread commercialisation is the high manufacturing and fabrication relative costs associated with these devices (Jay et al., 2014; Preis et al., 2014; Park, Lee, and Choi, 2015). While silicon-based p-n junction photovoltaic systems have been the focus of much research, the power conversion efficiency (PCE) of most commercial silicon-based solar cells remains in the range of 15-20% (Jay et al., 2014). Recent studies have highlighted the

potential of BDT[5]-based polymers, such as PBDTTT-C-T[6], PBDTTT-CF[7], PBDTTT-EFT[8] (PTB7-th), PTB7[9], and combined with acceptor materials like $PC_{70}BM$[10] using halogenated solvents such as chlorobenzene (CB) and 1,2-dichlorobenzene (ODCB), to achieve the highest applicable PCE for OSCs (7.73% to 8.44% - Wallace C. H. Choy, 2013; Komilian, Oklobia and Sadat-Shafai, 2018a).

Despite the rapid advancements in the organic photovoltaic (OPV) field, the predominant use of toxic chlorinated/halogenated solvents, including 1,2-dichlorobenzene (ODCB), chlorobenzene (CB), and chloroform (CF), in the fabrication process remains a significant concern (Zhao et al., 2015). These hazardous solvents pose risks to human health and the environment and also complicate the device fabrication process, thereby hindering the industrialisation of OPV technology. In contrast, halogen-free organic solvents offer a more sustainable and environmentally friendly alternative for mass industrial manufacturing of OPVs (Zang et al., 2014).

Eliminating this toxic effects of halogenated solvents from the large-scale manufacturing process of OPVs remains a formidable challenge. The urgent task for the OPV field is to replace these harmful solvents with eco-friendly alternatives, such as water or other low-toxicity, non-halogenated, and non-aromatic solvents (Zhang et al., 2016).

Another significant challenge lies in translating laboratory-scale fabrication methods to large-scale manufacturing of OSCs. Adapting these methods for mass production involves various adjustments, including modifications to the hardware of the fabrication equipment, consideration of the thermo-physical properties of the materials, and the design of robust production lines capable of maintaining high standards of quality assurance. Key aspects to address in this transition include managing the thickness of critical layers during fabrication processes, improving the physical and viscoelastic properties of the materials used, and implementing dynamic inspection protocols using high-speed manufacturing lines to ensure the quality and consistency of the produced devices. These challenges underscore the

[5] Benzodithiophene
[6] Poly[[4,8-bis[5-(2-ethylhexyl)-2-thienyl]benzo[1,2-b:4,5-b′]dithiophene-2,6-diyl][2-(2-ethyl-1-oxohexyl)thieno[3,4-b]thiophenediyl]] - $(C_{48}H_{56}OS_6)_n$
[7] Poly[1-(6-{4,8-bis[(2-ethylhexyl)oxy]-6-methylbenzo[1,2-b:4,5-b′]dithiophen-2-yl}-3-fluoro-4-methylthieno[3,4-b]thiophen-2-yl)-1-octanone] - $C_{40}H_{51}FO_3S_4$ ]$_n$
[8] Poly[4,8-bis(5-(2-ethylhexyl)thiophen-2-yl)benzo[1,2-b;4,5-b']dithiophene-2,6-diyl-alt-(4-(2-ethylhexyl)-3-fluorothieno[3,4-b]thiophene-)-2-carboxylate-2-6-diyl] - $(C_{49}H_{57}FO_2S_6)_n$
[9] Poly [[4,8-bis[(2-ethylhexyl)oxy]benzo[1,2-b:4,5-b']dithiophene-2,6-diyl][3-fluoro-2-[(2-ethylhexyl)carbonyl]thieno[3,4-b]thiophenediyl ]]
[10] [6,6]-Phenyl-C71-butyric acid methyl ester

complexity and multi-faceted nature of scaling up OSC manufacturing for broader commercial adoption.

## 1.5 Research Aim and Objectives

The primary aim of this research project is to investigate the potential benefits and challenges of substituting chlorinated solvents with environmentally friendly green solvents in current organic photovoltaic (OPV) systems. The study will delve into various aspects such as fabrication parameters, processing constraints, material aggregation, and distribution-related issues both within the bulk and on the surface of the devices. To achieve this overarching aim, the following specific objectives have been delineated:

- Identify and analyse the existing challenges and potential limitations hindering the industrialization of OPV technologies when utilising green solvents.
- Develop and implement experimental and analytical methodologies to gain a deeper understanding of the influence of green solvents on the nanostructure and overall performance of OPV devices.
- Employ selected successful techniques to investigate and elucidate the underlying causes of performance impediments in OPV devices.
- Explore alternative fabrication processes to potentially overcome identified obstacles.
- Evaluate the feasibility and scalability of using selected successful green solvents in large-scale OPV device fabrication.

## 1.6 Thesis Organisation

Chapter 2 provides a comprehensive review of the theoretical foundations of organic semiconductors and delves into the fundamental concepts associated with the fabrication techniques and operational principles of organic solar cells. This chapter offers an in-depth exploration of the working mechanisms of organic solar cells, focusing on the internal formation and interactions of active layer components in organic semiconductors.

In Chapter 3, the spotlight shifts to an overview of conjugated polymers commonly employed in OSC devices. Special attention is given to the low band gap polymer PBDTTT-EFT, recognised for its superior properties compared to other available polymers in the market. Additionally, the chapter briefly discusses the properties of fullerene acceptor materials, particularly $PC_{71}BM$, which is frequently used in combination with PBDTTT-EFT and other key materials in this thesis. A comprehensive list of materials utilised in this research is presented, accompanied by a brief discussion on solvent characteristics and their compatibility with a range of polymers.

Chapter 4 focuses on the characterisation methods and corresponding instrumentation employed in this research. This chapter elucidates the underlying principles and methodologies of the experimental techniques utilised throughout the project. It also introduces new analytical techniques developed during the course of this research to analyse and better understand the impact of green solvents on nanostructures.

Chapter 5 presents the results derived from an extensive array of measurements conducted throughout the study. This chapter offers a detailed discussion on the structural characteristics of thin films both in pristine form and when blended with green solvents. The newly developed analytical techniques are applied to analyse the corresponding electrical photovoltaic (PV) properties and structural attributes of the thin films in the context of OSC applications. Furthermore, this chapter explores the transition towards large-scale fabrication techniques using green solvents, providing insights into the potential strategies for developing large modules using these eco-friendly alternatives.

Finally, Chapter 6 encapsulates the thesis by offering a comprehensive conclusion that synthesises the key findings and insights gained throughout the research. This chapter also outlines potential avenues for future research, focusing on identifying suitable green solvents for OPV fabrication and exploring their impact on the internal structure of bulk heterojunctions.

# CHAPTER 2

# Theory of Organic Solar Cells

*"It doesn't matter how beautiful your theory is, it doesn't matter how smart you are. If it doesn't agree with experiment, it's wrong."*

***— Richard P. Feynman***

## 2.1 Introduction

Solid materials are typically categorized into three main groups: conductors, insulators, and semiconductors. Conductors facilitate electrical current, while insulators hinder its flow. Semiconductors, however, lie in between, with electrical resistivity ranging from $10^{-2}$ to $10^{9}$ $(\Omega cm)^{-1}$, falling between conductors and insulators (Bar-Lev, 1993; Yacobi, 2002). Semiconductors often possess unique traits like a negative temperature coefficient of resistance and variable electrical conductivity due to their diverse resistivity range, making them well-suited for various electronic applications.

Moreover, there's a notable subset known as organic semiconductors, which has gained traction in organic electronics, contrasting with conventional inorganic semiconductors like silicon. Nowadays, organic semiconductors play crucial roles in diverse electronic devices such as organic light-emitting diodes (OLEDs), organic field-effect transistors (OFETs or OTFTs), and organic solar cells (OSCs) (eds. Brütting & Adachi, 2012).

This chapter provides a detailed examination of the theoretical underpinnings of organic solar cells, encompassing the fundamental principles of semiconductors, the unique

properties of organic materials, and the mechanisms that drive their operation. The discussion begins with an exploration of semiconductors, delving into their energy band structures and the crucial concept of the Fermi level. It further distinguishes between intrinsic and doped semiconductors, highlighting how doping modifies their electrical properties. The chapter then transitions to organic semiconductors, examining their energy band theory and how it differs from inorganic counterparts.

A key focus is on bulk heterojunctions (BHJ), which are central to the architecture of high-efficiency organic solar cells. The working principles of these devices are elucidated, covering the processes of charge photogeneration, exciton dissociation, and the various characteristics that define photovoltaic performance. The equivalent circuit model of organic solar cells is discussed, providing insights into their electrical behaviour and efficiency metrics.

## 2.2 Semiconductors

In electronic devices, semiconductors are essential components, forming the basis for transistors, diodes, integrated circuits, and more. Their ability to precisely control electrical signals is fundamental to the functioning of advanced technologies like computers, smartphones, and communication systems. A deep understanding of semiconductor physics is crucial for designing, optimizing, and innovating these electronic devices.

### 2.2.1 Fermi level Energy and Band Structure

The electronic band structure of a solid, which consists of the valence band and the conduction band, dictates the material's electrical conductivity. The valence band is the highest range of electron energies that are occupied at absolute zero temperature, while the conduction band represents the lowest range of unoccupied electronic states. In nonmetals, the valence band lies below the conduction band, with an energy gap between them that determines the material's insulating or semiconducting properties. In metals, this distinction is less pronounced as conduction occurs in partially filled bands that exhibit characteristics of both valence and conduction bands (Nave, 1999).

The Fermi level, denoted as $\mu$ or $E_f$, is crucial for understanding this band structure. It represents the thermodynamic energy required to add a single electron to the solid-state

entity, but it doesn't account for the energy needed to remove the electron from its source. The Fermi level's position relative to the valence and conduction bands influences the electronic properties of the material, affecting voltage and charge flow in electronic circuits. In semiconductors, the Fermi level typically lies within the band gap, closer to the valence band in p-type materials and nearer the conduction band in n-type materials. Understanding the relationship between the Fermi level and the band structure is essential for grasping the electronic behaviour of different materials (Kittel, 2011; Oklobia, 2016).

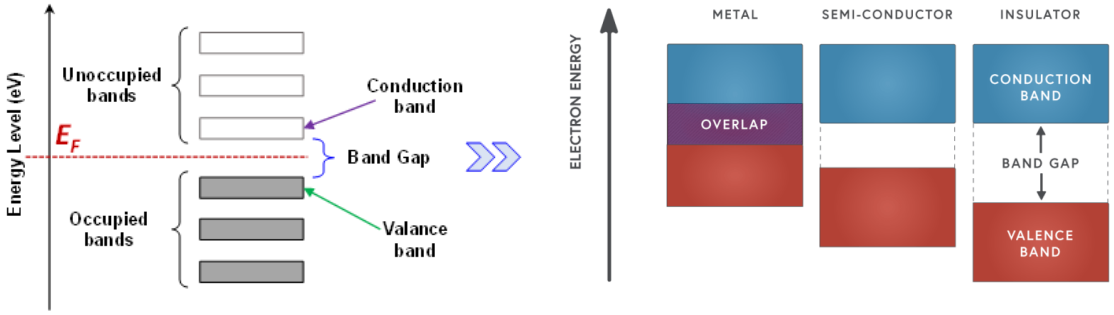


Figure 2.1: Energy band diagram illustrating different levels of valance and conduction band. Also showing the difference between conductor, semiconductor and insulator on energy band diagram.

Figure 2.1 illustrates that in conductors, the valence and conduction bands overlap, facilitating superior conductivity in materials of this type. A wider separation between the valence and conduction bands results in lower conductivity for a given solid; therefore, insulators possess the widest bandgap (Nave, C. R. ,1999).

### 2.2.2 Intrinsic and dopped semiconductors

In semiconductor manufacturing, doping refers to the intentional introduction of impurities into an intrinsic (undoped) semiconductor, thereby altering its electrical, optical, and structural properties. The doped material is then referred to as an extrinsic semiconductor. Figure 2.2 illustrates the doping process, wherein the intrinsic semiconductor based on Silicon becomes extrinsic through the introduction of impurities such as Boron and Antimony.

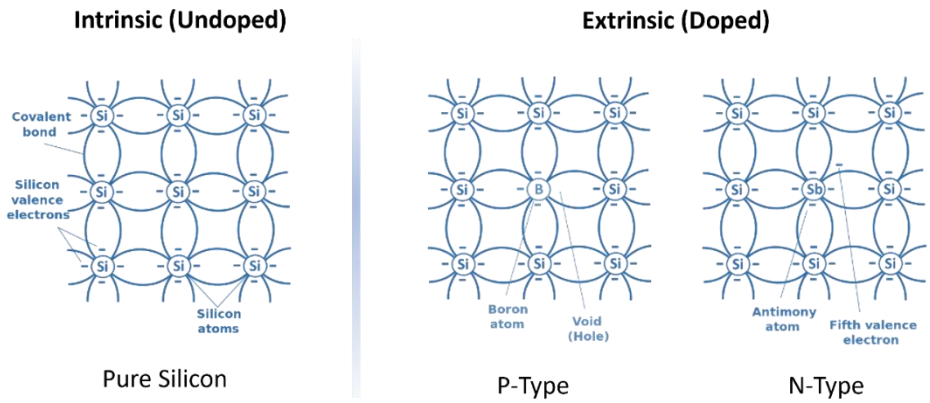


Figure 2.2- Doping of a pure silicon array. Silicon based intrinsic semiconductor becomes extrinsic when impurities such as Boron and Antimony are introduced

N-type semiconductors are created by doping an intrinsic semiconductor with an electron donor element during manufacture. The term n-type comes from the negative charge of the electron. In n-type semiconductors, electrons are the majority carriers and holes are the minority carriers. A common dopant for n-type silicon is phosphorus or arsenic. In an n-type semiconductor, the Fermi lies closer to the conduction band than the valence band (Neamen, Donald A. (2003).

P-type semiconductors are created by doping an intrinsic semiconductor with an electron acceptor element during manufacturing. The term p-type refers to semiconductors with excess positive charge or holes. In p-type semiconductors, holes are the majority carriers and electrons are the minority carriers. A common p-type dopant for silicon is boron or gallium. For p-type semiconductors the Fermi level is below the intrinsic semiconductor and lies closer to the valence band than the conduction band (Neamen, Donald A. (2003).

Even minute amounts of dopant atoms can exert significant influence on a semiconductor's conductivity. When roughly one dopant atom is added per 100 million atoms, it is categorized as low or light doping. Conversely, if a much larger number of dopant atoms are introduced, around one per ten thousand atoms, it is termed high or heavy doping. This is commonly indicated as n+ for n-type doping or p+ for p-type doping.

## 2.3 Organic semiconductors

Organic materials, often consisting of carbon-based compounds, play a significant role in modern optoelectronic devices due to their unique properties. Unlike traditional inorganic

materials like silicon, organic materials include synthetic molecules and polymers that exhibit intrinsic semiconducting behaviour. These materials can be engineered to have specific electronic properties, making them highly versatile for various applications.

The high cost of silicon crystals has been a major barrier to the widespread adoption of cheap, large-area photovoltaics. Organic semiconductors offer an attractive alternative, leveraging synthetic molecules with intrinsic semiconducting properties for optoelectronic devices (Organic Semiconductors | Optoelectronics, 2024). In contrast to their inorganic counterparts such as silicon (Si), organic semiconductors are typically characterized by intrinsic wide band gaps, usually ranging from 2 to 3 eV, which are larger than the band gaps of typical inorganic semiconductors like Si (1.12 eV) (Peter, 2009).

Despite this advantage, the application of organic semiconductors in electronic devices has been limited due to their inherent carrier trapping and relatively low charge-carrier mobility (Yacobi, 2002). However, they compensate for these limitations with relatively high absorption coefficients (typically $\geq 10^5$ $cm^{-1}$), allowing even thin films (< 100 nm) of organic materials to absorb photons effectively (Hoppe & Sariciftci, 2004).

Another key difference between organic and inorganic semiconductors is the relatively small exciton diffusion length in the active layer of organic materials, typically around ~10 nm (Halls et al., 1996; Haugeneder et al., 1999; Stübinger et al., 2001). This characteristic impacts the efficiency of devices like organic solar cells. A prominent example of an organic semiconductor is conjugated polymers, which have garnered significant attention, particularly following the award of the Nobel Prize in Chemistry in 2000 for the discovery and development of electrically conductive polymers (Peter, 2009).

### 2.3.1 Energy Band Theory

Polymers are large molecules composed of repeating structural units called monomers, which are covalently bonded to form long chains. These chains can vary in length and complexity, resulting in a diverse range of materials with various physical and chemical properties. Polymers are ubiquitous in everyday life, found in everything from plastics and rubbers to natural substances like DNA and proteins.

Conjugated polymers, a specialized class of polymers, are characterized by alternating single and double bonds between carbon atoms (-C=C-C=C-). This alternating bonding pattern is fundamental to the unique properties of organic semiconductors. Conjugation induces two

significant changes in the organic molecule: it splits discrete energy levels into nearly continuous energy bands and facilitates the delocalization of charges within these levels (Peter, 2009). This phenomenon is crucial for the semiconducting behaviour observed in these materials.

This theory underlying organic semiconductors helps in understanding their electronic structure, which is influenced by the unique bonding and molecular structures found in organic molecules (Petty, 2008). Conjugated polymers, such as polyacetylene, exemplify this principle. The alternating bonds in these polymers create a system where electrons can move more freely, leading to semiconducting properties. Figure 2.3 illustrates the principle of conjugation and the chemical structure of the simplest organic polymeric semiconductor, polyacetylene.

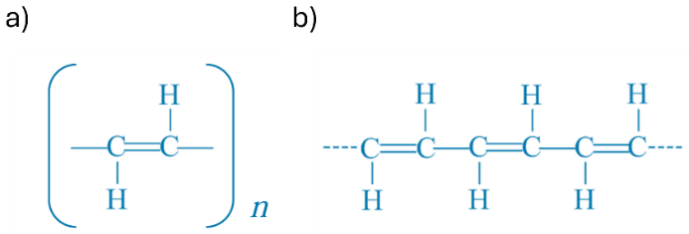


Figure 2.3- (a) Polyacetylene, the simplest organic polymeric semiconductor , (b) Principle of conjugation in organic electronic materials (alternating single and double bonds), (Peter, 2009).

Carbon possesses four valence electrons available for bond formation: three occupy the $sp^2$ hybridized orbitals, while the fourth occupies the pz orbital. In the bonding process of organic materials like ethylene ($C_2H_4$), the three $sp^2$ electrons form covalent bonds through σ molecular orbitals with neighbouring carbon atoms and hydrogen atoms. The remaining pz electron participates in forming covalent bonds via a π molecular orbital, as shown in Figure 2.4.

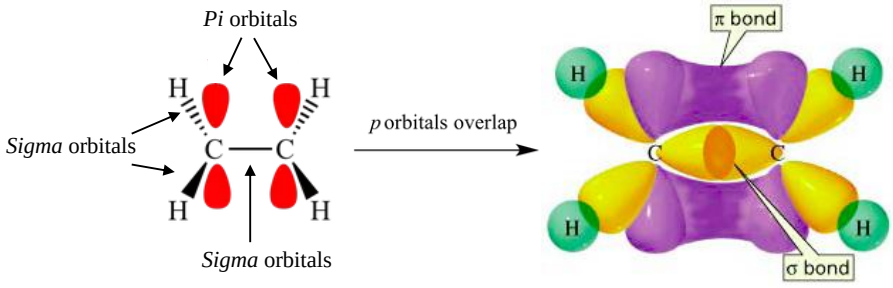


Figure 2.4 - Schematics illustration of ethylene molecule and its molecular orbital bonds π and σ (Oklobia, 2016).

In organic polymeric materials composed of extended chains of carbon atoms, conjugation results in a sequence of alternating single (σ only) and double (σ and π) bonds. The interaction between adjacent orbitals (pz atomic orbitals) leads to the splitting of π and π* molecular orbitals. In longer carbon chains, this splitting manifests as a smaller gap between the levels of discrete bonding π and antibonding π* states. π electrons occupy the π band, while the π* band remains unoccupied at lower energy levels (Jaiswal & Menon, 2006). These bands are identified as the highest occupied molecular orbital (HOMO) and lowest unoccupied molecular orbital (LUMO).

Figure 2.5 illustrates the formation of the Highest Occupied Molecular Orbital (HOMO) and the Lowest Unoccupied Molecular Orbital (LUMO) levels in a typical organic polymeric semiconductor.

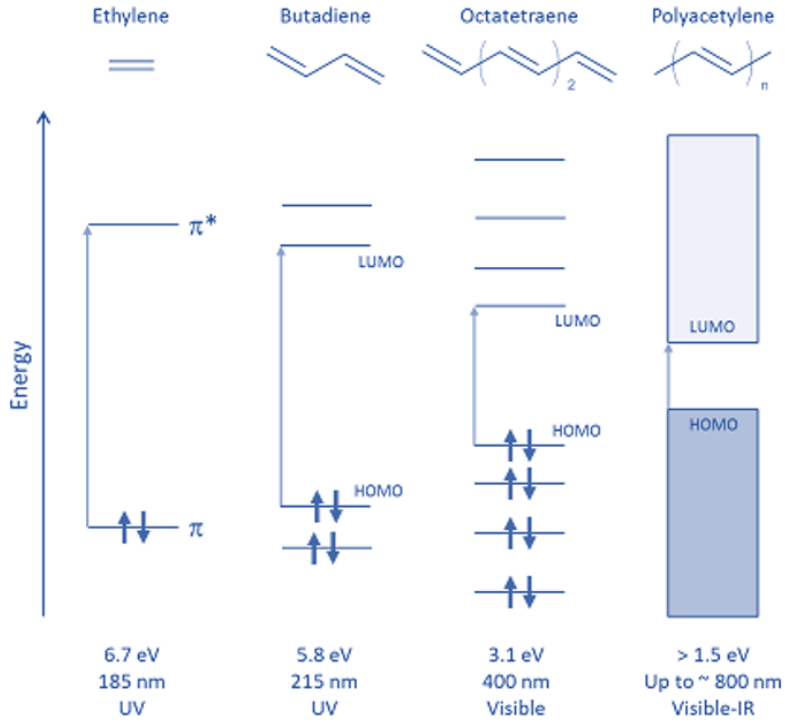


Figure 2.5- Molecular orbital interaction in the formation of energy bands in polyacetylene (Schematic of energy-level splitting and absorption in alkenes with increasing conjugation length, highlighting the lowest-energy optical transitions from HOMO to LUMO. The bandgap of polyacetylene depends on both the number of monomers n and the effective conjugation length in the polymer. Arrows represent spin-paired electrons)

In semiconductor physics, the HOMO and LUMO levels correspond to the valence and conduction bands, respectively. The energy difference between the HOMO and LUMO levels represents the energy band gap (Eg) (Jaiswal & Menon, 2006a). The figure also shows

the π and π* (pi and pi star) orbitals, highlighting their roles in the electronic structure of the polymer.

In general, increasing the length of conjugation tends to reduce the energy gap between the Highest Occupied Molecular Orbital (HOMO) and the Lowest Unoccupied Molecular Orbital (LUMO). However, this effect diminishes as the number of monomer units reaches a saturation point. Therefore, extending conjugation indefinitely isn't necessary due to the limited impact on reducing the bandgap. According to the particle in a box theory, the π electrons' delocalization along the conjugated carbon chain shifts the required energy for electronic absorption towards the infrared region, and the transition wavelength increases with the conjugated system's length. A more effective approach to reducing the bandgap and adjusting the electronic energy levels of conjugated polymers involves introducing an alternative structure comprising electron-rich donor (D) and electron-deficient acceptor (A) units into a single polymer backbone (Peng, H., et al, 2017).

## 2.4 Bulk Heterojunctions (BHJ)

As discussed in Chapter 1, single-layer and bilayer architectures form the foundational designs for organic semiconductor devices. In these configurations, the arrangement and interaction of different semiconductor materials are crucial for device performance. When two semiconductor materials with different energy gaps come into contact, the resulting junction is known as a heterojunction (Yacobi, 2002).

Heterojunctions are pivotal in organic semiconductor applications, particularly in electronic devices such as organic solar cells (OSCs). These semiconductor materials are typically classified as donor (electron-donating) and acceptor (electron-accepting) materials. The interaction between donor and acceptor materials at the heterojunction facilitates the separation of photogenerated charge carriers, which is essential for the efficient operation of OSCs. This mechanism enhances the overall efficiency and effectiveness of organic electronic devices, making heterojunctions a critical component in the development of advanced optoelectronic technologies.

Typically, bulk heterojunctions are achieved either by co-depositing donor and acceptor inks (Geens et al., 2002; Peumans et al., 2003) or by casting donor-acceptor blend solutions (eds. Krebs, 2008). Donor materials are p-type semiconductors (e.g., conjugated polymers acting

as electron donors), while acceptor materials are n-type semiconductors (e.g., fullerenes acting as acceptors) (Ma et al., 2005).

Both bilayer and bulk architectures, among the three types of OSC architectures discussed in section 1.2, rely on heterojunctions. The significance of the bulk heterojunction (BHJ) lies in its intimate mixing of donor and acceptor compositions distributed throughout a bulk volume, ensuring that donor/acceptor (D/A) interfaces are within the exciton diffusion length at each absorbing site (Hoppe & Sariciftci, 2004).

The schematic energy band diagram of the heterojunction (bilayer (a) and bulk (b)) in a typical OSC application is shown in Figure 2.6.

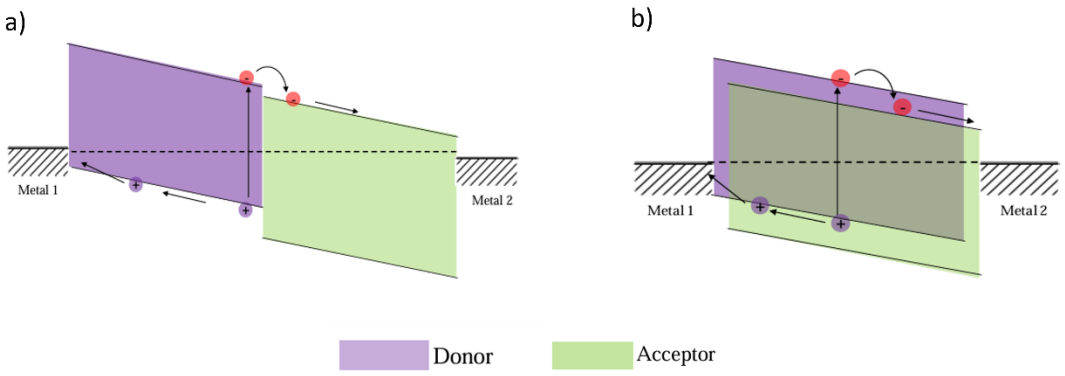


Figure 2.6- Schematic of Energy band diagram for BHJ system illustrating donor and acceptor material (Adapted from Yacobi, 2002).

Figure 2.7 presents a 3D schematic illustration of both a bilayer and bulk heterojunction (BHJ) device structure, with detailed explanations to follow in chapter 4.

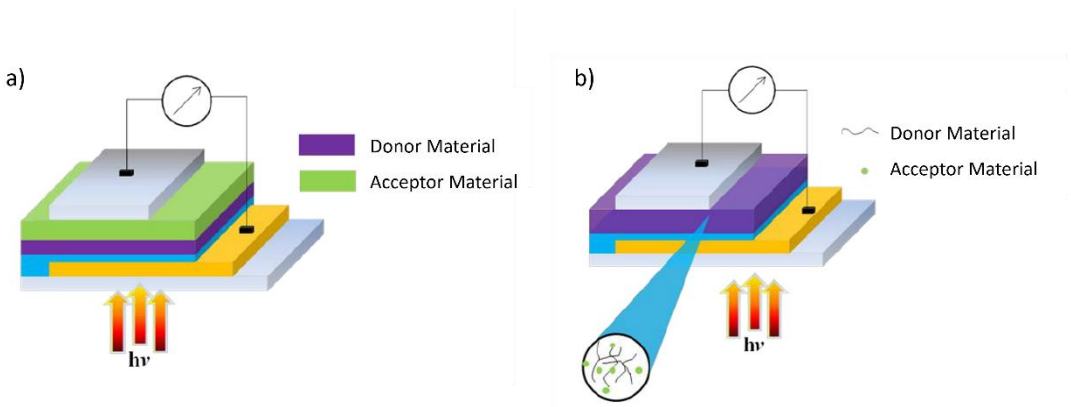


Figure 2.7- 3D schematic design of (a) a bilayer heterojunction organic solar cell (OSC), and (b) a bulk heterojunction (BHJ) OSC. In both designs, the photoactive layer is situated between a cathode and an anode for hole extraction..

Organic Solar Cell devices are generally fabricated with the BHJ architecture. The advantage of easy fabrication techniques is one of the reasons for the growing attractiveness of the BHJ organic solar cell with this order of layers. The active layer of these devices is mostly fabricated from solution – processable materials which is elaborated in Chapter 3 and 4 of the thesis.

## 2.5 Working Principles of Organic Solar Cells

The emission of solar radiation occurs in the form of electromagnetic waves or particles, known as photons. The energy of a photon (E) is determined by the Planck-Einstein relationship:

$$\mathrm{E\ (eV)} = \mathrm{hv} \qquad (2.1)$$

Where *v* is the photon's frequency and *h*, is Plank's constant. Since the photon's frequency can also be defined in terms of wavelength:

$$\mathrm{v\ (Hz)} = \frac{\mathrm{c}}{\lambda} \qquad (2.2)$$

and *c* is the speed of light in vacuum and $\lambda$ is the photon's wavelength. Plank – Einstein relationship can also be written as:

$$\mathrm{E\ (eV)} = \frac{\mathrm{hc}}{\lambda} \qquad (2.3)$$

In photovoltaic technology, the absorption of solar radiation, known as photons, is essential for effective generation of charge carriers. When a photon is absorbed by an organic semiconductor (OS), it generates exciton pairs, and an electron is excited from the highest occupied molecular orbital (HOMO) to the lowest unoccupied molecular orbital (LUMO) of the molecule. This process resembles an electron transitioning from the valence band to the conduction band in non-organic semiconductors.

It's noteworthy that non-organic semiconductors have a high dielectric constant, and excitons have a low binding energy typically in the range of a few millielectronvolts (meV), significantly lower than organic semiconductors, which typically range from 0.1 to 0.4 electronvolts (eV). Consequently, there's a weak Coulombic force between the electron-hole pair (exciton) in non-organic semiconductor materials (Gregg and Hanna, 2003; Mayer et al., 2007). Conversely, organic semiconductors have a low dielectric constant, resulting in a

stronger Coulombic force within the electron-hole pair. These differences lead to the conclusion that free charge carriers are more readily generated in non-organic semiconductor materials following photon absorption.

To produce electricity within OSC devices, exciton pairs must be separated into free charges. Tang et al. demonstrated this process in 1986 by utilizing two different organic materials with aligned band levels to create a heterojunction exciton (Tang, 1986). The operational mechanism of bulk heterojunction OSCs is described in four steps as follows (refer to Figure 2.8):

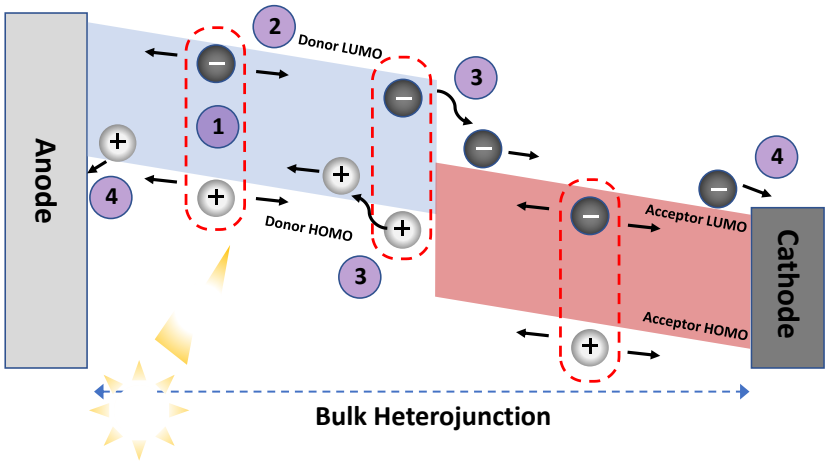


Figure 2.8- Operation of BHJ OSCs under illumination, indicating the primary four stages

- Step 1: An electron residing within the highest occupied molecular orbital (HOMO) of the organic material absorbs thermal energy from solar radiation, thereby transitioning into the lowest unoccupied molecular orbital (LUMO), generating an exciton, which is a hole-electron pair.
- Step 2: The exciton diffuses towards the interface of the two materials, forming a heterojunction.
- Step 3: At the heterojunction interface, the exciton dissociates.
- Step 4: The newly dissociated free charge carriers disperse towards the electrodes located at opposite ends of the cell, where they are collected.

When an exciton pair is generated, if there isn't a significant difference in work function between the donor and acceptor in the heterojunction, the exciton may fail to dissociate and produce charge carriers. Instead, it may recombine, resulting in low efficiency of exciton dissociation. This process is known as photoluminescence, which produces a brief flash of light.

There exists a critical distance that a diffused exciton must traverse successfully before recombination occurs. This distance is commonly referred to as the exciton diffusion length and is notably short for organic semiconductors, typically around 10 nanometers (Nunzi, 2002; Kietzke, 2007; Chen et al., 2009). Maintaining the thickness of the active layer within this range is crucial. However, it's essential to recognize that the thickness of the active layer also directly influences photon absorption.

Solar cells generate current by absorbing light, and this current can be measured as a function of voltage, typically depicted in a single plot to characterize OSCs. When a bias voltage is applied to the cell, an ideal solar cell (under dark conditions) would operate similar to a diode.

### 2.5.1 Charge Photogeneration and Exciton dissociation

Photons absorbed by the donor material initiate the generation of excitons. In contrast, inorganic semiconductors generate free charges directly upon photon absorption due to their low dielectric constants and enhanced electron-lattice interactions (Gregg. B. A., 2003; Bredas. J. L., 2002). The diminished dielectric constant in inorganic semiconductors necessitates less energy or electric field for free charge generation.

Exciton dissociation in organic semiconductors (OS) primarily follows a mechanism associated with the electronic energy gap between the donor and acceptor materials (Clarke. T. M., 2010). In bulk heterojunction (BHJ) systems, exciton dissociation occurs predominantly at the heterojunction of the donor-acceptor interface. Instead of directly dissociating into free charges, excitons initially undergo spatial electron-hole separation, forming a Coulomb-bound electron-hole pair referred to as a charge transfer (CT) state (Onsager. L., 1934).

The CT state represents an intermediate stage between bound electron-hole pairs and dissociated free charges, and the successful dissociation of CT states into free charge carriers

is crucial for generating photocurrent. However, not all electron-hole pairs in the CT state undergo complete dissociation into free charge carriers, as two recombination mechanisms, namely Geminate and Bimolecular recombination, impede this process (Clarke. T. M., 2010; Onsager. L., 1934). For electron-hole pairs to dissociate, they must overcome the Coulomb force binding them, which is influenced by the energy difference at the donor-acceptor interface.

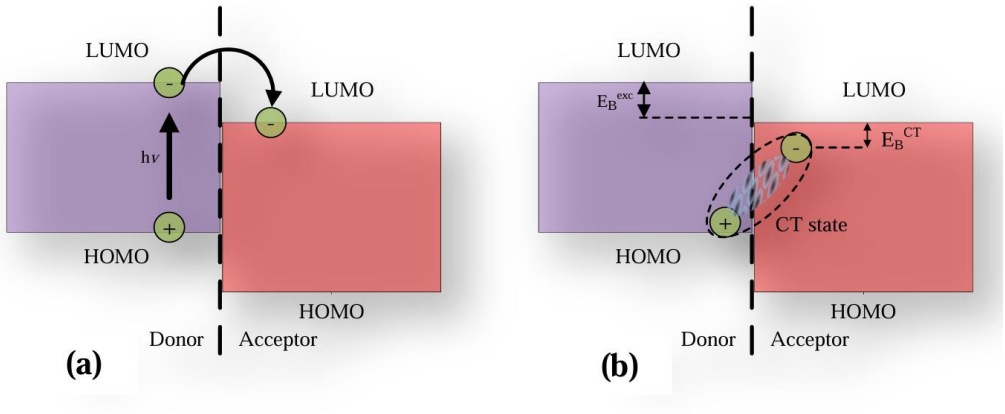


Figure 2.9. (a) Energy diagram of the donor-acceptor (D-A) interface, illustrating the excited electron in the lowest unoccupied molecular orbital (LUMO) level of the donor material following photon absorption. (b) The formation of a charge transfer (CT) state between the electron and hole, with $E_B^{exc}$ representing the exciton binding energy, which correlates with the difference between the LUMOs of the donor and acceptor materials (ΔLUMO), and $E_B^{CT}$ representing the binding energy of the charge transfer state.

Figure 2.9 presents a basic schematic diagram demonstrating the dissociation of excitons at the interface between donor (D) and acceptor (A) materials in a typical bulk heterojunction organic semiconductor (OSC). It indicates the initial dissociation process and the subsequent formation of a charge transfer (CT) state.

For the initial dissociation stage to occur, there must be a minimum energy gap between the donor and acceptor lowest unoccupied molecular orbital (LUMO) levels. This LUMO difference should exceed the exciton binding energy ($E_B^{exc}$), which initiates the formation of the charge transfer (CT) state (Bredas. J. L., 2002). Due to the close proximity of the donor-acceptor (D-A) interfaces, this initial electron transfer stage progresses into a spatial separation between the electron and hole, forming the CT state, typically within a distance comparable to the size of a molecule (approximately 0.5 – 1 nm). Applying these separation distances to the equation, Coulombic energies ranging from 0.1 to 0.5 eV are estimated,

referred to as the CT binding energy (EBCT) (Figure 2.8b). Comparing the magnitude of Coulombic energy to thermal energy (~ 0.025 eV), it becomes evident that thermal energy alone is insufficient to dissociate excitons.

Heeger et al. (Heeger. A., 2017) have determined that the origin of the open-circuit voltage ($V_{oc}$) for bulk heterojunction organic semiconductor (BHJ OSC) systems is associated with the difference between the highest occupied molecular orbital (HOMO) of the donor and the LUMO of the acceptor material (Bredas. J. L., 2002). Their investigation empirically deduced that a minimum LUMO difference of 0.3 eV between the acceptor and donor is necessary for efficient exciton dissociation. They proposed an equation to calculate $V_{oc}$ based on this finding.

$$V_{oc} = \frac{1}{q}\left(HOMO_{Donor} - LUMO_{Acceptor}\right) - 0.3V \qquad (2.4)$$

### 2.5.2 Characteristics of Photovoltaic cells

From a semiconductor physics perspective, the PV cell has similar operation principle to the p-n junction diode. Conceptually, the junction formed between two semiconductor materials of the same type but with opposite doping types constitutes a p-n junction. As mentioned earlier, the p-type semiconductor is characterized by an abundance of majority holes, while the n-type semiconductor is enriched with negative charge carriers due to doping with donor impurities (Sze, 1985; Tyagi, 1988; Singh, 1994). By employing the p-n junction diode as a reference device and leveraging the theory of equivalent circuits, the underlying operational principle of a typical PV cell can be elucidated.

#### 2.5.2.1 Equivalent circuit model of organic solar cells

Under dark conditions, organic solar cells (OSCs) behave akin to a diode, and their current-voltage (J-V) characteristics can be modelled similar to an ideal p-n junction diode. This is mathematically expressed as (O. Kasap and Sze, 2002):

$$J = J_s\left[\exp\left(\frac{qV}{k_B T}\right) - 1\right] \qquad (2.5)$$

Where, $J_s$ represents the saturation current density under reverse bias, q is the elementary charge, V is the applied bias voltage, $K_B$ is Boltzmann's constant, and T is the temperature in Kelvin. From the above equation, it can be concluded that the device will pass a higher current under forward bias voltage compared to reverse bias voltage. This is typical behaviour of a solar cell under dark conditions.

However, when the same device is examined under illumination, the J-V characteristics will be mathematically expressed as:

$$J_{ph} = J_s\left[\exp\left(\frac{qV}{k_B T}\right) - 1\right] - J_{sc} \qquad (2.6)$$

Where $J_{sc}$ is the short circuit current density when the applied bias voltage is zero (V=0). $J_{sc}$ is directly related to illumination intensity. Solar cells yield their highest voltage at open circuit condition when J=0, which is referred to as the open circuit voltage ($V_{oc}$). Therefore, $V_{oc}$ can be expressed mathematically as:

$$V_{oc} = \frac{k_B T}{q}\ln\left(\frac{J_{sc}}{J_s} + 1\right) \qquad (2.7)$$

It can be noted that $V_{oc}$ has a direct logarithmic relationship with $J_{sc}$ from the above equation. Figure 2.10 illustrates the J-V characteristic curve plots of an ideal solar cell under dark and illumination conditions.

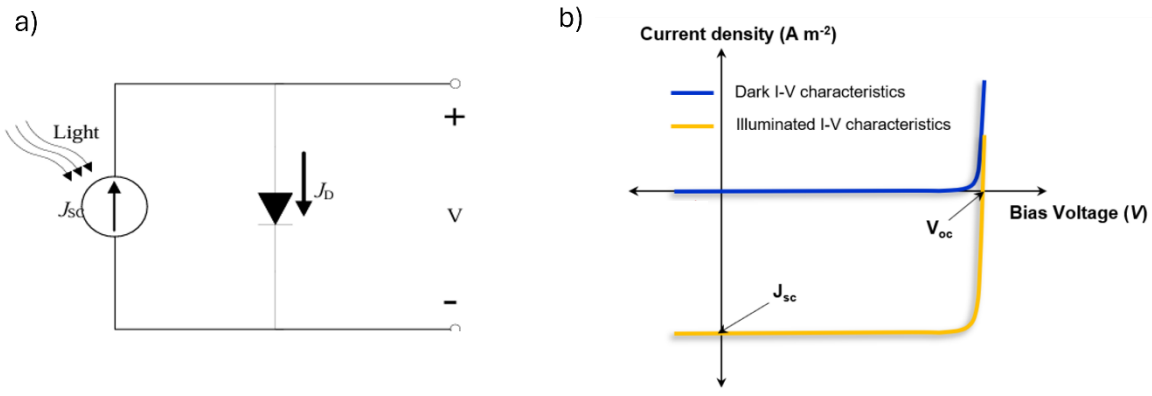


Figure 2.10- (a) Equivalent circuit model of an ideal solar cell (b) J – V characteristics of an ideal solar cell in the dark and under illumination.

### 2.5.2.2 Efficiency

The power generated can be calculated using the equation:

$$P = I.V \qquad (2.8)$$

By utilizing this equation and determining the maximum current ($I_{mp}$) and maximum voltage ($V_{mp}$) in the I-V curve of solar cells, the maximum power can be achieved with the following equation:

$$P_{max} = I_{mp}V_{mp} \qquad (2.9)$$

Figure 2.11 illustrates a presentation of the I-V curve and the Power curve (P-V). $P_{max}$ represents the shaded area 'A', and the theoretical $P_{max}$ is the shaded area 'B'. Fill Factor (FF) is defined as the ratio of the measured maximum power to the theoretical maximum power and is one of the most important I-V characteristics in solar cells. This parameter defines the quality of the device; an ideal solar cell device will have an FF of unity.

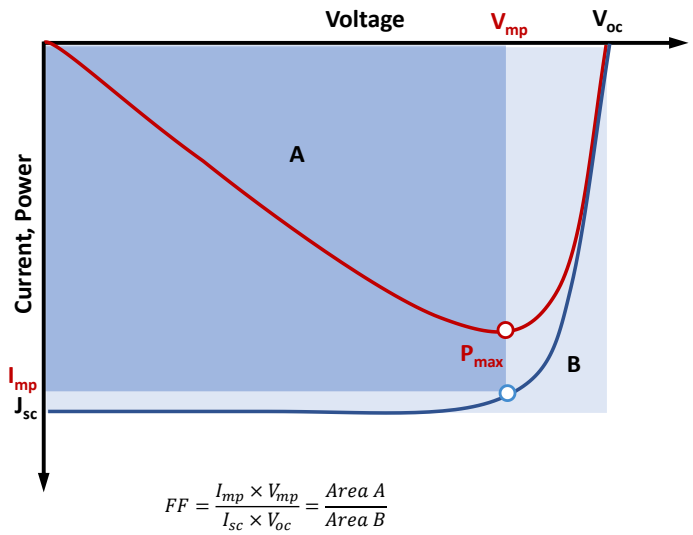


Figure 2.11- I.V and P.V curves which is also illustrating the FF parameter

By considering the FF and measuring the input solar power/radiation, the power conversion efficiency (PCE) can be calculated with the following equation:

$$PCE(\%) = \frac{P_{out}}{P_{in}} \times 100 \quad \text{or} \quad = FF \times \frac{J_{sc} \times V_{oc}}{P_{in}} \times 100 \qquad (2.10)$$

Where :

$$FF = \frac{J_{max} \times V_{max}}{J_{sc} \times V_{oc}} \qquad (2.11)$$

$P_{out}$ : output power

$P_{in}$ : input power (100 mW/cm$^2$)

$J_{sc}$ : short circuit current density (mA/cm$^2$)

$V_{oc}$ : open circuit voltage (volts, V)

FF : fill factor

$J_{max}$ : maximum point short circuit current density (mA/cm$^2$)

$V_{max}$ : maximum point open circuit voltage (volts, V)

A solar cell can also be represented as a circuit, where it resembles a current source in parallel with a diode. While the previous sections have described an ideal solar cell, in reality, imperfections exist that impact the power conversion efficiency (PCE) of solar cells. Parameters like contact resistance and current leakage affect the performance of the solar cell and can be incorporated into the model to calculate PCE by using their equivalents. This modelled circuit is shown in Figure 2.12.

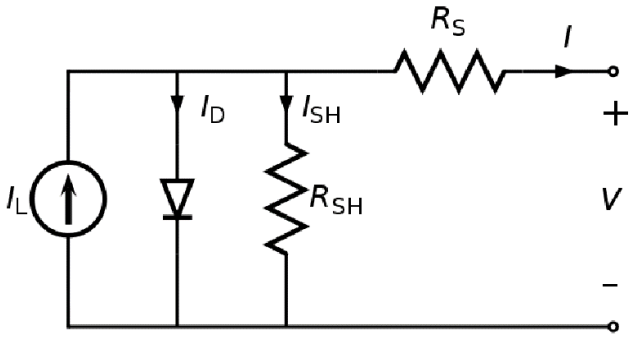


Figure 2.12- Modelled circuit representation of a solar cell, incorporating imperfections such as contact resistance and current leakage, impacting the power conversion efficiency (PCE)

In Figure 2.13, the circuit features a series resistance $R_s$ and a parallel resistance $R_{sh}$. Typically, the value of series resistance $R_s$ is much lower than the shunt resistance $R_{sh}$. In an ideal solar cell, $R_s$ would be zero, and $R_{sh}$ would be infinite.

Since the effect of $R_{sh}$ is insignificant near open circuit conditions, the inverse slope of the I-V curve in that vicinity serves as an indicator of $R_s$. The calculated series resistances

encompass both contact and bulk resistance, and they can be extracted from the slope of the I-V curve at higher voltages (Chirvase et al., 2004).

Conversely, since the effect of $R_s$ is negligible near short circuit conditions, the inverse slope of the I-V curve in that region indicates $R_{sh}$. Figure 2.12 illustrates how $R_s$ and $R_{sh}$ can be determined from the I-V graph.

Modelling the solar cell as a circuit demonstrates that the two primary factors influencing the curve's shape are the series resistance $R_s$ and the shunt or parallel resistance $R_{sh}$. Figure 2.14 illustrates this concept, with blue lines representing ideal I-V curves and red lines depicting the impact of resistance on the curve shape. Any changes in the I-V slopes, indicative of $R_s$ or $R_{sh}$, would affect the Fill Factor (FF) parameters and power conversion efficiency (PCE).

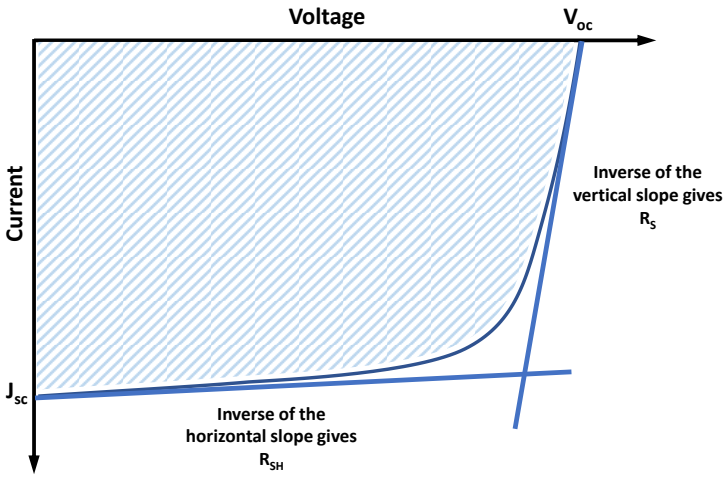


Figure 2.13- The determination of series resistance ($R_s$) and shunt resistance ($R_{sh}$) from the I-V graph of a solar cell

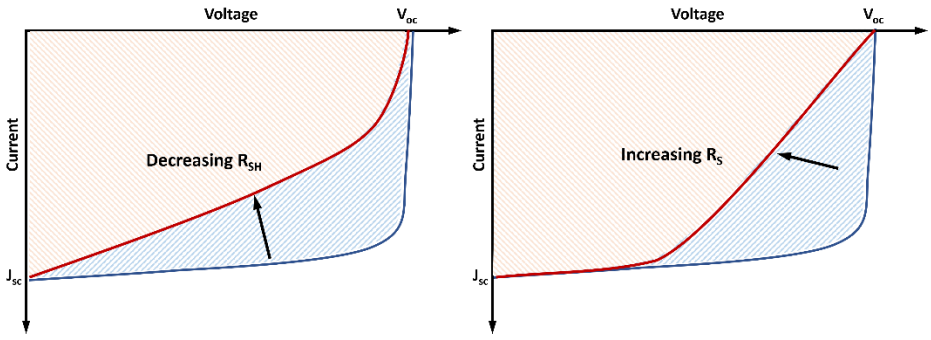


Figure 2.14 - The effect of $R_s$ and $R_{sh}$ on the J-V curve

When $R_s$ and $R_{sh}$ are integrated into the J-V characteristic model, the new mathematical representation for J as a function of applied bias voltage (V) will be:

$$J = J_{sc} - J_s\left[\exp\left(\frac{q(V - JR_s)}{nk_BT}\right) - 1\right] - \frac{V - JR_s}{R_{sh}} \quad (2.12)$$

$$V_{oc} = \frac{nk_BT}{q}\ln\left(\frac{J_{sc}}{J_s} + 1\right) \quad (2.13)$$

Where *n* represents the ideality factor of the diode component.

## 2.6 Summary

In this chapter, an overview was provided of the fundamental theories of organic semiconductors, and the current existing knowledge of how OS devices operate was demonstrated. The following can be summarized:

- Profound descriptions were provided of the formation of energy bands in OS materials with regards to the interaction of molecular orbitals. Definitions of the Highest Occupied Molecular Orbital (HOMO) and Lowest Unoccupied Molecular Orbital (LUMO) were included, along with their equivalent properties concerning valence and conduction bands in inorganic semiconductors.
- The operation mechanism of OSCs was discussed, including circuit modelling and the distinction between ideal and conventional devices. Deep illustration was given on how the series and shunt resistance would impact the Power Conversion Efficiency (PCE) and Fill Factor (FF) of OSCs.
- The mechanisms of charge transport and exciton dissociation within OS materials were explored.

# CHAPTER 3

# Organic Solar Cells Materials

*"The more clearly we can focus our attention on the wonders and realities of the universe about us, the less taste we shall have for destruction. "*

***– Rachel Carson***

## 3.1 Introduction

Conjugated polymers are organic compounds characterized by alternating single and double bonds. Known as "intrinsic wide band gap organic semiconductors," they typically have energy gaps exceeding 1.4 eV (Günes, Neugebauer, and Sariciftci, 2007). In 1977, Shirakawa and colleagues found that doping polyacetylene (the simplest form of a conjugated polymer) increased its conductivity significantly (Shirakawa and Macdiarmid, 1977). This discovery spurred rapid growth in organic electronics research. In the active layer of BHJ organic solar cells, most conjugated polymers and fullerene derivatives are blended together. Currently, electron-donating poly benzo di-thiophen ethyl-hexyl fluothane thiophene (PBDTTT-EFT), and electron-accepting [6,6] phenyl-C61-butyric acid methyl ester (PCBM) are among the most promising materials. This chapter reviews these materials and their applications in organic solar cells, along with a brief overview of compatible organic solvents.

## 3.2 Donor material (Polymers based on Benzo[1,2-b;4,5-b`]dithiophene)

Previous research on PPV-based[11] BHJ solar cells, such as MEH-PPV[12] and MDMO-PPV[13] with fullerenes, showed efficiencies ranging from 1.5 to 3.3% (Yu et al., 1995; Brabec et al., 2002). However, due to their large band gaps (>2 eV), devices based on PPV polymers had significantly limited current (Brabec et al., 2002). In contrast, the PT derivative P3HT offered potential for higher current densities because of its lower band gap (1.9 eV). P3HT is a typical conjugated polymer with a repeating unit backbone forming the polymer chain and side chains that impart solubility (Brabec et al., 2014). The side chains also significantly influence the polymer's molecular weight and processability.

Research by Oklobia (2016) indicated that the best power conversion efficiency for P3HT: PCBM organic solar cells was 3.84%, achieved with a 1:1 blend ratio and an optimum thermal annealing temperature of 150°C. Further studies are needed to better understand and develop novel concepts for organic solar cells, aiming to realize their potential for low-cost energy conversion. This involves not only achieving favourable nanoscale morphology control for improved efficiencies but also ensuring device stability over time and under varying temperatures. Consequently, it is worth exploring another group of polymers based on Benzo-dithiophene (BDT).

BDT-based polymers, initially developed for OFET applications in 2007 (Pan et al., 2007), have shown promising chemical structures, as depicted in Figure 3.1.

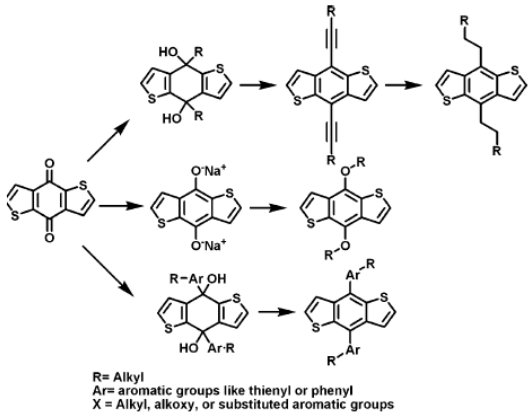


Figure 3.1: Chemical structure illustrating the synthesis of three possible substitutes of BDTs (Hou and Guo, 2013a).

[11] PPV-based refers to solar cells that use polymers derived from poly(p-phenylene vinylene) (PPV) as their active layer material. PPV is a conjugated polymer known for its semiconducting properties, making it suitable for use in organic electronic devices, including bulk heterojunction (BHJ) organic solar cells.

[12] poly[2-methoxy-5-(2-ethylhexyloxy)-1,4-phenylenevinylene]

[13] poly[2-methoxy-5-(3',7'-dimethyloctyloxy)-1,4-phenylenevinylene]

With various conjugated units/blocks possessing different electron withdrawing capacities, these polymers' band gaps can be readily adjusted. Initially, Hou et al. designed and synthesized eight distinct BDT-based polymers to investigate the relationship between conjugated backbones and the molecular energy band gap (Hou et al., 2008). Figure 3.2 illustrates the chemical structure of these polymers.

It has been reported that three types of functional groups can serve as side chains for Benzo[1,2-b;4,5-b']dithiophene (BDT) units to render them into soluble polymers. These functional groups include alkyl, alkoxy, and alkylthiophene (Hou et al., 2008; Hou and Guo, 2013a). BDT units possess a symmetrical planar conjugated structure, thus suggesting compact stacking in BDT-based conjugated copolymers (Pan et al., 2006).

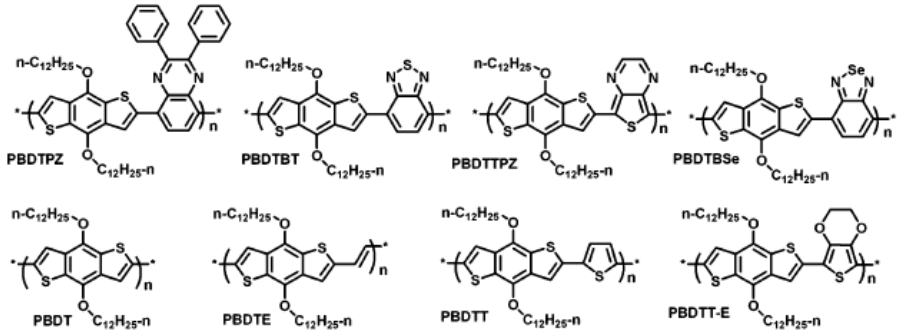


Figure 3.2: Chemical structure of eight BDT-based polymers with identical BDT units (Hou and Guo, 2013a).

Hou et al., extensively explored the relationship between the highest occupied molecular orbital (HOMO) levels of these polymers and the $V_{oc}$ values obtained when bulk heterojunction (BHJ) organic solar cells (OSCs) were fabricated using a blend of these polymers and $PC_{61}BM$. Their investigations revealed that the achieved $V_{oc}$ is directly correlated with the discrepancy between the donor's HOMO level (HD) and the acceptor's lowest unoccupied molecular orbital (LUMO) level (LA) (Hou et al., 2008).

Table 3.1 presents a compilation of BDT-based polymers utilized as donor materials in BHJ OSCs. These polymers were mixed with either $PC_{61}BM$ or $PC_{71}BM$ to form the active layer.

Table 3.1- OSC device characteristics for BDT-based polymers blended with $PC_{61}BM$ or $PC_{71}BM$.

| Polymer | $E_g$ (eV) | HOMO (eV) | LUMO (eV) | $J_{sc}$ (mA $cm^{-2}$) | $V_{oc}$ (V) | FF | PCE (%) | Refs |
|---|---|---|---|---|---|---|---|---|
| PBDT | 2.13 | -5.16 | -2.67 | - | - | - | - | (Hou *et al.*, 2013) |
| PBDTE | 2.03 | -5.07 | -2.86 | 1.16 | 0.56 | 0.38 | 0.3 | (Hou *et al.*, 2013) |
| PBDTT | 2.06 | -5.05 | -2.69 | 3.78 | 0.75 | 0.56 | 1.6 | (Hou *et al.*, 2013) |
| PBDTT-E | 1.97 | -4.56 | -2.66 | 2.46 | 0.37 | 0.40 | 0.4 | (Hou *et al.*, 2013) |
| PBDTPZ | 1.63 | -4.78 | -3.28 | 1.54 | 0.60 | 0.26 | 0.2 | (Hou *et al.*, 2013) |
| PBDTBT | 1.70 | -5.10 | –3.19 | 2.97 | 0.68 | 0.44 | 0.9 | (Hou *et al.*, 2013) |
| PBDTTPZ | 1.05 | -4.65 | -3.46 | 1.41 | 0.22 | 0.35 | 0.1 | (Hou *et al.*, 2013) |
| PBDTBSe | 1.52 | -4.88 | -3.33 | 1.05 | 0.55 | 0.32 | 0.2 | (Hou *et al.*, 2013) |
| PBDTTT-C | 1.61 | -5.12 | -3.35 | 14.70 | 0.70 | 0.64 | 6.6 | (Hou *et al.*, 2009) |
| PBDTTT-CT | 1.58 | -5.11 | -3.25 | 17.48 | 0.74 | 0.59 | 7.6 | (Huo *et al.*, 2011) |
| PBDTTT-CF | 1.60 | -5.22 | -3.45 | 15.20 | 0.76 | 0.67 | 7.7 | (Chen *et al.*, 2009) |
| PBDTTT-EF | 1.63 | -5.12 | -3.13 | 14.50 | 0.74 | 0.69 | 7.4 | (Liang and Yu, 2010) |
| PBDTTT-EFT | 1.58 | -5.24 | -3.66 | 16.17 | 0.78 | 0.68 | 8.6 | (Zhao *et al.*, 2014) |
| PBDTTTPD | 1.73 | -5.40 | - | 11.50 | 0.85 | 0.70 | 6.8 | (Peterson *et al.*, 2010) |
| PBDTFTAZ | 2.00 | -5.36 | -3.05 | 11.80 | 0.79 | 0.73 | 6.8 | (Price *et al.*, 2011) |
| PBDTDTffBT | 1.70 | -5.54 | -3.33 | 12.91 | 0.91 | 0.61 | 7.2 | (H. Zhou *et al.*, 2011) |

As shown in Table 3.1, PBDTTPZ is an excellent example of a material with a strong and broad absorption band of 1.05 eV. However, the $V_{oc}$ of the PBDTTPZ device is approximately 0.2 V, primarily due to a high HOMO value. Therefore, developing effective donor materials requires achieving the right balance between the energy band gap and the HOMO level of the donor polymer. Over the past decade, many BDT-based polymers have been designed and synthesized for application in BHJ OSCs, with some of the best-performing ones to date presented in Figure 3.3.

Among the BDT-based polymers listed in Table 3.1, the highest performing polymer is PBDTTT-EFT, which exhibits the highest PCE in this category. It has a $J_{sc}$ of 16.17 mA cm-2, a $V_{oc}$ of 0.78 V, and an FF of 0.68, resulting in a high PCE of 8.6% (Zhao et al., 2014). The chemical structure of the PBDTTT-EFT molecule is illustrated in Figure 3.4.

To improve the band gap, the 2-ethylhexyl-thienyl group is incorporated into the BDT unit of the PBDTTT-EFT low band gap polymer which enhances the co-planarity of the main chain. This modification extends the absorption band and achieves a lower band gap. Additionally, by advancing the fluorine-substituted TT unit (F-TT) with the 2-ethylhexyl carboxylate group, a higher HOMO level can be achieved.

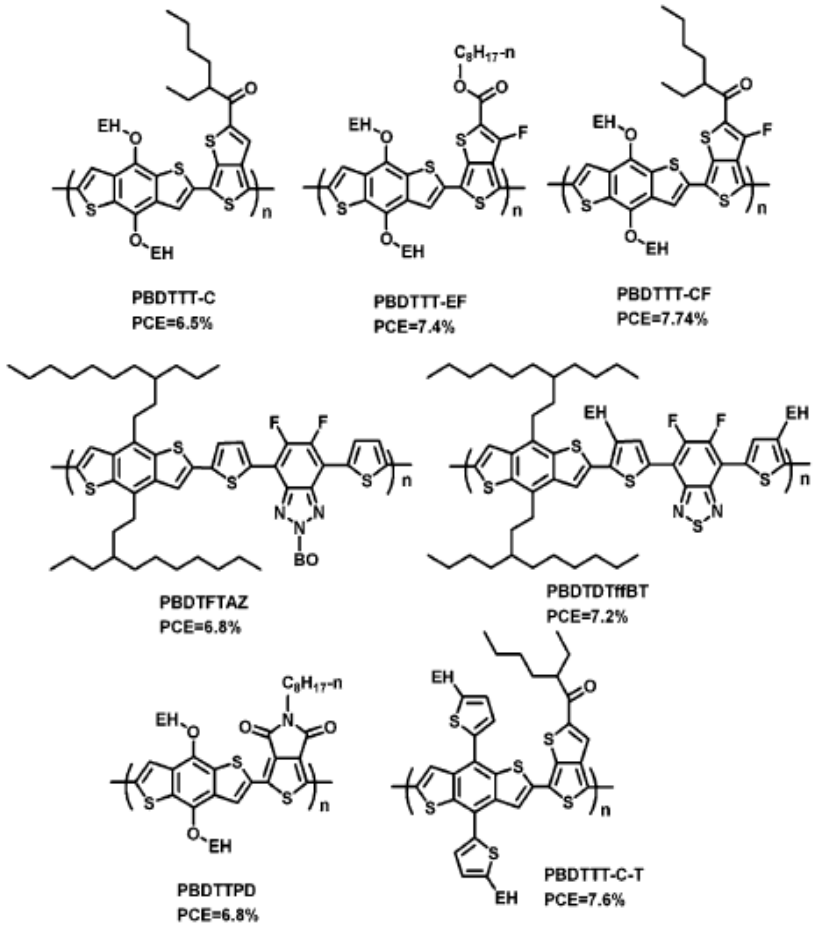


Figure 3.3- The molecular structure of BDT-based copolymers (Hou and Guo, 2013a).

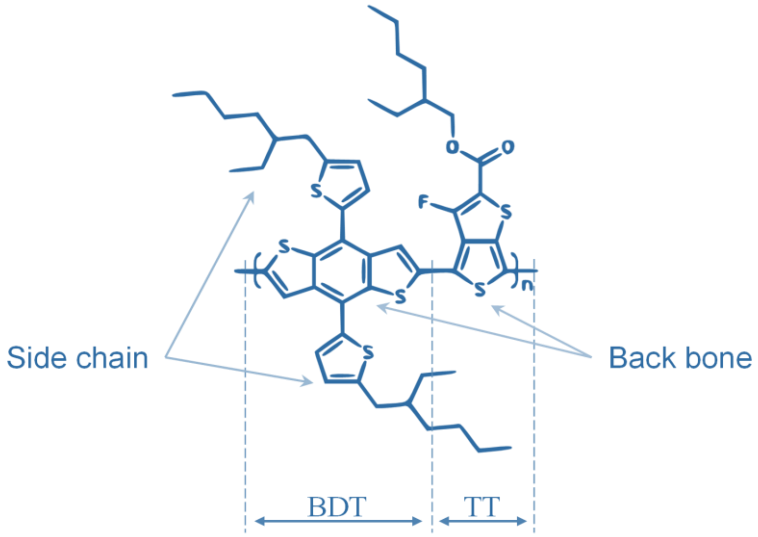


Figure 3.4- The molecular structure of PBDTTT-EFT, indicating BDT and TT units attachment as the building block of the molecule.

The literature reports that PCEs exceeding 9% can be achieved using this widely commercialized BDT-based polymer as the donor material for BHJ OSC devices (Zhang et al., 2014; Komilian, Oklobia, and Sadat-Shafai, 2018a). A basic statistical survey was conducted to examine the number of publications related to the PBDTTT-EFT polymer over the years. This was done using Google Scholar. Figure 3.5 presents a simple bar chart showing the number of journals/papers published with the phrase "PBDTTT-EFT" across different years.

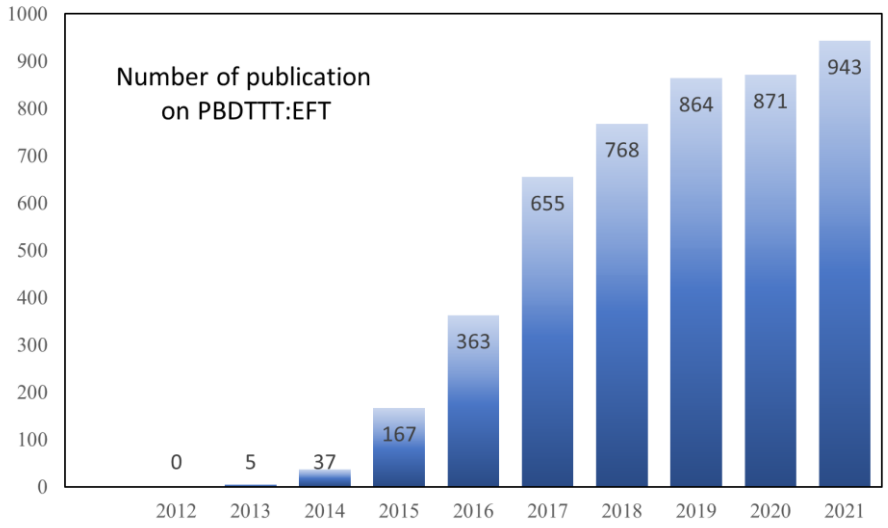


Figure 3.5- Bar chart representation of publications on PBDTTT-EFT base OSCs (Data source: Google Scholar, search terms: "PBDTTT-EFT", "PTB7-Th" and "PCE10").

As shown in Figure 3.5, PBDTTT-EFT was not introduced to the scientific community until 2013, with very few publications appearing initially. The PBDTTT-EFT molecule is also known by other names, such as PTB7-Th and PCE10. The data for Figure 3.5 was compiled by counting the number of articles using "Google Scholar." Over the past seven years, this polymer has garnered significant interest and is considered a promising candidate for use as a donor material in OSCs. Consequently, PBDTTT-EFT has been selected as the donor material for this project.

## 3.3 Acceptor material (PCBM[14] derivatives)

The first team to use $C_{60}$ as an electron acceptor and recognize the photo-induced ultrafast electron transport between donor-acceptor (D-A) was Sariciftci et al. in 1992 (Sariciftci et al., 1992). Fullerene $C_{60}$ has a well-symmetric molecular structure and exhibits excellent electron mobility because a single $C_{60}$ molecule can accept four electrons. Consequently, $C_{60}$ and its derivatives are regarded as suitable electron acceptor materials (Hou and Guo, 2013a). However, the solubility of $C_{60}$ is limited to selective solvents such as chlorobenzene (CB) and 1,2-Dichlorobenzene (ODCB). To enhance the solubility of $C_{60}$ in a broader range of organic solvents, its derivative [6,6]-phenyl-C61-butyric acid methyl ester ($PC_{61}BM$) was synthesized for application in OSCs. Over the past decade, $PC_{61}BM$ and its derivative $PC_{71}BM$ have been the primary acceptor materials in the field of OSCs. The molecular structures of $PC_{61}BM$ and $PC_{71}BM$ are illustrated in Figure 3.6.

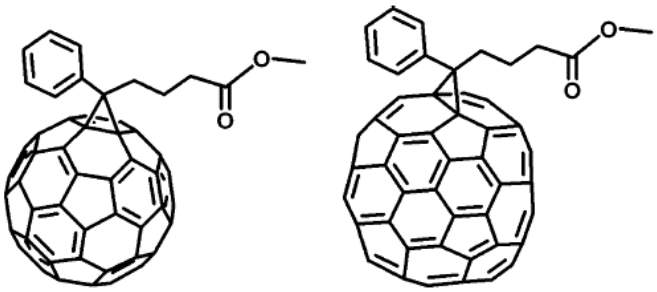

$PC_{61}BM$ $PC_{71}BM$

Figure 3.6- The molecular structure of $PC_{61}BM$ and $PC_{71}BM$.

One of the most noticeable distinctions between $PC_{61}BM$ and $PC_{71}BM$ is their optical absorption, as shown in Figure 3.7.

Both molecules are active in the ultraviolet (UV) region (200–400 nm). However, $PC_{71}BM$ exhibits stronger absorption in the visible region (400–700 nm) compared to $PC_{61}BM$. This is why OSC devices fabricated from $PC_{71}BM$ blends demonstrate higher performance levels (Zhang et al., 2012). Although the $PC_{71}BM$ molecule has garnered more interest as an electron acceptor material, it is important to note that $C_{70}$ ($C_{71}$) molecules are more expensive to synthesize than $C_{60}$ ($C_{61}$) due to complex purification processes (Hou and Guo, 2013b).

[14] Phenyl-C61(C71)-butyric acid methyl ester

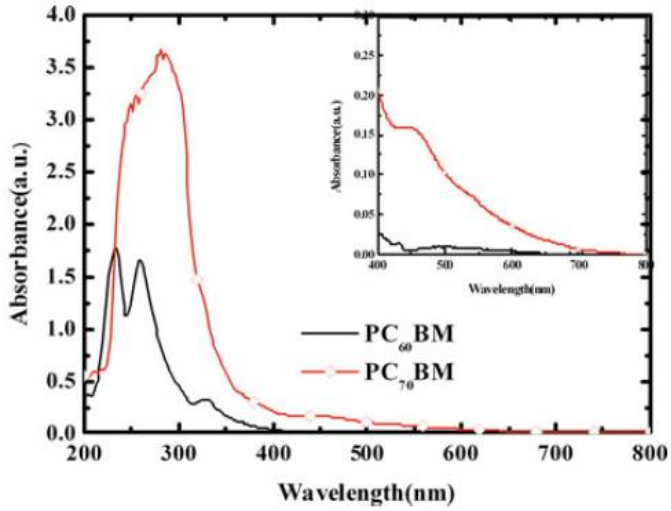


Figure 3.7- Optical absorption of PC61BM and PC71BM, inset: absorption in the 400–800 nm wavelength range (Hou and Guo, 2013b).

The energy levels of the acceptor materials play a crucial role in the performance of OSCs, as the open-circuit voltage ($V_{oc}$) is directly proportional to the difference between the highest occupied molecular orbital (HOMO) of the donor and the lowest unoccupied molecular orbital (LUMO) of the acceptor material in bulk heterojunction (BHJ) OSCs (Brabec, Sariciftci, and Hummelen, 2001; Brabec et al., 2006). Therefore, the LUMO level of fullerene and its derivatives is a critical parameter for determining the performance of OSCs. The LUMO levels of $PC_{61}BM$ and $PC_{71}BM$ are similar, measured to be approximately -3.91 to -4.0 eV (He and Li, 2011). However, the $C_{61}$ molecule has a deeper LUMO level of around -4.2 eV (Sariciftci et al., 1993). By using substituents to form a $PC_{61}BM$ molecule, it is possible to alter or enhance the LUMO level of the $C_{61}$ molecule. Since the LUMO level of the acceptor material is crucial in determining the $V_{oc}$ for OSCs, designing acceptor molecules with higher LUMO levels could potentially enhance the $V_{oc}$ value.

## 3.4 Charge Blocking & Buffer layers

In the fabrication of OSCs, buffer layer materials are commonly employed to both extract the desired charge from the associated electrode and block the undesirable charge. It is for

these characteristics that they are also referred to as electrode interfacial layer (Yin, Wei and Zheng, 2016). One of the most common materials used as a buffer layer for hole extraction is *poly* (*3, 4-ethylene dioxythiophene*) *polystyrene sulfonate*. PEDOT: PSS is an aqua base solution which is sandwiched between a clean ITO surface and the active layer (for conventional architecture) (Sariciftci *et al.*, 1993). Use of PEDOT: PSS as a buffer layer became noticeable when it was used in the fabrication of OLEDs in 1997, which resulted in enhancement performance and the stability of the OLED devices (Carter *et al.*, 1997). PEDOT: PSS was used as a buffer layer between the ITO and the active layer. The molecular structure of PEDOT: PSS is illustrated in Figure 3.8.

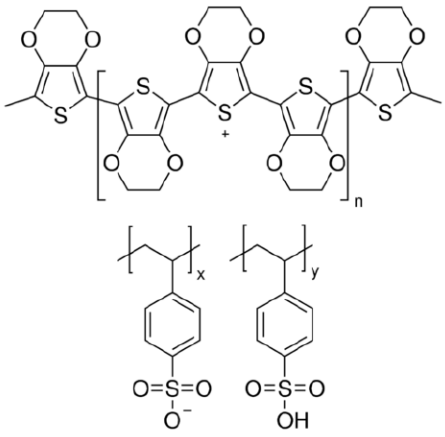

Figure 3.7- The molecular structure of PEDOT: PSS.

Using a spin coating process, a thin, transparent layer of PEDOT:PSS is typically fabricated on an ITO-coated substrate. This material possesses several key characteristics, including a smooth surface and strong electrical conductivity (Sariciftci et al., 1993).

As a hole-conducting layer, PEDOT:PSS has the ability to reduce the surface roughness of the ITO-coated substrate and stabilize the electrical contact between the active layer and the electrode (Krebs et al., 2008). This is attributed to the matching work function of PEDOT:PSS with the ITO electrode. Consequently, the energy barrier between the anode electrode and the active layer is minimized, leading to more efficient hole charge collection (Sariciftci et al., 1993).

Similarly, at the cathode electrode where electrons are collected, buffer or interfacial layers are employed. Examples of such materials include Calcium (Ca) and lithium fluoride (LiF) in conventional architectures (Li, Vamvounis, and Holdcroft, 2002; Wang et al., 2013). Due

to their low work function, these materials provide stable electrical contact between the cathode and the active layer. Both Ca and LiF are typically deposited via thermal deposition techniques on top of the active layer prior to electrode deposition.

For measuring charge carrier mobilities, it is crucial to fabricate single charge carrier devices resembling a diode configuration (Coropceanu et al., 2007). These devices are constructed with the active layer sandwiched between two buffer layer materials capable of blocking one type of charge (i.e., holes or electrons). For instance, PEDOT:PSS can only be utilized to fabricate a hole-only device since it is a hole-conducting material. Conversely, for an electron-only device, Cesium carbonate ($Cs_2CO_3$) serves as an ideal material to increase the energy barrier at the anode (ITO) electrode and block any injected holes (Shrotriya, Yao, et al., 2006).

## 3.5 Organic solvents

One of the primary challenges in using non-chlorinated solvents in OPV systems is the limited compatibility between polymers and these solvents. To address this issue, researchers have employed various analyses to initially screen potential green solvents. Among OPV systems, P3HT/PCBM stands out as one of the most extensively studied (Zang et al., 2014). The successful implementation of non-halogenated processing in the P3HT/PCBM system has spurred researchers to explore new combinations of capable OPV materials.

In an initial endeavour, researchers discovered that all-polymeric OPVs could be processed using toluene or o-xylene (o-XY), resulting in a PCE of 1–2% (E. Zhou et al., 2011; Zhou et al., 2014). More recently, a report showcased the first instance of non-halogenated solution processed OPVs based on non-fullerene small molecule acceptors (Zang et al., 2014). These fullerene-free OPV devices processed from o-xylene exhibited a relatively high PCE of 5.2%, albeit slightly lower than that obtained using traditional DCB, indicating favourable green solvent processability in existing non-fullerene acceptors.

Subsequent research studies have demonstrated the processing of other high-performance OPV materials using various halogen-free solvents, resulting in PCEs exceeding 7% (References in Table 3.2). Sprau et al. (2015) found that XY/anisaldehyde (AA) performed well in several systems. Particularly noteworthy is the green solvent system's ability to yield

a PCE of up to 9.5% in PffBT4T-2OD OPVs at a film thickness of 300 nm. These reported results underscore the significant trend that PCEs achieved through green-solvent-processing are comparable to those obtained using traditional toxic solvents.

Several green solvents, commonly mentioned in the literature as alternatives to chlorinated and halogenated solvents, are illustrated in Figure 3.9.

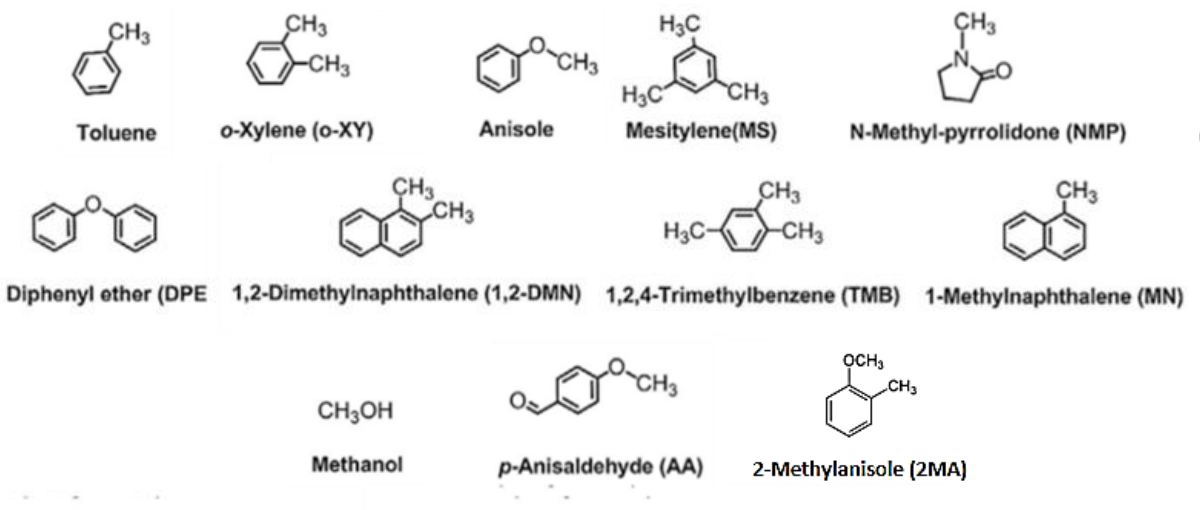


Figure 3.9 – The chemical structures of common non-halogenated solvents commonly reported in the literature as alternatives to chlorinated and halogenated solvents.

For this research study, three top-performing green solvents have been selected from Table 3.2 based on their compatibility parameters with the narrow band gap polymer PBDTTT-EFT (PTB7-th). These solvents are listed as follows:

- Dimethylnaphthalene (DMN)
- o-Xylene:p-Anisaldehyde (o-XY)
- 2-methylanisole (2MA)

Table 3.2 presents the electrical characterization results of commonly reported green solvents in the literature, serving as alternatives to chlorinated and halogenated solvents. The top three green solvents—DMN, o-Xylene, and 2MA—have been identified as the best options due to their compatibility with our chosen blend of polymer and acceptor.

.

Table 3.2 - Electrical characteristics of OPVs fabricated with commonly used various green solvents

| Light-harvesting layer | Halogen-free solvent | Voc (v) | Jsc (mA/cm2) | FF | PCE (%) | Ref. |
|---|---|---|---|---|---|---|
| P3HT/PC61BM | MS/AP (20%) | 0.58 | 8 | 0.66 | 3.4 | (Park *et al.*, 2011) |
| P3HT/PC71BM | o-XY/NMP (2%) | 0.61 | 10.47 | 0.61 | 3.87 | (Zhang *et al.*, 2016) |
| P3HT/IC60BA | Toluene/NMP (1%) | 0.85 | 10.3 | 0.75 | 6.6 | (Zhang *et al.*, 2016) |
| PBDTTT-TEG/PC71BM | NMP/DIO (5%) | 0.66 | 13.53 | 0.59 | 5.23 | (Chen *et al.*, 2014) |
| PBDTTT-S-TEG/PC71B-DEG | Anisole | 0.75 | 12.41 | 0.49 | 4.5 | (Chen *et al.*, 2015) |
| PIDT-phanQ/PC71BM | Toluene/MN (2%) | 0.87 | 10.8 | 0.65 | 6.11 | (Chen *et al.*, 2012) |
| PFDT2BT-8/PC71BM | CS2/Acetone (20%) | 0.94 | 10.68 | 0.68 | 6.81 | (Griffin *et al.*, 2015) |
| PBDT-DTNT/PC71BM | o-XY/1,2-DMN (2.5%) | 0.79 | 11.82 | 0.65 | 6.1 | (Kaduwal *et al.*, |
| PIDTT-DFBT/PC71BM | o-XY/1,2-DMN (2.5%) | 0.97 | 12.89 | 0.57 | 7.15 | (Chueh *et al.*, 2013) |
| P(1FIID-BT)/PC61BM | *o*-XY | 0.89 | 14.5 | 0.58 | 7.46 | (Dong *et al.*, 2015) |
| PTB7/PC71BM | o-XY/NMP (2%) | 0.73 | 16.4 | 0.65 | 7.74 | (Zhang *et al.*, 2016) |
| PDTSTPD/PC71BM | TMB/1,5-DMN | 0.9 | 13.42 | 0.7 | 8.45 | (Zang et al., 2014) |
| PBDT-TS1/PC71BM | 2-Methyl Anisole | 0.79 | 17.39 | 0.70 | 9.67 | (He *et al.*, 2011) |
| PffBT4T-2OD/PC71BM | o-XY/AA (1%) | 0.74 | 18 | 0.69 | 9.5 | (Sprau *et al.*, 2015) |

Radar analysis, also referred to as a spider chart or web chart, is used to display multivariate data in a two-dimensional chart. This type of analysis is particularly useful when different options need to be compared based on multiple criteria.

The critical parameters impacting the performance of OSC devices are power conversion efficiency (PCE), short circuit current density (Jsc), open circuit voltage (Voc), and fill factor (FF). For the top three green solvents with the highest PCE in this table, data points were plotted on the respective axes using this analysis, and the points for each solvent were then connected to form a polygon. Each polygon represents the performance of one solvent across all parameters. Better overall performance is indicated by larger polygons if higher values are preferable. Figure 3.10 shows this radar analysis chart.

Based on the parameters presented in this table, and balancing each parameter on a four-axis scale while aiming for the highest power conversion efficiency, it is concluded that the polygons for 2MA and o-Xylene are larger and more balanced compared to DMN.

Therefore, 2MA and o-Xylene are determined to be better optimal components and are expected to exhibit better compatibility with the chosen polymer/acceptor system, thus warranting further investigation.

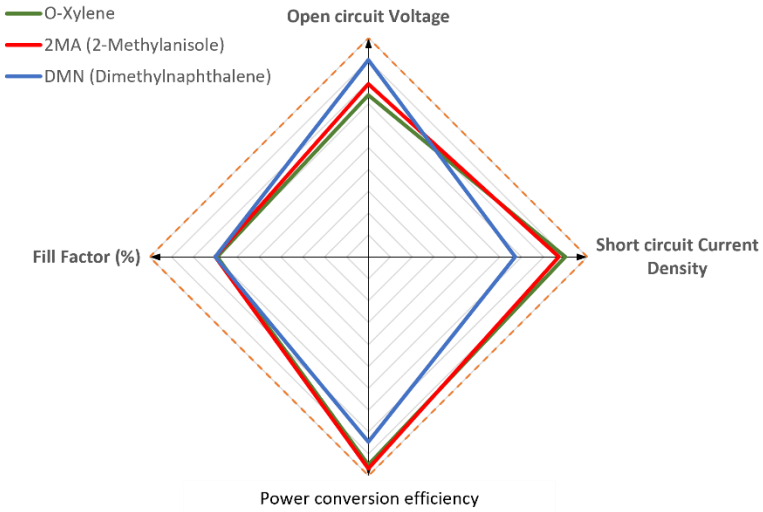


Figure 3.10 – Radar analysis of critical parameters in OSC devices

## 3.6 Summary

The polymer selected for this project was PBDTTT-EFT (PTB7-th) from the narrow band gap polymers category, used as the donor material in the active layer. This choice was made because PBDTTT-EFT has been reported to have high potential as a donor material for OSC applications. The fullerene derivative $PC_{71}BM$ was chosen as the electron acceptor material in the active layer, based on previous studies (Komilian, Oklobia, and Sadat-Shafai, 2018b) that indicated the best compatibility and performance with this polymer.

The molecular structures of these materials are shown in Figure 3.11 below.

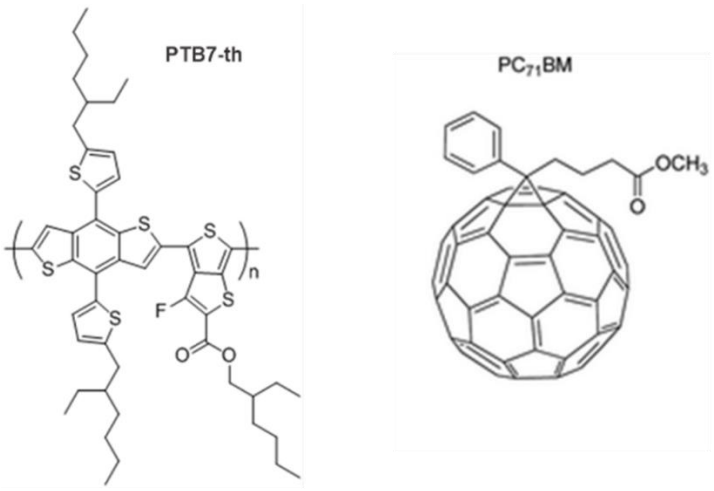


Figure 3.11– Molecular structure for commonly used highly efficient polymer and fullerene derivative acceptor

Since 2019, the outcome of this project has been utilized in one of the significant funding initiatives in the UK, the British Council's "Newton Fund." In this project, other NFA (Non-Fullerene Acceptors) materials such as Y6, Y7, and D18 have been investigated as alternative compatible donor pairs, though this exploration is beyond the scope of this thesis.

D18, also known as PCE18, is a narrow bandgap copolymer with a backbone alternating between electron-donating benzodithiophene (BDT) and electron-accepting fused-ring dithienobenzothiadiazole (DTBT) units. Due to its larger molecular plane structure and higher degree of conjugation from the fused ring DTBT, D18 exhibits a high hole mobility of $1.59 \times 10^{-3}$ $cm^2$ $V^{-1}$ $s^{-1}$ (Liu et al., 2020).

Y6 (BTP-4F) is a highly conjugated organic semiconductor composed of a fused thienothienopyrrolo-thienothienoindole (TTP-TTI) core base and 2-(5,6-difluoro-3-oxo-2,3-dihydro-1H-inden-1-ylidene) malononitrile (2FIC) end units. These 2FIC end units are believed to promote intermolecular interactions and enhance optical absorption. With an A-DAD-A structure, this molecule is electron-deficient and is used in highly efficient OPV devices as a non-fullerene electron acceptor (NFA). The absorption of Y6 peaks around 810 nm and extends to 1100 nm, corresponding to the near-infrared range, which can improve the absorption range in OPV devices (Liu et al., 2020).

Figure 3.12 shows the molecular structures of these two molecules.

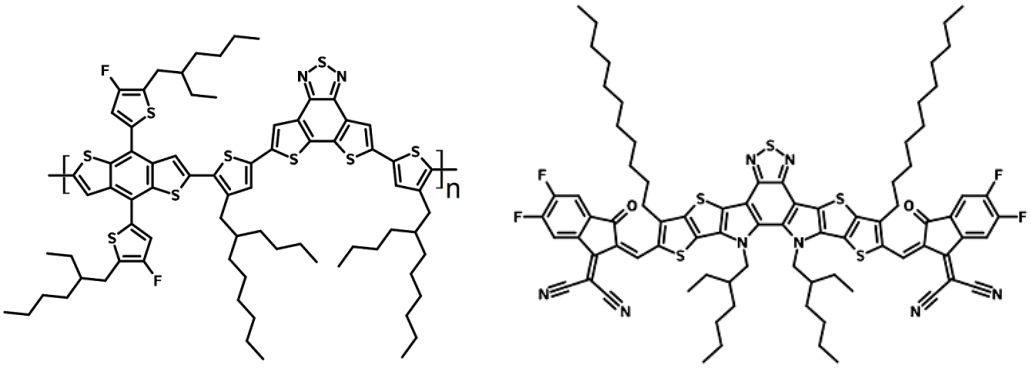

**D18** **Y6**

Figure 3.12– Molecular structure for polymer and Non-fullerene derivative acceptor which is used in Newton Grant Project

# CHAPTER 4

# Methodology & Experimental Approach

*"An experiment is a question which science poses to Nature, and a measurement is the recording of Nature's answer."*

***- Max Planck, Theoretical Physicist***

## 4.1 Introduction

Most of the investigation in this research project was conducted through experimental methods. These methods were chosen to facilitate a better understanding of new materials, eco-friendly solvents, and the structural aspects of devices used in organic solar cell (OSC) fabrication. Samples were prepared with an active layer thickness of approximately 100 nanometers. Throughout the fabrication process, other variables were kept constant to highlight the impact of employing different eco-friendly solvents.

To deepen comprehension of fundamental issues related to OSC pre-fabrication processes, such as the use of eco-friendly solvents and the exploration of novel approaches to enhance OSC performance, a wide range of literature was reviewed. A selection of appropriate eco-friendly solvents was made based on this review. Subsequently, further research and testing were conducted on these materials and the developed analysis techniques.

All experimental work in this project was carried out at Staffordshire University using the university's equipment. The location of this equipment on campus is indicated in the accompanying figure captions.

## 4.2 Experimental Procedures

In this section, the experimental procedures and techniques for sample and device fabrication are described sequentially. Each step is meticulously outlined to provide a comprehensive understanding of the fabrication process. From material selection to sample preparation and device assembly, every aspect is carefully considered to ensure precision and accuracy.

### 4.2.1 Device Architecture

The architecture typically used for the fabrication of Organic Solar Cell (OSC) devices for I-V characteristics, as depicted in Figure 4.1, follows a specific layering order. The simplicity of the fabrication techniques involved is a key factor contributing to the increasing appeal of this structure in BHJ organic solar cells. These devices predominantly feature an active layer made from solution-processable materials.

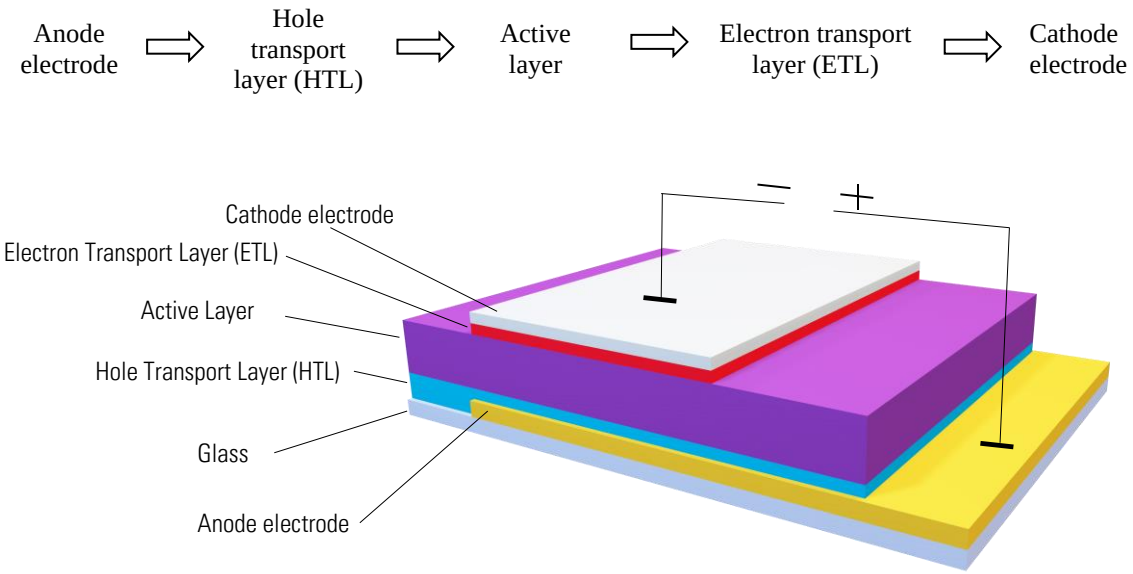


Figure 4.1 – Bulk heterojunction architecture of organic solar cells

The Electron Transporting Layer (ETL) and Hole Transporting Layer (HTL) serve as optional buffer layers commonly utilized in Organic Solar Cells (OSCs) fabrication. They play a crucial role in extracting the desired charge from the associated electrode and blocking undesirable charge, as noted by Olivier et al. (2014).

Below, Table 4.1 presents a comprehensive list of materials and chemicals utilized in fabricating thin film samples and devices for this project.

Table 4.1- Summation of materials and chemicals used in this project.

| | Materials / Chemicals |
|---|---|
| Buffer layers | Hole transport layer: Poly(3,4-ethylenedioxythiophene)-poly(styrenesulfonate) (**PEDOT:PSS**), Electron transport layer: Calcium (**Ca**) |
| Electrode contacts | Cathode: Aluminium (**Al**), Silver (**Ag**), Anode: Indium Tin Oxide (**ITO**) |
| Active layers | Poly[4,8-bis(5-(2-ethylhexyl)thiophen-2-yl)benzo[1,2-b;4,5-b']dithiophene-2,6-diyl-alt-(4-(2-ethylhexyl)-3-fluorothieno[3,4-b]thiophene-)-2-carboxylate-2-6-diyl)] (**PBDTTT-EFT / PTB7-Th**), [6,6]-Phenyl-C61-butyric acid methyl ester (**$PC_{61}BM$**), [6,6]-Phenyl-C71-butyric acid methyl ester (**$PC_{71}BM$**), 1',1'',4',4''-tetrahydro-di[1,4]methanonaphthaleno[5,6]fullerene-C60 (**ICBA**) |
| Solvents | Chlorobenzene anhydrous, 99.8% (**CB**), 1,2-Dichlorobenzene anhydrous 99% (**ODCB**), **Methanol**, **Ethanol**, **Acetone**, 2-Propanol (Isopropanol) (**IPA**), **DMN** (Dimethylnaphthalene), **o-XY:AA** (o-Xylene:p-Anisaldehyde), **2MA** (2-methylanisole) |

### 4.2.2 Substrates

In this project, three types of substrates are employed for various purposes:

- Indium Tin Oxide (ITO) coated glass substrates (25 mm × 25 mm): These substrates are utilized for the fabrication of OSC devices.
- Quartz substrates (25 mm × 25 mm): These substrates are chosen for optical and material characteristics analysis.
- Indium Tin Oxide (ITO) coated Polyethylene terephthalate (PET) flexible substrates (100 mm × 100 mm): These larger substrates are used for fabricating prototype OSC devices.

Quartz substrates are preferred over glass due to their distinct optical absorption coefficient, making them more suitable for collecting optical absorption data of thin films (Philipp, 1971; Cody et al., 1980). Glass substrates are not ideal for this purpose.

Since ITO is both electrically conducting and transparent, it needs to be patterned to identify the cell size and prevent short-circuiting during device fabrication (Tang, 1986b; Wu, 2004). ITO is coated only on one side of the glass substrate. To determine the conducting (ITO) side of the substrate, a multimeter was used in ohmic mode.

Once the coated side is identified, the patterning of the ITO can be achieved through two methods: the 'Etching' process, as depicted in Figure 4.2, or Surface laser etching using a laser cutter machine, described in the subsequent section.

### 4.2.3 Etching process / Laser surface patterning

As mentioned, the common technique for patterning the ITO layer involves using strong etching materials like Hydrochloric acid (HCl) to dissolve unwanted ITO from the surface. While this method is straightforward, one of its drawbacks is its limited accuracy in achieving the desired pattern, which is crucial for ensuring the cell size matches the design specifications.

The stages of the etching method are illustrated in Figure 4.2 and described as follows:

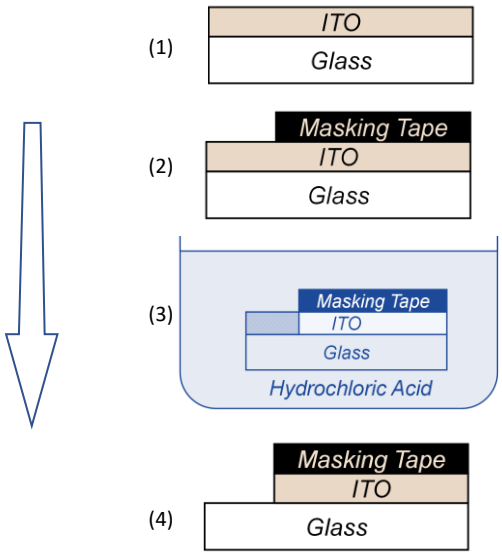


Figure 4.2- Schematic illustration of the ITO substrate Etching process.

1. The ITO-coated substrate is first covered with masking tape. It's important to use PTFE (polytetrafluoroethylene) tape, commonly known as Teflon tape, as it is highly resistant to a wide range of chemicals, including strong acids like HCl. This ensures the masking tape remains intact during the etching process.

2. The masking tape is then cut to the desired length, leaving a portion of the ITO exposed.
3. The masked substrate is submerged into a weak solution of Hydrochloric acid (HCl) for approximately 10 minutes. During this time, the HCl acid dissolves the exposed ITO.
4. After the allotted time, the substrate is removed from the HCl solution. The exposed ITO is now dissolved, leaving only the glass substrate behind. The substrate then undergoes a cleaning process to prepare it for the subsequent fabrication steps (refer to section 4.2.4).

The second method for identifying patterns on the ITO surface involves using a laser engraver. During the laser engraving process, the sample is secured onto the base plate of the laser machine, as illustrated in Figure 4.3.

Figure 4.3- Fixing sample on laser cutter/engraver machine base plate

As the laser beam interacts with the material, it generates intense heat. Depending on the duration of exposure, the material either evaporates or burns, resulting in colour changes and creating a visible contrast. The resulting laser etching is highly durable and resistant to abrasion. This technique is akin to printing: the engraving layout is first created in a graphics program such as Photoshop, AutoCAD, or Illustrator. The graphic is then sent to the laser using the printer driver. With a simple push of a button, the selected material is engraved or cut according to the predefined settings. Advanced settings can be adjusted using the provided laser software. Depending on the laser beam and hardware specifications, this method offers high accuracy and fast processing speeds.

In this project, the laser engraver used was the 'Trotec Speedy 400', located in the Smart Hub labs at Staffordshire University, as depicted in Figure 4.4.


Figure 4.4- Trotec speedy 400 laser cutter/engraver machine – (Smart Hub, Staffordshire University)

The design for patterning is initially created in Creo Parametric, a software for 2D and 3D computer-aided design (CAD) models. Once the pattern is verified to be fully compatible and overlapping with other layers modelled in Creo, the finalized model is imported into Adobe Illustrator.

Figure 4.5 showcases various ITO patterning designs prepared for the laser engraving machine, indicating which sections of the ITO need to be removed and which should remain intact. The white sections represent the ITO pattern, while the black sections show areas to be removed, ensuring proper electrical connections between cells.

Researchers often use a 3-cell pattern on one substrate for OSC fabrication due to several reasons. A major factor is the variation in uniformity across layers between the edges and the centre of the substrate, which can result from fabrication techniques. Additionally, etching techniques allow researchers to control the accuracy of the cell's surface area. These factors highlight the importance of the 3-cell pattern in optimizing OSC fabrication processes and ensuring consistent performance across substrates.

In this research, the 3-cell pattern shown in Figure 4.5 (a-c) was predominantly used in most cases. However, another pattern involved fitting 12 cells onto one substrate, as shown in Figure 4.5 (d-e). This arrangement aimed to investigate the passivation effect on cell efficiency following the application of suitable green solvents, with varying combinations of series and parallel connections.

Figure 4.5 (f) displays the Trotec Speedy 400 head while engraving the sample for a specific pattern. Figure 4.5 (f) shows the Trotec Speedy 400 head while engraving the sample for a specific pattern.

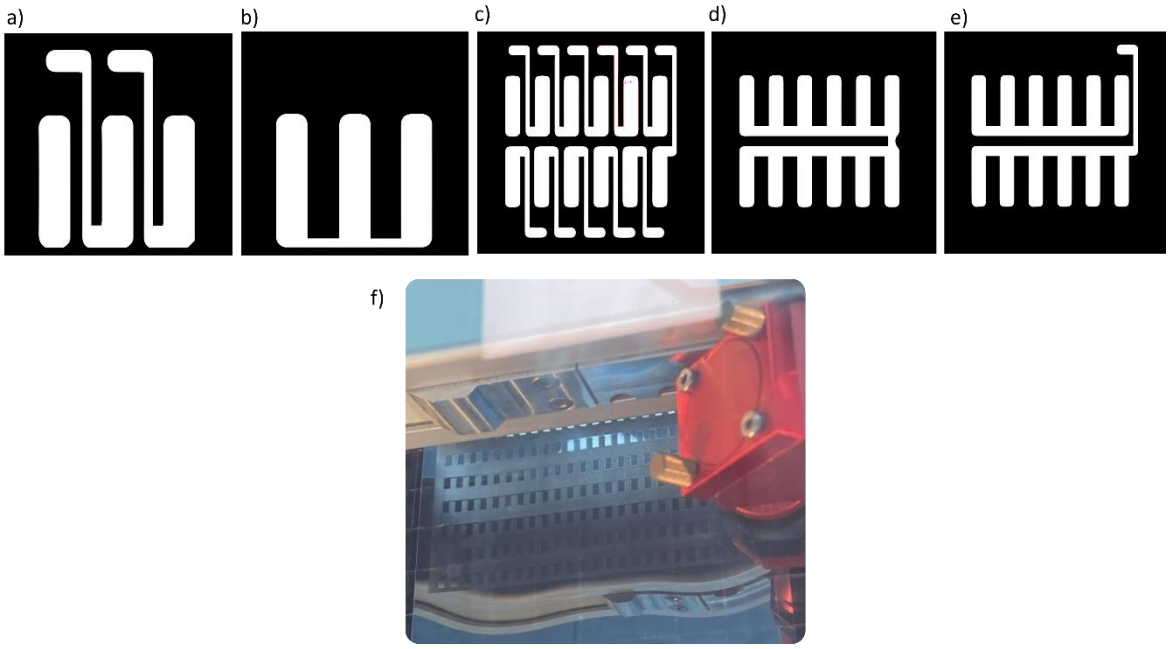


Figure 4.5- Various ITO patterning designs for organic solar cell (OSC) fabrication used in this research, a) 3-cells in series b) 3-cells in parallel c) 12-cells in series d) 12-cells in parallel e) 12-cells in combination of series and parallel f) the trotec speedy 400 laser oblations while engraving the sample for specific pattern

Using the laser surface patterning technique, patterns featuring either 3-cells or 12-cells in each substrate, arranged in series and parallel combinations, were designed and imported to the laser engraver to create the pattern on the ITO layer. Figure 4.6 below illustrates an example of an ITO patterned substrate after using this technique, which is now ready for the next step in cell fabrication. To measure the cells' output power and calculate the efficiency of the entire pattern, the same solar cell simulator was used, as described in section 4.2.6. The cells' connections and active area were designed based on a substrate size of 25mm × 25mm, resulting in an active area of 0.02 $cm^2$ for each cell in the 12-cell pattern and 0.13 $cm^2$ in the 3-cell pattern, when the top cathode electrode layer overlaps in the final fabrication step, defining this active area.

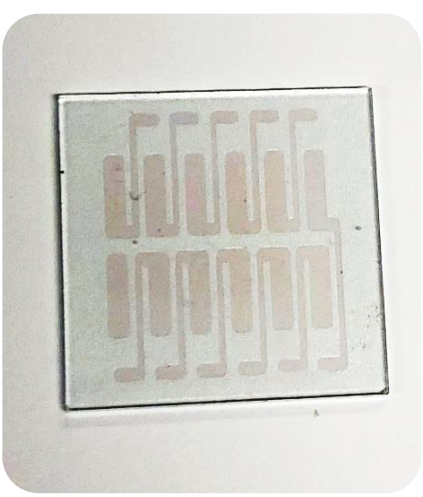

Figure 4.6- Example of the laser patterned ITO-substrate after using the laser engraving technique

If all the solar cells in a module have identical electrical characteristics and experience the same insolation and temperature, they will operate at the same current and voltage. In this case, the I-V output of the photovoltaic (PV) module mirrors that of the individual cells, except that the voltage and current are increased. The overall $I_{sc}$ (short-circuit current) and $V_{oc}$ (open-circuit voltage) of a set of identically connected solar cells are shown in equations 4.1 and 4.2 below. The total current is the current of an individual cell multiplied by the number of cells in parallel, and the total voltage is the voltage of an individual cell multiplied by the number of cells in series:

$$I_{SC}(\text{Total}) = I_{SC}(\text{Cell}) \times n \qquad (4.1)$$

$$V_{OC}(\text{Total}) = V_{oc}(\text{Cell}) \times m \qquad (4.2)$$

Here, *n* represents the number of solar strings in parallel, and *m* represents the number of solar cells in one series line.

The fill factor is typically lower when cells are combined due to mismatches, which may arise from manufacturing errors or variations in the light each cell receives. Under certain conditions, mismatch losses can significantly impact PV modules and arrays because the output of the entire PV module is controlled by the solar cell with the lowest output. For example, if one solar cell in a module is shaded while others are not, the power produced by the better-performing cells may be dissipated by the lower-performing cell rather than used to power the load. Therefore, having the proper pattern is crucial in designing large-scale PV modules (Mismatch Effects | PVEducation, 2019).

Chapter 5 will provide details on how these connection patterns significantly impact solar cell modules, including the results of using these patterns for the fabrication of prototype semi-large-scale modules.

### 4.2.4 Substrate cleaning procedure

Once the ITO-coated substrate is etched and patterned, it undergoes a cleaning process that is identical for both types of substrates used in this project. The cleaning process ensures that the substrates are free from any contaminants. This is achieved through three sequential stages using an ultrasonic bath. Each stage employs a different solvent:

- Stage 1: Submerge the substrates in a beaker filled with deionized water (DI $H_2O$) and place the beaker in the ultrasonic bath. Sonicate for 10 minutes.
- Stage 2: Repeat the process using acetone as the solvent.
- Stage 3: Finally, use isopropyl alcohol (IPA) in the same manner. After each stage, dry the substrates thoroughly. After the final IPA stage, place the dried substrates in a Petri dish and transfer them into a nitrogen ($N_2$)-filled glove box as shown in Figure 4.7, maintaining environmental conditions of less than 1 ppm (parts per million) of $O_2$ and $H_2O$.

All sample preparation and fabrications for this project are carried out inside the $N_2$ glove box.

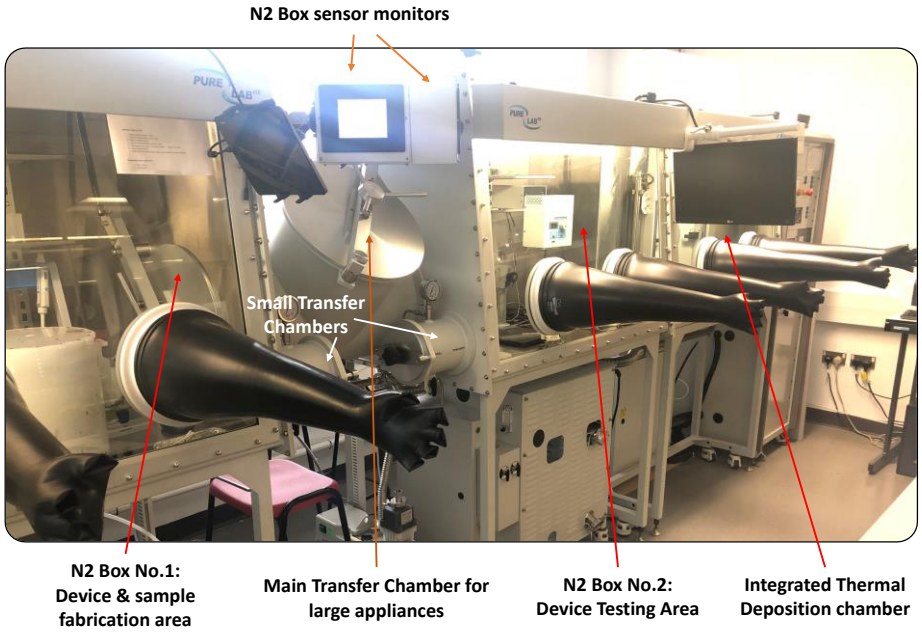


Figure 4.7- $N_2$ Glovebox system at R117 Thin Film Laboratory.

### 4.2.5 Samples fabrication procedure

With the samples now cleaned using the described cleaning process, the fabrication process proceeds with the remaining three steps (Figure 4.8):

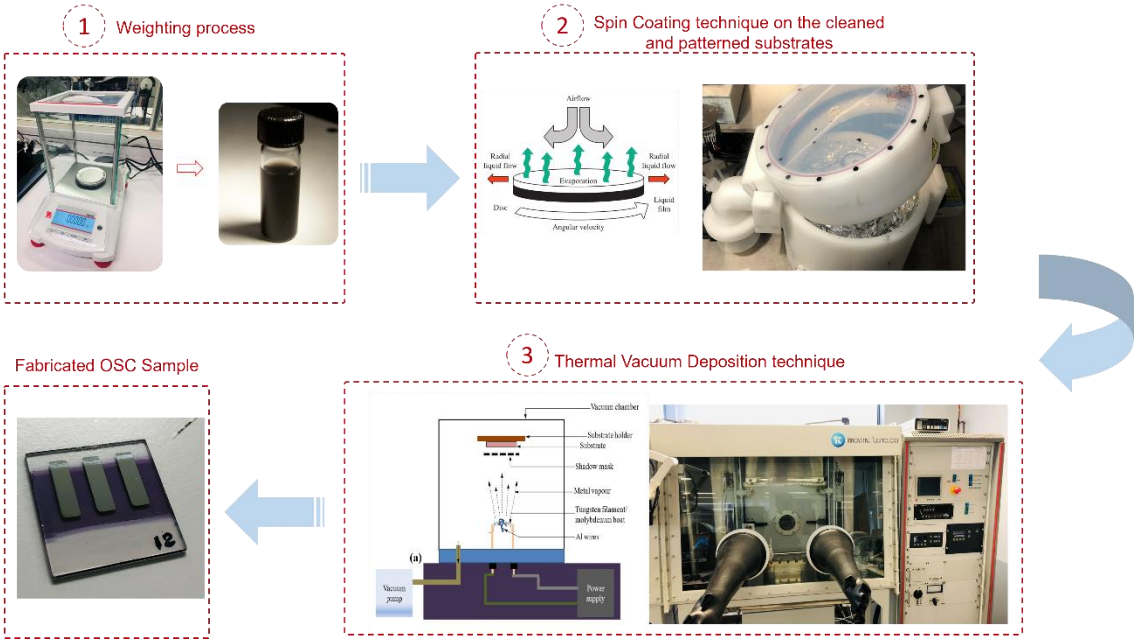


Figure 4.8- The OSC sample fabrication process after the cleaning step. (1) Weighing the materials for the layer solutions. (2) Spin coating the prepared solutions onto the cleaned and patterned substrates. (3) Depositing the top electrode pattern using the thermal vacuum deposition technique.

First, the materials used for the active layer of the OSCs need to be prepared into a solution form for fabrication. This involves dissolving the Donor-Acceptor materials in a solvent suitable for deposition onto the substrate. The process depends on the following parameters:

- The concentration of the solution
- The type of solvent (single or mixed)
- The D:A ratio

All active layer solutions are prepared according to the weights, concentrations, solvents, and D:A ratios specified in Table 4.2.

To prepare each sample or solution, the required weight of the materials is first measured in a vial using a scale. The vial is then transferred into the $N_2$ glove box. At this stage, the appropriate amount of solvent(s) is added to the materials, along with a disposable permanent magnet. The vial is then placed on a magnetic stirrer to ensure thorough dissolution of the solution, as shown in Figure 4.9.

Table 4.2- Summary of solution preparation in this project

| Material(s) | D:A | weight (mg) | Solvent [mixing ratio] | Concentration (mg $mL^{-1}$) |
|---|---|---|---|---|
| PBDTTT-EFT | n/a | 10 | ODCB | 10 |
| $PC_{71}BM$ | n/a | 10 | ODCB | 10 |
| PBDTTT-EFT | n/a | 10 | DMN | 10 |
| $PC_{71}BM$ | n/a | 10 | DMN | 10 |
| PBDTTT-EFT | n/a | 10 | o-XY:AA [100:1] | 10 |
| $PC_{71}BM$ | n/a | 10 | o-XY:AA [100:1] | 10 |
| PBDTTT-EFT | n/a | 10 | 2MA | 10 |
| $PC_{71}BM$ | n/a | 10 | 2MA | 10 |
| PBDTTT-EFT: $PC_{71}BM$ | 1:2 | 8.3: 16.7 | ODCB: CB [3:1] | 25 |
| | 1:2 | 8.3: 16.7 | DMN | 25 |
| | 1:2 | 8.3: 16.7 | o-XY:AA [100:1] | 25 |
| | 1:2 | 8.3: 16.7 | 2MA | 25 |

Each active solution was stirred for a recorded period before being used for device fabrication. This period is referred to as the ageing process. For solutions with ODCB[15]: CB[16] [3:1] solvents (Komilian, 2019), the ageing process is set to 48 hours. For green solvents, the ageing process exceeds 72 hours, depending on the solvent's dissolvability parameters.

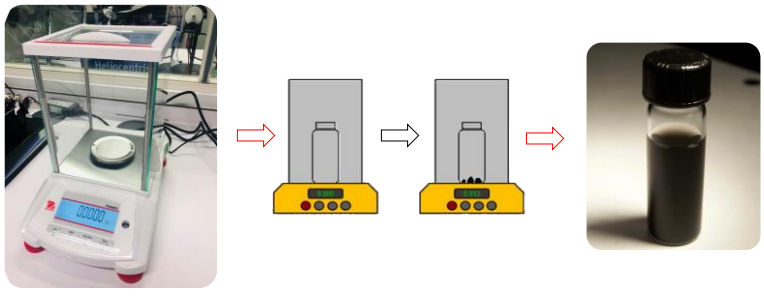

Step 1: Weighting the Polymer powder using an accurate analytical lab scale

Step 2: Adjust the amount of powder regarding the required concentration of the dispersion

Step 3: Mixing with appropriate solvent to prepare the solution processes material

Figure 4.9- Pictures and diagram illustrating the stages of active solution preparation.

[15] 1,2-Dichlorobenzene
[16] Chlorobenzene

In the subsequent step, spin coating is employed to fabricate samples onto the cleaned and patterned substrates (ITO/Quartz). This method has been widely preferred for fabricating OSCs (Norrman, Ghanbari-Siahkali, & Larsen, 2005; Krebs, 2009; Krebs et al., 2009). The process involves applying liquid to the surface of a substrate, which then spins at a predetermined rotational speed, acceleration, and period. This can be achieved by either initially applying the liquid to the substrate or during spinning. The angular velocity of the substrate's rotation causes any excess liquid to be expelled, leaving behind a thin film on the substrate.

As depicted in Figure 4.10, the spin coater utilized in this project was sourced from "Laurell Technologies," a renowned company in this field. It has the capacity to accommodate up to ø150mm wafers and 5" × 5" (127mm × 127mm) substrates, with a maximum rotational speed of 12,000 rpm (based on a ø100mm silicon wafer).

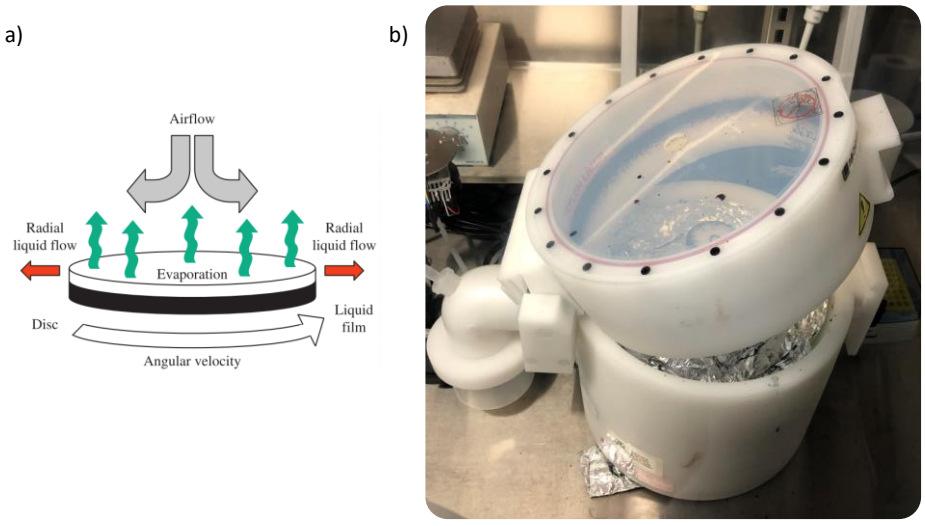


Figure 4.10- a)Schematic of Spin coating technique (Krebs, 2009) - b) Spin Coater system in R117 Thin film laboratory

When employing the spin casting technique, it is noted that the thickness and morphology of the film achieved for a specific concentration, material, and solvent can be replicated with minimal variations (Krebs, 2009). By adjusting parameters such as spin rotation speed, acceleration, and spin time, the desired film thickness can be attained. However, it is important to recognize that certain solution properties, including viscosity, volatility, and molecular weight of the materials, impose constraints on the achievable film thickness

(Krebs, 2009). Generally, the experimentally obtained film thickness $d$ can be mathematically expressed by a power-law relationship:

$$d = k\omega^{\alpha} \qquad (4.3)$$

Where $\omega$ represents the angular velocity, $k$ and $\alpha$ are empirical constants. These constants are determined by the physical properties of the solution, as previously mentioned (Krebs, 2009). This topic has been extensively reviewed and can be found in the literature (Norrman, Ghanbari-Siahkali, & Larsen, 2005; Krebs et al., 2009). By adjusting the spin speed, the film thickness will vary accordingly. An example of this phenomenon, following the equation above, is illustrated in Figure 4.11.

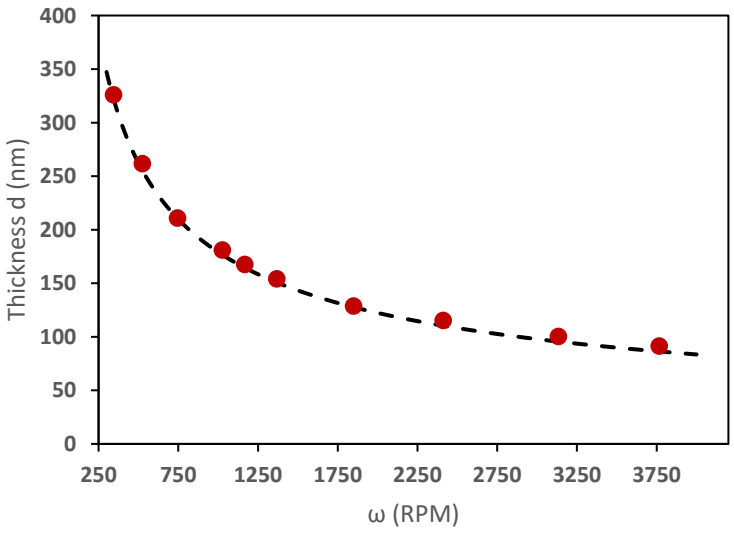


Figure 4.11- Plot of ω against d. Random Data generated using equation 4.3.

The final stage in fabricating OSC devices involves depositing the Electron Transporting Layer (ETL) buffer material, such as Calcium (Ca), and metal electrodes like Aluminum (Al) and Silver (Ag), using the thermal vacuum deposition technique. This process is commonly carried out using a thermal vacuum deposition system. In this project, the AUTO-500 vacuum deposition system from HHV Ltd was utilized. A schematic diagram of this system is presented in Figure 4.12.

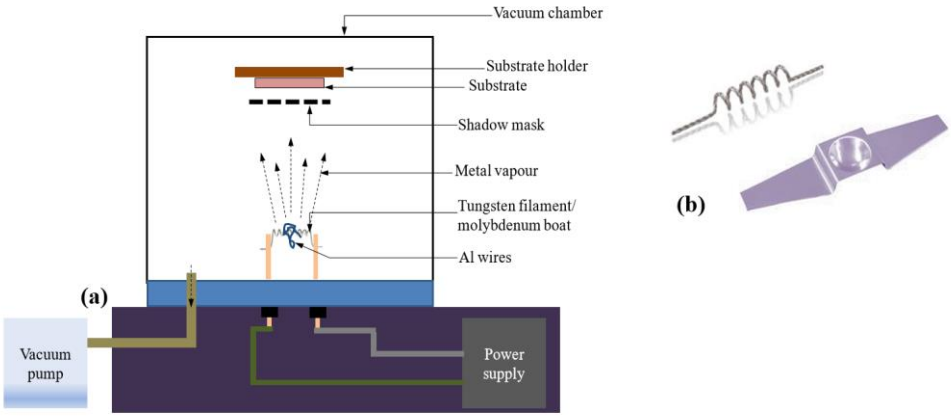


Figure 4.12- (a) schematic diagram of AUTO-500 thermal evaporation system used for electrode deposition. (b) Pictures of evaporation sources: Tungsten element and molybdenum dimple boat. (Oklobia, 2016).

During thermal deposition, the material(s) slated for deposition are evaporated within a high vacuum environment, typically around 10-7 mbar. Once the source material reaches its melting point, it evaporates. The resulting vapours then traverse through a shadow/lithography mask before settling onto the substrate's surface. Constructed and designed with holes, this mask serves as a barrier between the source and the substrate, permitting the deposition of vapor only in specific areas of the film. The lithography mask employed in this project was designed, developed, and manufactured by the author of this thesis. An example of such a mask is depicted in Figure 4.13.

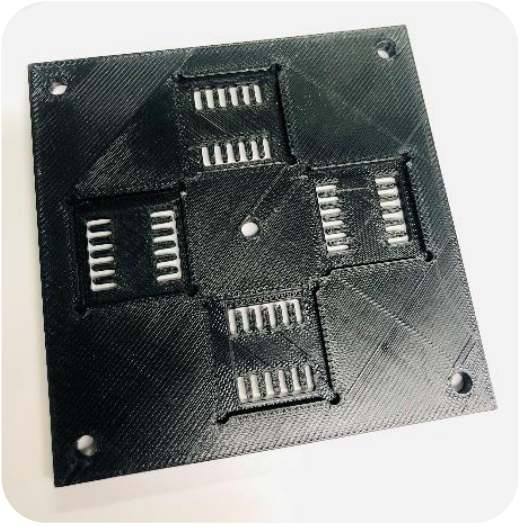

Figure 4.13- A Shadow mask example which is designed and developed for 12 cells in each substrate using in thermal vacuum deposition technique

The evaporated material condenses to create a layer on top of the active layer film. To monitor the thickness of this layer, a quartz crystal growth rate monitor, IL-150 (Intellemetric), is utilized. The IL-150 monitor operates by tracking alterations in the crystal's resonance frequency. The deposition rate of the source material(s) modifies the crystal's resonance frequency, which diminishes linearly with thickness. This change enables the determination of the thickness of the deposited material on the film (Buzea and Robbie, 2005). Figure 4.14 illustrates the Intellemetric system monitor.


Figure 4.14- Picture of Intellemetric IL-150 Quartz crystal growth monitor.

The Intellemetric monitor computer displays both the rate (nm/sec) and the total thickness of the deposited material. The deposition rate is adjustable by varying the electrical current supplied to the evaporation source. Depending on the material slated for thermal deposition, the corresponding evaporation source depicted in Figure 4.12 is installed. For materials such as Al and Ca, Tungsten elements are employed, while molybdenum dimple boats are utilized as evaporation sources for Ag.

### 4.2.6 Solar Simulator

Fabricated devices undergo testing in both illuminated and dark environments to evaluate OSC performance. The illumination power must be calibrated and standardized to match 1 sun power before OSC devices are tested under illuminated conditions. Solar simulators are utilized to provide this illumination. In this project, the ORIEL LSH-7320 solar simulator, featuring class ABA uniformity and matched with a 1.5 AMG (air mass global) sun spectrum, is employed (Figure 4.15).

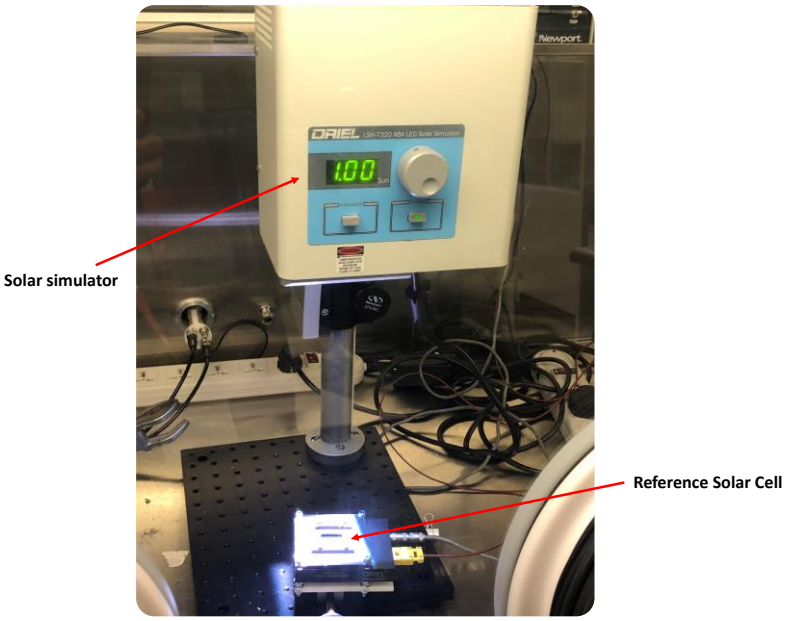


Figure 4.15- Pictures of ORIEL LSH-7320 ABA Solar simulator and Silicone solar cell reference

The light emitted by the solar simulator serves as the input power source for the fabricated OSC devices. The illumination light is adjusted and calibrated to generate a power density equivalent to 1 sun under 1.5 AMG conditions. This entails calibrating its input power density to 100 mW $cm^{-2}$ and regulating its spectral irradiance to 1.5 AMG, as depicted in Figure 4.16.

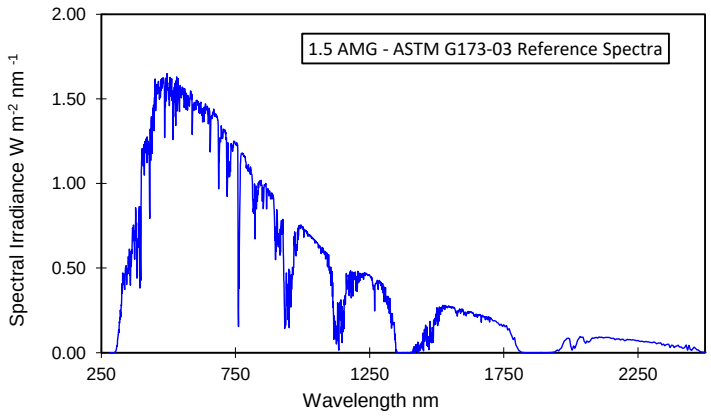


Figure 4.16- The plot of solar light against Spectral irradiance of 1.5 AMG with ASTM G173-03 standards.

To ensure that the input power density is accurately calibrated to 1 sun, a calibrated silicone reference cell and a meter (Newport 91150V) are utilized to monitor and calibrate the output power of the solar simulator (Figure 4.17). Light from the solar simulator, directed onto the

reference cell, is measured and displayed in sun units on the meter. The power of the solar simulator can be adjusted by modifying the electric current supplied to the system.

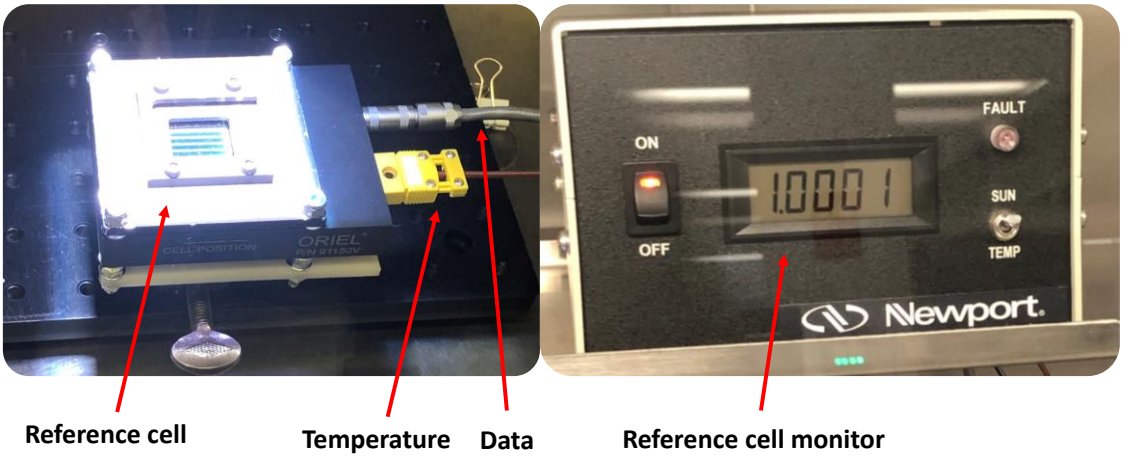


Figure 4.17- Pictures of left) Newport 91150V reference cell, right) reference cell monitor

In addition to adjusting the electric current supplied to the solar simulator, the power of the light source can also be modified by varying the distance between the solar simulator and the reference cell/OSC device. For this purpose, an XYZ stage mount compatible with the solar simulator's main power system and stand is employed.

## 4.3 Characterisation and analysis procedures

In this section, various methods will be employed to determine all the I-V electrical characteristics of the fabricated devices, including open-circuit voltage ($V_{oc}$), short-circuit current density ($J_{sc}$), fill factor (FF), and power conversion efficiency (PCE). These electrical characteristics are collectively referred to as DC-Characteristics. Additionally, structural and compositional techniques will be utilized for pre- and post-fabrication investigation analysis.

### 4.3.1 I-V measurement system

For measuring the I-V characteristics, the source meter unit (SMU) was utilized. Initially, the completed substrate was placed into a testing fixture with a shadow mask. Subsequently, the testing fixture cables were connected to the source meter unit (SMU), which is controlled by integrated software. The software enables the plotting of current (I) in amperes and

voltage (V) in volts for each set of three solar cells fabricated on one substrate. The number of solar cells depends on the pattern of the mask used for the thermal evaporation technique. Measurements are conducted both in dark conditions and under illumination at 100 mW/cm². Prior to this step, the intensity of the light source was calibrated to 1 Sun (100 mW/cm²) using a standard light cell, as described in Section 4.2.6 above.

The Keysight B2902A source-meter unit (SMU), as depicted in Figure 4.18, was employed to determine the current-voltage (I-V) characteristics of the OSCs. This equipment was consistently utilized throughout the project for collecting I-V data.

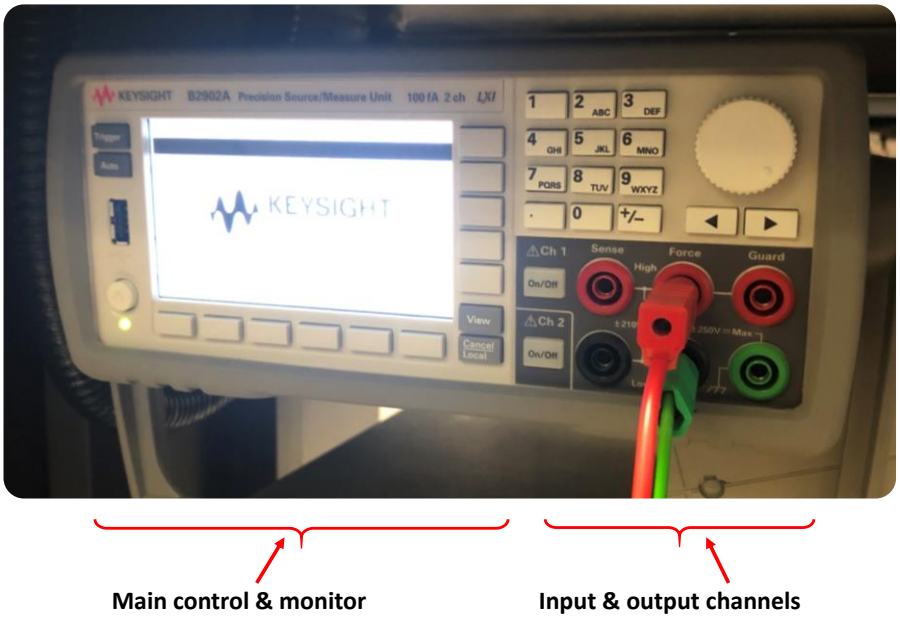


Figure 4.18- Keysight B2902A source-meter which is used in this project.

Integrated software from Keysight facilitated communication with and control of the SMU for data collection purposes. Parameters for data collection were configured within the software prior to initiating data collection. OSC devices were tested using a custom-built test station, presented in Figure 4.19. This test station facilitated the collection of I-V characteristics under both dark and illuminated conditions.

By importing the data of current (mA) and voltage (V) into spreadsheet software such as Excel, the current density of the cell's active area (mA/cm²) and other important parameters such as series resistance ($R_s$), shunt resistance ($R_{sh}$), fill factor (FF), short-circuit current ($I_{sc}$), and open-circuit voltage ($V_{oc}$) can be readily extracted using methods outlined in Chapter 2.5.

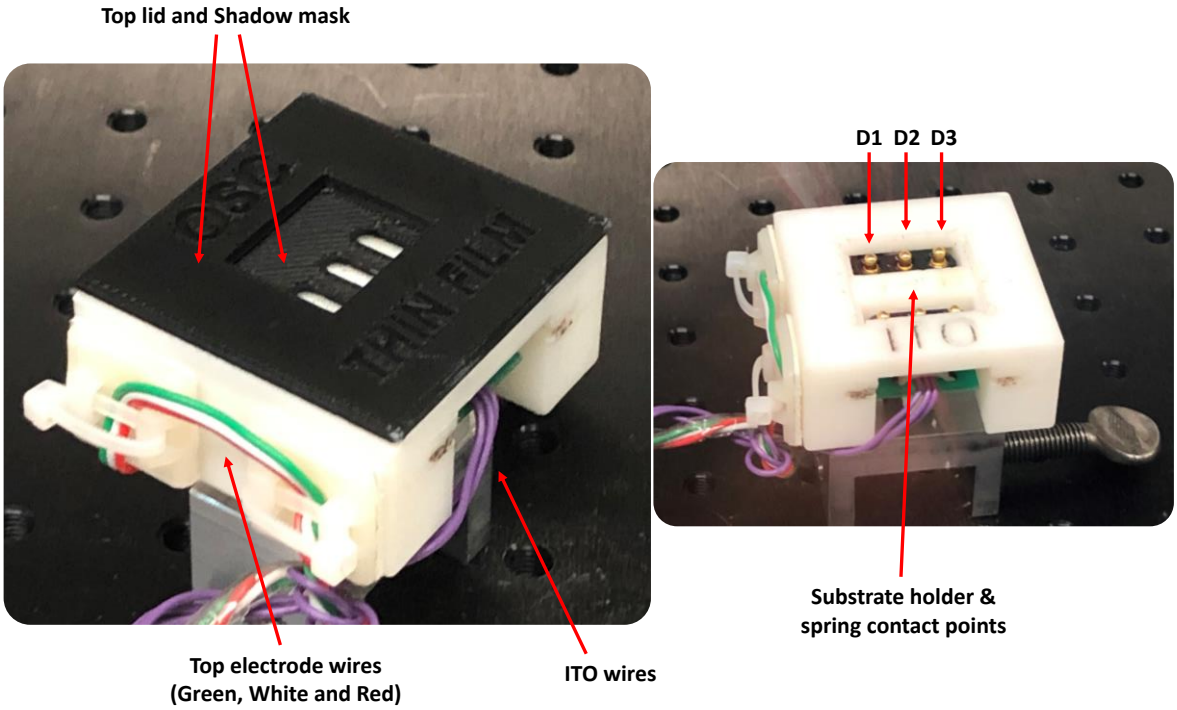


Figure 4.19- Pictures of the OSC device test station, left) top lid and the shadow mask designed for the substrates, OSC device test station fully mounted, identifying each connection wire: D1, D2, D3 (Green, White, Red) respectively and ITO wires (Purple), right) the substrate holder identifying the spring contact point.

### 4.3.2 Cyclic Voltammetry Measurement

Cyclic Voltammetry (CV) measurements were conducted in this work to determine the energy levels corresponding to the Highest Occupied Molecular Orbital (HOMO) and Lowest Unoccupied Molecular Orbital (LUMO) levels of polymers and acceptors. This technique has been previously utilized to provide direct information on the electrochemical p-doping and n-doping potentials ($\varphi_p$ and $\varphi_n$) of organic materials (Li et al., 1999). These potentials are also considered the reduction and oxidation potentials of the material. The CV measurement is based on the electrochemical mechanism, which includes both charge-transfer and charge-transport processes between an electrode and the material under study. Consequently, it is an appropriate technique for researching electroactive compounds (Kissinger and Heineman, 1983). Given that most organic materials are recognized as electroactive, CV measurements have proven effective in evaluating their energy levels (Dissanayake et al., 2008; Yoo et al., 2011).

In electrochemical terms, p-doping corresponds to the removal of electrons from the HOMO energy level, while n-doping corresponds to the addition of electrons to the LUMO energy level of the organic material (Misra et al., 2005). The HOMO and LUMO energy levels of the organic materials were evaluated from the onset potential of the p-doping ($\varphi_p^{ons}$) and the onset potential of the n-doping ($\varphi_n^{ons}$), respectively, according to the method reported by Li et al. (1999). The potential difference, i.e., $\Delta\varphi = \varphi_p^{ons} - \varphi_n^{ons}$, can be used to estimate the electrochemical energy gap of the material.

According to Leeuw et al. (1997), the HOMO and LUMO energy levels (in electron volts, eV), can be calculated using the formulae:

$$E_{HOMO} = -e(\varphi_p^{ons} + 4.4) \qquad (4.4)$$

$$E_{LUMO} = -e(\varphi_n^{ons} + 4.4) \qquad (4.5)$$

All electrode potential values are referenced against the Saturated Calomel Electrode (SCE). The SCE is widely used in electrochemical measurements due to its stable and reproducible potential. It consists of mercury in contact with a saturated solution of potassium chloride (KCl) and mercury(I) chloride ($Hg_2Cl_2$), commonly known as calomel. This setup provides a stable reference potential necessary for accurate voltage regulation in cyclic voltammetry (CV) measurements. The potential at the working electrode is controlled using forward and reverse voltage scans. The value 4.4 in Equations (4.4) and (4.5) is a scale factor in volts relating the SCE to the vacuum level (Albery et al., 1983). A typical electrochemistry setup with three electrodes in an electrolytic medium is depicted in Figure 4.16a.

In this work, a silver (Ag) wire was employed as a quasi-reference electrode. Following a method similar to that of Leeuw et al. (1999), the Ag wire was calibrated to be -0.01 V versus SCE. Therefore, Equations (4.6) and (4.7) can be expressed as follows:

$$E_{HOMO} = -e(\varphi_p^{ons} + 4.39) \qquad (4.6)$$

$$E_{LUMO} = -e(\varphi_n^{ons} + 4.39) \qquad (4.7)$$

A platinum wire was used as the counter electrode, while a polymer or fullerene/ITO served as the working electrode. The electrolyte used in this study consisted of lithium tri-

fluoromethanesulfonate (Li triflate) and tetrabutylammonium tetrafluoroborate (TBA BF4) salts dissolved in acetonitrile at a concentration of 0.01M.

All cyclic voltammetry (CV) measurements were conducted using an Agilent 5500 Atomic Force Microscope (AFM) equipped with an electrochemistry workstation. The measurements were performed at a scan rate of 50 mV/s. The Agilent 5500 AFM includes a potentiostat[17] and a galvanostat[18], which are used for controlling the voltage and measuring the corresponding current resulting from electron transfer processes. The setup of the Agilent 5500 AFM electrochemistry workstation is shown in Figure 4.20.

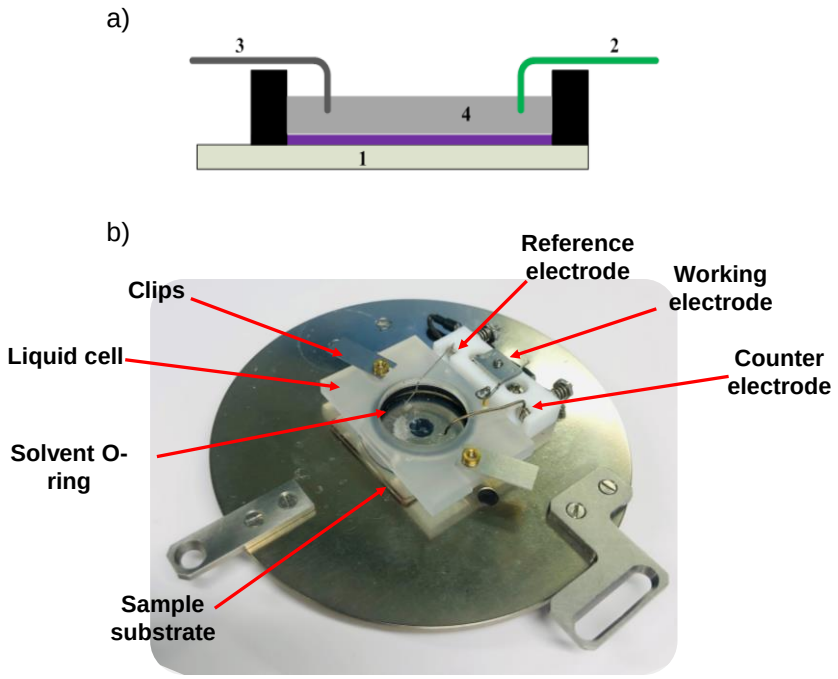


Figure 4.20 - (a) Schematic of the electrochemistry (CV) experiment setup: (1) working electrode, (2) reference electrode, (3) counter electrode, (4) electrolyte solution, (b) Picture of Agilent 5500 AFM electrochemistry station.

To determine the structure of the materials and devices, structural characterization will be employed. This helps in understanding the structure in depth, surface morphology, and assessing the impact of nano-structure formation on the device's output parameters, such as electrical characteristics. The methods used for this purpose will be explained in the following sections.

[17] A potentiostat is an instrument that measures. and controls the potential difference between a working electrode and a reference electrode

[18] A galvanostat (also known as amperostat) is a control and measuring device capable of keeping the current through an electrolytic cell in coulometric titrations constant, disregarding changes in the load itself

### 4.3.3 GIXRD – X-ray diffraction

The Grazing Incident X-ray Diffraction (GIXRD) method is utilized for characterizing the molecular structuring of materials in thin films. This technique offers valuable insights into the crystallography of the materials within the thin film, such as Donor and Acceptor materials.

The GIXRD system operates by directing a collimated X-ray beam onto the surface of the sample, with the beam's scattering pattern corresponding to the structure of the material(s) within the film, particularly the active layer. The scattered beam(s) are then detected by a detector. The incident beam is directed at an angle θ relative to the plane of the sample, and when interacting with the crystalline or micro-crystalline segments of the active layer, it undergoes diffraction.


Figure 4.21- Brucker D8 Advance X-ray diffraction machine – (Science building, Staffordshire University)

The intensity of the measured X-rays is dependent on the diffraction angle 2θ and the crystalline orientation. Figure 4.21 illustrates the GIXRD machine used in this research.

The equipment is configured with an XYZ stage, enabling the measurement of diffraction patterns of the thin film in 'out-of-plane' mode, as shown in Figure 4.22.

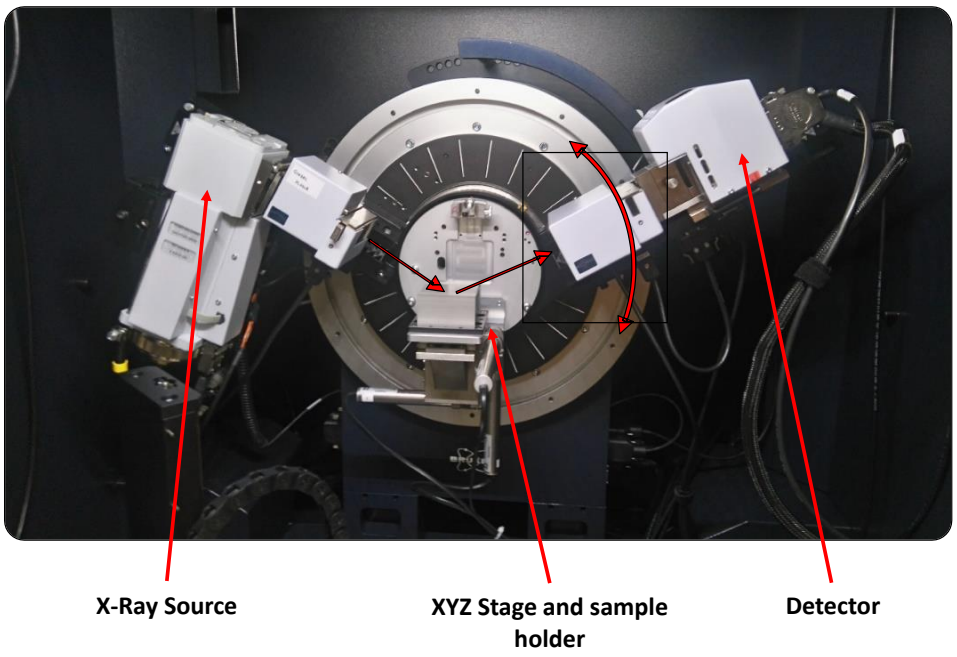


Figure 4.22- Brucker D8 Advance X-ray diffraction machine in XYZ setup position (Science building, Staffordshire University)

To enhance peak characteristics and optimize peak analysis on each sample, data from the diffractogram profile of the thin film coated onto the substrate is subtracted from the profile of a clean quartz substrate, isolating the profile of the films. This process is depicted in Figure 4.23.

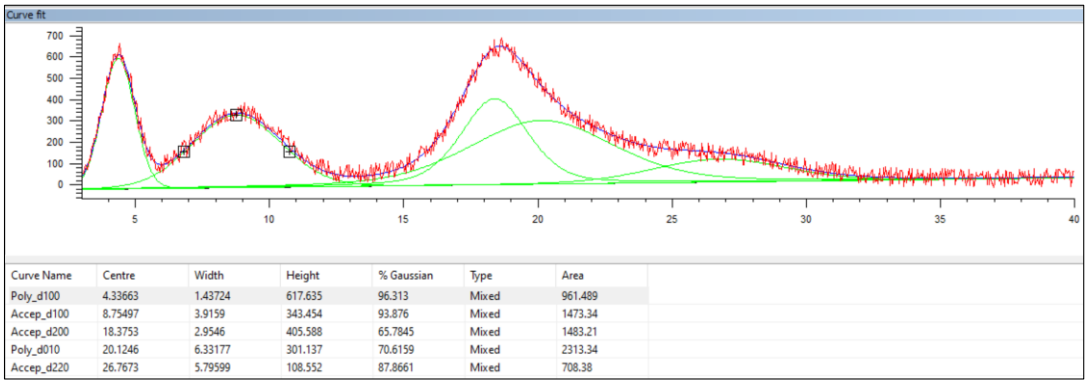


| Curve Name | Centre | Width | Height | % Gaussian | Type | Area |
|---|---|---|---|---|---|---|
| Poly_d100 | 4.33663 | 1.43724 | 617.635 | 96.313 | Mixed | 961.489 |
| Accep_d100 | 8.75497 | 3.9159 | 343.454 | 93.876 | Mixed | 1473.34 |
| Accep_d200 | 18.3753 | 2.9546 | 405.588 | 65.7845 | Mixed | 1483.21 |
| Poly_d010 | 20.1246 | 6.33177 | 301.137 | 70.6159 | Mixed | 2313.34 |
| Accep_d220 | 26.7673 | 5.79599 | 108.552 | 87.8661 | Mixed | 708.38 |

Figure 4.23. Out-of-Plane GIXRD diffractograms profile curve fit applied to PTB7-Th:$PC_{71}BM$ 1:2 [D:A] blend ratio for 100 nm film thickness. The software employs Gaussian and Lorentzian models for its best fit. Individual curve names are associated either to the donor or acceptor material. The miller indices planes of each material (dhkl) has been previously reported in the literature (Collins et al., 2013a).

The resulting diffractogram profile exclusively represents the fabricated thin film, as demonstrated in Figure 4.23.

All collected Out-of-Plane (OOP) GIXRD diffractogram profiles will be provided after the subtraction of the clean quartz substrate profile, a step included in the integrated computer software utilized for GIXRD data collection. Gaussian and Lorentzian curve fit techniques were employed to develop a computer model for each diffractogram profile with the best curve-fit match. All plots exhibit these computer-generated models as smoothed curves alongside the raw scattered data, along with diffractogram data for pristine materials.

### 4.3.4 AFM – Atomic Force Microscopy

In contrast to GIXRD, Atomic Force Microscopy (AFM) is a surface probing technique that is mechanically restricted to characterizing the surface of thin films. The surface morphology of thin films plays a crucial role in influencing the electrical performance of Bulk Heterojunction Organic Solar Cells (BHJ OSCs). AFM operates based on the interaction between a cantilever tip and the film surface.

To conduct the analytical part of this project, which involves comparing the electrical and physical properties of BHJ OSCs, surface morphology analysis of thin films was performed using Atomic Force Microscopy (AFM) measurement techniques, provided by Agilent Technologies, a prominent method in this field. Figure 4.24 illustrates the AFM machine used in this project.

The use of Atomic Force Microscopy dates back to 1986 when researchers first utilized the idea of AFM, employing ultra-small tips at the end of a cantilever beam to investigate the properties of non-conductive materials. Prior to this technique, a similar method was used in 1929 to amplify the movement distance at the end of a cantilever beam, magnifying it by a thousand times. This was known as a surface profile machine (Binnig and Quate, 1986).

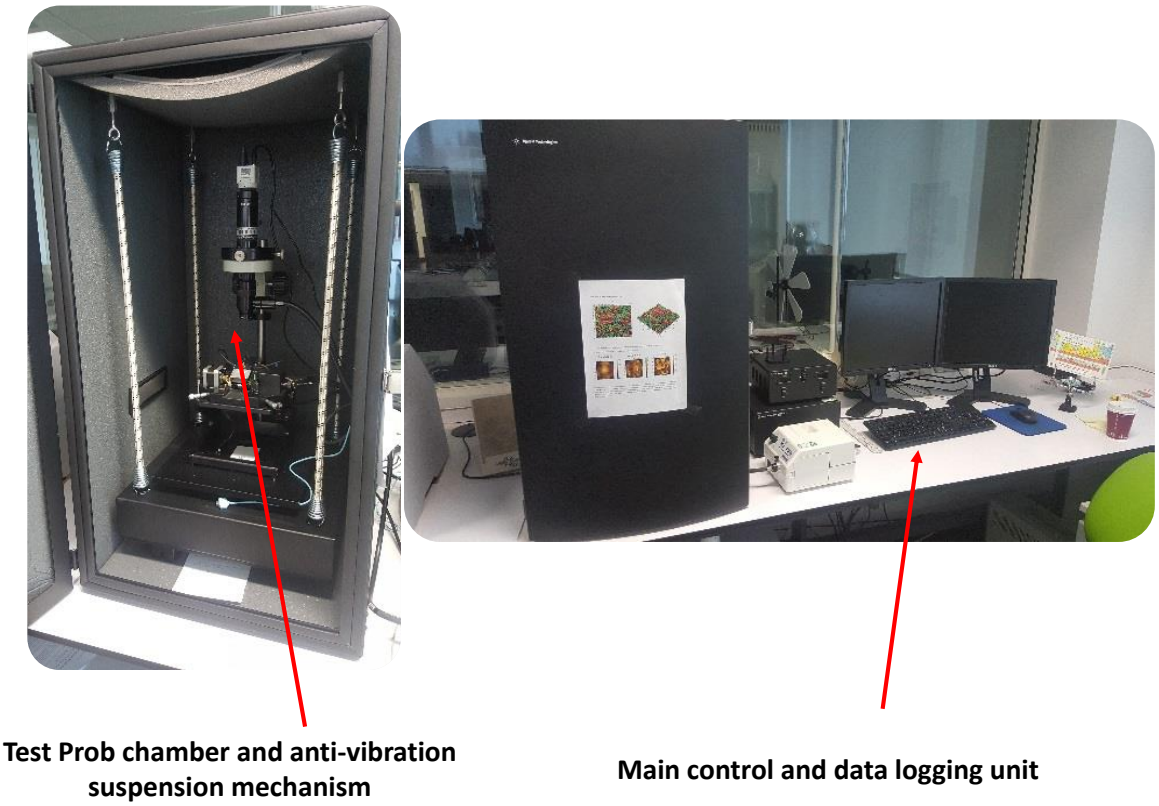


Figure 4.24- AFM Agilent 5500 Atomic Force Microscope (Thin film Lab R117, Science building, Staffordshire University)

Figure 4.25 depicts the schematic of general components and their functions from a control point of view. The principle of AFM is based on a laser diode, which is positioned at the back side of the tip head at the end of the cantilever. The laser beam is then reflected and detected by a position-sensitive photodetector.

The tip is divided into two parts: the cantilever and the head. The cantilever acts as a spring, deflecting while the probe head scans the sample surface. The probe tip senses the surface properties, causing the cantilever to deflect.

A PC control system is responsible for data acquisition, display, and analysis of the data obtained from the machine. To control the tip's z position, a feedback loop is integrated internally in the control system to make the output sensible.

These principles are illustrated in the figure, and the flowchart depicts the data transportation flows in the system schematically.

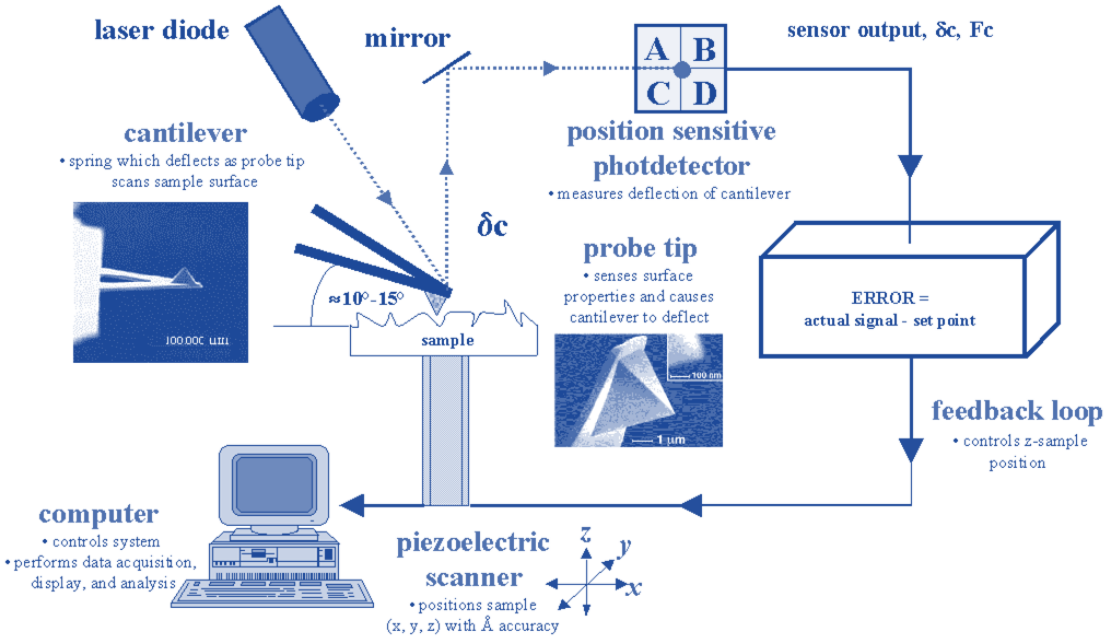


Figure 4.25- AFM machine components and their function inside control system (Li et al., 2012)

Different AFM imaging modes provide corresponding outputs. There are three types of imaging collections based on tips (Figure 4.26):

- Contact mode: In this mode, the feedback control system aims to maintain a constant cantilever deflection.
- Non-contact mode: The resonance frequency oscillates the tips, and the control system in this mode tries to keep the oscillation constant.
- Tapping mode: This mode sits somewhere in the middle of the previous two modes but is typically a subset of the non-contact mode.

The crucial aspect of these modes is that they rely on feedback control mechanisms to maintain a steady oscillation amplitude. The system includes a piezoelectric scanner for all modes imaging techniques, offering higher resolution with less damage to the film (Tessmer et al., 2013).

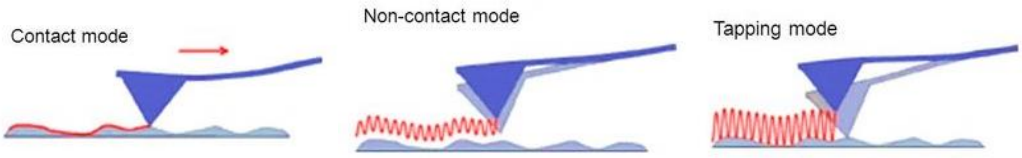


Figure 4.26- Various modes of imaging techniques with AFM tips: (a) Contact mode, where the tip maintains constant contact with the sample surface, (b) Non-contact mode, where the tip oscillates close to the surface without contact, and (c) Tapping mode, a combination of contact and non-contact modes. Each mode offers unique advantages in imaging samples with Atomic Force Microscopy (AFM), catering to different sample properties and imaging requirements.

### 4.3.5 RAMAN Spectroscopy and mapping

Raman and Photoluminescence (PL) spectroscopy serve as crucial techniques for analysing thin film samples. In this project, these spectroscopic methods were conducted using the InVia Raman microscope by Renishaw, as illustrated in Figure 4.27.

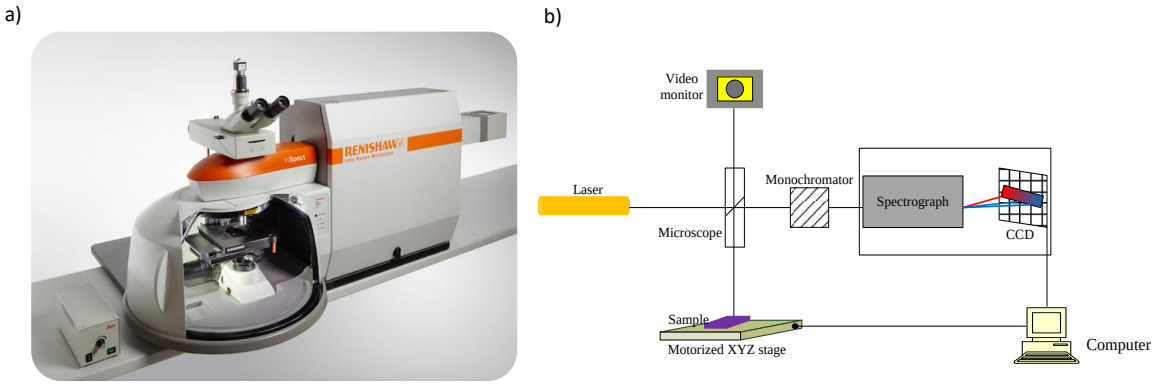


Figure 4.27 – a) Renishaw Raman and PL spectroscopy microscope which is used in this study (Science building, Staffordshire University), b) Principle of a conventional micro Raman spectrometer - Adapted from (Gouadec et al., 2007)

Raman spectroscopy functions by detecting the frequency shift of scattered light when it interacts with the sample under scrutiny. This phenomenon, known as Raman scattering, occurs when electromagnetic waves scatter light at both similar and different frequencies compared to the incident light. The frequency shift, termed Raman shift, corresponds to the energy of vibration of the scattering molecule.

Raman spectra serve as distinctive spectral and molecular "fingerprints," providing valuable qualitative and quantitative insights. They facilitate the identification and characterization of composite materials commonly utilized in organic electronics, such as blends of polymers or polymers/fullerenes for LEDs or solar cells. Qualitative analysis of Raman spectra can also map composite materials, while quantitative analysis correlates peak intensities with concentrations of functional groups.

Moreover, Raman spectroscopy delves into the nature of nanodomain conformation within composite materials, aiding in understanding their impact on OSC performance. Analysis of Raman spectra can correlate the full width at half maximum (FWHM) of peaks with polymer self-organization and crystallinity.

In this project, Raman mapping was employed as a technique to quickly observe changes in Raman parameters across different positions within the sample. This method facilitated the acquisition of spectrum information from various spots in the sample, enabling a comprehensive analysis of the entire Raman spectrum. Raman mapping generated Raman images, providing detailed insights into the spectral characteristics of the sample. Utilizing mapping methods such as point-by-point mapping and line focus mapping allowed for efficient data collection from multiple sample locations, enhancing the thoroughness of the analysis.

In this project, Raman data were obtained using 514 nm laser excitation, as $PC_{71}BM$ does not absorb light around 785 nm, the other available laser excitation. Therefore, identical Raman spectra were not observed at this wavelength due to the absence of vibration absorption in this range.

### 4.3.6 PL-Spectroscopy – To determine the (Photoluminescence)

PL spectroscopy is another technique employed in this project, working in conjunction with UV-Vis[19] and Raman spectroscopy to identify material characteristics. This method operates based on the spontaneous emission of light following photon absorption by the substance. When excitons, which are unable to be dissociated, recombine, it results in this light emission.

[19] Ultraviolet-visible spectroscopy

During PL measurements, the sample is excited with a laser of a chosen excitation wavelength. The photon emission from the material(s) is then condensed through an optical lens and measured by a spectrometer connected to a photodetector. This data is transferred to a computer to produce PL spectra.

PL spectra plots are constructed by plotting the emission counts (y-axis) against the emission wavelength (x-axis). PL mode typically utilizes different laser power densities and longer exposure times compared to Raman measurements. Figure 4.28 illustrates a typical experimental set-up for PL spectrum measurements.

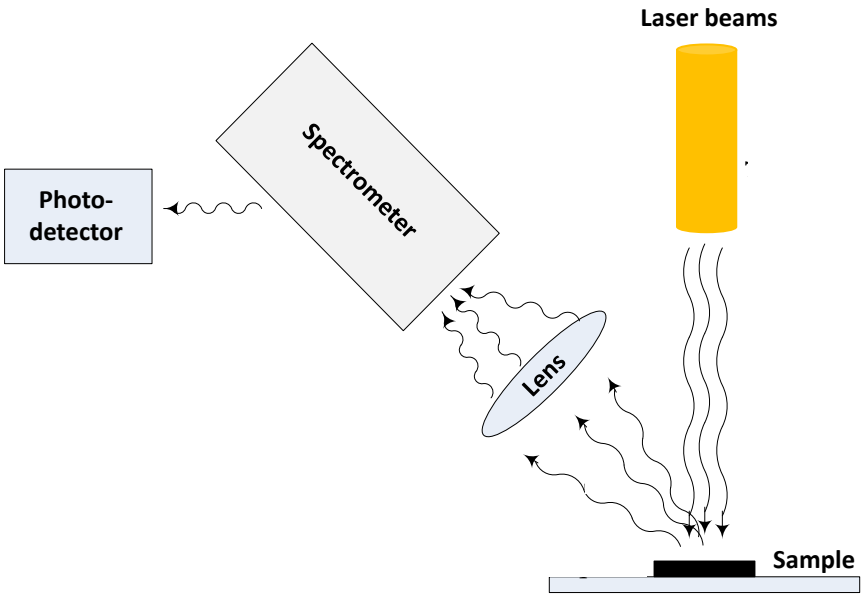


Figure 4.28- A typical experimental set-up for PL spectrum measurements.

### 4.3.7 UV-Vis Absorption spectroscopy

The measurement of absorption spectra within the Ultraviolet-Visible (UV-Vis) wavelength range is crucial for characterizing the energy absorption of thin films, particularly in solar cell applications. The Varian Cary bio 60 UV-Vis spectrophotometer has been employed in this project to acquire optical absorption spectra of all thin film samples. Figure 4.29 illustrates the operational schematic of the Varian Cary bio 60.

UV-Vis spectra of thin films provide essential physical data about nanomaterials, encompassing both optical and electrical properties. This spectroscopic technique relies on electronic transitions within the material, which dictate its ability to absorb light across specific wavelengths. Absorption spectroscopy, therefore, serves as a fundamental tool for measuring absorbed light and understanding the material's absorption behaviour.

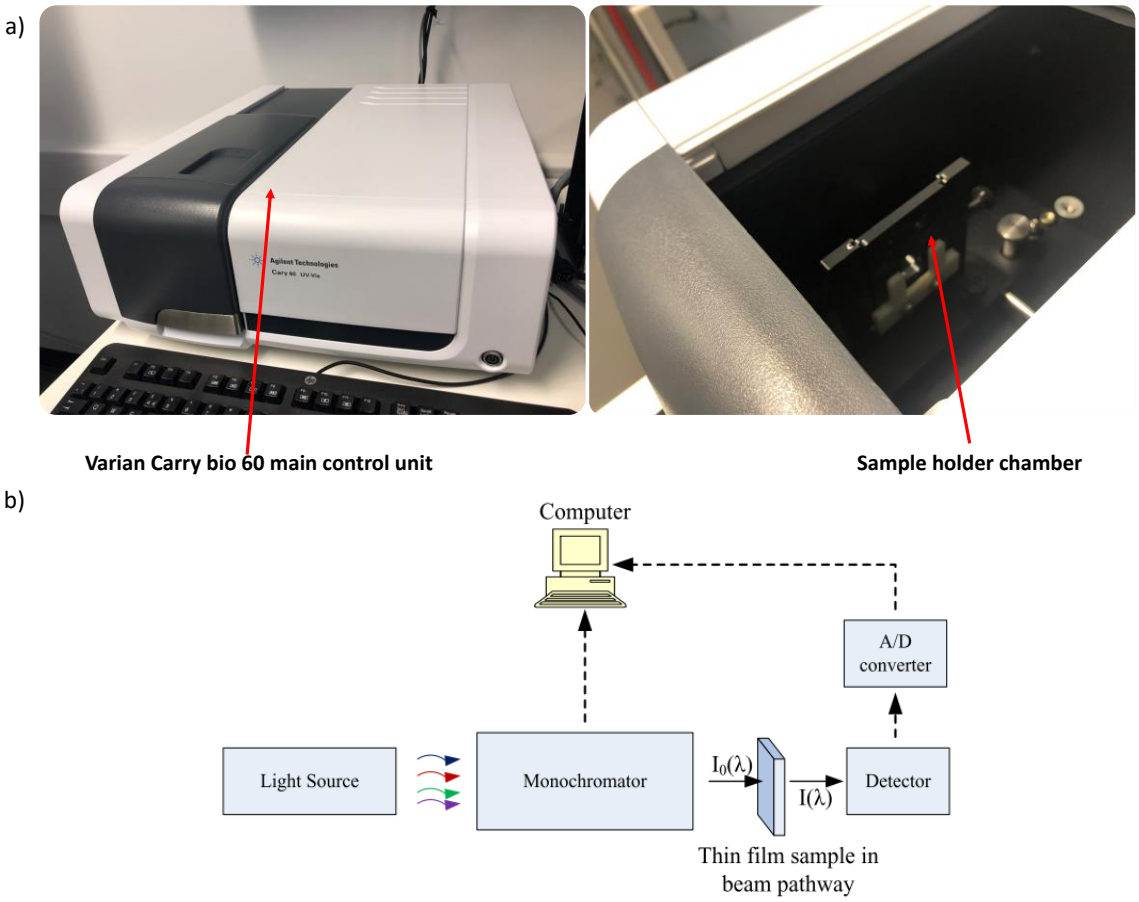


Figure 4.29- a) Cary bio 60 UV – Vis Spectrophotometer (Thin film Lab R117, Science building, Staffordshire University) and integrates sample holder, b) Schematic illustration of the main instrumentation components of a typical UV- Vis spectrophotometer - Adapted from (Gouadec *et al.*, 2007)

The principle underlying the acquisition of absorption spectra is based on Beer's law, where absorption (A) is determined by the ratio of incident light intensity (I0) to transmitted light intensity (I), expressed as:

$$A = \log (I_0/I) = -\log_{10} T \qquad (4.8)$$

Here, $T$ represents the transmittance ($I/I_0$). The absorption spectrum is represented by plotting $A$ as a function of light wavelength.

The UV-Vis spectra of thin films provide crucial insights into optical absorption and energy band gap. The energy band gap ($E$) can be extracted from the UV-Vis spectra using the onset wavelength ($\lambda$) and Planck's equation:

$$E(eV) = {}^{h.c}/_{\lambda} \qquad (4.9)$$

Where $h$ is Planck's constant, $c$ is the speed of light in vacuum, and $\lambda$ is the onset wavelength from the UV-Vis spectra.

The Varian Cary 60 UV-Vis spectrophotometer is utilized in this laboratory to measure the UV-Vis absorption spectra of thin films. This instrument comprises a light source, detector, and optics. The schematic illustration of the key components is depicted in Figure 4.27b. The intensity of the light source is initially measured with a blank sample (i.e., clean quartz glass without a thin film coating), and subsequently with the thin film sample. The resulting reduction in transmitted light intensity following absorption at characteristic wavelengths of the material allows for the computation of absorbance ($A$) using Beer's law.

UV-Vis absorption spectra studies offer valuable data that correlates with nanostructure characteristics in thin films, such as polymer conjugation and interchain interaction. Furthermore, this technique can be applied to a certain extent for structural characterization of thin films. Analysis of the collected spectra provides insights into the structural characteristics of the film and the optical band gap, facilitating a comprehensive understanding of the material within the thin film.

### 4.3.8 Four-Probs technique for measuring sheet resistance

Sheet resistance or surface resistivity is a critical property of materials that reflects their ability to conduct charge across uniform thin films. In photovoltaic applications, low sheet resistance materials are crucial for efficient charge extraction. The determination of

resistivity (and consequently conductivity) from sheet resistance measurements enables the electrical characterization of a material.

The four-probe method is the most commonly used technique for measuring sheet resistance. This method involves four equally spaced probes, known as a four-point probe, making electrical contact with the material. In many commercial applications, sharp needle probes used in this method may damage delicate materials often found in thin film electronic devices. To address this issue, rounded head and spring-mounted tips are employed to eliminate scratching or piercing. These rounded tips increase the contact surface area of the probes, distributing the downward force uniformly applied to the sample. A schematic representation of these probes is depicted in Figure 4.30.

a)

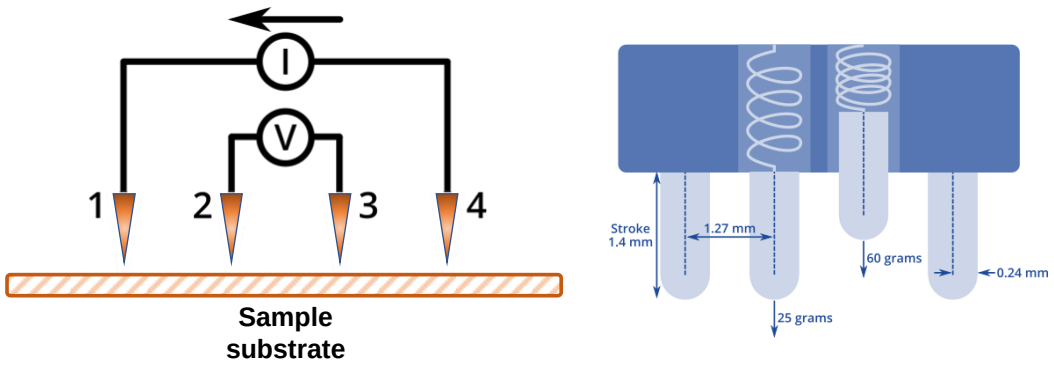


b)


Figure 4.30- a) Schematic diagram of a four-point probe circuit and b) Ossila sheet resistivity four-point probe (Thin film Lab R117, Science building, Staffordshire University)

In the four-probe method, a DC current is applied between the outer two probes (1 and 4), while a voltage drop is measured between the inner two probes (2 and 3). The sheet resistance can then be calculated using the following equation (4.10):

$$R_s = \frac{\pi}{\ln(2)} \frac{\Delta V}{I} \qquad (4.10)$$

Here, $R_s$ represents the sheet resistance, $\Delta V$ is the change in voltage measured between the inner probes, I is the applied current between the outer probes, l is the distance between the inner probes, and W is the width of the material. The sheet resistance is typically expressed in units of ohms per square (Ω/sq). If the thickness of the material is known, the sheet resistance can be used to calculate its resistivity.

$$\rho = R_s . t \qquad (4.11)$$

Here, ρ is the resistivity, and t is the thickness of the material.

### 4.3.9 Image Processing technique for quantitative material identification

Recent studies on AFM image analysis have highlighted a significant challenge: the absence of universal image processing methods for extracting morphological parameters numerically from AFM pictures, including both topography and phase images. Addressing this gap, a novel method introduced in this project aims to derive comparable parameters from phase images and convert them into relevant values for correlating phase image parameters in the OSC characterization procedure.

This technique, developed using MATLAB software and integrated image processing toolbox, combines various image analysis source code to create a comprehensive algorithm tailored for processing AFM phase images. The initialization of this technique involves several steps, as illustrated in Figure 4.31. This figure showcases the groups of filters and activities initially applied to raw AFM pictures to prepare them as input for further investigation in image analysis algorithms.

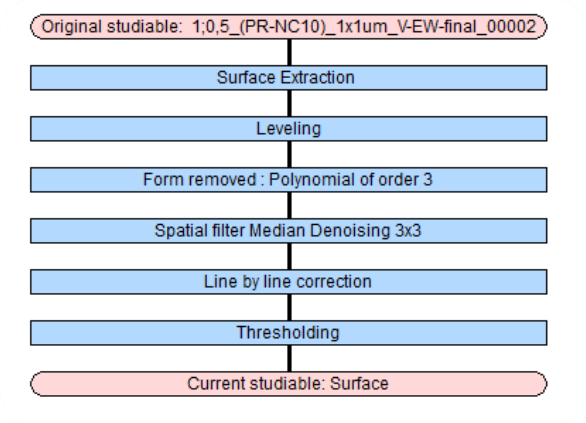


Figure 4.31- preliminary image processing algorithm implemented on AFM images to ready them for subsequent analysis.

The initial processing steps were performed using Pico Image Basic software, which is integrated with the AFM machine and provided by Agilent Company. This software is commonly used for basic image processing techniques to enhance image features for comprehensive analysis.

These processing activities aimed to address various anomalies such as disturbance noises (levelling), high-frequency contrast points, shapes fitted to polynomial curves (form removal), and fading lines caused by improper initial data collection configuration (line-by-line correction). As a result, the processed images exhibited higher contrast and improved quality, suitable for further analysis. Figure 4.32 illustrates a sample AFM phase image before and after applying these initial processing steps.

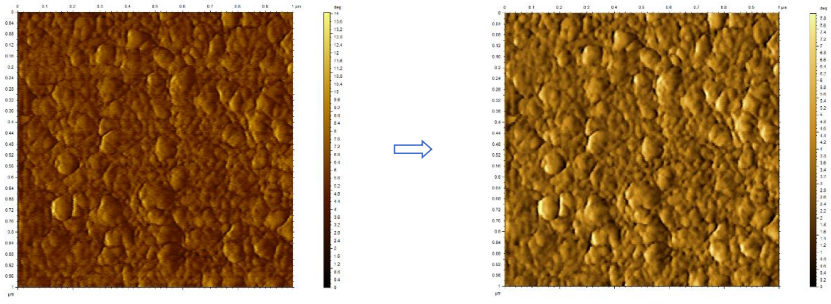

Figure 4.32- Initial image processing steps applied to AFM sample phase image to preparing them for further steps

Subsequently, a suitable grey-level threshold was applied to the image to distinguish regions with specific phase degrees. This generated a binary image where pixels with intensity colors higher than the required phase degree were converted to white (1 value), while others were changed to black (0 value). This process, similar to traditional threshold techniques, yielded a threshold phase image.

Figure 4.33 depicts the algorithm flowchart used for applying the grey-level threshold technique, while Figure 4.34 illustrates the outcome of this threshold initialization.

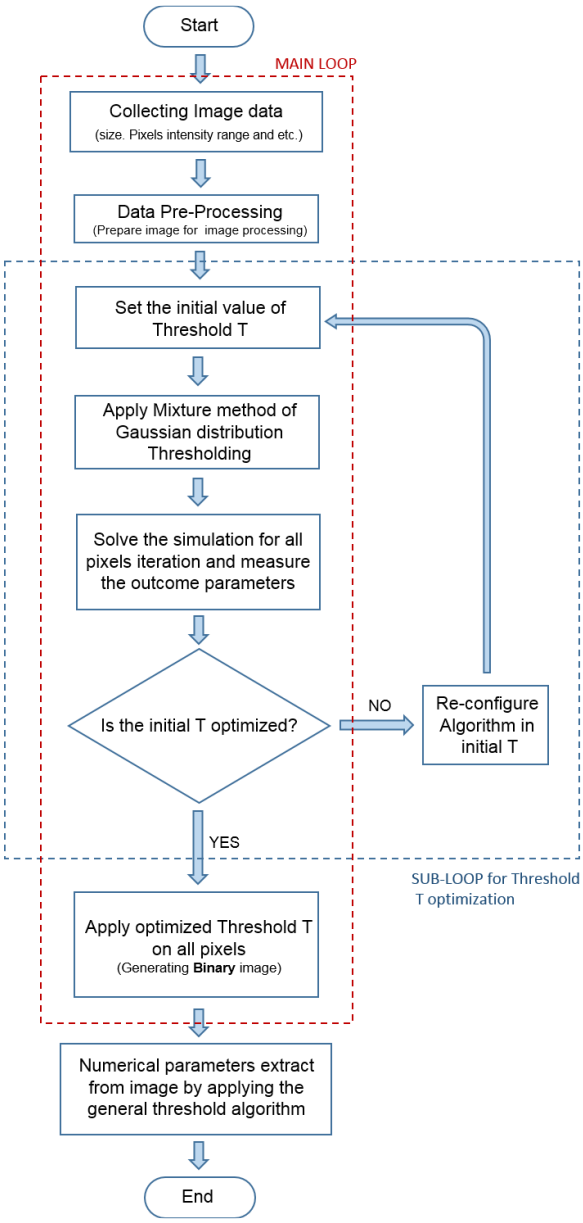


Figure 4.33 - Algorithm flowchart which is used to generate the image data to be collected

Recent studies have indicated that the brightest-coloured regions in phase images, where phase degrees change imperceptibly, can represent pristine materials used in donor-acceptor

blends as pure domains. By utilizing the brightest-coloured regions to determine the initial appropriate phase degree, the initial binary image was generated using threshold grey levelling and Gaussian distribution threshold methods. A sub-loop for threshold optimization was then employed to re-initiate the threshold parameter.

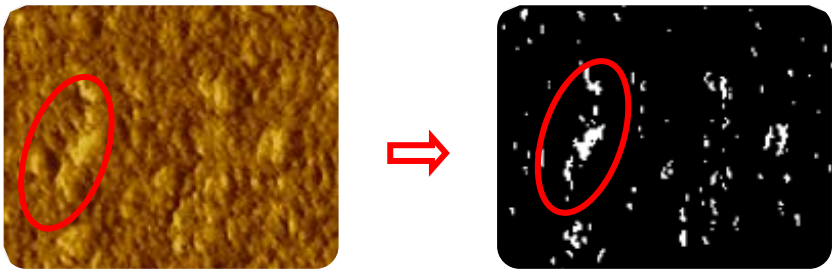

Figure 4.34- Using Bright colour region to find out phase degree distinguishing region

Using MATLAB® Algorithm with image processing libraries, various morphological characteristics such as area, perimeter, centroid position of each bright region, and equivalent diameter, along with the percentage of bright area to the whole image, were extracted from the optimized phase images. These parameters are valuable and comparable in specific datasets for further investigation. These AFM analysis techniques were later utilized in Chapter 5.2 to identify important characteristics from phase images collected from fabricated samples.

### 4.3.10 2D Raman mapping technique

Raman image mapping has previously been utilized to understand the correlation between power conversion efficiency and the morphology of OPV devices (Oklobia and Shafai, 2013), as well as for identifying grain size and orientation in organic and inorganic materials (Ilchenko et al., 2019). To deepen our understanding of surface morphological analysis, the 2D Raman mapping technique was selected to examine the distribution of blend components on the film surface. This mapping technique is one of the output datasets derived from Raman Spectroscopy, as discussed earlier in Chapter 4 section 3.5.

While this technique has not been extensively explored by other researchers for identifying materials such as EFT[20] and $PC_{71}BM$[21] in blends, further investigation is necessary to optimize it for our specific purposes. Therefore, we decided to develop the Raman mapping technique using samples dissolved in chlorinated solvents to confirm its feasibility. Subsequently, we planned to apply this technique to identify materials in blends using green solvents.

A recent study by Komilian, Oklobia, and Sadat-Shafai (2018b) investigated the impact of $PC_{71}BM$ loading on EFT blends dissolved in chlorinated solvents. Their results revealed noticeable changes in bright-coloured regions on the surface images obtained from AFM with increasing percentages of $PC_{71}BM$ in the blend. Hence, the output dataset from this study was utilized in our project as a pilot dataset for developing Raman mapping techniques.

Figure 4.36 and the main loop flowchart in Figure 4.35 illustrate how the mapping technique utilizes spectra data for each pristine component profile.

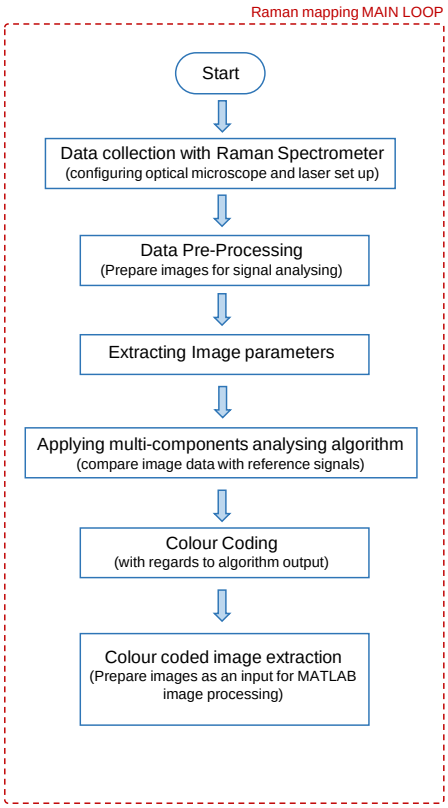


Figure 4.35 – The algorithm flowchart of optimised Raman mapping technique used in WiRETM software

[20] PBDTTT:EFT - Poly[4,8-bis(5-(2-ethylhexyl)thiophen-2-yl)benzo[1,2-b;4,5-b']dithiophene-2,6-diyl-alt-(4-(2-ethylhexyl)-3-fluorothieno[3,4-b]thiophene-)-2-carboxylate-2-6-diyl]
[21] [6,6]-Phenyl-C71-butyric acid methyl ester

These visual aids depict the process of utilizing Raman mapping to analyse blend components on the film surface, providing insights into material distribution and morphology.

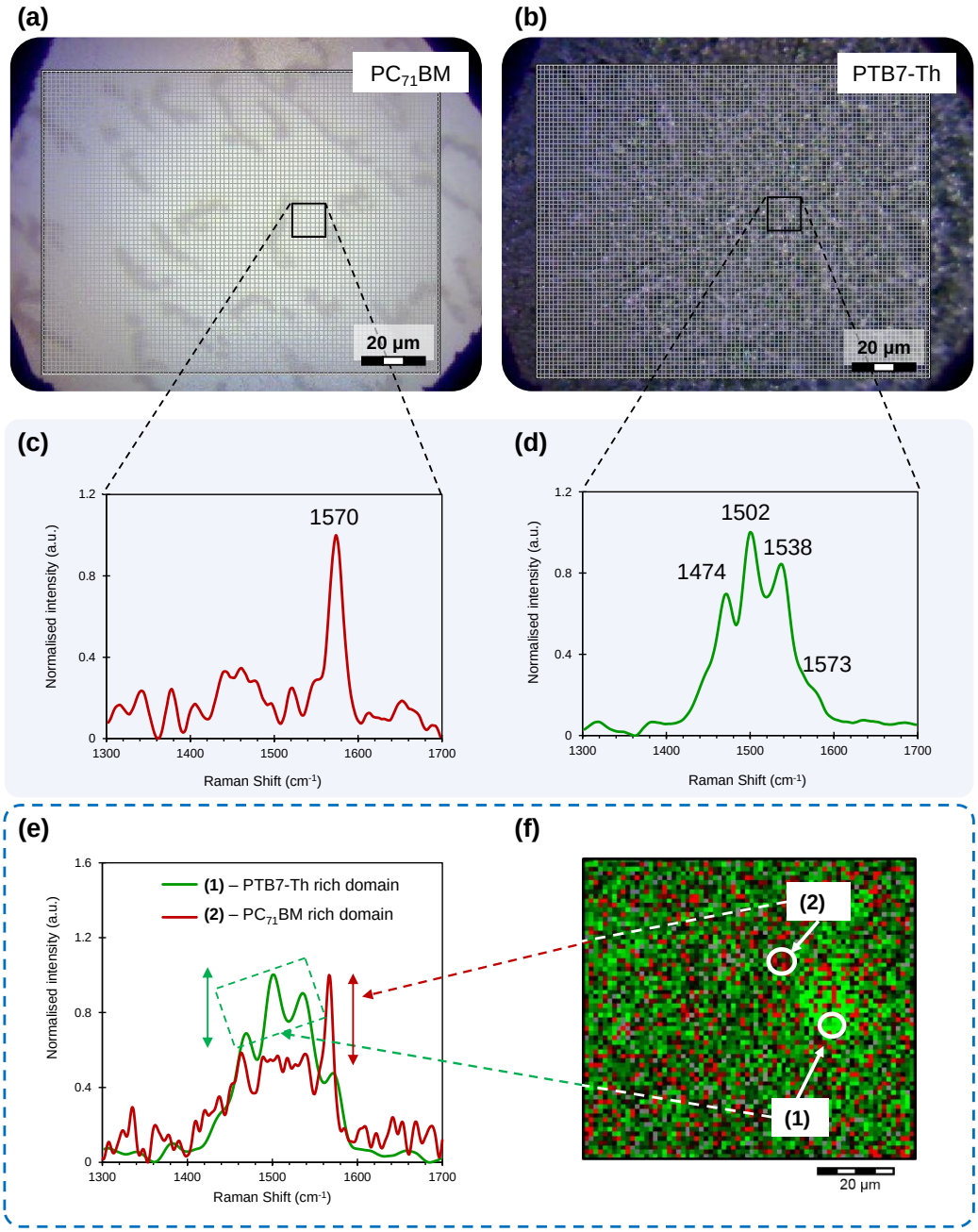


Figure 4.36 - (a,b) Optical microscopic images for pristine $PC_{71}BM$ and PTB7-Th with associated mesh for Raman mapping, (c,d) corresponding line profile spectrum under 514nm excitation laser, (e) line profile spectrum for blended composition ratio of 1:1 and (f) corresponding colour coded 2D generated Raman map. These techniques, developed in conjunction with the image processing algorithm outlined in Section 4.3.9, provide insights into material distribution and morphology on the film surface.

The colour identification in Raman mapping is determined by the variations in peak intensities observed in the spectrum profiles of pristine EFT and pristine $PC_{71}BM$, as depicted in Figures 4.36(a) and 4.36(b), respectively. Corresponding line profiles are shown in Figures 4.36(c) and (d).

This methodology is extended to films casted from blended solutions with 1:1 composition ratios, illustrated by the line profiles in Figure 4.36(e). These techniques, developed alongside the image processing algorithm detailed in Section 4.3.9, enable the generation of colour-coded Raman maps highlighting $PC_{71}BM$/PTB7-Th rich regions, as seen in Figure 4.36(f). In these maps, red indicates $PC_{71}BM$ and green indicates PTB7-Th. The results for the pristine donor and acceptor materials used in this project can be found in Chapter 5.4. The resulting images from this technique provide valuable insights into the morphological analysis of film surfaces.

### 4.3.11 Surface washing technique for reducing the film thickness after fabrication

Researchers have discovered that washing the top surface of the active layer with alcohol-based solvents like methanol ($CH_3OH$) or ethanol ($C_2H_5OH$) can enhance the performance of OSC devices, especially for low bandgap BDT-based polymers (Khan et al., 2014; Sun et al., 2015). Due to the solvency properties of alcohol-based solvents when used as surface washing agents, slight changes in surface roughness compared to as-cast active layer fabrication without washing have been observed. Building on this observation, it was hypothesized that by employing this method with appropriate technique adjustments, the thickness of the active layer could be slightly reduced during alcohol-based solvent drop casting on the layer's surface (Mijovic and Koutsky, 2013).

For further molecular structural analysis, the active layer for each sample was fabricated onto quartz substrates under the same conditions, and identical chemical etching was incrementally applied to reach the internal reference surface by reducing the film thickness of the layer for subsequent research and study. To achieve optimal layer reduction, each etching process involved dispensing 60µL of ethanol while the sample was spinning at 5,000rpm for 60 seconds, and the Bruker DektakXT thickness profiler was used to measure the thicknesses. Approximately 20nm of the active layer thickness was removed during each process, with the possibility of continuing until the film thickness reached 40 nm.

To elucidate the impact of blend composition ratios on constituents' self-organization within the bulk, the above processes were repeated for different ratios of Donor: Acceptor loading. A novel technique employed in Chapter 5 involved the 3D visualization of Raman maps for different loadings and various thicknesses of the active layer material. The schematic of the chemical etching technique is depicted in Figure 4.37 below.

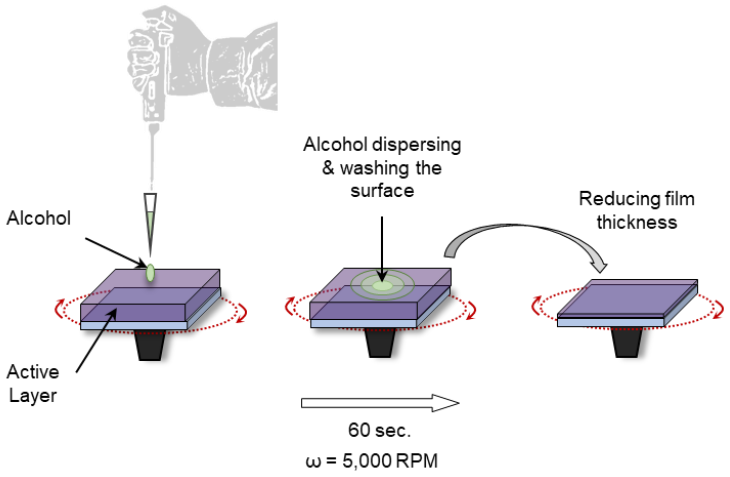


Figure 4.37 – Schematic illustration of the chemical etching technique used to incrementally reduce the thickness of the active layer for molecular structural analysis.

## 4.4 Summary

This chapter delved into the various experimental techniques employed throughout the research. It detailed the setup and operation of UV-Vis spectroscopy for analysing energy absorption in thin films. The significance of cyclic voltammetry in determining polymer and acceptor energy levels was outlined, along with the electrochemical setup involved. AFM's role in studying surface characteristics affecting device performance was discussed, as was the importance of Raman spectroscopy and PL in material characterization. The application of Raman mapping in analysing surface morphologies and blend components distribution was emphasized. Additionally, the development of an image processing algorithm for AFM and the use of chemical etching to reduce active layer thickness were highlighted.

Overall, Chapter 4 provided a comprehensive overview of the experimental techniques used in this research project for fabrication and characterisation of OPV devices. Furthermore,

some of the techniques developed in the current work, has led to the understanding of the self-organised nanostructuring of the electron donor and acceptor material in the active layer, leading to higher power conversion efficiencies.

# CHAPTER 5

# Results & Discussions

*"To conquer frustration, one must remain intensely focused on the outcome, not the obstacles."*

***— T.F. Hodge***

## 5.1 Introduction

This chapter details the research progress and divided into two main areas: (a) developing a novel experimental technique to study the morphology of the active layer based on self nanostructuring of the electron donor and acceptor, and (b) study the impact of such distribution on power conversion efficiency of the bulk heterojunction solar cell. To achieve comprehensive internal structure analysis, a new technique was introduced in Chapter 4, Sections 4.3.9 and 4.3.10, addressing the limitations of existing methods which only characterize crystallographic and nano-structural details in thin films. Prior methods failed to adequately identify clustered $PC_{71}BM$[22] regions or any potential molecular conformities on the surface, thus necessitating the employment of advanced techniques.

The chapter is organized as follows:

Sections 5.2 and 5.3 deploying this improved technique, for analysing the morphology of thin film materials and blend devices under the influence of chlorinated solvents. These sections describe the integration of AFM[23] image processing and Raman mapping techniques for quantitative surface analysis. Additionally, 3D depth-profiling techniques are discussed to investigate the bulk internal structure formation.

[22] [6,6]-Phenyl-C71-butyric acid methyl ester
[23] Atomic Force Microscopy

Sections 5.4, 5.5, and 5.6 focus on device characterization using various methods to evaluate the performance of OSCs based on PBDTTT-EFT[24] polymer when chlorinated and selected green solvents are introduced. Section 5.4 examines the pristine materials and blends, comparing results with those obtained using green solvents. Section 5.5 continues this analysis with a focus on thin film mixtures. Section 5.6 utilizes techniques such as film thickness analysis, enhanced Raman mapping, and in-depth X-Ray analysis to study the impact of green solvents on molecular structure and device performance.

Finally, Section 5.7 analyses the performance of large-scale prototype patterned devices to confirm the effects of green solvents on the morphological, contact quality, and internal structure formation of OSCs[25].

The preparation of all samples was discussed in Chapter 4, Section 4.2.5, and the results from the experiments are categorized and presented in the subsequent sections.

## 5.2 Novel 2D Image Processing for quantitative material identification from blended BHJ thin films

As mentioned in Sections 4.3.9 and 4.3.10, a 2D analysis technique was developed to numerically extract morphological parameters from AFM phase images and apply the same procedures to Raman mapping images. One key application of this 2D processing technique was calculating the percentage of specific coloured areas in color-coded Raman mapping images.

The sections below present the results from the analysis of 2D Raman mapping images using this 2D image processing technique, which proved to be highly useful for material identification in blended BHJ films. To optimize these two techniques, as discussed in previous chapters, their algorithm adaptation was based on active layers films fabricated employing chlorinated solvents.

[24] Poly[4,8-bis(5-(2-ethylhexyl)thiophen-2-yl)benzo[1,2-b;4,5-b']dithiophene-2,6-diyl-alt-(4-(2-ethylhexyl)-3-fluorothieno[3,4-b]thiophene-)-2-carboxylate-2-6-diyl]

[25] Organic Solar Cells

### 5.2.1 AFM Phase image processing for quantitative material identification

Figure 5.1 displays AFM phase images for PBDTTT-EFT blends at ratios of 1:1, 1:1.5, 1:2, and 1:3, dissolved in chlorinated solvent from left to right. Additionally, the figure includes the algorithm outcome images after applying the grey threshold model developed in Section 4.3.9.

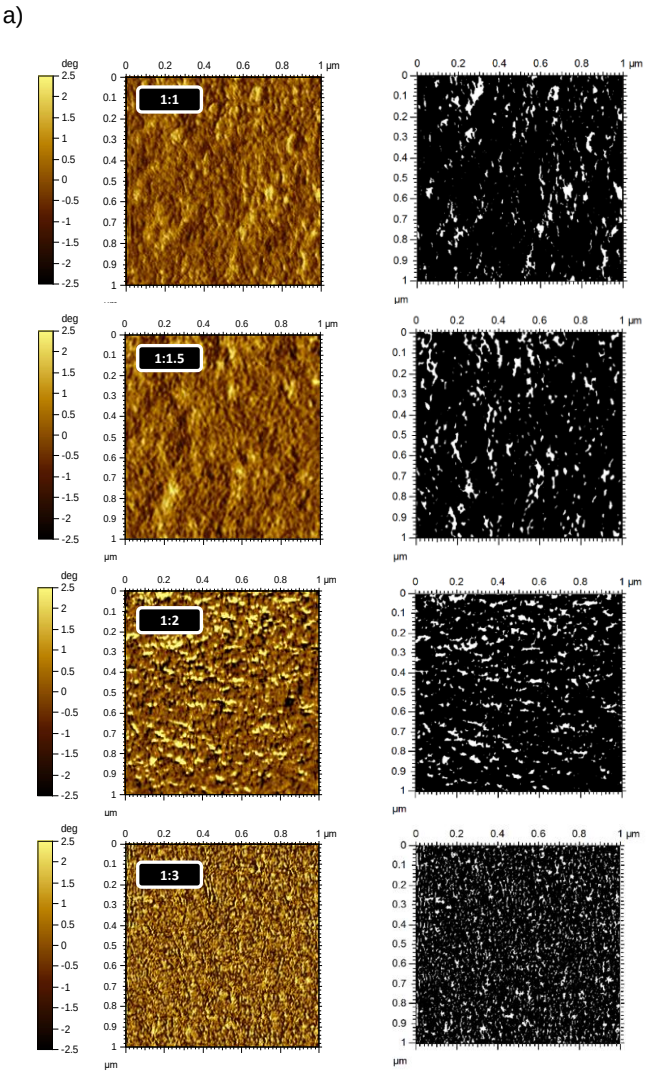


Figure 5.1- AFM phase image for PBDTTT-EFT: $PC_{71}BM$ corresponding to different blend ratios and dissolved with chlorinated solvent, also the outcome pictures after using threshold algorithm

Table 5.1 presents the effective percentage area of bright regions extracted from the phase images using the newly developed comprehensive image processing algorithm.

Table 5.1 - Image processing data extracted from AFM phase images for PBDTTT-EFT: $PC_{71}BM$ at different blend ratios

| | | D:A ratio (EFT:$PC_{71}BM$) | | | |
|---|---|---|---|---|---|
| | | 1:1 | 1:1.5 | 1:2 | 1:3 |
| AFM phase image | % of white pixels | 6.8 | 8.8 | 9.3 | 11.4 |

The data clearly indicate that the percentage of bright areas in the phase images increases with the $PC_{71}BM$ concentration in the blend. This suggests that the white areas in the AFM phase images correspond to $PC_{71}BM$-rich domains on the film surface. These results support the hypothesis that the bright regions in the phase images are indicative of $PC_{71}BM$-rich domains, providing valuable insight into the morphological characteristics of the blends.

### 5.2.2 Raman mapping image processing

Using the 2D Raman mapping technique described in Chapter 4 section 4.3.10, and the software provided by Raman inVia Renishaw, color-coded Raman mapped images were generated and are shown in Figure 5.2. In these images, red regions correspond to $PC_{71}BM$-rich areas and green regions correspond to EFT-rich areas.

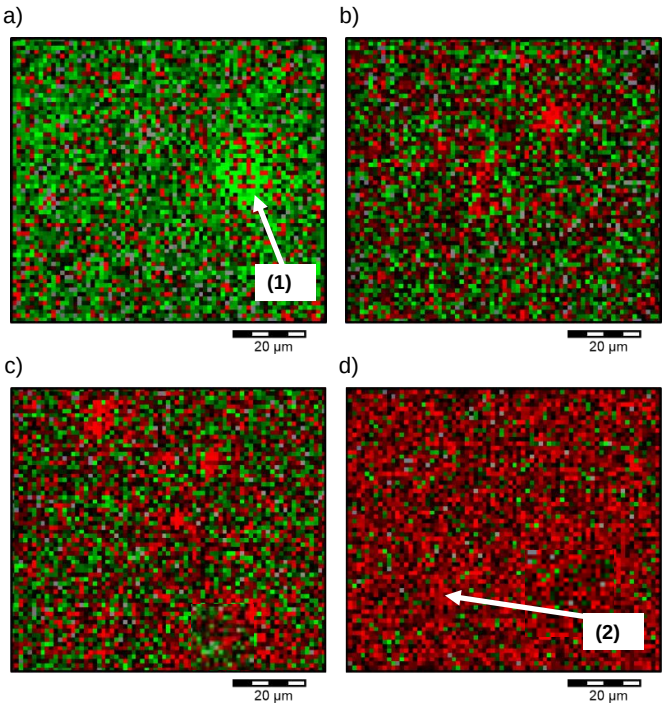


Figure 5.2 - Raman spectrum mapping for PBDTTT-EFT: $PC_{71}BM$ with different blend ratios under 514 nm excitation laser; (a-d) represents Raman mapping images at 1:1, 1:1.5, 1:2 and 1:3 respectively.

A similar MATLAB®-developed image processing algorithm, as illustrated in Chapter 4.3.9, was used to determine the percentage of red-coloured areas on the film surface. The results are presented in Table 5.2(a) and compared with AFM phase image data in Table 5.2(b).

Table 5.2 - Image processing data extracted from Raman mapping images for PBDTTT-EFT: $PC_{71}BM$ at different blend ratios

| | | | D:A ratio (EFT:$PC_{71}BM$) | | | |
|---|---|---|---|---|---|---|
| | | | 1:1 | 1:1.5 | 1:2 | 1:3 |
| (a) | RAMAN mapping image | % of Red pixels ($PC_{71}BM$) | 27.51 | 57.11 | 63.03 | 88.93 |
| | | % of Green pixels (EFT) | 72.49 | 42.89 | 36.97 | 11.07 |
| (b) | AFM phase image | % of white pixels | 6.8 | 8.8 | 9.3 | 11.4 |

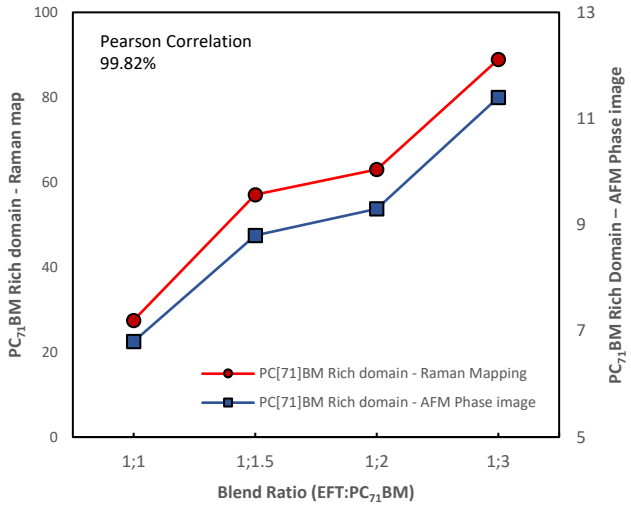


Figure 5.3– Correlation between Image processing data extracted from Raman mapping and AFM phase images for PBDTTT-EFT: $PC_{71}BM$ at different blend ratios

The correlation between the percentage of red area in Raman mapping images and the percentage of bright area in AFM phase images, shown in Figure 5.3, reveals a Pearson coefficient of 99.82%. This high correlation indicates that as the $PC_{71}BM$ loading in the blend increases, both the percentage of red areas identified by the Raman mapping technique

and the percentage of bright areas calculated by AFM phase image analysis increase in a similar trend.

Thus, it can be noted that the red areas in the Raman mapping images correspond to $PC_{71}BM$-rich domains on the film surface, validating the AFM phase image analysis.

## 5.3 Novel 3D Depth-profiling for Thin films via Surface Etching

Understanding how electron donors and acceptors facilitate rapid charge transfer states and create favourable pathways for extracting charge carriers is crucial for developing efficient bulk heterojunction solar cell devices (Ebenhoch et al., 2015; Coropceanu et al., 2019). Consequently, there is significant interest in discerning how these components manifest to form an optimal nanostructure within the bulk.

The important question is: can a 3D profile of the bulk heterojunction be developed through the current morphology studies? To address this, a morphology study was proposed for blended films of PTB7-Th[26] and $PC_{71}BM$, involving a chemical etching process as detailed in Chapter 4.3.11.

### 5.3.1 J-V characterisation of etched samples

A series of devices were fabricated using the process detailed in Chapter 4.2.5, which had been optimized based on recent studies (Komilian, Oklobia, and Sadat-Shafai, 2018b). The fabrication utilized the same facilities and configuration to ensure consistency and avoid any influence on the study outcomes. Different blend solutions with ratios of donor-to-acceptor (D:A) [1:1], [1:1.5], [1:2], and [1:3] were prepared.

In order to explore the impact of the films fabricated from these solutions on JV characteristics, chemical etching was employed. In previous section we identified that distribution of electron donor and acceptor on the film surface, and in the bulk is dependent on the percentage loading of the electron donor and acceptor. This necessitates fabricating devices using chemical etching to reduce the thickness by 20 nm each time, conducting J-V characteristics to see the corelation between J-V results and the nanostructuring of the bulk

[26] Another synonym for PBDTTT:EFT

at different depth. This sequential process led to a total thickness reduction of about 60 nm for samples.

Each sample comprised three devices, and their averaged J-V characteristics—$V_{oc}$, $J_{sc}$, $R_s$, $R_{sh}$, FF, and PCE—were extracted and are presented in Table 5.3 and Figure 5.4.

Table 5.3- The averaged J-V characteristic parameters extracted from different blend ratio of EFT:$PC_{71}BM$ as a function of different thickness while chemical etching applied

| Sample | Thickness (nm) | $J_{sc}$ (mA/cm$^{-2}$) | $V_{oc}$ (V) | FF (%) | PCE (%) | $R_s$ (Ω cm$^2$) | $R_{sh}$ (Ω cm$^2$) |
|---|---|---|---|---|---|---|---|
| 1:1 (10:10) 20mg/ml | 100 | 12.80 | 0.79 | 51.80 | 5.24 | 16.0 | 464 |
| | 80 | 13.60 | 0.78 | 53.48 | 5.67 | 13.3 | 516 |
| | 60 | 14.00 | 0.79 | 54.00 | 5.97 | 13.6 | 557 |
| | 40 | 14.30 | 0.78 | 54.04 | 6.06 | 12.2 | 552 |
| 1:1.5 (10:15) 25mg/ml | 100 | 18.85 | 0.79 | 59.00 | 8.79 | 8.3 | 858 |
| | 80 | 16.13 | 0.79 | 57.00 | 7.26 | 10.5 | 725 |
| | 60 | 13.80 | 0.79 | 55.10 | 6.01 | 13.2 | 649 |
| | 40 | 11.90 | 0.79 | 54.00 | 5.08 | 16.0 | 655 |
| 1:2 (10:20) 30mg/ml | 100 | 18.45 | 0.80 | 64.10 | 9.47 | 7.8 | 2407 |
| | 80 | 16.54 | 0.79 | 60.00 | 7.84 | 9.2 | 1137 |
| | 60 | 14.30 | 0.79 | 58.20 | 6.57 | 11.3 | 986 |
| | 40 | 12.10 | 0.80 | 55.07 | 5.33 | 16.3 | 752 |
| 1:3 (10:30) 40mg/ml | 100 | 11.85 | 0.78 | 48.80 | 4.51 | 18.5 | 353 |
| | 80 | 11.10 | 0.80 | 65.20 | 5.79 | 12.5 | 3529 |
| | 60 | 9.10 | 0.80 | 58.90 | 4.29 | 18.9 | 1789 |
| | 40 | 7.20 | 0.78 | 52.10 | 2.92 | 26.5 | 837 |

It can be observed from the above table and Figure 5.4 that, although all samples were fabricated identically with an active layer thickness of around 100nm, the best solar cell device performance was achieved with a ratio of [1:2], as previously reported by Komilian, Oklobia, and Sadat-Shafai (2018b). The fill factor parameter reached its highest value at this thickness. In terms of the $J_{sc}$ current density, the ratio of [1:1.5] showed the highest value at 100nm thickness. There is a slight fluctuation in $V_{oc}$ values across all devices, and it has

been noted that, as reported earlier, $V_{oc}$ could be strongly impacted by the internal work function differences of the materials (Chen et al., 2009).

As the thickness of the active layer decreased, samples with ratios from [1:1.5] to [1:3] exhibited a declining trend in $J_{sc}$ current density as they were etched away. However, the sample with a [1:1] ratio showed an increasing trend. This suggests that an internal molecular restructuring may have occurred within the active layer of the [1:1] sample. This trend is similarly reflected in the fill factor (FF) for the [1:1] samples.

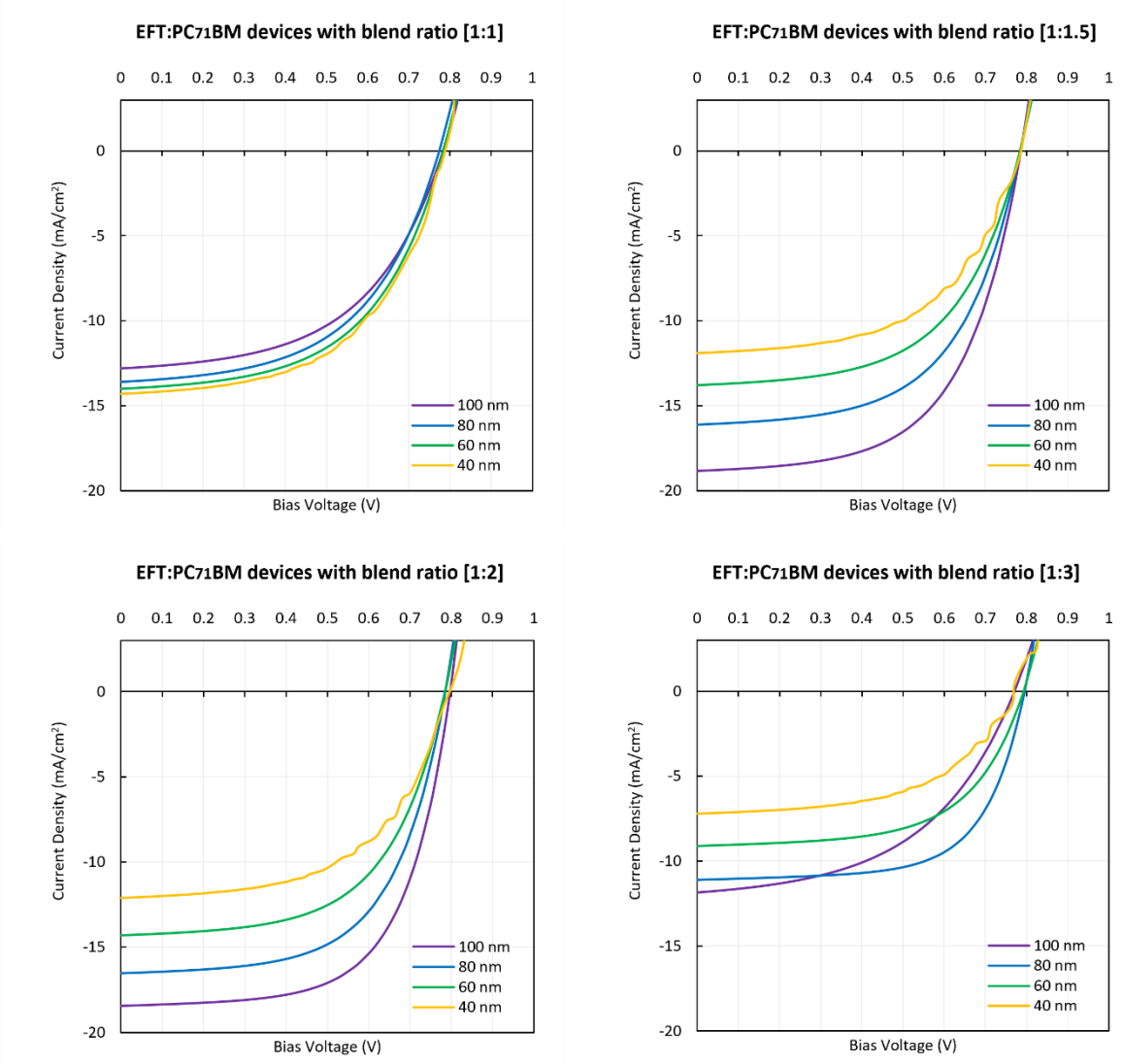


Figure 5.4– The averaged J-V plots extracted from different blend ratio of EFT:PC71BM as a function of different thickness while chemical etching applied

### 5.3.2 Optimising the 2D Raman mapping techniques for different blend ratio as function of different film thicknesses while samples etched down

As detailed in earlier sections (see sections 5.2.1 and 5.2.2), the basic 2D Raman mapping technique was employed to generate mapped images of the sample surfaces, focusing on variations in peak intensities in the spectra of pristine EFT and pristine $PC_{71}BM$. Subsequently, MATLAB® algorithms incorporating image processing libraries were used to quantify the percentage of red areas in these images through a threshold model. This process resulted in the generation of outcome images and corresponding percentage data.

To further enhance this technique for analysing internal structural layers within bulk materials, Raman mapping was employed with different blend ratios ([1:1], [1:1.5], [1:2], [1:3]) and the active layer film thickness was systematically reduced using a chemical etching technique. Subsequently, 2D Raman mapped images were generated for each blend ratio as a function of varying film thicknesses, as shown in Figure 5.5.

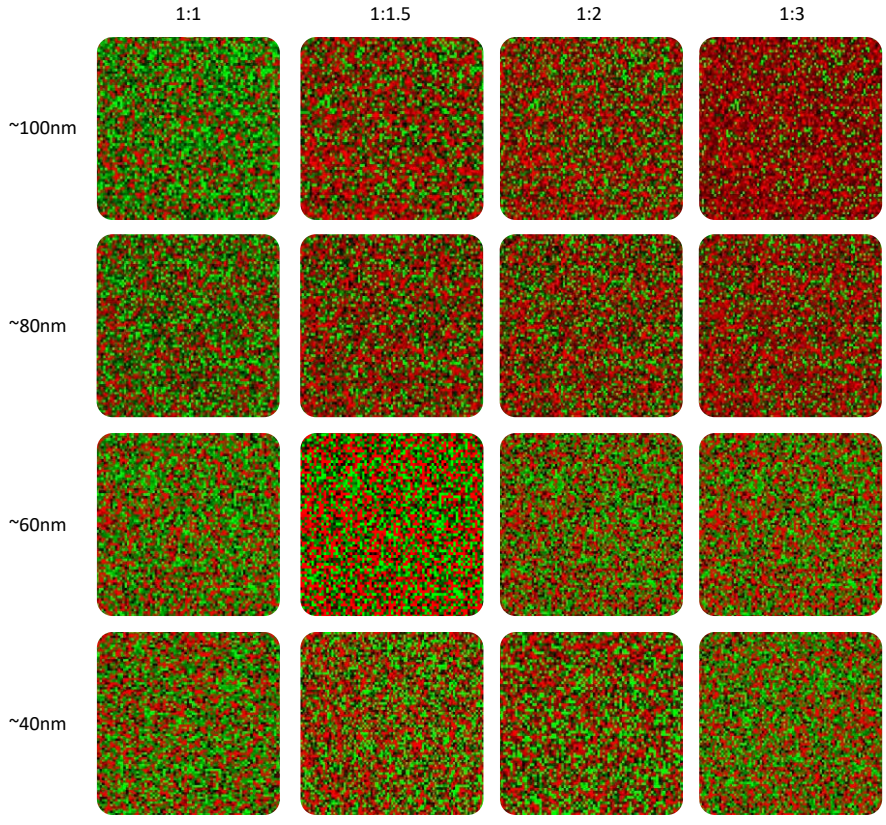


Figure 5.5 – 2D Raman mapped images for different blend ratio as function of different film thicknesses after etching processed.

According to the essential peaks identified from pristine $PC_{71}BM$ and pristine EFT, red colours signify $PC_{71}BM$-rich regions, while green colours denote EFT-rich regions. It is

evident that in 100nm films, increasing the amount of $PC_{71}BM$ in the blend ratio from [1:1] to [1:3] visually increases the red area. To validate this observation, an optimized image processing algorithm was used, adjusting internal parameters to measure the percentage of red areas on the surface as the film thickness decreased to 40nm for each blend ratio via chemical etching.

Table 5.4 below presents the percentage of $PC_{71}BM$-rich regions extracted from the film surface at different PTB7-Th blend ratios as a function of varying film thicknesses. The colour-coded images generated illustrate how the $PC_{71}BM$ content changes on the surface with variations in film thickness and blending ratios.

Interestingly, as the active layer thickness decreased due to etching, a decreasing trend in exposed $PC_{71}BM$ on the film surface was observed for the [1:3], [1:2], and [1:1.5] ratios. In contrast, for the [1:1] ratio, the presence of $PC_{71}BM$ on the film surface increased as the thickness reduced to approximately 40nm. As the thickness decreased across all samples, the structural influence became evident, with the percentage of $PC_{71}BM$ converging to around 50% on the surface layer at approximately 40nm depth within the bulk. This suggests an equilibrium formation of $PC_{71}BM$ molecules in the lower layers of the active layer film.

Table 5.4- Percentage of $PC_{71}BM$ rich regions extracted from the film surface of different PTB7-Th: $PC_{71}BM$ blend ratios as a function of different film thicknesses via washing technique.

| Blend ratio | 1:3 | 1:2 | 1:1.5 | 1:1 |
|---|---|---|---|---|
| Thickness (nm) | $PC_{71}BM$ rich region (%) | | | |
| ~100 | 82.9 | 61.8 | 55.3 | 29.2 |
| ~80 | 63.3 | 56.1 | 53.1 | 39.4 |
| ~60 | 52.9 | 53.6 | 51.3 | 44.7 |
| ~40 | 48.6 | 51.1 | 50.4 | 48.6 |
| ~30 | 46.5 | 50.6 | 48.9 | 49.2 |

Figure 5.6 shows this trend for all samples across different blend ratios and thicknesses. Notably, for all samples, as the active layer thickness decreased, a consistent formation of molecules occurred around 40nm depth, with approximately 50% $PC_{71}BM$ detected on the surface.

This funnel-like behaviour in the percentage of $PC_{71}BM$ has significant implications for understanding how the components of active layers form their molecular structures during drying, and for determining optimal thresholds for blend ratios and thicknesses of the active layer.

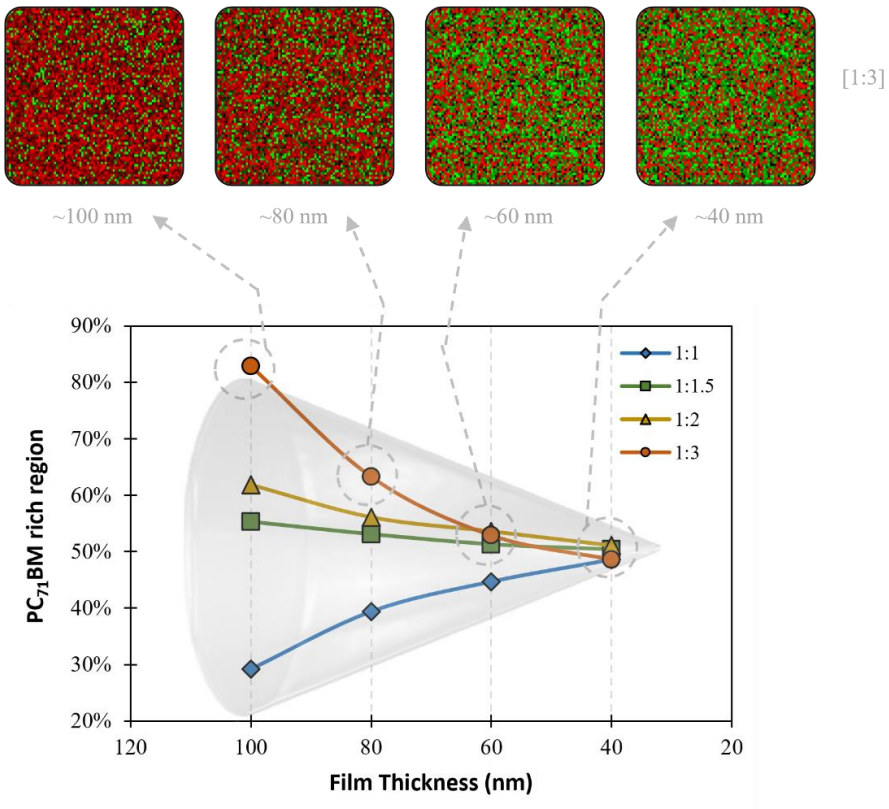


Figure 5.6 - $PC_{71}BM$ rich regions from Raman analysis for different blend ratios as a function of film thickness

Furthermore, the experimental evidence suggests that the quantity of $PC_{71}BM$ in the blend dictates its distribution profile. When films are cast from solution, PTB7-Th, which predominantly exhibits face-on orientations (Komilian, Oklobia, and Sadat-Shafai, 2018b), impedes $PC_{71}BM$ migration to the film surface. Therefore, for a [1:1] blend, the percentage of $PC_{71}BM$ at the film surface is lower and gradually increases within the bulk. Conversely, for blends with ratios greater than [1:1], $PC_{71}BM$ induces PTB7-Th to transition from face-on to edge-on orientations, facilitating $PC_{71}BM$ migration towards the film surface, as evident from Table 5.4 and Figure 5.6.

Understanding the distribution and orientation of materials within the active layer is crucial for optimizing photovoltaic (PV) device performance. The data presented here provided valuable insights into how variations in blend ratios and film thicknesses affect the distribution of $PC_{71}BM$ and PTB7-Th within the active layer. This knowledge is essential for engineering active layers that promote efficient charge generation, transport, and collection, ultimately enhancing the overall efficiency and stability of PV devices. By correlating molecular distribution with device performance metrics such as power conversion efficiency and stability, researchers can tailor active layer compositions and processing conditions to achieve higher-performing solar cells.

### 5.3.3 Depth-Profiling using optimised images

To gain deeper insights into the internal molecular structures and the formation of $PC_{71}BM$ molecules on the surface layers during chemical etching, a custom MATLAB© image processing algorithm was developed. This algorithm utilized principles similar to the colour coding used in 2D Raman mapping techniques for each 2D frame. Subsequently, a final integration algorithm was applied to consolidate all layers of varying thicknesses into a cohesive three-dimensional cube, representing the bulk material of the active layers used in the samples.

Figure 5.7 illustrates the 3D Raman mapping results for PTB7-Th blends at [1:3] and [1:1] ratios. In the [1:3] sample, as previously noted, a decreasing trend in $PC_{71}BM$ content across different surface depths in the bulk is evident. The density of red colours diminishes significantly as the analysis penetrates deeper into the bulk, gradually transitioning to green pixels. Conversely, a contrasting trend is observed in the [1:1] ratio sample.

This molecular arrangement, depicted for the first time through 3D Raman mapping, highlights a novel finding not previously reported by other researchers.

At this stage, the algorithm was optimized to predict layer intercalation during the etching process down to approximately 40nm. However, its capability could potentially be extended to optimize for the entire bulk thickness if comprehensive data were available.

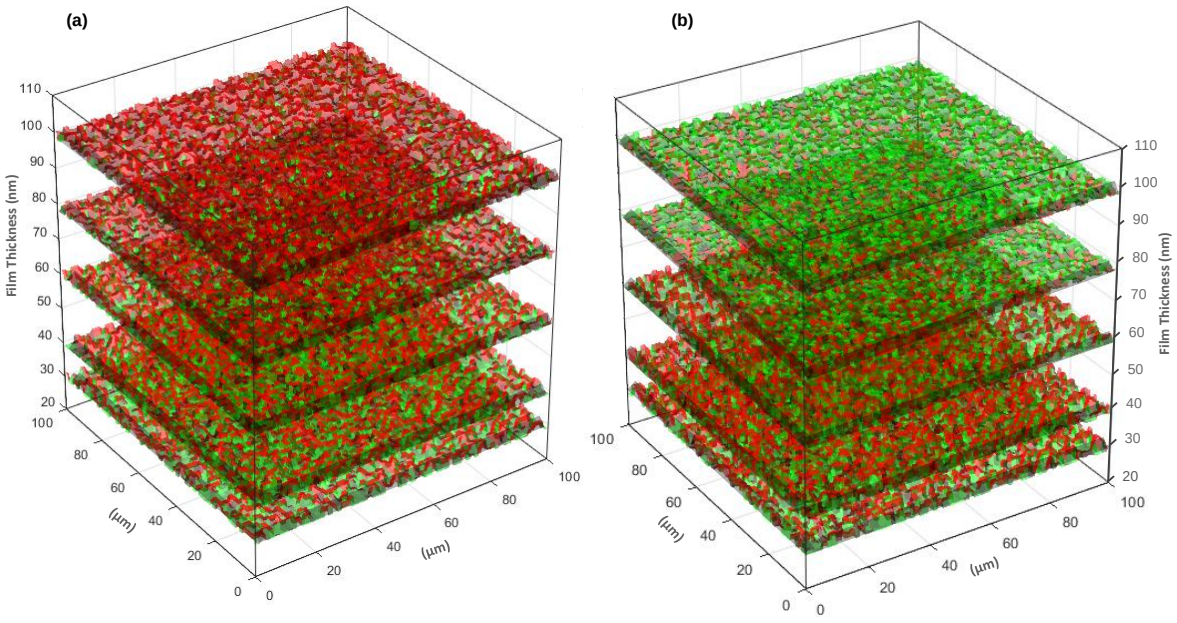


Figure 5.7- 3D Raman mapping of PTB7-Th:$PC_{71}BM$ for (a)1:3 and (b)1:1 blend ratio

### 5.3.4 GIXRD depth diffractograms profile for different blend ratio of PBT7-Th: $PC_{71}BM$

To elucidate the mechanisms underlying the distribution profile of donor/acceptor materials within the bulk, the films from our earlier investigations underwent further analysis using Grazing Incidence X-ray Diffraction (GIXRD). By removing the baseline from the raw GIXRD data, the peaks corresponding to each molecular crystallography plane and material structure became distinctly visible in the datasets. Figure 5.8 presents the depth diffractogram profiles from GIXRD, illustrating the ratio of PTB7-Th at different film thicknesses.

Renishaw WiRE™ 3.4 software was employed to perform curve fitting on each X-ray diffractogram line profile. This software utilizes Gaussian and Lorentzian models for optimal fitting, with an example shown in Figure 5.8 (e). These findings closely align with prior studies on PTB7 (Collins et al., 2013b). Each curve is labelled either "Poly" for the donor material or "Accep" for the acceptor material, with the miller indices (dhkl) planes of each material being well-documented in the literature (Collins et al., 2013b).

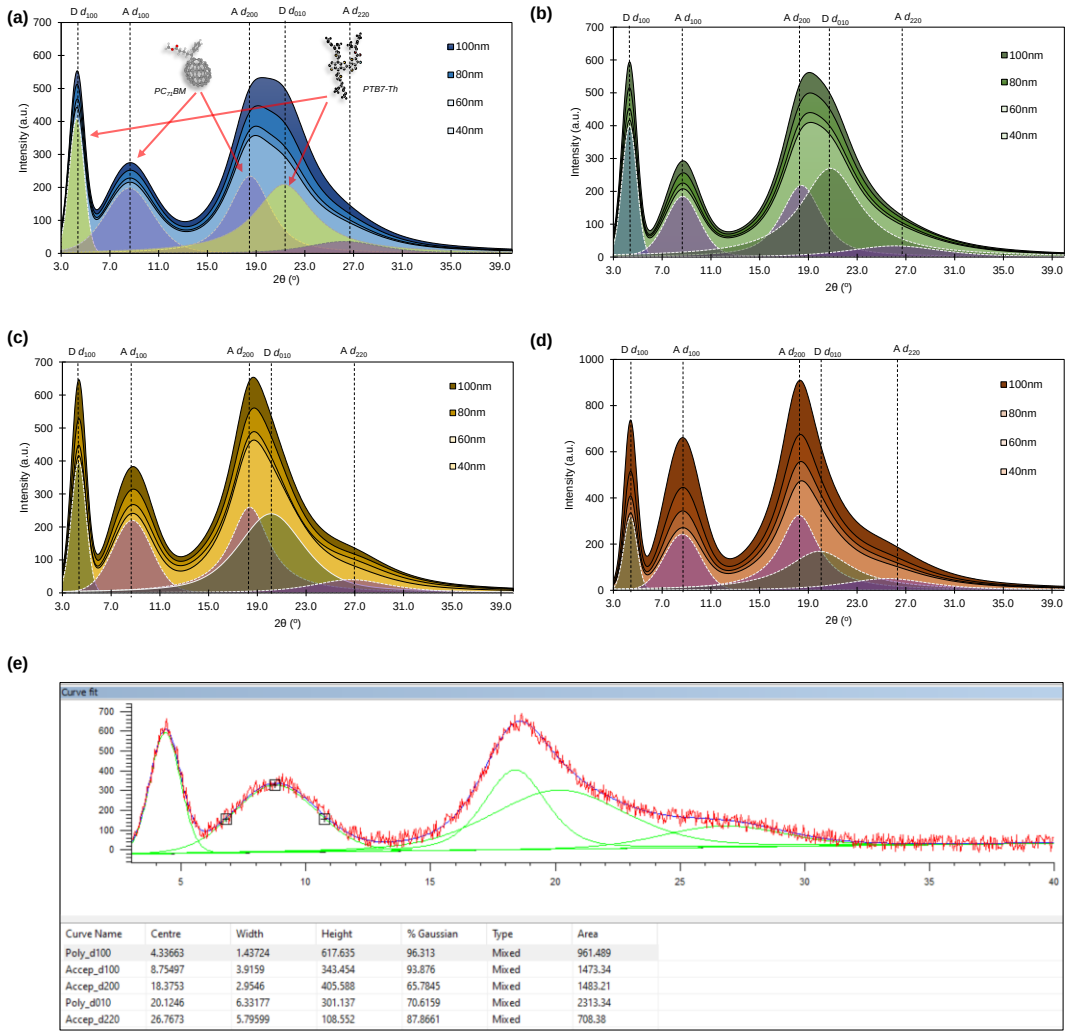


Figure 5.8- Out-of-Plane GIXRD depth diffractograms profile for different blend ratio of PTB7-Th: PC71BM. (a) 1:1, (b) 1:1.5, (c) 1:2 and (d) 1:3. Donor (PTB7-Th) and acceptor (PC71BM) geometrical planes peak position have shown for each figure. (e) shows the curve fit applied to PTB7-Th:$PC_{71}BM$, 1:2 [D:A] blend ratio for 100 nm film thickness

It is crucial to emphasize that most polymers used in Organic Photovoltaic (OPV) applications typically exhibit either face-on or edge-on orientations (Olivier et al., 2014). Based on this understanding, several key insights can be gleaned from the graphs, which hold significant implications. According to X-ray crystallography analyses in the literature (Huang et al., 2015; Komilian, Oklobia, and Sadat-Shafai, 2018; Song et al., 2019), the 2θ range for the EFT $d_{010}$ face-on orientation plane is typically between 20-23°, while the $d_{100}$ edge-on plane for EFT exists around 2θ of 3-6°.

The crystallographic data extracted from computer-generated models, superimposing the sub-curves corresponding to each planar condition of EFT and $PC_{71}BM$, reveal that as one moves deeper into the bulk layers, the intensity of $PC_{71}BM$ molecules (particularly $d_{200}$

intensity, as noted by Supasai et al., 2017) and all peak intensities decrease with decreasing film thickness. However, it is noteworthy that these curves converge within the bulk, showing no significant difference in intensity between the 40nm and 60nm samples. This observation aligns with the findings from Raman mapping, indicating a balanced threshold of around 50% $PC_{71}BM$ presence on the surface at a 40nm depth within the bulk.

Moreover, as the percentage of $PC_{71}BM$ increases, all peaks gradually merge and become sharper, as shown in Figure 5.8 (a–d). Additionally, the peak intensity attributed to $PC_{71}BM$'s $d_{200}$ also increases with higher composition ratios, indicating a greater concentration of $PC_{71}BM$ at the unetched film surface. It can be inferred that $PC_{71}BM$ itself induces the rotation of PTB7-Th from face-on to edge-on orientation, facilitating the migration of $PC_{71}BM$ towards the film surface.

Table 5.5 - OOP GIXRD parameter extracted from curve fits for PTB7-Th at different blend ratios and different film thickness

| Sample | | $PC_{71}BM$ | | | | PTB7-Th | | | | |
|---|---|---|---|---|---|---|---|---|---|---|
| D:A Ratio | Thickness (nm) | $d_{100}$ | | $d_{200}$ | | $d_{100}$ | | $d_{010}$ | | Edge-on/ Face-on Ratio |
| | | 2θ (º) | Intensity (a.u.) | 2θ (º) | Intensity (a.u.) | 2θ (º) | Intensity (a.u.) | 2θ (º) | Intensity (a.u.) | |
| 1:1 | 100 | 8.62 | 246 | 18.51 | 291 | 4.30 | 509 | 21.30 | 395 | 1.29 |
| | 80 | 8.63 | 229 | 18.53 | 274 | 4.29 | 474 | 21.31 | 296 | 1.60 |
| | 60 | 8.61 | 209 | 18.52 | 247 | 4.31 | 432 | 21.32 | 234 | 1.84 |
| | 40 | 8.60 | 182 | 18.50 | 218 | 4.28 | 409 | 21.30 | 209 | 1.96 |
| 1:1.5 | 100 | 8.69 | 274 | 18.44 | 321 | 4.32 | 569 | 20.81 | 349 | 1.63 |
| | 80 | 8.70 | 242 | 18.44 | 283 | 4.31 | 494 | 20.80 | 320 | 1.54 |
| | 60 | 8.66 | 215 | 18.42 | 251 | 4.30 | 432 | 20.82 | 287 | 1.51 |
| | 40 | 8.68 | 201 | 18.43 | 224 | 4.32 | 398 | 20.81 | 270 | 1.48 |
| 1:2 | 100 | 8.75 | 343 | 18.37 | 405 | 4.34 | 618 | 20.12 | 301 | 2.06 |
| | 80 | 8.77 | 279 | 18.39 | 330 | 4.35 | 504 | 20.15 | 280 | 1.80 |
| | 60 | 8.76 | 270 | 18.38 | 280 | 4.33 | 427 | 20.10 | 251 | 1.70 |
| | 40 | 8.73 | 230 | 18.37 | 270 | 4.34 | 397 | 20.13 | 240 | 1.65 |
| 1:3 | 100 | 8.66 | 612 | 18.20 | 723 | 4.40 | 702 | 19.92 | 202 | 3.48 |
| | 80 | 8.67 | 407 | 18.19 | 503 | 4.41 | 489 | 19.91 | 193 | 2.54 |
| | 60 | 8.65 | 296 | 18.21 | 384 | 4.39 | 387 | 19.93 | 181 | 2.14 |
| | 40 | 8.66 | 224 | 18.25 | 306 | 4.40 | 316 | 19.92 | 169 | 1.87 |

Table 5.5 above presents the out-of-plane GIXRD parameters extracted from curve fits for PTB7-Th at different blend ratios and film thicknesses.

The second approach revealed distinct trends among samples [1:1.5], [1:2], and [1:3], where the relative slope between the $d_{200}$ and $d_{010}$ 2θ positions exhibited consistent patterns. In

contrast, the curve's curvature in this region for the [1:1] sample showed a contradictory and negative increase compared to the other samples. This discrepancy arose due to a significant reduction in the intensity of EFT $d_{010}$ molecules as the analysis penetrated deeper into the bulk of the [1:1] sample. In contrast, the reduction in $PC_{71}BM$ $d_{200}$ peak intensity was less pronounced, leading to a negatively increased slope in this region compared to samples [1:1.5], [1:2], and [1:3].

This unexpected decrease in EFT face-on molecules in the [1:1] sample suggests that the presence of $PC_{71}BM$ molecules would be more noticeable in surface Raman mapping analyses, resulting in a higher observed percentage in the [1:1] sample than initially expected.

### 5.3.5 Compare the GIXRD and Raman mapping results in Depth-profile analysis

One of the insights gleaned from the GIXRD results in previous sections was the emergence of a 2θ peak around 4°, indicating an increase in signal intensity at this peak. This peak corresponds to the EFT $d_{100}$ edge-on molecules. To understand how the presence of $PC_{71}BM$ molecules on the surface impacts the formation of these internal molecules, further analysis of the extracted in-depth GIXRD parameters was conducted.

A key observation aimed at providing evidence of $PC_{71}BM$'s vertical distribution is the relationship between the ratio of edge-on to face-on PTB7-Th molecules as a function of film thickness across all composition ratios. In this study, an inverse of the conventional face-on to edge-on ratio is used to signify the correlation between this parameter and the percentage of $PC_{71}BM$ on the film surfaces, as observed in Raman mapping.

Figure 5.9 illustrates these two graphs. It is evident that there exists a strong functional relationship between the presence of $PC_{71}BM$ molecules (analysed via Raman mapping data) and the proportion of PTB7-Th molecules transitioning from a face-on to an edge-on orientation (analysed via GIXRD data).

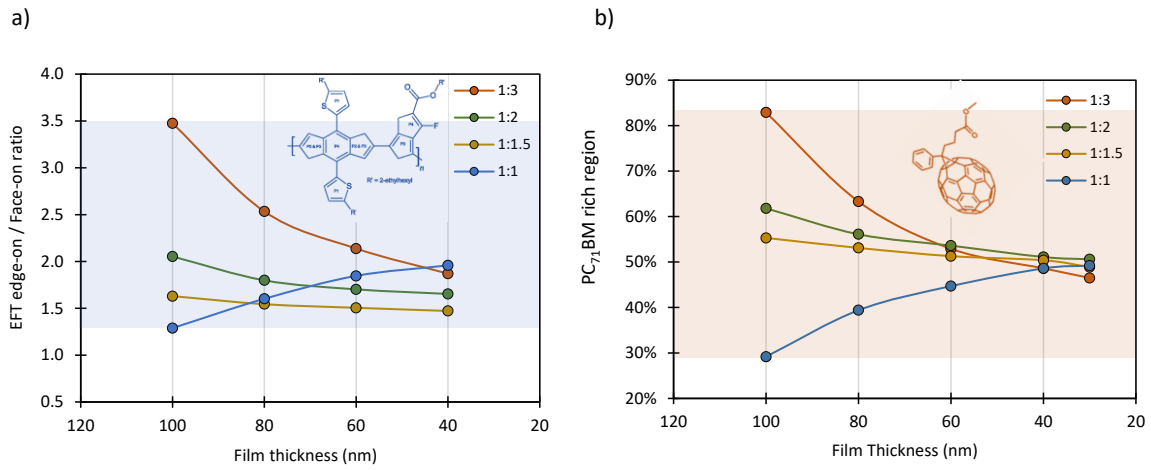


Figure 5.9- a) Ratio between PTB7-Th Edge-on and Face-on molecules at different blend ratios and different film thickness in GIXRD analysis b) Plot of $PC_{71}BM$ rich regions from Raman analysis for different blend ratios as a function of film thickness.

For all composition ratios except [1:1], there is a decrease in the edge-on to face-on ratio with decreasing film thickness, indicating a reduction in $PC_{71}BM$ concentration at the film surface as the film thickness decreases. However, for the [1:1] ratio, the concentration profile of $PC_{71}BM$ exhibits a different vertical distribution. At lower $PC_{71}BM$ concentrations, PTB7-Th predominantly maintains a face-on orientation, which restricts the vertical migration of $PC_{71}BM$ toward the film surface. This phenomenon is confirmed by the Raman mapping results (Figure 5.5), where lower $PC_{71}BM$ concentrations were observed at the surface (100 nm depth) compared to 40 nm depth for the [1:1] composition ratio. Conversely, as the composition ratio increases, PTB7-Th shifts from a face-on to an edge-on orientation, facilitating the vertical migration of $PC_{71}BM$ toward the surface.

It is noteworthy that for all composition ratios of [1:1.5] and above, more $PC_{71}BM$ is found at the surface of thicker films. This aligns with the trends observed in the Raman mapping data analysed in the previous section, underscoring the role of $PC_{71}BM$ in shaping the distribution of the polymer/acceptor network, influencing photocurrent generation, and establishing suitable pathways for charge extraction that impact the electrical parameters in OPV[27] devices.

[27] Organic Photovoltaic

### 5.3.6 Molecular orientation impact on Electrical Parameters of OPV

In previous sections, extensive investigation was conducted into the nanostructure dependence on composition ratios and its influence on molecular orientations to elucidate the self-organization mechanisms of donor/acceptor materials in bulk heterojunction devices. Now, the focus shifts to exploring the implications of nanomorphology and nano-structuring on electrical parameters in Organic Photovoltaic (OPV) devices.

Table 5.3 in section 5.3.1 provides electrical parameters for all etched devices at corresponding thicknesses. Figure 5.10 (a) illustrates the relationship between current density and the percentage of $PC_{71}BM$ on the film surface. It is evident across all composition ratios that current density increases with the percentage of $PC_{71}BM$ present on the device surface. However, notable differences emerge in the behaviour of the [1:1] ratio device, where the percentage of $PC_{71}BM$ on the surface increases through the chemical etching process. This observation aligns well with the interpretation that at higher concentrations (above [1:1] ratio), the shift in orientation from face-on to edge-on facilitates the migration of $PC_{71}BM$ toward the device surface.

Furthermore, the dependence of current density on $PC_{71}BM$ content is not uniform and varies across different composition ratios. Although a closer trend is observed for [1:1.5] and [1:2] devices, indicating a potential linear relationship at lower $PC_{71}BM$ concentrations, deviations from this trend are noted at higher loadings. This discrepancy is attributed to fullerene distribution disparities within the bulk and on the film surface, impacting exciton dissociation and charge carrier pathways to the respective electrodes.

To further investigate the impact of bulk nanostructure on current density, Figure 5.10 (b) illustrates the dependence of current density on GIXRD data (specifically $d_{200}$), as presented in Table 5.5.

These findings underscore the intricate relationship between nanostructure, composition ratios, and electrical performance in OPV devices, highlighting the importance of optimizing material distributions and orientations to enhance device efficiency and stability.

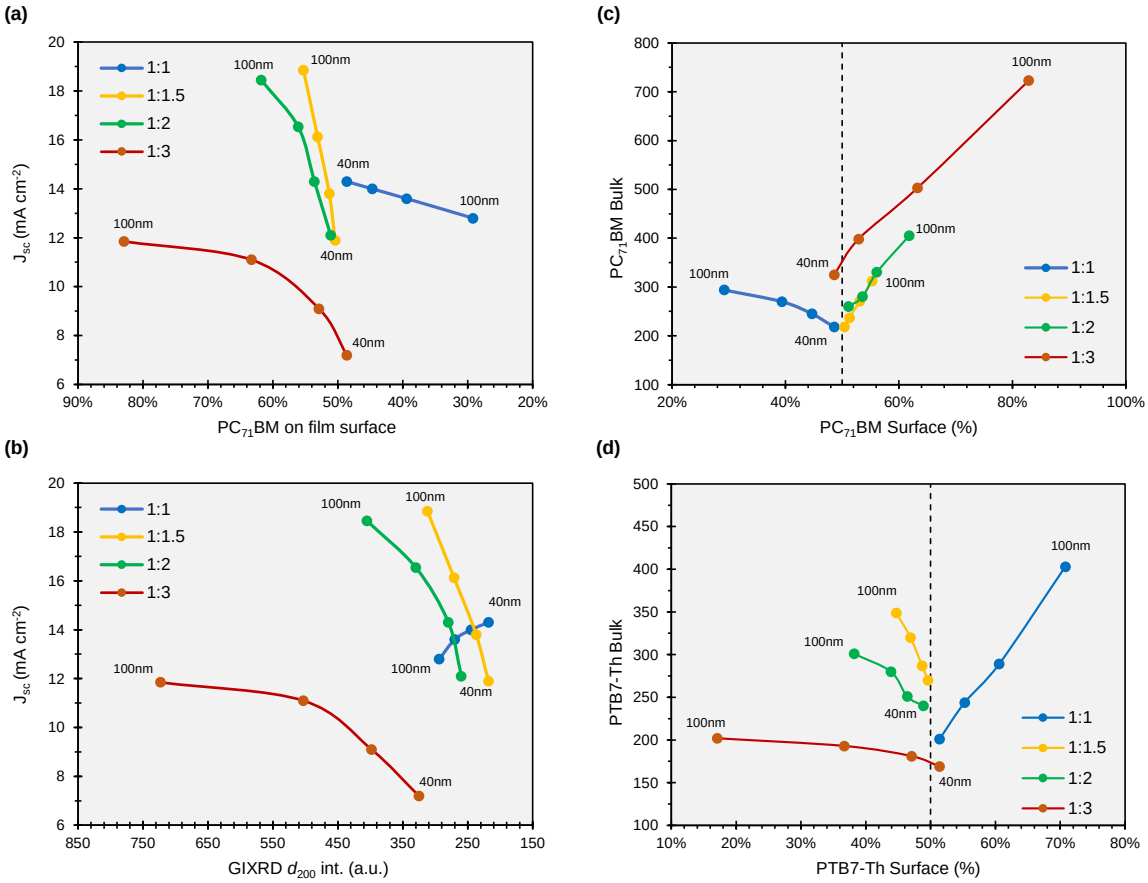


Figure 5.10 - a) Plot of short circuit current density versus $PC_{71}BM$ percentage on film surface and b) GIXRD d200 intensity; c) the relationship between percentages of acceptor and d) donor material on the surface and in the bulk.

For the [1:1] composition ratio, the observed trend differs from Figure 5.10 (a) because the current density is influenced by both $PC_{71}BM$ content in the bulk and on the film surface. As successive chemical etching reduces $PC_{71}BM$ in the bulk, $PC_{71}BM$ on the surface is simultaneously increased. This aligns with previous findings that $PC_{71}BM$ is more concentrated deeper within the film for the [1:1] ratio.

Conversely, despite higher $PC_{71}BM$ concentrations on the film surface, lower current density is observed in the [1:3] composition ratio compared to other ratios. This discrepancy stems from an imbalance in $PC_{71}BM$ distribution between bulk and surface, and the significantly lower amount of PTB7-Th used in the [1:3] ratio relative to $PC_{71}BM$, impacting photocurrent generation.

To validate this, the relationship between $PC_{71}BM$ percentages on the film surface and in the bulk was examined. An almost linear relationship across all ratios is shown in Figure

5.10 (c), though this dependency weakens with higher ratios. Figure 5.10 (d) illustrates a similar linear trend for PTB7-Th across all ratios, but notably, the [1:3] ratio exhibits a lower $d_{010}$ peak intensity (around 200) with less than 20% surface concentration.

Despite these observations, higher PTB7-Th concentrations on the film surface are revealed by repeated chemical etching for the [1:3] devices. However, reduced efficiency is still exhibited by these devices due to lower current density from decreased PTB7-Th in the bulk, increased series resistance ($R_s$) disrupting charge pathways, higher contact resistance at the cathode, and reduced shunt resistance ($R_{sh}$) leading to leakage currents and lower fill factors.

## 5.4 Thin film materials characterisation

As mentioned previously in the introduction, from this section onward, device characterization involves applying numerous methods and techniques to evaluate the performance of OSCs based on PBDTTT-EFT polymer, using both chlorinated solvents and selected green solvents.

To understand the behaviour of these materials as blends, it is essential to first characterize them in their pristine form. Understanding the various properties of these thin films is crucial for optimizing devices based on this information. One important aspect of thin film characterization for devices is determining their optical spectroscopic properties. Most organic semiconducting materials are often categorized as "intrinsic wide band gap" semiconductors, meaning their absorption bands tend to be relatively narrow (Nicholson and Castro, 2010).

### 5.4.1 Optical absorption

The UV-Vis optical absorption spectroscopy was conducted on each pristine donor and acceptor material dissolved in CB[28] solution, as shown in Figure 5.11 under a spectral irradiance of 1.5 AMG (Air mass global). The 1.5 AMG spectra irradiance conforms to the standard set by the ‘American Society for Testing and Materials’ (ASTM) G-173 (ASTM G173 - 03(2020); Marzo et al., 2017), which is consistent with the solar simulator used in this study. The ASTM-G173 spectrum shows a peak irradiance between 450 – 500 nm,

[28] Chlorobenzene

tapering off as wavelengths increase. Therefore, an ideal donor material should exhibit absorbance in the range of 450 – 800 nm to efficiently harness solar energy.

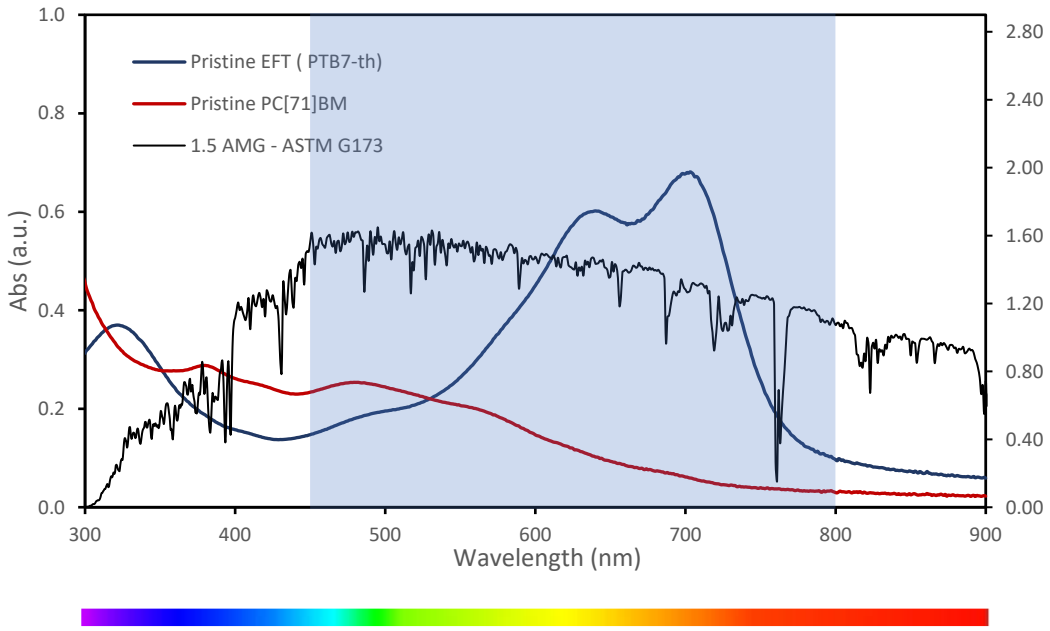


Figure 5.11 – Optical absorption for pristine EFT and pristine $PC_{71}BM$ dissolved with CB:ODCB and 1.5 AMG spectral irradiance

The optical band gap of a material can be determined from its absorption spectrum. In the case of EFT[29], the optical band gap is found to be 1.58 eV, derived from an absorption onset wavelength of approximately 785 nm shown in Figure 5.12. A detailed explanation of how band gap measurement is conducted from an optical absorption curve is provided in chapter 4.3.7.

Figure 5.12 also illustrates two peaks attributed to EFT around 638 nm and 700 nm, and one peak around 200-300 nm attributed to $PC_{71}BM$. These peaks provide critical information for comparing the absorption characteristics of these materials and assessing their suitability for photovoltaic applications.

[29] PBDTTT:EFT

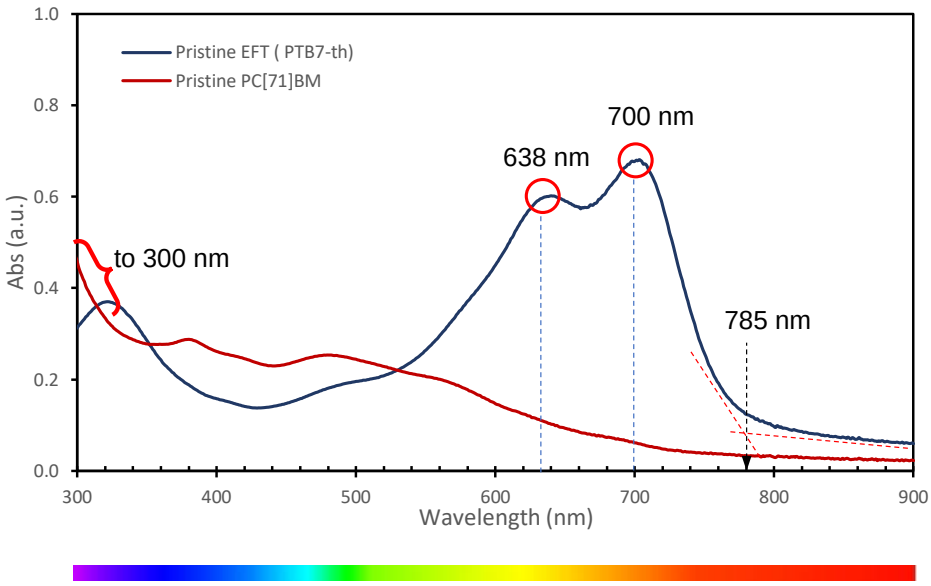


Figure 5.12 – UV-Vis Spectrum of PBDTTT-EFT and $PC_{71}BM$ with estimated optical absorption onset wavelength and its primary peak identifications dissolved with CB:ODCB

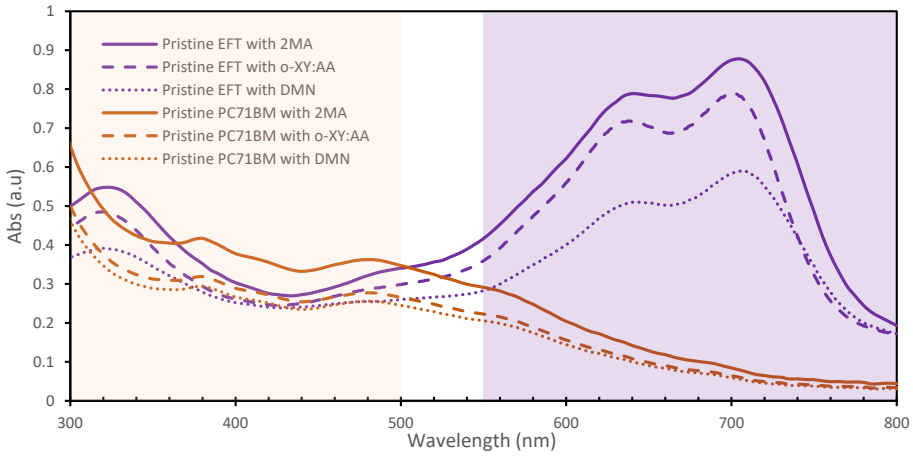


Figure 5.13 – UV-Vis Spectrum of PBDTTT-EFT and $PC_{71}BM$ when Green solvents applied in pristine materials

Figure 5.13 illustrates that the total absorption area of spectra using green solvents is greater compared to those using non-organic solvents. Remarkably, the peaks corresponding to PBDTTT-EFT at around 638 nm and 700 nm exhibit minimal wavelength shifts, but their intensities vary depending on the solvent used. Thin film samples prepared with 2MA green solvents show the least reduction in peak intensities at 638 nm and 700 nm, indicating minimal impact on the molecular backbone and π-π structure.

### 5.4.2 Photoluminescence Spectroscopy

In this section, Photoluminescence (PL) and Raman spectroscopy results are presented, shown in Figure 5.14 and Figure 5.15 below.

Figure 5.14 illustrates that the PL intensity of the EFT polymer is notably higher than that of $PC_{71}BM$. This difference arises because EFT acts as the donor material, absorbing a significant portion of incident light and generating higher excitons. Photoluminescence occurs when these excitons recombine without dissociating. The PL spectrum of pristine PBDTTT-EFT exhibits a broad peak with a flat emission extending from 770 nm to 800 nm. In contrast, the PL spectrum of $PC_{71}BM$, as a fullerene derivative acceptor material, shows distinct peaks around 713 nm and 775 nm.

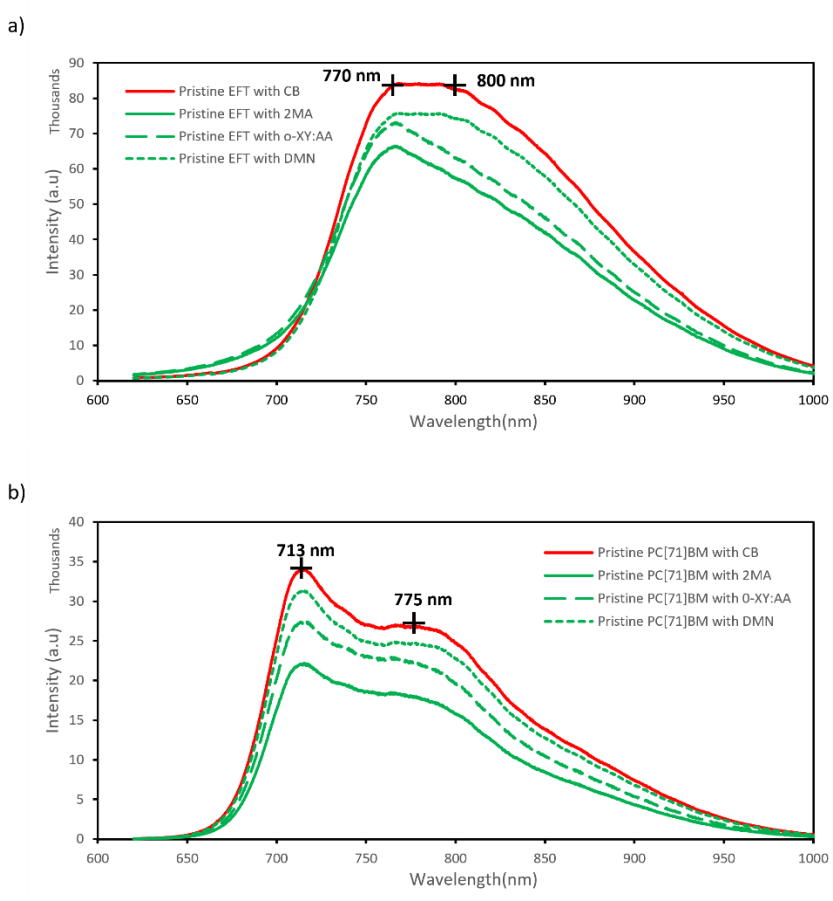


Figure 5.14 - PL for pristine EFT and $PC_{71}BM$ dissolved with CB:ODCB and compared with green solvents

When these materials are mixed with green solvents, the photoluminescence (PL) emission levels show differences not only in the positions of peaks and humps for each acceptor

material but also in their overall intensity. Particularly, the sample treated with 2MA as the green solvent exhibits the highest PL intensity among the three samples. This observation aligns with the higher absorption capabilities demonstrated by the material when mixed with 2MA.

### 5.4.3 Raman Spectroscopy

In an ideal scenario, resonant Raman spectroscopy involves using an excitation laser whose wavelength matches the maximum absorption of the material being studied (Liao et al., 2013; Razzell-Hollis et al., 2014). For instance, PBDTTT-EFT exhibits its peak optical absorption at 700 nm (see Figure 5.13). Therefore, to conduct resonant Raman spectroscopy on PBDTTT-EFT, an excitation laser with a wavelength of 700 nm would be ideal.

However, the Raman microscope used in this project is limited to excitation lasers with wavelengths of 514 nm and 785 nm. When using the 785 nm laser, which is closer to the absorption peak of PBDTTT-EFT, only the PBDTTT-EFT molecules would be excited (though requiring high laser power), and the profiles of acceptor materials would not be observed. On the other hand, using the 514 nm laser allows both donor and acceptor materials to produce Raman spectra.

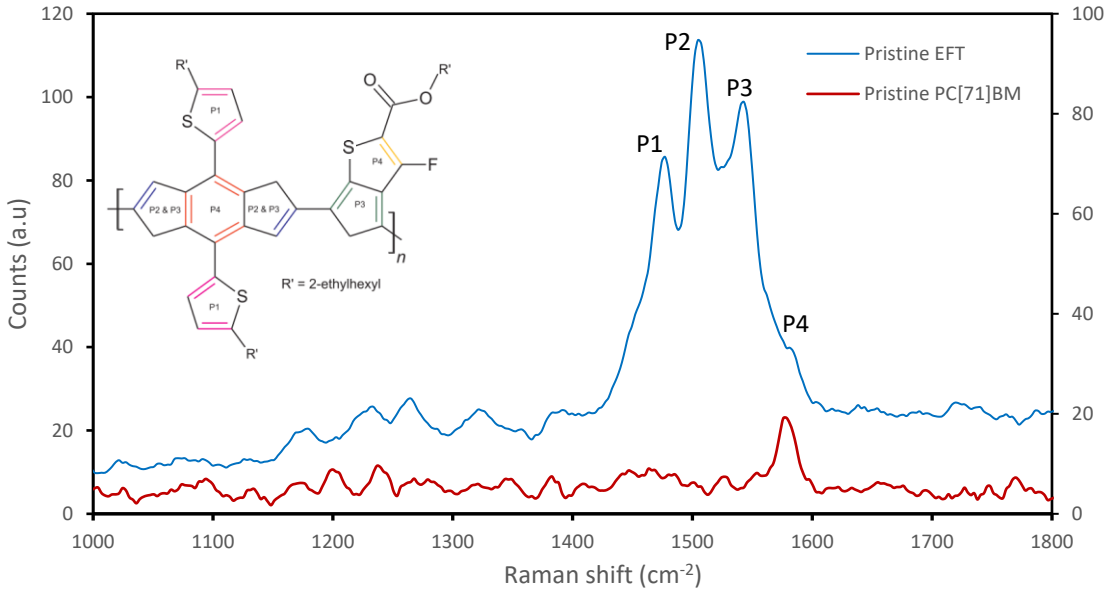


Figure 5.15 – Raman spectroscopy for pristine EFT and $PC_{71}BM$ dissolved with CB:ODCB

Figure 5.15 illustrates the Raman spectra obtained for pristine PBDTTT-EFT and $PC_{71}BM$ materials mixed with CB, collected under a 514 nm laser excitation.

Based on previous studies (Komilian, 2019), each peak observed in Raman spectroscopy corresponds to specific bonds within the molecule's structure. In the case of PTB7-th (PBDTTT-EFT), peaks P1 to P3 in the Raman spectra are associated with stretching modes of specific bonds within the molecule, while peak P4, occurring around 1576 $cm^{-1}$, is predominantly attributed to $PC_{71}BM$.

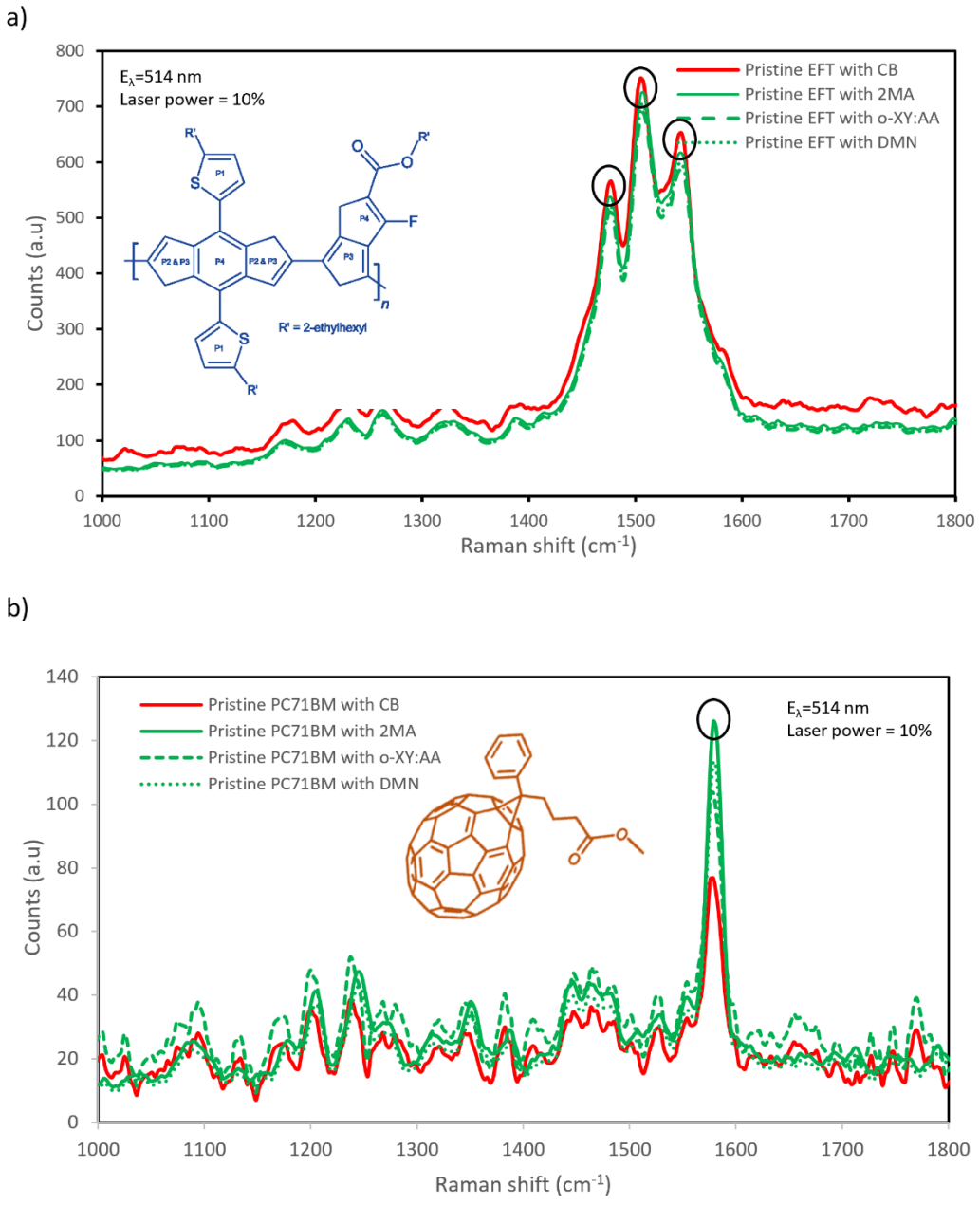


Figure 5.16 – Raman spectroscopy for pristine EFT and $PC_{71}BM$ dissolved with green solvents

Figure 5.16 illustrates the impact of green solvents when introduced into the mixture of pristine PBDTTT-EFT and $PC_{71}BM$. The analysis shows that there are no significant shifts in the positions of the peaks compared to mixtures using conventional solvents like CB. This suggests that the use of green solvents did not induce any noticeable changes in the molecular configuration or backbone length of the materials.

These identified Raman peaks can be valuable for future investigations aimed at determining the surface composition of blended materials using Raman spectroscopy. Understanding these peaks and their shifts in wavenumbers ($cm^{-1}$) provides insights into the molecular structure and can aid in analysing the texture and composition of the material surfaces. (For detailed information on each peak and their corresponding Raman shifts, refer to Komilian (2019), where these peaks are extensively discussed and assigned to specific bonds within the PBDTTT-EFT molecule)

### 5.4.4 GIXRD Analysis

Based on the GIXRD[30] diffractograms collected, data were analysed for pristine PBDTTT-EFT and pristine $PC_{71}BM$ dissolved in green solvents, comparing them with samples prepared using chlorinated solvents. Each sample was fabricated as a thin film on a quartz substrate to achieve a thickness of approximately 100 nm, a parameter optimized for the best performance based on literature findings. The fabrication process maintained consistent parameters to minimize induced defects.

To enhance peak characteristics and ensure optimal peak analysis for each sample, the diffractogram profile of the thin film on the substrate was subtracted from that of a clean quartz substrate, as detailed in Chapter 4.3.3. By subtracting the quartz substrate baseline, the distinctive peaks corresponding to specific crystallographic planes and molecular arrangements within the materials become more pronounced and discernible. This method facilitates a detailed analysis of the structural properties and orientation of the materials under investigation.

The extracted out-of-plane GIXRD parameters are presented in Table 5.6 and illustrated in Figure 5.17 , providing detailed insights into the structural characteristics of the materials analysed.

[30] Gracing Incidence X-ray Diffraction

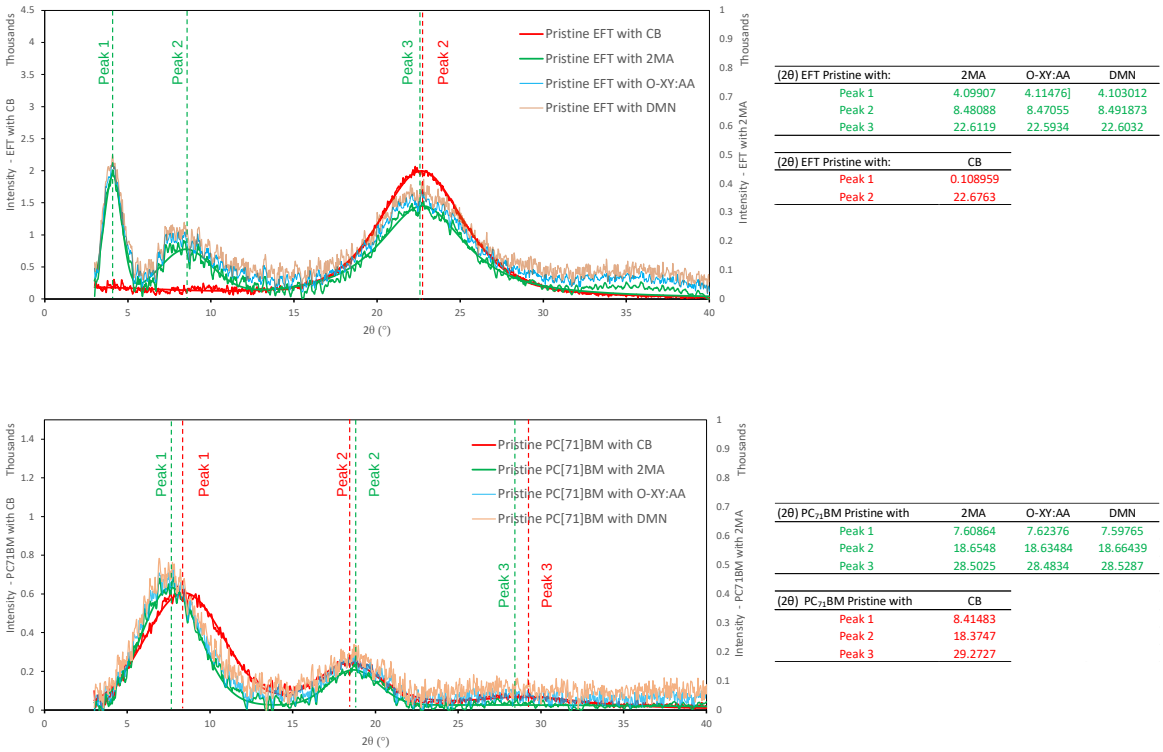


| (2θ) EFT Pristine with: | 2MA | O-XY:AA | DMN |
|---|---|---|---|
| Peak 1 | 4.09907 | 4.11476] | 4.103012 |
| Peak 2 | 8.48088 | 8.47055 | 8.491873 |
| Peak 3 | 22.6119 | 22.5934 | 22.6032 |

| (2θ) EFT Pristine with: | CB |
|---|---|
| Peak 1 | 0.108959 |
| Peak 2 | 22.6763 |

| (2θ) $PC_{71}BM$ Pristine with | 2MA | O-XY:AA | DMN |
|---|---|---|---|
| Peak 1 | 7.60864 | 7.62376 | 7.59765 |
| Peak 2 | 18.6548 | 18.63484 | 18.66439 |
| Peak 3 | 28.5025 | 28.4834 | 28.5287 |

| (2θ) $PC_{71}BM$ Pristine with | CB |
|---|---|
| Peak 1 | 8.41483 |
| Peak 2 | 18.3747 |
| Peak 3 | 29.2727 |

Figure 5.17 – Out of plane GIXRD diffraction pattern for Pristine EFT and $PC_{71}BM$ dissolved with green solvents and compared with CB:ODCB (quartz base removed).

Table 5.6 - OOP GIXRD parameter for Pristine EFT and $PC_{71}BM$ dissolved with green solvents and compared with CB:ODCB

| Sample | | Pristine $PC_{71}BM$ | | | | Pristine PTB7-Th | | | |
|---|---|---|---|---|---|---|---|---|---|
| Green solvent | Thickness (nm) | $d_{100}$ (Peak 1) | | $d_{200}$ (Peak 2) | | $d_{100}$ (Peak 1) | | $d_{010}$ (Peak 3) | |
| | | 2θ (º) | Intensity (a.u.) | 2θ (º) | Intensity (a.u.) | 2θ (º) | Intensity (a.u.) | 2θ (º) | Intensity (a.u.) |
| 2MA | 100 | 7.60 | 415 | 18.65 | 123 | 4.09 | 414 | 22.61 | 321 |
| O-XY:AA | 100 | 7.62 | 419 | 18.63 | 135 | 4.11 | 416 | 22.59 | 332 |
| DMN | 100 | 7.59 | 421 | 18.66 | 139 | 4.10 | 420 | 22.60 | 337 |
| CB | 100 | 8.41 | 594 | 18.37 | 241 | 0.11 | 171 | 22.67 | 1995 |

Based on the GIXRD results presented, two significant observations are noted when comparing the use of green solvents versus chlorinated solvents:

1. Reduction in Peak Intensity and Shift in Position: There is a noticeable decrease in peak intensity around 22° for PBDTTT-EFT (EFT) polymer and around 18° for $PC_{71}BM$ when green solvents are used compared to chlorinated solvents. Additionally, there is a slight shift in the 2θ position of these peaks.

2. Appearance of New Peak at 4°: Upon using green solvents, there is an emergence of a peak around 4° with increased signal intensity in the GIXRD spectra.

According to X-ray crystallography analyses reported in other studies, such as those from the NREL (NREL Developing Improved Tech to Lower Costs for Multi-Junction Solar Cells, 2018), the π-π stacking planes of PBDTTT-EFT (PTB7-Th) polymer are identified. Specifically:

- The face-on plane ($d_{010}$) of EFT exists at 2θ around 20-23°.
- The edge-on plane of EFT exists at 2θ around 3-6°.

Therefore, the increased intensity observed in the GIXRD data around 4°, corresponding to the $d_{100}$ plane of EFT, suggests a possible rotation in the molecular structure. This rotation could indicate changes in the π-π stacking arrangement of the polymer, potentially influenced by the use of green solvents compared to chlorinated solvents. Such changes in molecular orientation can significantly impact the structural properties and performance of the material in optoelectronic devices like solar cells.

### 5.4.5 Cyclic Voltammetry

Based on the cyclic voltammograms presented in Figure 5.18 and the subsequent calculations using Equations 4.4 and 4.5 (covered in section 4.3.2), the electrochemical reduction-oxidation potentials and energy levels (HOMO and LUMO) for both PBDTTT polymer and $PC_{71}BM$ were determined under different solvent conditions.

The onset potentials (i.e., either n- or p-doping) were determined from the intersection of the two tangents drawn at the rising current (oxidation or reduction) and background current in the cyclic voltammograms (Li et al., 1999). The estimated HOMO and LUMO energy levels for pristine PBDTTT and $PC_{71}BM$ are taken from the onset potentials identified in Figure 5.18 and are presented in Table 5.7.

In this table, the estimated HOMO and LUMO energy levels for pristine PBDTTT and $PC_{71}BM$ when dissolved in chlorinated solvents indicate energy band gaps of approximately 1.57 eV and 2.26 eV, respectively. These values align closely with the optical band gap values previously determined.

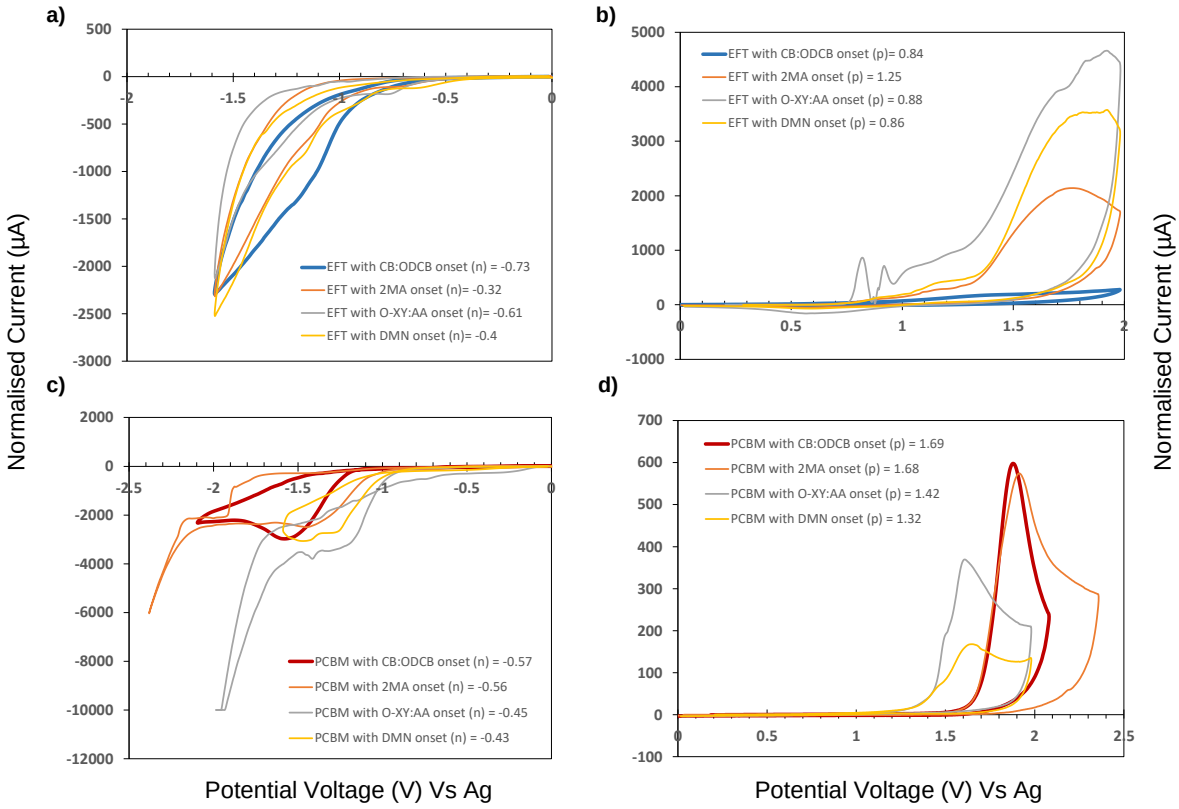


Figure 5.18 – Cyclic voltammograms of pristine PBDTTT:EFT (a,b) and $PC_{71}BM$ (c,d); oxidation and reduction potentials while mixed with CB and different green solvents

Table 5.7- Calculated HOMO and LUMO energy level for Pristine EFT and $PC_{71}BM$ while mixed with CB and compared with green solvents

| | HOMO (eV) | LUMO (eV) | Eg $_{donor/Acceptor}$ (eV) |
|---|---|---|---|
| EFT with CB:ODCB | -5.23 | -3.66 | -1.57 |
| EFT with 2MA | -5.64 | -4.07 | -1.57 |
| EFT with O-XY:AA | -5.27 | -3.78 | -1.49 |
| EFT with DMN | -5.25 | -3.99 | -1.26 |
| $PC_{71}BM$ with CB:ODCB | -6.08 | -3.82 | -2.26 |
| $PC_{71}BM$ with 2MA | -6.07 | -3.83 | -2.24 |
| $PC_{71}BM$ with O-XY:AA | -5.81 | -3.94 | -1.87 |
| $PC_{71}BM$ with DMN | -5.71 | -3.96 | -1.75 |

When the green solvent 2MA was used:

- PBDTTT:EFT - There was a significant change observed in the HOMO and LUMO energy levels compared to when chlorinated solvents were used. However, the energy band gap remained identical to that observed with chlorinated solvents.

- $PC_{71}BM$ - The energy levels and band gap did not show considerable changes when compared between chlorinated and 2MA solvents.

These findings suggest that while the choice of solvent can influence the electrochemical properties of the materials, particularly the HOMO and LUMO energy levels of PBDTTT, it does not significantly alter the overall energy band gap determined by electrochemical methods compared to optical measurements. This consistency between different measurement techniques reinforces the reliability of the band gap values obtained for these materials under various solvent conditions.

### 5.5 Devices Performance characteristics of OSCs blended in green solvents

In subsequent stages, the goal was to identify the most effective green solvents compatible with the blend of PBDTTT-EFT and $PC_{71}BM$ as donor and acceptor materials. Sample devices were fabricated using an optimized process based on recent studies (Komilian, Oklobia, and Sadat-Shafai, 2018b), ensuring consistency by utilizing the same fabrication facilities and configuration. This approach aimed to minimize any potential influence on the outcomes of the case study, thereby pinpointing the most suitable non-halogenated solvents for enhancing device performance between the materials mixed with green solvents.

#### 5.5.1 J-V characterisation

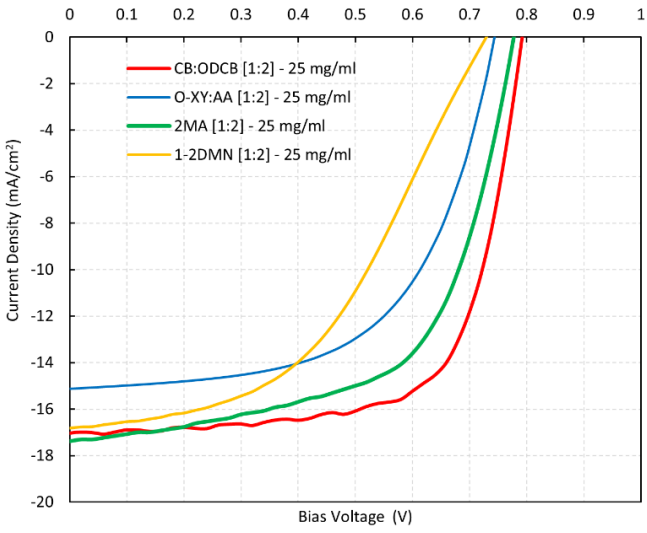


Figure 5.19– J-V curve for blend of EFT:$PC_{71}BM$ with different green solvent and compared with CB:ODCB

Figure 5.19 presents averaged data from three cells per sample, showing the J-V characteristics including $V_{oc}$, $J_{sc}$, $R_s$, $R_{sh}$, FF, and PCE, as detailed in Table 5.8.

Table 5.8 – J-V characteristics for blend of EFT:$PC_{71}BM$ with different green solvent

| EFT:$PC_{71}BM$ dissolved with | $J_{sc}$ (mA/cm$^2$) | $V_{oc}$ (V) | $R_s$ (Ω cm$^2$) | $R_{sh}$ (Ω cm$^2$) | PCE(%) | FF(%) |
|---|---|---|---|---|---|---|
| CB:ODCB | 17.09 | 0.79 | 6.31 | 929.1 | **9.30** | 0.69 |
| O-XY:AA [1:100] | 15.13 | 0.75 | 6.61 | 426.2 | **6.64** | 0.59 |
| **2MA** | 17.39 | 0.78 | 7.38 | 372.41 | **8.17** | 0.60 |
| 1-2 DMN100% | 16.83 | 0.73 | 20.22 | 371.70 | **5.75** | 0.47 |

Analysis of each sample revealed that the highest performance was achieved using 2-Methyl Anisole (2MA) as the primary solvent. This sample exhibited $J_{sc}$ of 17.39 mA cm$^{-2}$, $V_{oc}$ of 0.78 V, FF of 60%, and PCE of 8.17%. These results indicate that devices using 2MA as the solvent perform best among the selected green solvents and closely match the performance of the control sample dissolved in ODCB:CB[31].

### 5.5.2 Optical absorption

Figure 5.20 illustrates further investigations conducted on the samples, specifically focusing on their optical absorption characteristics. Within the wavelength range corresponding to EFT (approximately 500 – 800 nm), there were no significant changes in intensity observed. However, a noticeable decrease in absorption within the UV range (200 to 350 nm), associated with $PC_{71}BM$, can be observed when comparing samples using green solvents versus chlorinated solvents (indicated by the red line).

[31] 1,2-Dichlorobenzene:Chlorobenzene

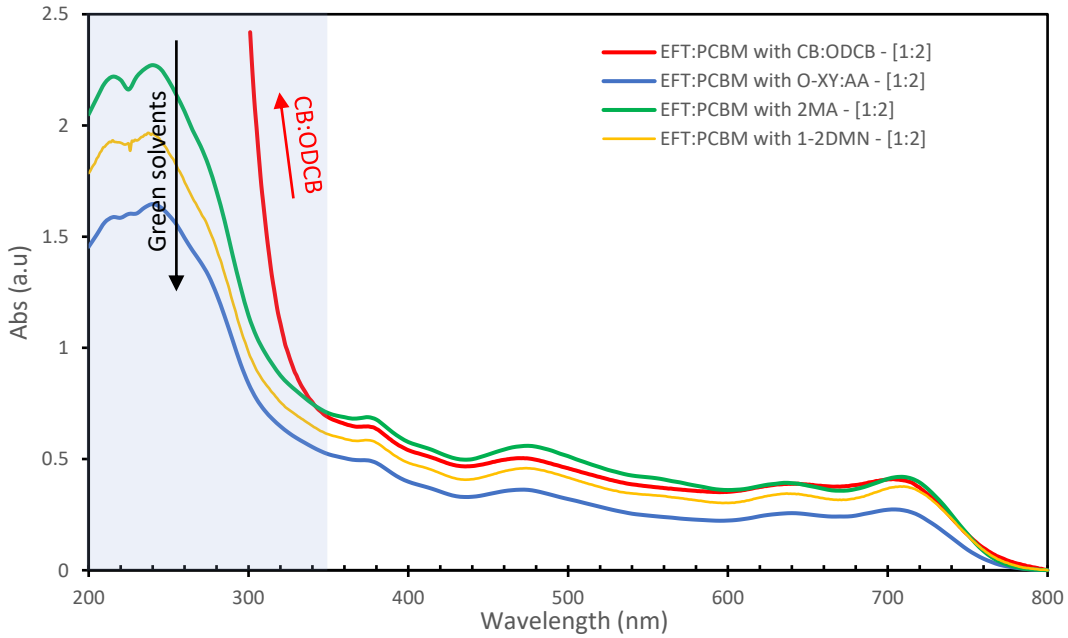


Figure 5.20 – Optical absorption for EFT:$PC_{71}BM$ dissolved with different green solvent and compared with CB:ODCB

This intensity deterioration could possibly be associated with the formation of $PC_{71}BM$ clusters. A similar trend has been reported previously by other researchers when they used blends of P3HT (Oklobia and Shafai, 2013).

The next section will delve into the study of Raman spectroscopy and PL to investigate any potential observations resulting from the application of different green solvents to the blends.

### 5.5.3 Raman Spectroscopy

In chapter 5.4.3, the specifics regarding the configuration and laser power used for Raman spectroscopy were detailed. As shown in Figure 5.21, there were no discernible changes observed in the Raman spectra when utilizing green solvents as compared to halogenated solvents.

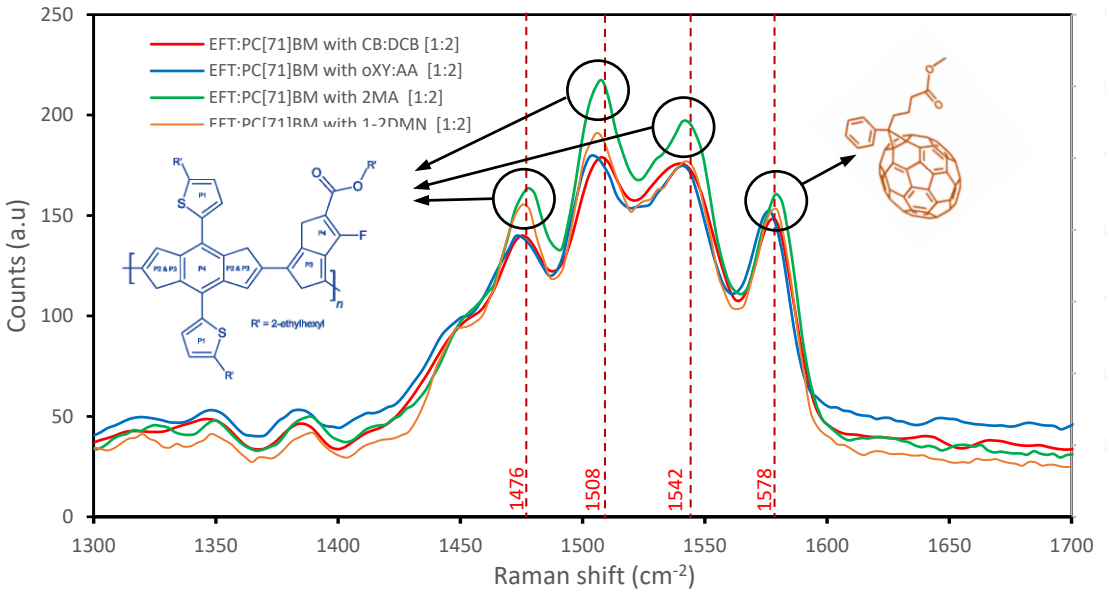


Figure 5.21 – Raman spectroscopy for EFT:$PC_{71}BM$ dissolved with different green solvent. (Red colour belongs to the peak position for control sample dissolved with CB:ODCB)

It is expected, based on the results of J-V characteristics from Table 5.8, that any changes in the J-V characteristics could be attributed to morphological and internal molecular structure deformations or alterations in chemical bonds within the polymer blend. Therefore, shifts in Raman spectra ($cm^{-1}$) should be observable. However, as indicated by the shift positions shown in Figure 5.21, the Raman spectra peaks for the control sample (highlighted in red) were nearly identical in position compared to the other samples.

Based on this observation, it can be suggested that green solvents did not induce any significant impact on the internal molecular structure, and there were no observable chemical changes to the EFT polymer due to the introduction of green solvents into the system. In the study conducted by Komilian (2019), it was noted that the peaks corresponding to EFT molecule structure are located at 1476 $cm^{-1}$, 1508 $cm^{-1}$, and 1542 $cm^{-1}$ respectively. The peak for $PC_{71}BM$ excitation was also observed at 1578 $cm^{-1}$, which aligns with its presence in both pristine materials and the blend spectra. Thus, $PC_{71}BM$ appears to exert a notable influence on the blend spectra within this excitation range.

### 5.5.4 Photoluminescence Spectroscopy

To comprehend the influence of the donor-acceptor (D:A) blend and its significance in charge dissociation, the photoluminescence (PL) spectra profiles for blends of PBDTTT-EFT with $PC_{71}BM$ were collected and are presented in Figure 5.22.

It is evident that the peak intensities for blends using green solvents are consistently higher compared to those using chlorinated solvents. Additionally, blends with green solvents exhibited less quenching compared to those with chlorinated solvents, indicating a potentially reduced recombination process.

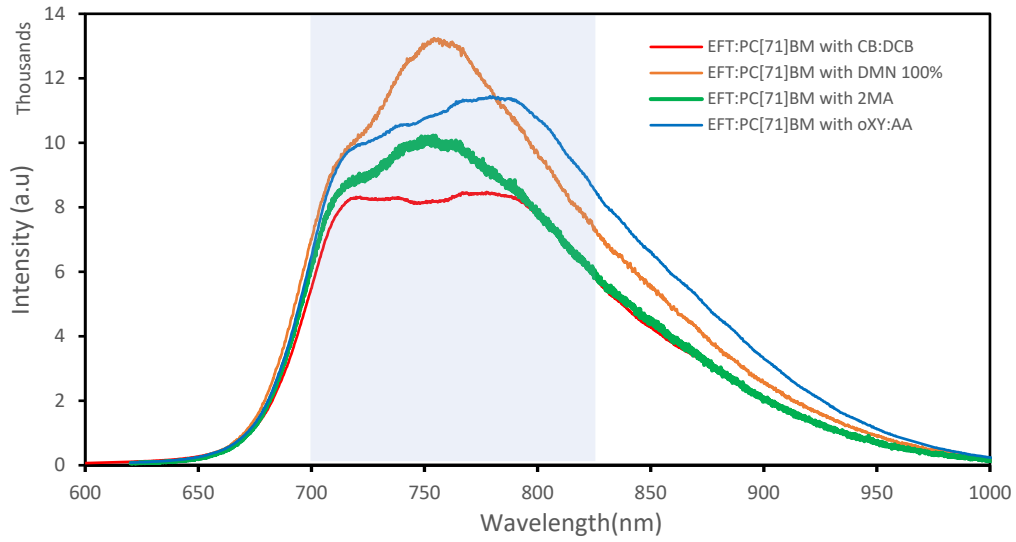


Figure 5.22 – PL for EFT:$PC_{71}BM$ blend dissolved with different green solvents

From the blended materials photoluminescence (PL) spectra, it is evident that the PL intensity is lower compared to their respective pristine films, as previously discussed in section 5.4.2. Specifically, the blend of PBDTTT-EFT dissolved with 2MA green solvent exhibits the most quenched PL spectrum profile among the three samples, closely followed by the sample mixed with CB, suggesting a favourable donor/acceptor interface. In contrast, the blend with DMN Green solvent shows less quenching, indicating a potentially less optimal donor/acceptor interface.

Analysing the PL emission profiles of each blended thin film reveals a visible hump on the right side of the profile, more pronounced in the 700-850 nm range. This observation suggests an uneven distribution or presence of one of the components more prominently on the surface of the thin film. Since PL spectroscopy probes the surface, these findings imply

that PBDTTT-EFT samples tend to have a higher concentration of one component's molecules on the film surface.

Considering these observations and their potential impact on device performance when green solvents are used, further investigation into the internal structure and deeper understanding of the blends was conducted using GI-XRD (Grazing Incidence X-ray Diffraction), as detailed in the next section.

### 5.5.5 GIXRD full Analysis in blend

Based on the J-V characteristics results presented in section 5.3.1 and the compositional analysis up to this point, it appears that 2MA solvent demonstrates the best compatibility with the chosen donor-acceptor (D:A) blend. Therefore, 2MA will be selected as the primary green solvent for further investigation in this research, using an identical fabrication process. The aim is to understand why there might be a slight decrease in performance observed when 2MA is introduced into the system.

Figure 5.23 illustrates the GIXRD diffraction pattern of the blend with 2MA compared to chlorinated solvent, with detailed data extracted for GIXRD analysis provided in Table 5.9.

A notable observation is that using 2MA as the solvent enhances a peak associated with the lower 2θ region corresponding to the $d_{100}$ plane of EFT molecules within the blend. This plane is indicative of EFT molecules in an Edge-on orientation (Komilian, 2019), suggesting a possible change in the planarity of EFT polymer when 2MA is introduced into the blend.

Furthermore, when comparing samples dissolved in 2MA versus chlorinated solvents, the intensity of the $PC_{71}BM$ $d_{200}$ plane remains relatively unchanged, but the full-width-half-maximum (FWHM) parameters notably increase. Additionally, there is a leftward shift in the 2θ position. A shift towards lower 2θ values typically indicates an increase in the distance between the polymer backbones (π-stacking), as suggested by Komilian, Oklobia, and Sadat-Shafai (2018). These observations strongly suggest that $PC_{71}BM$ molecules likely form clusters in the presence of 2MA solvent.

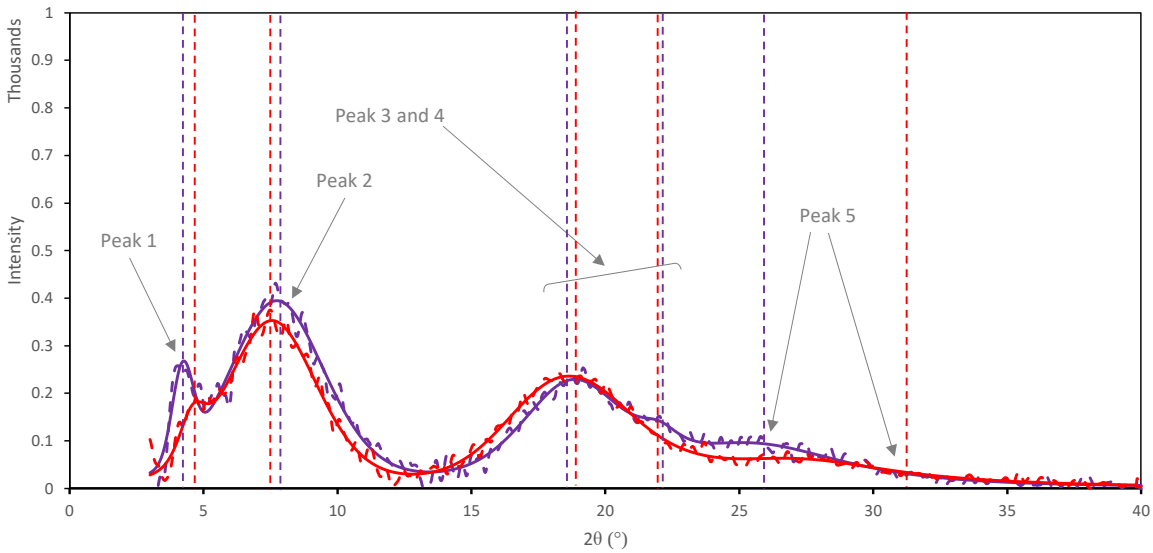


| EFT:$PC_{71}BM$ blend with 2MA [1:2] (2θ) | |
|---|---|
| Peak 1 | 4.1 |
| Peak 2 | 8 |
| Peak 3 | 18.5 |
| Peak 4 | 22.8 |
| Peak 5 | 26.2 |
| EFT:$PC_{71}BM$ blend with CB:ODCB (2θ) | |
| Peak 1 | 4.91 |
| Peak 2 | 7.7 |
| Peak 3 | 18.7 |
| Peak 4 | 22.6 |
| Peak 5 | 32 |

Figure 5.23 - Out of plane GIXRD diffraction pattern for EFT:$PC_{71}BM$ blend dissolved with 2MA and compared with CB:ODCB (quartz base removed)

Table 5.9 - OOP GIXRD parameter for EFT:$PC_{71}BM$ blend dissolved with 2MA and compared with CB:ODCB

| | $PC_{71}BM$ | | | | | | PTB7-Th | | | | | |
|---|---|---|---|---|---|---|---|---|---|---|---|---|
| Green solvent | $d_{100}$ (Peak 2) | | | $d_{200}$ (Peak 3) | | | $d_{100}$ (Peak 1) | | | $d_{010}$ (Peak 4) | | |
| | 2θ (°) | FWHM | Intensity (a.u.) | 2θ (°) | FWHM | Intensity (a.u.) | 2θ (°) | FWHM | Intensity (a.u.) | 2θ (°) | FWHM | Intensity (a.u.) |
| 2MA | 8.02 | 4.17 | 394 | 18.50 | 4.51 | 229 | 4.10 | 1.14 | 285 | 22.80 | 5.32 | 151 |
| CB | 7.70 | 4.12 | 356 | 18.70 | 3.92 | 227 | 4.91 | 1.55 | 192 | 22.60 | 5.85 | 128 |

When comparing samples dissolved in 2MA to those dissolved in chlorinated solvents, notable changes are observed in the GIXRD analysis of the EFT $d_{010}$ and $d_{100}$ planes. Specifically:

1. FWHM (Full-Width-Half-Maximum): The FWHM has decreased for both the $d_{010}$ and $d_{100}$ planes of EFT when using 2MA solvent compared to chlorinated solvents.

This indicates a narrower peak width and potentially improved crystallinity or reduced disorder in the molecular packing of EFT.

2. 2θ Position Shifts: The 2θ position has shifted to higher values for the $d_{010}$ plane and lower values for the $d_{100}$ plane when using 2MA solvent. These shifts suggest changes in the intermolecular spacing or packing density within the polymer layers.

These changes in d-spacing in the EFT planes suggest a dynamic interaction where the formation of $PC_{71}BM$ clusters on the layer surfaces likely influences the conformation of EFT molecules from their preferred orientation. This interaction could impact the distribution and arrangement of the donor-acceptor pair within the active layer materials.

The observed effects, including internal intercalation and nano-structural development (such as clustering), are likely significant factors contributing to the slightly poorer fill factor (FF) observed in devices with 2MA solvent. These phenomena underscore the intricate interplay between solvent choice, molecular packing, and device performance in organic photovoltaics.

### 5.6 Applying Novel 3D Profiling techniques for most optimised green solvent

In previous sections, the goal was to identify the best-performing green (non-halogenated) solvents for fabricating organic solar cells (OSCs). Sample devices were fabricated using an optimized process, and their J-V characteristics were evaluated (Figure 5.19 and Table 5.8). It was found that devices using 2-Methyl Anisole (2MA) as the main solvent exhibited the best performance, with $J_{sc}$ of 17.39 mA $cm^{-2}$, $V_{oc}$ of 0.78 V, FF of 60%, and PCE of 8.17%. These characteristics were closest to those of the control sample using CB:ODCB solvent.

However, despite achieving similar $J_{sc}$ and $V_{oc}$ values to the control sample, devices with 2MA showed higher series resistance ($R_s$) and lower shunt resistance ($R_{sh}$), which had a significant impact on their overall performance. The lower fill factor (FF) observed in the 2MA samples was primarily attributed to these out-of-range $R_s$ and $R_{sh}$ values.

Fill factor is one of the crucial parameters determining the efficiency of OSCs, although it is less understood compared to $V_{oc}$ and $J_{sc}$. Factors influencing FF include carrier extraction, recombination processes, and carrier mobility imbalances. Poor interfacial morphology between electrodes and the active layer can also adversely affect FF (Qi and Wang, 2013; Jao, Liao, and Su, 2016).

Given that 2MA showed the best device performance among the green solvents tested, further investigation into the causes of FF deterioration when using 2MA is essential. This deeper analysis aims to identify opportunities for improving OSC fabrication to mitigate or eliminate the undesired FF decrease associated with 2MA as the solvent of choice.

### 5.6.1 J-V characteristics for the blend of EFT:$PC_{71}BM$ dissolved with 2MA

At this point, to better understand the nanostructure formation in samples fabricated using 2-Methyl Anisole (2MA), optimized Raman mapping techniques were applied to analyse the surface and in-depth structures of the devices. The internal nanostructure and potential unexpected conformations were compared with in-depth GIXRD analysis to identify issues arising from the introduction of green solvents.

For this approach, each sample's active layer thickness was reduced by approximately 20 nm using a chemical etching technique, previously described in section 4.3.11. The cathode layer was then deposited as the top layer of the device. This process was sequentially employed, reducing each sample's thickness by up to 40 nm.

Figure 5.24 presents the average data sets from three cells per sample, extracted and shown in Table 5.10 for samples where the green solvent 2MA was applied.

Based on these results, the best performance was observed in the sample with an optimum active layer thickness of 100 nm. The J-V characteristics for this sample were $J_{sc}$ of 17.75 mA $cm^{-2}$, $V_{oc}$ of 0.80 V, FF of 58.4%, and PCE of 8.26%. The data was gathered from cells with thicknesses of 100, 80, 60, and 40 nanometres after applying the washing technique.

The PCE at 100 nm thickness was 13.9% higher than that at 80 nm thickness. The trends in current density and power conversion efficiency were very similar, indicating that current density played a significant role in controlling device performance. The reduction in current density with surface washing, which removes part of the absorbing layers, was expected and contributed to the observed trends.

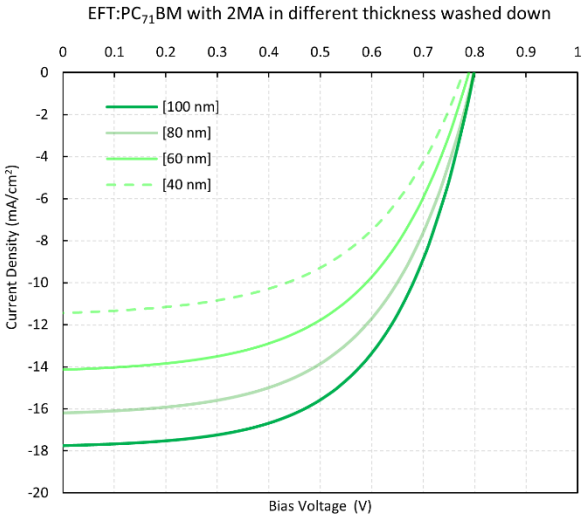


Figure 5.24– J-V curve for blend of EFT:$PC_{71}BM$ with 2MA in different active layer thickness

Table 5.10 – J-V characteristics for blend of EFT:$PC_{71}BM$ with 2MA green solvent in different thicknesses

| EFT:$PC_{71}BM$ with 2MA | $J_{sc}$ (mA/cm$^2$) | $V_{oc}$ (V) | $R_s$ (Ω cm$^2$) | $R_{sh}$ (Ω cm$^2$) | PCE(%) | FF(%) |
|---|---|---|---|---|---|---|
| 1st wash (100 nm) | 17.75 | 0.80 | 7.8 | 956 | **8.26** | 58.4 |
| 2nd Wash (80 nm) | 16.20 | 0.80 | 11.2 | 782 | **7.25** | 56.3 |
| 3rd Wash (60 nm) | 14.15 | 0.79 | 14.5 | 585 | **5.91** | 53.2 |
| 4th Wash (40 nm) | 11.45 | 0.78 | 22.40 | 420 | **4.35** | 49.1 |

### 5.6.2 2D Raman mapped images for the blend of EFT:$PC_{71}BM$ dissolved with 2MA as function of different film thicknesses washed down with etching technique

Recent research by Komilian et al. (2018) demonstrated that, based on J-V characteristic curves and extracted electrical parameters, the performance of fabricated devices improves with increasing $PC_{71}BM$ content up to a donor-to-acceptor (D:A) blend ratio of [1:2]. Beyond this ratio, any further increase in $PC_{71}BM$ results in reduced device performance and power conversion efficiency (PCE). Consequently, all sample devices in this study were fabricated using this optimized D:A ratio of [1:2], following the same fabrication facilities and configurations as previous studies to ensure consistency and avoid impacting the case study outcomes. This approach aimed to identify the most suitable non-halogenated solvents.

The 2D Raman mapping data on the surface of a sample with approximately 100 nm thickness indicated that, although using the green solvent in the active layer mixture achieved appropriate performance characteristics, clustering formation occurred both on the surface and within the bulk.

To investigate this phenomenon further, optimized 2D Raman mapping techniques were employed on active layers of varying thicknesses using a chemical etching technique. The results, shown in Figure 5.25, confirmed that clustering of one component of the active layer material occurred when 2MA was used as an alternative green solvent.

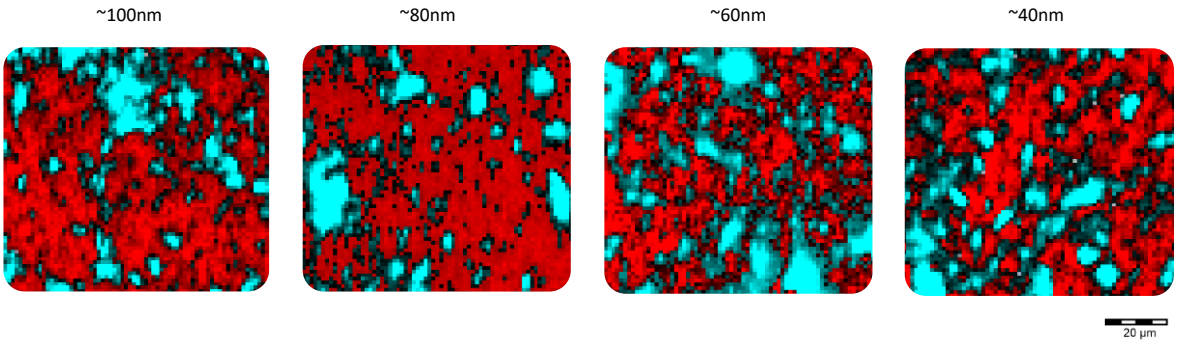


Figure 5.25 – 2D Raman mapped images for blend of EFT:$PC_{71}BM$ ([1:2] 25 mg/ml) dissolved with 2MA as function of different film thicknesses while chemical etching was used.

Raman mapping analysis revealed that in blends of the active layer with green solvent, extra dissolving occurred, probably resulting in an unhomogenized structure. This created more undissolved clotted areas, clearly observable in the mapped images. Red areas indicate $PC_{71}BM$-rich domains, while cyan areas indicate EFT-rich domains. The distribution of clotted cyan areas changed upon decreasing the thickness through chemical etching. Table 5.11 and Figure 5.26 show the percentage of $PC_{71}BM$-rich regions extracted from the film surface of the blends dissolved with 2MA, as a function of different film thicknesses, using the optimized MATLAB© image processing algorithm illustrated in previous sections.

The declining trend in $PC_{71}BM$ percentage on the surface as a function of active layer thickness decrease was the expected behaviour, observed similarly in samples with chlorinated solvents.

Table 5.11 - Percentage of $PC_{71}BM$ rich regions extracted from the film surface of different PTB7-Th: $PC_{71}BM$ blend dissolved with 2MA

| EFT : $PC_{71}BM$ with 2MA | [1:2] | | |
|---|---|---|---|
| | Thickness | $PC_{71}BM$ rich domain | EFT rich domain |
| 1st wash | 100 | 66.15 | 33.85 |
| 2nd wash | 80 | 60 | 40 |
| 3rd wash | 60 | 56.3 | 43.7 |
| 4th wash | 40 | 53.9 | 46.1 |

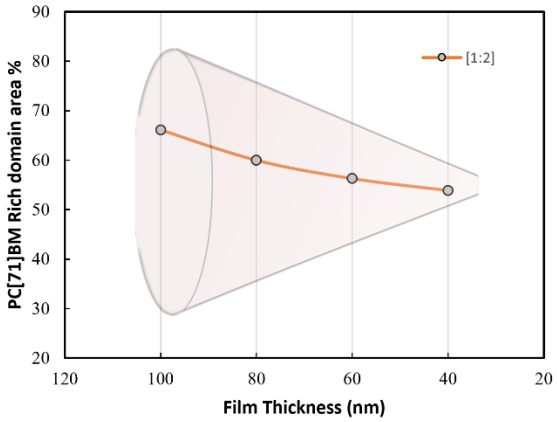


Figure 5.26 - Percentage of $PC_{71}BM$ rich regions extracted from the film surface of different PTB7-Th: $PC_{71}BM$ blend dissolved with 2MA while chemical etching used

The influence of structural formation was clearly observed in previous sections, where the $PC_{71}BM$ percentage converged to about 50% in the layer of roughly 40 nm in the bulk as the film thickness in all samples decreased. This indicates that $PC_{71}BM$ molecules tend to accumulate in the bottom layers of the active layer film under equilibrium conditions. This pattern, previously shown in Figure 5.5 and Figure 5.6 for various blend ratios and thicknesses with chlorinated solvents, demonstrates a steady molecular formation that shapes a funnel behaviour for these samples.

Figure 5.26 further illustrates this funnel behaviour in the $PC_{71}BM$ percentage trend, which is crucial for a thorough understanding of molecular intercalation in depth when using green solvents in the system. The optimized 2D Raman mapping and the chemical etching techniques applied in this study provided insights into how the distribution and clustering of $PC_{71}BM$ and EFT molecules affect the overall morphology and performance of the active layer.

These observations underscore the importance of examining the internal structure and distribution of materials within the active layer. The steady accumulation of $PC_{71}BM$ at lower thicknesses suggests that achieving an optimal blend distribution requires careful control of the solvent and fabrication process. This understanding is vital for further optimizing the performance of organic solar cells (OSCs) using non-halogenated, green solvents.

### 5.6.3 OOP GIXRD parameter extracted from curve fits for the blend of EFT:$PC_{71}BM$ while dissolved with 2MA and different film thickness

After the chemical etching technique was applied to samples with green solvents, the out-of-plane Bruker D8 Advance X-ray diffraction technique was employed to extract the GIXRD parameters. The results are shown in Table 5.12.

Table 5.12 – OOP GIXRD parameter extracted from curve fits for PTB7-Th and $PC_{71}BM$ films while dissolved in blend with 2MA and different film thickness

| | | EFT | | | | | | PCBM | | |
|---|---|---|---|---|---|---|---|---|---|---|
| Sample Ratio | Thickness ~(nm) | $d_{100}$ | | | $d_{010}$ | | | $d_{200}$ | | |
| | | 2θ (°) | FWHM | Intensity (a.u.) | 2θ (°) | FWHM | Intensity (a.u.) | 2θ (°) | FWHM | Intensity (a.u.) |
| 1:2 | 100 | 4.02 | 1.12 | 289 | 22.85 | 5.3 | 155 | 18.50 | 4.5 | 225 |
| | 80 | 3.96 | 1.15 | 247 | 22.8 | 5.3 | 139 | 18.51 | 4.53 | 192 |
| | 60 | 3.99 | 1.11 | 212 | 22.79 | 5.27 | 127 | 18.49 | 4.51 | 167 |
| | 40 | 3.98 | 1.14 | 185 | 22.82 | 5.31 | 117 | 18.53 | 4.57 | 153 |

According to crystallography theory, sharper peaks have lower full width half maximum (FWHM) with higher intensity, and powder materials exhibit sharper peaks than materials in solution form. Thus, samples in solution form with more clustering (as non-homogenized particles) display sharper peaks in GIXRD analysis (Komilian, Oklobia, and Sadat-Shafai, 2018).

In Table 5.12, it is evident that all three planar intensities for $PC_{71}BM$ and EFT molecules decreased with the reduction of thickness when chemical etching was applied. This is because the total amount of diffracted X-ray beams penetrating the layer decreased as the sample thickness was reduced.

A key comparison between GIXRD samples with 2MA (Table 5.12) and chlorinated solvents (Table 5.9) further supports the hypothesis of molecular conformation changes when 2MA is used. As previously discussed in sections 5.4.4 and 5.5.5, the intensity of the $PC_{71}BM$ $d_{200}$ plane remained consistent between samples dissolved with 2MA and those with chlorinated solvents. However, the FWHM parameters increased significantly, and the 2θ position shifted to the left. A shift toward lower 2θ indicates an increase in d-spacing between the polymer's backbone (π-π stacking) (Komilian, Oklobia, and Sadat-Shafai, 2018). These observations suggest that $PC_{71}BM$ molecules likely formed clusters.

For the EFT $d_{010}$ and $d_{100}$ planes, it was observed that the FWHM decreased compared to samples dissolved with chlorinated solvents. Additionally, the 2θ position shifted to a higher value for the $d_{010}$ plane and a lower value for the $d_{100}$ plane. This change in d-spacing in these two planes caused a seesaw effect, confirming that $PC_{71}BM$ cluster formation on the layer surface likely impacted the preferred orientation of EFT molecules.

These findings indicate that the donor and acceptor pair distribution texture in active layer materials is influenced by the internal intercalation between green solvents and the presence of acceptors. This internal intercalation and nanostructure formation (the main reason for clustering phenomena) are crucial factors contributing to the poorer fill factor (FF) in devices using 2MA.

### 5.6.4 Summary

The nanostructure and nanomorphology of the active layer in OSC devices fabricated using the green solvent 2MA have been better understood through the utilization of developed Raman mapping and in-depth profiling techniques in this study. These investigations have highlighted the significant role of fullerenes in self-organization, with results used to identify the percentages of both donors and acceptors on the film surface.

Since halogen-free green solvents are not yet employed in manufacturing processes for commercial or industrial solar systems, it is crucial for the field to successfully use the

selected green solvent to create highly effective OSCs with available photovoltaic materials. To this end, the next section will encompass a study aimed at large-area manufacturing, utilizing the most optimized green solvent to establish specific patterns and characteristics to overcome the issues outlined in previous sections.

## 5.7 Step towards Large fabrication of OSCs using green solvent

OPVs face challenges such as susceptibility to UV radiation, atmospheric moisture, and oxygen, which shorten their lifespan (Girtan and Rusu, 2010; Omrane et al., 2010). Developing OPVs that are stable in normal atmospheric conditions, cost-effective, and achieve high power conversion efficiencies is crucial for commercial viability (Lo et al., 2012).

Over the past decade, significant advancements have been made in developing thousands of materials, including conjugated polymers and fullerene derivatives, and refining processing methods for fabricating active layers in polymer solar cells (PSCs). These efforts have notably improved the power conversion efficiencies (PCEs) of PSCs with bulk heterojunction (BHJ) structures. However, the predominant use of halogenated solvents in PSC fabrication remains a concern.

Addressing this issue is urgent for the PSC field, given the rapid progress in PCEs. This research has focused on exploring alternatives to halogenated solvents, with promising results demonstrating that OSCs with relatively high efficiencies can be fabricated using the non-halogenated solvent 2-methyl anisole (2MA) in the active layer materials PTB7, as detailed in Chapter 5.6.

While halogen-free solvents are not yet integrated into commercial or industrial photovoltaic manufacturing lines, utilizing selected green solvents to replicate highly efficient OSCs using current photovoltaic materials would be pivotal for advancing the field (Zhao et al., 2015).

### 5.7.1 Fabrication of Prototype OSCs by using green solvent and laser patterning technique

To address the challenges discussed earlier, achieving specific patterns and characteristics for large-area fabrication using optimized green solvents is imperative. One viable technique for large-scale production is the roll-to-roll (R2R) method, which has demonstrated potential but faces limitations in uniformity and device thickness, impacting efficiencies (Krebs, Gevorgyan and Alstrup, 2009; Søndergaard et al., 2012; Søndergaard, Hösel and Krebs, 2013).

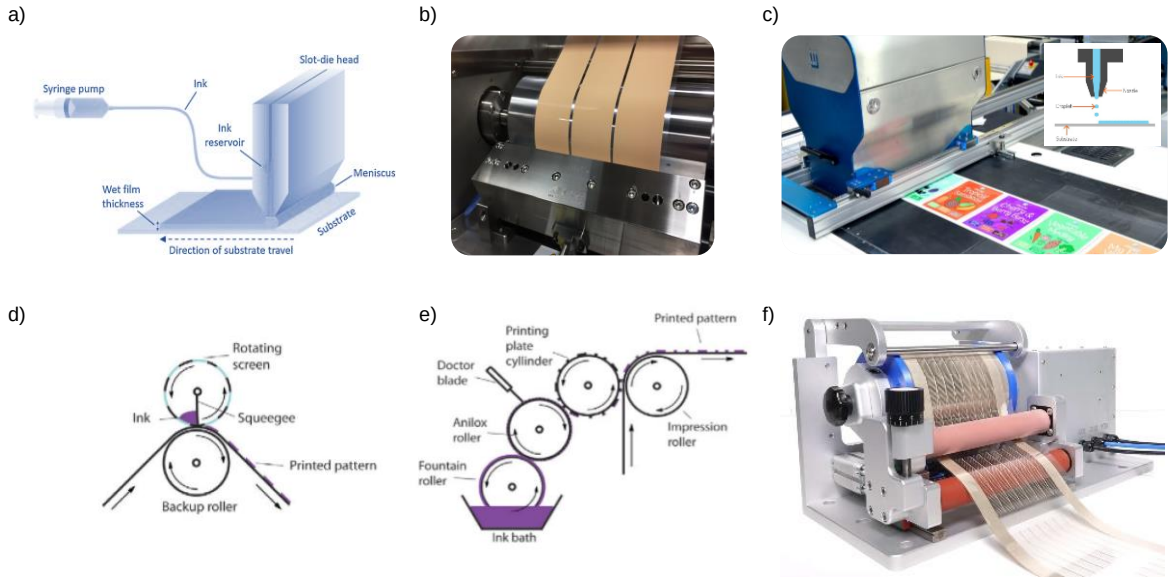


Figure 5.27- a,b) schematic illustration of knife coating and slot-die coating where excess ink is kept ahead of the knife, c) continuous inkjet printing. d) Screen/Rotary printing technique, e,f) Flexography printing ((Krebs, 2009; Søndergaard *et al.*, 2012)

Various printing and coating techniques are also utilized for large-scale fabrication on flexible substrates like PET (polyethylene terephthalate), with the choice critical for success depending on electrode materials and surface processing (Figure 5.27). Coating methods involve applying a continuous wet layer along a web's length without direct contact, ensuring superior control over wet thickness. Techniques like knife coating and slot-die coating are commonly employed for fabricating active multi-layers in continuous lines.

Printing methods, on the other hand, transfer ink to substrates through physical contact, creating two-dimensional patterns. Flexography printing, suitable for low-viscosity inks, offers high fabrication speeds but faces challenges in minimal ink transfer capability. Screen

printing allows for very thick wet layers, beneficial for applications requiring high conductivity, such as printed electrodes for polymer solar cells. Inkjet printing, with its ability to print specific patterns by depositing ink droplets without contact, offers flexibility but is limited by ink compatibility and setup complexity (Krebs, 2009; Nie, Wang and Zou, 2012; Søndergaard, Hösel and Krebs, 2013; Ganesan, Mehta and Gupta, 2019).

In this project, the goal of prototype large-scale fabrication was to utilize the most optimized green solvent while treating cells within the designed module as real large modules in series or parallel configurations. To simplify fabrication and identify optimal patterns, the design principles focused on minimizing the impact of fabrication techniques. The critical steps included defining patterns in the bottom ITO-coated layer and top cathode layer, achievable through methods like thermal deposition or inkjet printing with nanoparticle inks.

Designing the ITO layer pattern involved applying basic electrical principles of series and parallel circuits. Laser engraving techniques, as detailed in Chapter 4.2.2, were employed to pattern the ITO-coated layer in two main configurations: parallel and series connections, investigating their impact on large-scale designs when using green solvents in devices.

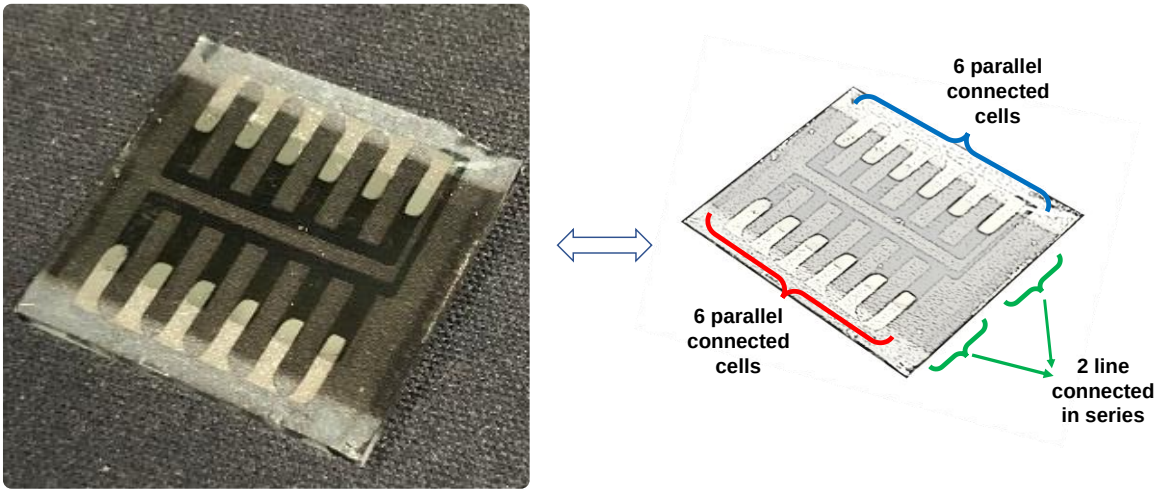


Figure 5.28- Fabricated 12 devices on patterned ITO layer using laser engraving and green solvent in active layer materials PTB7:$PC_{71}BM$

Figure 5.28 illustrates the configuration of 12 fabricated cells connected in series and parallel. Each line consists of 6 cells connected in parallel, and the two lines are connected in series. During fabrication, stringent parameters were maintained across all devices to minimize induced defects, ensuring consistency and reliability across the 12 devices in both series and parallel configurations.

### 5.7.2 J-V Results characterisation

In section 4.2.2, the active area of the devices was defined by overlapping two layers during fabrication: the ITO-coated layer patterned using laser surface engraving and the top conductive electrode layer patterned via thermal evaporation deposition with a mask. These patterns collectively formed an active area of 2 $mm^2$. Given the consistent substrate size of 25 × 25 $mm^2$, a total of 12 cells were accommodated, each occupying an area of 24 $mm^2$, for current density calculations under illumination from a solar simulator.

To maintain consistency and minimize the impact of induced defects, the same solar simulator employed in previous sections and the conclusions chapter was used throughout this study. This approach ensured uniform testing conditions across all experimental phases, facilitating accurate comparison and evaluation of the prototype module's performance under simulated sunlight.

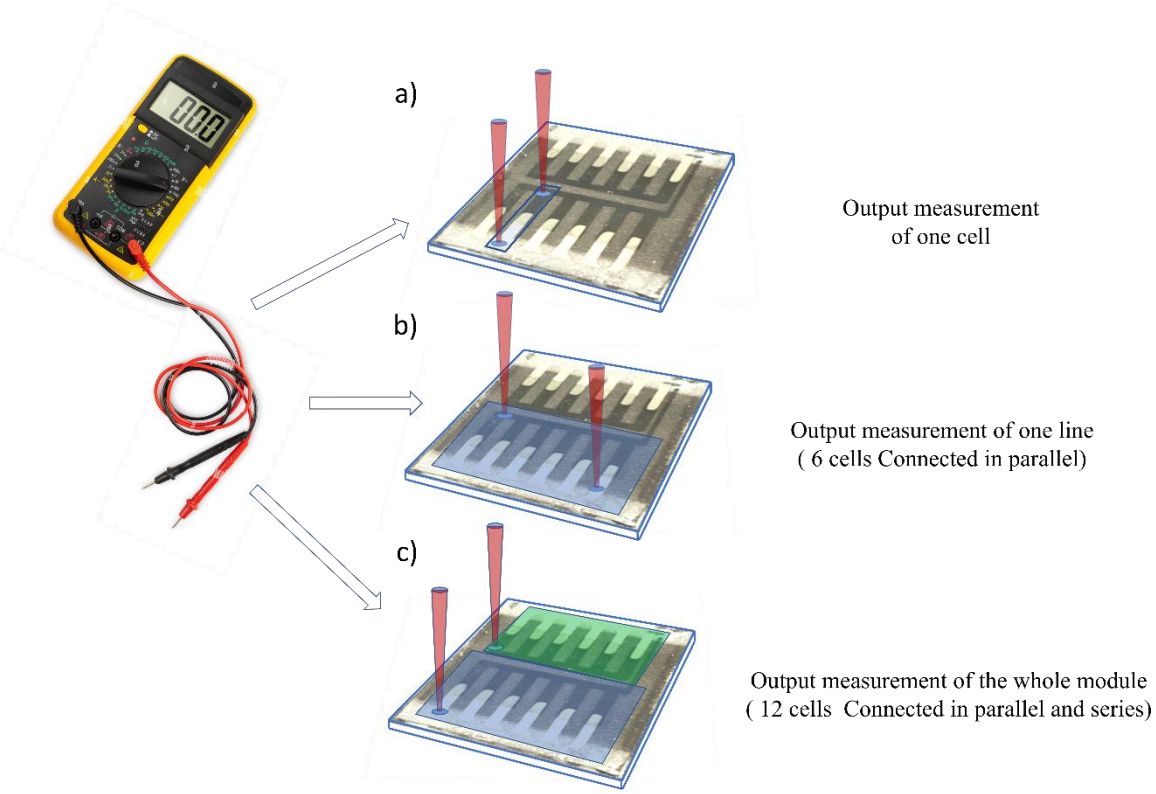


Figure 5.29- Output measurement of prototype fabricated 12 devices on patterned ITO layer with active layer materials PTB7:$PC_{71}BM$ and dissolved with green solvent 2MA

For measuring the output of individual cells, the neighbouring cells were covered with a non-transparent black layer to prevent any potential reverse current flow. Figure 5.29 (a) illustrates the placement of probes on the module to measure the output of a single cell. Figures 5.29 (b) and 5.29 (c) depict the specific points on the module's surface where probes were positioned to measure the output of 6 cells in parallel and the combined pattern of 12 cells in series and parallel, respectively.

The results of the J-V characteristics are presented in Figure 5.30 and Table 5.13 for the different series and parallel connections. The voltage output from the PV module is determined by the number of solar cells connected in series, while the current output depends on the size of the solar cells and the number connected in parallel. Therefore, increasing the number of cells in series increases the module's voltage output, whereas increasing the cells in parallel boosts the current output. These fundamental principles guide the configuration of cell connections within the module to achieve specific performance characteristics, within the limitations imposed by the number of cells available in the module.

Table 5.13 – J-V characteristics for blend of EFT:$PC_{71}BM$ with 2MA green solvent connected in different pattern as one module

| EFT:$PC_{71}BM$ with 2MA | $J_{sc}$ (mA/cm$^2$) | $I_{sc}$ (mA) | $V_{oc}$ (V) | $R_s$ (Ω cm$^2$) | $R_{sh}$ (Ω cm$^2$) | PCE(%) | FF(%) |
|---|---|---|---|---|---|---|---|
| 1 cell separately (Randomly selected) | 18.12 | 0.362 | 0.81 | 5.87 | 997 | **9.09** | 62.1 |
| 12 cells connected in parallel | 18.05 | 4.332 | 0.81 | 6.12 | 985 | **8.87** | 60.9 |
| 12 cells connected in series | 1.50 | 0.36 | 9.61 | 6.05 | 991 | **8.71** | 60.5 |
| 12 cells connected in two series lines while connected in parallel within each line | 9.02 | 2.164 | 1.60 | 6.08 | 989 | **8.74** | 60.7 |
| 12 cells connected in two parallel lines while connected in series within each line | 3.01 | 0.722 | 4.80 | 6.07 | 990 | **8.76** | 60.8 |

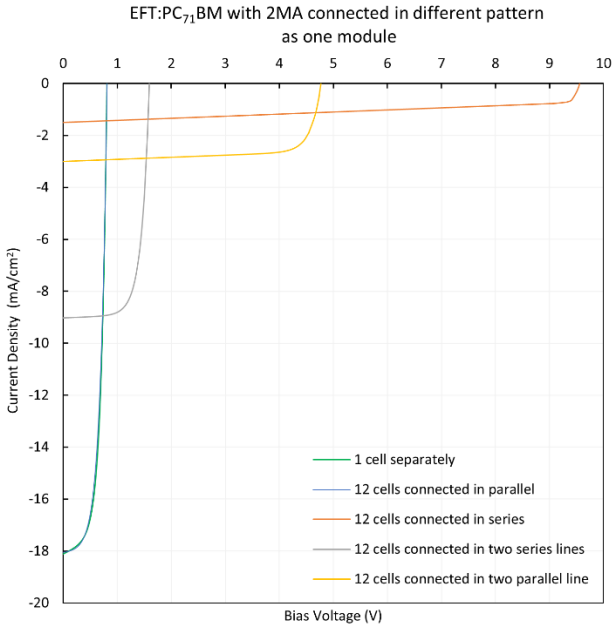


Figure 5.30- I-V curves for blend of EFT:$PC_{71}BM$ with 2MA green solvent connected in different pattern as one module

Table 5.13 demonstrates that when solar cells are connected in series, the overall I-V curve shows an increase in voltage, reaching 9.61 V for the 12-cell series configuration. However, the short-circuit current density ($J_{sc}$) decreases due to the larger active area of the cells. On the other hand, connecting cells in parallel results in a significant increase in the overall current output. Despite each cell maintaining a similar current density to that of a single cell, the total output current scales up approximately twelvefold to 4.33 mA. The non-uniformity among the 12 cells, including variations in active area, affects the fill factor when cells are arranged in series or parallel, thereby influencing the total current extracted from the module. While this disparity has minimal impact on series resistance ($R_s$) and shunt resistance ($R_{sh}$), it is a critical consideration when designing combined series-parallel patterns.

Previous studies have documented a power conversion efficiency (PCE) of 5.2% for organic photovoltaic (OPV) devices using O-xylene as a green solvent (Zhang et al., 2016). Other research employing various halogen-free solvents has achieved PCEs around 7% (as referenced in Table 3.1). Notably, Sprau et al. (2015) reported a PCE of 9.5% using the green solvent XY/anisaldehyde (AA) in OPV systems based on the PffBT4T-2OD polymer/acceptor pair. As indicated in Table 5.13, prototype large-scale samples in this project achieved PCEs ranging from 8.7% to 8.9%, which are significant and promising

results when utilizing selected green solvents as alternatives to prevalent chlorinated solvents in current market applications. These green solvents were found to be highly compatible with the PBDTTT-EFT polymer donor material and $PC_{71}BM$ fullerene derivative acceptor, based on previous studies highlighting their potential for organic solar cell (OSC) applications (Komilian, Oklobia, and Sadat-Shafai, 2018b).

## 5.8 Summary of Results and Discussions

Advanced Raman mapping techniques were employed to investigate the nanostructure and nanomorphology of the active layer in organic solar cells (OSCs) in this study. The study highlighted the pivotal role of fullerene in the self-organization process within these devices. Through Raman mapping, precise estimates of the distribution percentages of both the donor (PTB7-Th) and acceptor ($PC_{71}BM$) on the film surface were achieved.

The use of methanol in chemical etching processes facilitated controlled adjustments to the thickness of the active layer, essential for optimizing device fabrication. Raman mapping of chemically etched film surfaces provided detailed insights into the surface distribution of $PC_{71}BM$ and PTB7-Th at different depths within the film. Notably, the study demonstrated how $PC_{71}BM$ influences the orientation of PTB7-Th, shifting it from a face-on to edge-on configuration.

Moreover, X-ray diffraction (XRD) analysis of etched film surfaces with varying $PC_{71}BM$ loadings validated the findings from Raman mapping, confirming vertical migration of $PC_{71}BM$ within the film structure. This migration directly impacted the electrical characteristics of the devices, emphasizing the significance of $PC_{71}BM$ distribution between the film surface and bulk in determining device performance.

The study also explored the effects of patterning the ITO coated layer using laser engraving techniques, assessing parallel and series configurations at a large scale. The results demonstrated that prototype OSCs achieved competitive power conversion efficiencies (PCEs) ranging from 8.7% to 8.9%, positioning them favourably in the market for organic photovoltaic applications.

In conclusion, this research integrates advanced characterization techniques with innovative fabrication methodologies to advance the understanding and performance of OSCs. The findings underscore the importance of precise control over nanostructure formation and

material distribution in optimizing OSC device performance, paving the way for further developments in green solvent-based OSC technologies.

# CHAPTER 6

# Conclusion & Future Work

As previously mentioned, addressing the persistent challenge of mitigating the toxic effects of halogenated solvents in large-scale manufacturing processes of OPVs remains critical and urgent. This chapter consolidates the conclusions drawn from experimental results and their analysis, aiming to guide future researchers in this field.

## 6.1 Conclusions

The primary objective of this study was to examine how green solvents influence existing OPV systems and potentially offer solutions to replace chlorinated solvents. Extensive literature was reviewed to address key challenges in OSCs' pre-fabrication processes. A variety of suitable green solvents were selected, and further research and investigation were conducted on these materials.

The selected donor and acceptor materials were utilized exactly as in previous recent reports, known for their high performance potential. Therefore, this project focused on identifying compatible green solvents for existing OPV systems. DMN (Dimethylnaphthalene), o-Xylene:NMP (N-Methyl pyrrolidone), and 2MA (2-methylanisole) were identified as the top-performing green solvents due to their suitable compatibility parameters with the selected narrow band gap polymers. Radar analysis indicated that 2MA and o-Xylene showed the best compatibility with the chosen polymer system (D:A).

For the first time in the Organic Solar Cells field, novel analytical techniques have been developed and applied to investigate the internal structure formation of molecules both on the surface and within the bulk. These advancements have enabled the detailed 3D profiling of bulk heterojunctions in OPV systems, as outlined in Figure 6.1:

- A new 2D morphological analysis method has been devised to extract numerical morphological parameters from AFM[32] phase images. These parameters are then applied to Raman mapping images using consistent procedures.
- Furthermore, a study was conducted on blended films containing PTB7-Th and $PC_{71}BM$, which underwent a chemical etching process. By precisely adjusting the technique configuration, the thickness of the active layer could be slightly reduced through drop-casting alcohol-based solvents onto the layer's surface.
- To gain deeper insights into the internal molecular structures and the formation of $PC_{71}BM$ molecules at the surface layers during chemical etching, an advanced MATLAB© image processing algorithm was employed. This algorithm facilitated the generation of 3D representations depicting the internal composition of each etched layer.

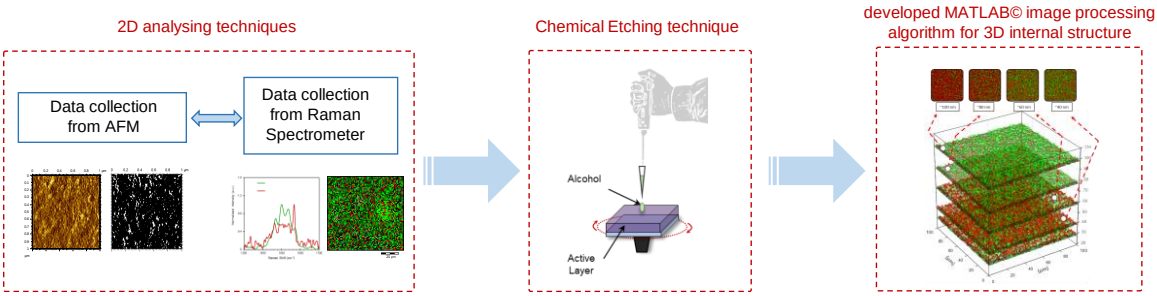


Figure 6.1- The Novel comprehensive analysing techniques flowchart showing the steps of using developed techniques for 3D profiling of bulk heterojunctions of OPV systems

The analytical findings indicate that devices using 2-Methyl Anisole (2MA) as the solvent exhibited superior performance among the selected green solvents, closely approaching the counterpart sample dissolved in CB:ODCB at a blend ratio of [1:2]. This sample yielded J-V characteristics of $J_{sc}$ at 17.39 mA $cm^{-2}$, $V_{oc}$ at 0.78 V, FF at 60%, and PCE at 8.17%.

To explore the reasons behind the slightly diminished performance observed when introducing 2MA to the system, further investigations focused on both the surface and internal nano-structuring of the active layer components. AFM phase results revealed a

[32] Atomic Force Microscopy

phenomenon where blend components clustered and appeared prominently on the surface in bright colours when 2MA was used as the green solvent. Another analysis demonstrated a correlation between surface Raman mapping data and AFM phase images, highlighting red areas in Raman mapping images as $PC_{71}BM$-rich domains on the film surface.

GIXRD analysis of pristine EFT and $PC_{71}BM$ dissolved with 2MA revealed an intriguing observation: the solvent intensified a peak associated with the $d_{100}$ plane of EFT molecules at lower $2\theta$, potentially indicating a change in the preferred orientation of EFT polymer molecules towards an edge-on configuration.

By penetrating to the lower active layers in the film by detailed washing and using the sophisticated techniques, it becomes apparent that a consistent molecular formation is observed around 40nm into the lower active layers of the film. Approximately 50% of $PC_{71}BM$ molecules are detected on the surface of each sample. This gradual increase in $PC_{71}BM$ concentration plays a pivotal role in deepening our understanding of the internal nano-structural formation of donor and acceptor components.

Further in-depth analysis using GIXRD with samples dissolved in chlorinated solvents has revealed that the presence of $PC_{71}BM$ molecules significantly affects the conformation of EFT molecules, shifting their preferred orientation from face-on to edge-on. There exists a strong functional relationship between the concentration of $PC_{71}BM$ molecules and the amount of EFT molecules oriented in the edge-on configuration. Subsequent steps investigate the implications of nano-morphology and nano-structuring on OPV electrical parameters using these samples. Results indicate a correlation between current density and the percentage of $PC_{71}BM$ on the film surface. This finding aligns well with the understanding that higher concentrations (above 1:1) facilitate the migration of $PC_{71}BM$ to the device surface, potentially enhancing charge collection at the cathode. However, this migration could also implicate exciton dissociation and alter charge carrier pathways to the respective electrodes due to reduced $PC_{71}BM$ quantity in the bulk.

Furthermore, a higher concentration of $PC_{71}BM$ at the film surface may enhance $R_{sh}$ and fill factor, but it can disrupt charge carrier pathways. Consequently, the lower efficiency observed in these devices is attributed to i) reduced current density due to lower PTB7-Th presence in the bulk, impacting photocurrent generation, ii) increased Rs from disrupted charge carrier pathways and higher contact resistance due to concentrated PTB7-Th at the cathode, and iii) reduced $R_{sh}$ leading to leakage current and lower fill factor.

Additionally, advanced analytical techniques, complemented by chemical etching and washing procedures, have been employed to analyse samples of the blended ratio [1:2] dissolved with 2MA. These methods were compared with chlorinated samples to explore the rationale behind potential clustering formation in these systems.

Raman mapping analysis has revealed that in the blend of the active layer with a green solvent, an additional dissolving phenomenon has occurred, resulting in an uneven structure with more undissolved clustered areas. These clustered regions are clearly visible in mapped images as regions where clusters have formed. There is a noticeable decrease in the percentage of $PC_{71}BM$ on the surface as the thickness of the active layer decreases. This behaviour mirrors what is typically observed with acceptors in samples using chlorinated solvents, with the threshold limit appearing to stabilize around 50%.

Analysing GIXRD results from samples with 2MA and comparing them with chlorinated solvents has shown that $PC_{71}BM$ molecules exhibit cluster formation, confirming earlier indications. It is strongly suggested that the clustering of $PC_{71}BM$ can indeed occur when green solvents are used in the system. This phenomenon leads to unexpected disruptions in charge carrier networks within the active layer, thereby potentially increasing the rate of recombination.

In the final phase of the research, the focus shifted to the deliberate prototyping of large-scale fabrication of the system using the most optimized green solvent, with cells in the designed module intended to mimic real large-scale modules configured in series or parallel patterns. Utilizing laser engraving techniques, the ITO-coated layer was patterned into two primary configurations: parallel and series connections, aimed at studying their impact on large-scale design. Prototype devices were fabricated in five different patterns.

The results indicate that in series connection, the overall J-V curve of a set of identically connected solar cells exhibited increased voltage but decreased $J_{sc}$ due to larger active cell areas. Conversely, when cells were connected in parallel, the current density from 12 cells connected in parallel remained comparable to that of a single cell, while the overall output current increased approximately twelvefold compared to individual cells. The overall fill factor may have been influenced by areas of mismatch, which in turn could affect the total current achievable from the output channels. These configurations had a negligible impact

on $R_s$ and $R_{sh}$ resistances but are important considerations when combining parallel or series patterns in design.

Based on these findings, the achieved PCE of 8.7-8.9% with prototype large-scale samples represents a significant and promising outcome, especially considering the use of green solvents as an alternative to chlorinated solvents in the current market.

## 6.2 Future works

In future research endeavours, the impact of using green solvents on device performance, aimed at eliminating the toxic effects of halogenated solvents in large-scale manufacturing processes of organic photovoltaics (OPVs), will continue to be a pivotal focus. The methodologies developed in this study can serve as a foundational framework for future investigations, facilitating the transition from traditional lab-scale fabrication methods to scalable manufacturing of organic solar cells, particularly emphasizing comprehensive analytical techniques for detailed morphological analysis.

The prototype large-scale fabrication undertaken in this project utilized the most optimized green solvent, treating cells within the module as authentic large modules configured in series or parallel patterns. To minimize fabrication impacts and determine the optimal pattern for large-scale production, the design principles were deliberately kept straightforward. For future work, selecting the appropriate fabrication technique for the top cathode layer, such as inkjet printing using nanoparticle inks or thermal deposition processes, is crucial. The choice of technique will significantly influence manufacturing efficiency, ensuring accuracy and speed necessary for viability in the OPV industry.

Additionally, future research could leverage the developed techniques introduced in this study to explore alternative materials for various aspects of OSCs manufacturing. For instance, investigating Carbon Nano Tubes (CNTs) or graphene derivatives as non-metal electrodes presents promising alternatives. Optimizing these materials for ideal inkjet-printing techniques could overcome current challenges faced by researchers, potentially enhancing efficiency and performance in OPV production processes.

# *References*


Adir Bar-Lev. (1993). *Semiconductor and electronic devices (1993 edition) | Open Library*. Prentice-Hall in New York. https://openlibrary.org/books/OL1726115M/Semiconductor_and_electronic_devices

Aernouts, T., Vanlaeke, P., Geens, W., Poortmans, J., Heremans, P., Borghs, S., Mertens, R., Andriessen, R., & Leenders, L. (2004a). Printable anodes for flexible organic solar cell modules. *Thin Solid Films*, *451–452*, 22–25. https://doi.org/10.1016/j.tsf.2003.11.038

*AFM-phase-images-of-P3HT-PCBM-blends-mixed-with-varying-wt-loads-of-P3HT-b-PS-all-3*. (n.d.).

Aizawa, N., Pu, Y. J., Watanabe, M., Chiba, T., Ideta, K., Toyota, N., Igarashi, M., Suzuri, Y., Sasabe, H., & Kido, J. (2014). Solution-processed multilayer small-molecule light-emitting devices with high-efficiency white-light emission. *Nature Communications*, *5*, 1–7. https://doi.org/10.1038/ncomms6756

Albery, W. J., Bartlett, P. v, Electroanal Chem, J., Hiinig, S., Brédas, J. L., Silbey, R., Boudreaux, D. S., & Chance, R. R. (1983). Chain-Length Dependence of Electronic and Electrochemical Properties of Conjugated Systems: Polyacetylene, Polyphenylene, Polythiophene, and Polypyrrole. *Journal of the American Chemical Society*, *105*(22), 6555–6559. https://doi.org/10.1021/JA00360A004

Andrienko, D. (2008). *Cyclic Voltammetry* (Issue Cv). http://www2.mpip-mainz.mpg.de/~andrienk/journal_club/cyclic_voltammetry.pdf

Angmo, D., Gevorgyan, S. A., Larsen-Olsen, T. T., Søndergaard, R. R., Hösel, M., Jørgensen, M., Gupta, R., Kulkarni, G. U., & Krebs, F. C. (2013). Scalability and stability of very thin, roll-to-roll processed, large area, indium-tin-oxide free polymer solar cell modules. *Organic Electronics*, *14*, 984–994. https://doi.org/10.1016/j.orgel.2012.12.033

*ASTM G173 - 03(2020) Standard Tables for Reference Solar Spectral Irradiances: Direct Normal and Hemispherical on 37° Tilted Surface*. (n.d.). https://www.astm.org/Standards/G173

Babics, M., Liang, R. Z., Wang, K., Cruciani, F., Kan, Z., Wohlfahrt, M., Tang, M. C., Laquai, F., & Beaujuge, P. M. (2018). Solvent Vapor Annealing-Mediated Crystallization Directs Charge Generation, Recombination and Extraction in BHJ Solar Cells. *Chemistry of Materials*, *30*(3), 789–798. https://doi.org/10.1021/acs.chemmater.7b04286

Bachmann, J., Buerhop-Lutz, C., Deibel, C., Riedel, I., Hoppe, H., Brabec, C. J., & Dyakonov, V. (2010). Organic solar cells characterized by dark lock-in thermography. *Solar Energy Materials and Solar Cells*, *94*(4), 642–647. https://doi.org/10.1016/j.solmat.2009.11.006

Bar, G., Thomann, Y., Brandsch, R., Cantow, H.-J., & Whangbo, M.-H. (1997). *Factors Affecting the Height and Phase Images in Tapping Mode Atomic Force Microscopy. Study of Phase-Separated Polymer Blends of Poly(ethene-co-styrene) and Poly(2,6-dimethyl-1,4-phenylene oxide)*.

Baran, D., Balan, A., Celebi, S., Meana Esteban, B., Neugebauer, H., Sariciftci, N. S., & Toppare, L. (2010). Processable multipurpose conjugated polymer for electrochromic and photovoltaic applications. *Chemistry of Materials*, *22*(9), 2978–2987. https://doi.org/10.1021/cm100372t

Bergqvist, J., Österberg, T., Melianas, A., Ever Aguirre, L., Tang, Z., Cai, W., Ma, Z., Kemerink, M., Gedefaw, D., Andersson, M. R., & Inganäs, O. (2018). Asymmetric photocurrent extraction in semitransparent laminated flexible organic solar cells. *Npj Flexible Electronics*, *2*(1), 4. https://doi.org/10.1038/s41528-017-0017-6

*Best Research-Cell Efficiency Chart | Photovoltaic Research | NREL*. (2021). https://www.nrel.gov/pv/cell-efficiency.html

Bi, P., & Hao, X. (2019). Versatile Ternary Approach for Novel Organic Solar Cells: A Review. *Solar RRL*, *3*(1), 1800263. https://doi.org/10.1002/solr.201800263

Binnig, G., & Quate, C. F. (1986). Atomic Force Microscope. *Physical Review Letters*, *56*(9), 930–933. https://doi.org/10.1103/PhysRevLett.56.930

Bisquert, J., & Garcia-Belmonte, G. (2011). On voltage, photovoltage, and photocurrent in bulk heterojunction organic solar cells. *Journal of Physical Chemistry Letters*, *2*(15), 1950–1964. https://doi.org/10.1021/jz2004864

Brabec, C. J. (Christoph J. ), Scherf, U., D′i͡akonov, V. A., & Angmo, Dechan. (2014). *Organic photovoltaics : materials, device physics, and manufacturing technologies*. http://libcat.staffs.ac.uk/cgi-bin/koha/opac-detail.pl?biblionumber=193353

Brabec, C. J., Sariciftci, N. S., & Hummelen, J. C. (2001). Plastic Solar Cells. *Advanced Functional Materials*, *11*(1), 15–26. https://doi.org/10.1002/1616-3028(200102)11:1<15::AID-ADFM15>3.0.CO;2-A

Brabec, C. J., Shaheen, S. E., Winder, C., Sariciftci, N. S., & Denk, P. (2002). Effect of LiF/metal electrodes on the performance of plastic solar cells. *Applied Physics Letters*, *80*(7), 1288. https://doi.org/10.1063/1.1446988

Bré das, J. L., Calbert, J. P., da Silva Filho, D. A., & Cornil, J. (2002). Organic semiconductors: A theoretical characterization of the basic parameters governing charge transport. In *PNAS April* (Vol. 30, Issue 9). www.pnas.orgcgidoi10.1073pnas.092143399

Brütting, W. (2006). Physics of Organic Semiconductors. In *Physics of Organic Semiconductors*. John Wiley and Sons. https://doi.org/10.1002/3527606637

Buzea, C., & Robbie, K. (2005). State of the art in thin film thickness and deposition rate monitoring sensors. *Reports on Progress in Physics*, *68*(2), 385–409. https://doi.org/10.1088/0034-4885/68/2/R04

Cai, W., Liu, P., Jin, Y., Xue, Q., Liu, F., Russell, T. P., Huang, F., Yip, H. L., & Cao, Y. (2015). Morphology Evolution in High-Performance Polymer Solar Cells Processed from Nonhalogenated Solvent. *Advanced Science*, *2*(8), 1–7. https://doi.org/10.1002/advs.201500095

Carter, S. A., Angelopoulos, M., Karg, S., Brock, P. J., & Scott, J. C. (1997). Polymeric anodes for improved polymer light-emitting diode performance. *Applied Physics Letters*, *70*(16), 2067–2069. https://doi.org/10.1063/1.118953

Chambers, E., Svensson, K., & Johansson, L. (2013). *AFM Studies of Pristine PCBM Changes Under Light Exposure*.

Chen, F. C., Ko, C. J., Wu, J. L., & Chen, W. C. (2010). Morphological study of P3HT:PCBM blend films prepared through solvent annealing for solar cell applications. *Solar Energy Materials and Solar Cells*. https://doi.org/10.1016/j.solmat.2010.09.004

Chen, H. Y., Hou, J., Zhang, S., Liang, Y., Yang, G., Yang, Y., Yu, L., Wu, Y., & Li, G. (2009). Polymer solar cells with enhanced open-circuit voltage and efficiency. *Nature Photonics*, *3*(11), 649–653. https://doi.org/10.1038/nphoton.2009.192

Chen, K. S., Yip, H. L., Schlenker, C. W., Ginger, D. S., & Jen, A. K. Y. (2012). Halogen-free solvent processing for sustainable development of high efficiency organic solar cells. *Organic Electronics: Physics, Materials, Applications*, *13*(12), 2870–2878. https://doi.org/10.1016/j.orgel.2012.08.026

Chen, Y., Cui, Y., Zhang, S., & Hou, J. (2015). Molecular design toward efficient polymer solar cells processed by green solvents. *Polymer Chemistry*, *6*(22), 4089–4095. https://doi.org/10.1039/c5py00431d

Chen, Y., Zhang, S., Wu, Y., & Hou, J. (2014). Molecular design and morphology control towards efficient polymer solar cells processed using non-aromatic and non-chlorinated solvents. *Advanced Materials*, *26*(17), 2744–2749. https://doi.org/10.1002/adma.201304825

Cheng, P., Li, Y., & Zhan, X. (2014). Efficient ternary blend polymer solar cells with indene-C60 bisadduct as an electron-cascade acceptor. *Energy and Environmental Science*, *7*(6), 2005–2011. https://doi.org/10.1039/c3ee44202k

Chirvase, D., Chiguvare, Z., Knipper, M., Parisi, J., Dyakonov, V., & Hummelen, J. C. (2004). *Electrical and optical design and characterisation of regioregular poly(3-hexylthiophene-2,5diyl)/fullerene-based heterojunction polymer solar cells*. https://doi.org/10.1016/S0379-6779(03)00027-4

Chueh, C. C., Yao, K., Yip, H. L., Chang, C. Y., Xu, Y. X., Chen, K. S., Li, C. Z., Liu, P., Huang, F., Chen, Y., Chen, W. C., & Jen, A. K. Y. (2013). Non-halogenated solvents for environmentally friendly processing of high-performance bulk-heterojunction polymer solar cells. *Energy & Environmental Science*, *6*(11), 3241–3248. https://doi.org/10.1039/C3EE41915K

Clarke, T. M., & Durrant, J. R. (2010). Charge photogeneration in organic solar cells. *Chemical Reviews*, *110*(11), 6736–6767. https://doi.org/10.1021/CR900271S/ASSET/CR900271S.FP.PNG_V03

Cody, G. D., Wronski, C. R., Abeles, B., Stephens, R. B., & Brooks, B. (1980). Optical characterization of amorphous silicon hydride films. *Solar Cells*, *2*(3), 227–243. https://doi.org/10.1016/0379-6787(80)90028-9

Collins, B. A., Li, Z., Tumbleston, J. R., Gann, E., Mcneill, C. R., & Ade, H. (2013). Absolute measurement of domain composition and nanoscale size distribution explains performance in PTB7:PC71bm solar cells. *Advanced Energy Materials*, *3*(1), 65–74. https://doi.org/10.1002/aenm.201200377

Coropceanu, V., Chen, X. K., Wang, T., Zheng, Z., & Brédas, J. L. (2019). Charge-transfer electronic states in organic solar cells. *Nature Reviews Materials*, *4*(11), 689–707. https://doi.org/10.1038/s41578-019-0137-9

Cravino, A., Schilinsky, P., & Brabec, C. J. (2007). Characterization of organic solar cells: The importance of device layout. *Advanced Functional Materials*, *17*(18), 3906–3910. https://doi.org/10.1002/adfm.200700295

Coropceanu, V., Cornil, J., Silva, D., A, D., Olivier, Y., Silbey, R., Bredas, J. L., da Silva Filho, D. A., Brédas, J.-L. J.-L., Olivier, Y., Silbey, R., & Brédas, J.-L. J.-L. (2007). Charge transport in organic semiconductors. *Chemical Reviews*, *107*(4), 926–952. https://doi.org/10.1007/128_2011_218

Czajkowski, A. (2010). Optical coating technology and applications : *Technical Paper*, 2–5.

Dang, X D; Nguyen, T. Q. (2010). Photoconductive Atomic Force Microscopy for Understanding Nanostructures and Device Physics of Organic Solar Cells. *Asylum Research*, 1–6.

Dang, X.-D., Tamayo, A. B., Seo, J., Hoven, C. v., Walker, B., & Nguyen, T.-Q. (2010). Nanostructure and Optoelectronic Characterization of Small Molecule Bulk Heterojunction Solar Cells by Photoconductive Atomic Force Microscopy. *Advanced Functional Materials*, *20*(19), 3314–3321. https://doi.org/10.1002/adfm.201000799

Deutsche Gesellschaft für Sonnenenergie. (2008). *Planning and installing photovoltaic systems : a guide for installers, architects, and engineers*. Earthscan. http://libcat.staffs.ac.uk/cgi-bin/koha/opac-detail.pl?biblionumber=150349

Diffraction, X., & Sources, I. (1970). Bragg ' s Law. *Production*, *5*(6), 371–372. https://doi.org/10.1088/0031-9120/5/6/113

Dissanayake, D. M. N. M., Lutz, T., Curry, R. J., & Silva, S. R. P. (2008). Measurement and validation of PbS nanocrystal energy levels. *Applied Physics Letters*, *93*(4), 043501. https://doi.org/10.1063/1.2964203

Dong, X., Deng, Y., Tian, H., Xie, Z., Geng, Y., & Wang, F. (2015). Isoindigo-based low bandgap conjugated polymer for o-xylene processed efficient polymer solar cells with thick active layers. *Journal of Materials Chemistry A*, *3*(39), 19928–19935. https://doi.org/10.1039/c5ta05352h

Doping (semiconductor) - Wikipedia. (n.d.). https://en.wikipedia.org/wiki/Doping_(semiconductor)

Doumon, N. Y., Houard, F. v., Dong, J., Christodoulis, P., Dryzhov, M. v., Portale, G., & Koster, L. J. A. (2019). Improved photostability in ternary blend organic solar cells: the role of [70]PCBM. *Journal of Materials Chemistry C*, *7*(17), 5104–5111. https://doi.org/10.1039/C8TC06621C

Ebenhoch, B., Thomson, S. A. J., Genevičius, K., Juška, G., & Samuel, I. D. W. (2015). Charge carrier mobility of the organic photovoltaic materials PTB7 and PC71BM and its influence on device performance. *Organic Electronics*, *22*, 62–68. https://doi.org/10.1016/j.orgel.2015.03.013

Elumalai, N. K., & Uddin, A. (2016). Open circuit voltage of organic solar cells: An in-depth review. *Energy and Environmental Science*, *9*(2), 391–410. https://doi.org/10.1039/c5ee02871j

*Electricity Production Data | World Electricity Statistics | Enerdata*. (2021). https://yearbook.enerdata.net/electricity/world-electricity-production-statistics.html

Erb, T., Zhokhavets, U., Hoppe, H., Gobsch, G., Al-Ibrahim, M., & Ambacher, O. (2006). Absorption and crystallinity of poly(3-hexylthiophene)/fullerene blends in dependence on annealing temperature. *Thin Solid Films*, *511–512*, 483–485. https://doi.org/10.1016/J.TSF.2005.12.064

Fabregat-Santiago, F., Garcia-Belmonte, G., Mora-Seró, I., & Bisquert, J. (2011). Characterization of nanostructured hybrid and organic solar cells by impedance spectroscopy. *Physical Chemistry Chemical Physics*, *13*(20), 9083. https://doi.org/10.1039/c0cp02249g

Fahlman, B. D. (2011). *Materials Chemistry*. *207890*. https://doi.org/10.1007/978-94-007-0693-4

Falzon, E. (2011). *Acceptor materials for organic solar cells*. https://doi.org/10.6100/IR718921

Farahat, M. E., Perumal, P., Budiawan, W., Chen, Y.-F., Lee, C.-H., & Chu, C.-W. (2017). Efficient molecular solar cells processed from green solvent mixtures. *Journal of Materials Chemistry A*, *5*(2), 571–582. https://doi.org/10.1039/C6TA09626C

Fauzia, V., Umar, A. A., Salleh, M. M., & Yahaya, M. (2011). Study Phase Separation of Donor:Acceptor in Inkjet Printed Thin Films of Bulk Heterojunction Organic Solar Cells Using AFM Phase Imaging. *Advanced Materials Research*. https://doi.org/10.4028/www.scientific.net/AMR.364.465

Fox, T. (2013). *population: one planet, too many people? | Science Media Centre*. IMechE. http://www.sciencemediacentre.org/population-one-planet-too-many-people/

Fu, X., Xu, H., Zhou, D., Cheng, X., Huang, L., Chen, L., & Chen, Y. (2018). Ternary thick active layer for efficient organic solar cells. *Journal of Materials Science*. https://doi.org/10.1007/s10853-018-2130-x

Galagan, Y., Zimmermann, B., Coenen, E. W. C., Jørgensen, M., Tanenbaum, D. M., Krebs, F. C., Gorter, H., Sabik, S., Slooff, L. H., Veenstra, S. C., Kroon, J. M., & Andriessen, R. (2012). Current collecting grids for ITO-free solar cells. *Advanced Energy Materials*, *2*(1), 103–110. https://doi.org/10.1002/aenm.201100552

Gao, H. L., Zhang, X. W., Meng, J. H., Yin, Z. G., Zhang, L. Q., Wu, J. L., & Liu, X. (2015). Quantitative characterization of phase separation in the photoactive layer of polymer solar cells by the phase image of atomic force microscopy. *Thin Solid Films*, *576*, 81–87. https://doi.org/10.1016/j.tsf.2015.01.009

Ghosekar, I. C., & Patil, G. C. (2020). Impact of concentration variation and thermal annealing on performance of multilayer OSC consisting of sandwiched P3HT layer between PEDOT:PSS and P3HT:PCBM. *Microelectronic Engineering*, *221*, 111195. https://doi.org/10.1016/j.mee.2019.111195

Girtan, M., & Rusu, M. (2010). Role of ITO and PEDOT:PSS in stability/degradation of polymer:fullerene bulk heterojunctions solar cells. *Solar Energy Materials and Solar Cells*, *94*(3), 446–450. https://doi.org/10.1016/j.solmat.2009.10.026

Gouadec, G., Colomban, P., Raman Spectroscopy, P. C., & Gouadec, G. (2007). How Spectra Relate to Disorder, Particle Size and Mechanical Properties. *Progress in Crystal Growth and Characterization of Materials*, *53*(1), 1–56. https://doi.org/10.1016/j.pcrysgrow.2007.01.001ï

Green, M., Emery, K., Hiahikawa, Y., Warta, W., Dunlop, E., Barkhouse, D., Gunawan, O., Gokmen, T., Todorov, T., and Mitzi, D., (2012). Solar cell efficiency tables (version 40). *Ieee Trans Fuzzy Syst*, *20*(6), 1114–1129. https://doi.org/10.1002/pip

Gregg, B. A., & Hanna, M. C. (2003). Comparing organic to inorganic photovoltaic cells: Theory, experiment, and simulation. *Journal of Applied Physics*, *93*(6), 3605–3614. https://doi.org/10.1063/1.1544413

Griffin, J., Pearson, A. J., Scarratt, N. W., Wang, T., Dunbar, A. D. F., Yi, H., Iraqi, A., Buckley, A. R., & Lidzey, D. G. (2015). Organic photovoltaic devices with enhanced efficiency processed from non-halogenated binary solvent blends. *Organic Electronics: Physics, Materials, Applications*, *21*, 216–222. https://doi.org/10.1016/j.orgel.2015.03.019

Grovenor, C. (2009). *Introduction to AFM Analysis*. 1–15. papers2://publication/uuid/680FD7E6-6C42-45EF-8E5B-B108F9F42454

Gu, S., Neugebauer, H., & Sariciftci, N. S. (2007). *Conjugated Polymer-Based Organic Solar Cells*. 1324–1338.

Günes, S., Neugebauer, H., & Sariciftci, N. S. (2007). Conjugated polymer-based organic solar cells. *Chemical Reviews*, *107*(4), 1324–1338. https://doi.org/10.1021/cr050149z

Guo, S., Cao, B., Wang, W., Moulin, J.-F. O., & Mü Ller-Buschbaum, P. (2016). Effect of Alcohol Treatment on the Performance of PTB7:PC 71 BM Bulk Heterojunction Solar Cells. *Applied Materials and Interfaces*. https://doi.org/10.1021/am5079418

Guo, X., Zhang, M., Cui, C., Hou, J., & Li, Y. (2014). Efficient polymer solar cells based on poly(3-hexylthiophene) and indene-C60 bisadduct fabricated with non-halogenated solvents. *ACS Applied Materials and Interfaces*, *6*(11), 8190–8198. https://doi.org/10.1021/am500836u

Habekost, A. (2019). Simulation and Fitting of Cyclic Voltammetry and Chronoamperometry Curves of Electrochemical Reactions with Different Mechanisms — A Didactic Perspective. *World Journal of Chemical Education*, *7*(2), 53–64. https://doi.org/10.12691/WJCE-7-2-4

Hales, D. (2020). Renewables 2020, Global Status Report. In *REN21*. https://doi.org/978-3-9818911-3-3

Han, T.-H., Lee, Y., Choi, M.-R., Woo, S.-H., Bae, S.-H., Hong, B. H., Ahn, J.-H., & Lee, T.-W. (2012). Extremely efficient flexible organic light-emitting diodes with modified graphene anode. *Nature Photonics*, *6*(2), 105–110. https://doi.org/10.1038/nphoton.2011.318

Hansen, C. M. (2013). Hansen Solubility Parameters A User's Handbook. In *Journal of Chemical Information and Modeling* (Vol. 53, Issue 9). https://doi.org/10.1017/CBO9781107415324.004

Hartman, B., & Andersson, S. B. (2017). Feature tracking for high speed AFM: Experimental demonstration. *Proceedings of the American Control Conference*, *2*(1), 773–778. https://doi.org/10.23919/ACC.2017.7963046

He, Y., & Li, Y. (2011). Fullerene derivative acceptors for high performance polymer solar cells. *Phys. Chem. Chem. Phys.*, *13*(6), 1970–1983. https://doi.org/10.1039/C0CP01178A

He, Z., Xiao, B., Liu, F., Wu, H., Yang, Y., Xiao, S., Wang, C., Russell, T. P., & Cao, Y. (2015). Single-junction polymer solar cells with high efficiency and photovoltage. *Nature Photonics*, *9*(3), 174–179. https://doi.org/10.1038/nphoton.2015.6

He, Z., Zhong, C., Huang, X., Wong, W. Y., Wu, H., Chen, L., Su, S., & Cao, Y. (2011). Simultaneous enhancement of open-circuit voltage, short-circuit current density, and fill factor in polymer solar cells. *Advanced Materials*, *23*(40), 4636–4643. https://doi.org/10.1002/adma.201103006

He, Z., Zhong, C., Su, S., Xu, M., Wu, H., & Cao, Y. (2012). Enhanced power-conversion efficiency in polymer solar cells using an inverted device structure. *Nature Photonics*, *6*(9), 591–595. https://doi.org/10.1038/nphoton.2012.190

Hedley, G. J., Ward, A. J., Alekseev, A., Howells, C. T., Martins, E. R., Serrano, L. A., Cooke, G., Ruseckas, A., & Samuel, I. D. W. (2013). Determining the optimum morphology in high-performance polymer-fullerene organic photovoltaic cells. *Nature Communications*. https://doi.org/10.1038/ncomms3867

Heeger, A. J. (2014). 25th anniversary article: Bulk heterojunction solar cells: Understanding the mechanism of operation. *Advanced Materials*, *26*(1), 10–28. https://doi.org/10.1002/adma.201304373

Hoppe, H., & Sariciftci, N. S. (2004). Organic solar cells: An overview. *Journal of Materials Research*, *19*(7), 1924–1945. https://doi.org/10.1557/JMR.2004.0252

Hoppe, H., & Sariciftci, N. S. (2006). Morphology of polymer/fullerene bulk heterojunction solar cells. *J. Mater. Chem.*, *16*(1), 45–61. https://doi.org/10.1039/B510618B

Hösel, M., Søndergaard, R. R., Angmo, D., & Krebs, F. C. (2013). Comparison of fast roll-to-roll flexographic, inkjet, flatbed, and rotary screen printing of metal back electrodes for polymer solar cells. *Advanced Engineering Materials*, *15*(10), 995–1001. https://doi.org/10.1002/adem.201300011

Hou, J., Chen, H.-Y., Zhang, S., Chen, R. I., Yang, Y., Wu, Y., & Li, G. (2009). Synthesis of a Low Band Gap Polymer and Its Application in Highly Efficient Polymer Solar Cells. *Journal of the American Chemical Society*, *131*(43), 15586–15587. https://doi.org/10.1021/ja9064975

Hou, J., & Guo, X. (2013). Active Layer Materials for Organic Solar Cells. *Green Energy and Technology*, *128*, 17–42. https://doi.org/10.1007/978-1-4471-4823-4_2

Hou, J., Inganäs, O., Friend, R. H., & Gao, F. (2018). Organic solar cells based on non-fullerene acceptors. *Nature Materials*, *17*(2), 119–128. https://doi.org/10.1038/nmat5063

Hou, J., Park, M., Zhang, S., Yao, Y., Chen, L.-M., Li, J.-H., & Yang, Y. (2008). Bandgap and Molecular Energy Level Control of Conjugated Polymer Photovoltaic Materials Based on Benzo[1,2-b :4,5- b ′]dithiophene. *Macromolecules*, *41*(16), 6012–6018. https://doi.org/10.1021/ma800820r

Hsieh, Y. J., Huang, Y. C., Liu, W. S., Su, Y. A., Tsao, C. S., Rwei, S. P., & Wang, L. (2017). Insights into the Morphological Instability of Bulk Heterojunction PTB7-Th/PCBM Solar Cells upon High-Temperature Aging. *ACS Applied Materials and Interfaces*, *9*(17), 14808–14816. https://doi.org/10.1021/acsami.7b01296

Huang, J., Li, G., & Yang, Y. (2008). A semi-transparent plastic solar cell fabricated by a lamination process. *Advanced Materials*, *20*(3), 415–419. https://doi.org/10.1002/adma.200701101

Huang, W., Chandrasekaran, N., Prasad, S. K. K., Gann, E., Thomsen, L., Kabra, D., Hodgkiss, J. M., Cheng, Y.-B., & McNeill, C. R. (2016). Impact of Fullerene Mixing Behavior on the Microstructure, Photophysics, and Device Performance of Polymer/Fullerene Solar Cells. *ACS Applied Materials & Interfaces*, *8*(43), 29608–29618. https://doi.org/10.1021/acsami.6b10404

Huang, W., Gann, E., Chandrasekaran, N., Prasad, S. K. K., Chang, S. Y., Thomsen, L., Kabra, D., Hodgkiss, J. M., Cheng, Y. B., Yang, Y., & McNeill, C. R. (2017). Influence of Fullerene Acceptor on the Performance, Microstructure, and Photophysics of Low Bandgap Polymer Solar Cells. *Advanced Energy Materials*, *7*(11), 1–10. https://doi.org/10.1002/aenm.201602197

Huang, W., Gann, E., Thomsen, L., Dong, C., Cheng, Y. B., & McNeill, C. R. (2015). Unraveling the morphology of high efficiency polymer solar cells based on the donor polymer PBDTTT-EFT. *Advanced Energy Materials*, *5*(7). https://doi.org/10.1002/aenm.201401259

Huang, Y., Kramer, E. J., Heeger, A. J., & Bazan, G. C. (2014). Bulk heterojunction solar cells: Morphology and performance relationships. In *Chemical Reviews*. https://doi.org/10.1021/cr400353v

Huo, L., Zhang, S., Guo, X., Xu, F., Li, Y., & Hou, J. (2011). Replacing Alkoxy Groups with Alkylthienyl Groups: A Feasible Approach To Improve the Properties of Photovoltaic Polymers. *Angewandte Chemie International Edition*, *50*(41), 9697–9702. https://doi.org/10.1002/anie.201103313

Ilchenko, O., Pilgun, Y., Kutsyk, A., Bachmann, F., Slipets, R., Todeschini, M., Okeyo, P. O., Poulsen, H. F., & Boisen, A. (2019). Fast and quantitative 2D and 3D orientation mapping using Raman microscopy. *Nature Communications*, *10*(1), 5555. https://doi.org/10.1038/s41467-019-13504-8

Ilkhani, H., Ganjali, M. R., Arvand, M., Faridbod, F., & Norouzi, P. (2012). Cyclic voltammetry. *Materials Science and Engineering C*, *32*(4), 653–658. https://doi.org/10.1016/j.msec.2012.01.002

Irena. (2019). *Future of solar photovoltaic*. https://www.irena.org/publications/2019/Nov/Future-of-Solar-Photovoltaic

Ito, M., Palanisamy, K., Kumar, A., Murugesan, V. S., Shin, P. K., Tsuda, N., Yamada, J., & Ochiai, S. (2014). Characterization of the organic thin film solar cells with active layers of PTB7/PC71BM prepared by using solvent mixtures with different additives. *International Journal of Photoenergy*. https://doi.org/10.1155/2014/694541

Iwan, A., Sikora, A., Hamplová, V., & Bubnov, A. (2015). AFM study of advanced composite materials for organic photovoltaic cells with active layer based on P3HT:PCBM and chiral photosensitive liquid crystalline dopants. *Liquid Crystals*. https://doi.org/10.1080/02678292.2015.1011243

Jaiswal, M., & Menon, R. (2006a). Equivalent circuit for an organic field-effect transistor from impedance measurements under dc bias. *Applied Physics Letters*, *88*(12), 123504. https://doi.org/10.1063/1.2186989

Jaiswal, M., & Menon, R. (2006b). Review Polymer electronic materials: a review of charge transport Manu. *Polymer International*, *57*(April), 171–180. https://doi.org/10.1002/pi.2111/

Jay, F., Muñoz, D., Desrues, T., Pihan, E., Amaral De Oliveira, V., Enjalbert, N., & Jouini, A. (2014). Advanced process for n-type mono-like silicon a-Si:H/c-Si heterojunction solar cells with 21.5%

efficiency. *Solar Energy Materials and Solar Cells*, *130*, 690–695. https://doi.org/10.1016/j.solmat.2014.02.025

Jovanov, V., Yumnam, N., Müller, A., Gruber, M., & Wagner, V. (2017). Determining Material-Specific Morphology of Bulk-Heterojunction Organic Solar Cells Using AFM Phase Imaging. *Journal of Physical Chemistry C*. https://doi.org/10.1021/acs.jpcc.7b01924

Khan, T. M., Zhou, Y., Dindar, A., Shim, J. W., Fuentes-Hernandez, C., & Kippelen, B. (2014). Organic photovoltaic cells with stable top metal electrodes modified with polyethylenimine. *ACS Applied Materials and Interfaces*, *6*(9), 6202–6207. https://doi.org/10.1021/am501236z

Kietzke, T. (2007). Recent advances in organic solar cells. *Advances in OptoElectronics*, *2007*. https://doi.org/10.1155/2007/40285

Kim, Y. J., Jang, W., Ahn, S., Park, C. E., & Wang, D. H. (2016). Dramatically enhanced performances and ideally controlled nano-morphology via co-solvent processing in low bandgap polymer solar cells. *Organic Electronics*, *34*, 42–49. https://doi.org/10.1016/j.orgel.2016.04.010

Kini, G. P., Jeon, S. J., & Moon, D. K. (2020). Design Principles and Synergistic Effects of Chlorination on a Conjugated Backbone for Efficient Organic Photovoltaics: A Critical Review. *Advanced Materials*, *32*(11), 1–38. https://doi.org/10.1002/adma.201906175

Kissinger, P. T., & Heineman, W. R. (1983). Cyclic voltammetry. *Journal of Chemical Education*, *60*(9), 702–706. https://doi.org/10.1021/ED060P702

Kittel, C. (2011). Introduction to Solid State Physics Solution Manual, 8th Edition. *Wiley*, 704. https://www.wiley.com/en-us/Introduction+to+Solid+State+Physics%2C+8th+Edition-p-9780471415268

Klimov, E., Li, W., Yang, X., Hoffmann, G. G., & Loos, J. (2006). Scanning Near-Field and Confocal Raman Microscopic Investigation of P3HT−PCBM Systems for Solar Cell Applications. *Macromolecules*, *39*(13), 4493–4496. https://doi.org/10.1021/MA052590X

Komilian, S. (2019). *Investigation into Device Optimisation of Organic Solar Cells Using Narrow Bandgap Polymer and the role of acceptor material*. *August*.

Komilian, S., Oklobia, O., & Sadat-Shafai, T. (2018a). Controlling intercalations of PBDTTT-EFT side chain to initiate suitable network for charge extraction in PBDTTT-EFT:PC71BM blended bulk heterojunction solar cell. *Solar Energy Materials and Solar Cells*, *175*(July 2017), 35–40. https://doi.org/10.1016/j.solmat.2017.10.007

Komilian, S., Oklobia, O., & Sadat-Shafai, T. (2018b). Data related to the PC71BM loading and it's impact on nanostructuring for blend of PBDTTT-EFT:PC71BM bulk heterojunction solar cell. *Data in Brief*, *16*, 506–510. https://doi.org/10.1016/j.dib.2017.11.076

Kovacik, P. (2012). *Vacuum deposition of organic molecules for photovoltaic applications*.

Kovalenko, A., Stoyanova, D., Pospisil, J., Zhivkov, I., Fekete, L., Karashanova, D., Kratochvílová, I., Vala, M., & Weiter, M. (2015). Morphology versus vertical phase segregation in solvent annealed small molecule bulk heterojunction organic solar cells. *International Journal of Photoenergy*. https://doi.org/10.1155/2015/238981

Krebs, F. C. (2009). Fabrication and processing of polymer solar cells: A review of printing and coating techniques. *Solar Energy Materials and Solar Cells*, *93*(4), 394–412. https://doi.org/10.1016/j.solmat.2008.10.004

Krebs, F. C., Jørgensen, M., Norrman, K., Hagemann, O., Alstrup, J., Nielsen, T. D., Fyenbo, J., Larsen, K., & Kristensen, J. (2009). A complete process for production of flexible large area polymer solar cells entirely using screen printing—First public demonstration. *Solar Energy Materials and Solar Cells*, *93*(4), 422–441. https://doi.org/10.1016/j.solmat.2008.12.001

Krebs, F. C., JÃ¸rgensen, M., Bundgaard, E., de Bettignies, R., Krebs, F. C., Katz, E. A., Norrman, K., Bundgaard, E., Krebs, F. C., Norrman, K., Cros, S., de Bettignies, R., Firon, M., Krebs, F. C., Aernouts, T., Cros, S., Krebs, F. C., & Krebs, F. C. (2008). *Polymer Photovoltaics: A Practical Approach*. Society of Photo-Optical Instrumentation Engineers. https://doi.org/10.1117/3.737854

Krishnan Jagadamma, L., Taylor, R. G. D., Kanibolotsky, A. L., Sajjad, M. T., Wright, I. A., Horton, P. N., Coles, S. J., Samuel, I. D. W., & Skabara, P. J. (2019). Highly efficient fullerene and non-fullerene based ternary organic solar cells incorporating a new tetrathiocin-cored semiconductor. *Sustainable Energy and Fuels*, *3*(8), 2087–2099. https://doi.org/10.1039/c9se00343f

Kroon, R., Lenes, M., Hummelen, J. C., Blom, P. W. M., & de Boer, B. (2008). Small bandgap polymers for organic solar cells (polymer material development in the last 5 years). In *Polymer Reviews* (Vol. 48, Issue 3). https://doi.org/10.1080/15583720802231833

Kymissis, I. (2009). *Organic Field Effect Transistors*. Springer US. https://doi.org/10.1007/978-0-387-92134-1

Leonat, L., Sbârcea, G., & Braĥzoi, I. V. (2013). Cyclic voltammetry for energy levels estimation of organic materials. *UPB Scientific Bulletin, Series B: Chemistry and Materials Science*, *75*(3), 111–118. https://doi.org/ISSN 1454-2331

Li, G., Yao, Y., Yang, H., Shrotriya, V., Yang, G., & Yang, Y. (2007). "Solvent Annealing" Effect in Polymer Solar Cells Based on Poly(3-hexylthiophene) and Methanofullerenes. *Advanced Functional Materials*, *17*(10), 1636–1644. https://doi.org/10.1002/ADFM.200600624

Li, M.-Y., Lee, J., Wang, Z., Hirono, Y., Wu, J., Song, S., Koo, S.-M., Kim, E.-S., & Salamo, G. J. (2012). Inside Back Cover: Sharp contrast of the density and size of Ga metal droplets on photolithographically patterned GaAs (100) by droplet epitaxy under an identical growth environment (Phys. Status Solidi A 6/2012). *Physica Status Solidi (a)*, *209*(6), n/a-n/a. https://doi.org/10.1002/pssa.201290013

Li, Y., Vamvounis, G., & Holdcroft, S. (2002). Tuning Optical Properties and Enhancing Solid-State Emission of Poly(thiophene)s by Molecular Control: A Postfunctionalization Approach. *Macromolecules*, *35*(18), 6900–6906. https://doi.org/10.1021/ma020140o

Li, Z., Ying, L., Zhu, P., Zhong, W., Li, N., Liu, F., Huang, F., & Cao, Y. (2019). A generic green solvent concept boosting the power conversion efficiency of all-polymer solar cells to 11%. *Energy and Environmental Science*, *12*(1), 157–163. https://doi.org/10.1039/c8ee02863j

Liang, Q., Jiao, X., Yan, Y., Xie, Z., Lu, G., Liu, J., & Han, Y. (2019). Separating Crystallization Process of P3HT and O-IDTBR to Construct Highly Crystalline Interpenetrating Network with

Optimized Vertical Phase Separation. *Advanced Functional Materials*, *29*(47), 1–12. https://doi.org/10.1002/adfm.201807591

Liang, Y., Xu, Z., Xia, J., Tsai, S. T., Wu, Y., Li, G., Ray, C., & Yu, L. (2010). For the bright future-bulk heterojunction polymer solar cells with power conversion efficiency of 7.4%. *Advanced Materials*, *22*(20), 135–138. https://doi.org/10.1002/adma.200903528

Liang, Y., & Yu, L. (2010). A New Class of Semiconducting Polymers for Bulk Heterojunction Solar Cells with Exceptionally High Performance. *Accounts of Chemical Research*, *43*(9), 1227–1236. https://doi.org/10.1021/ar1000296

Liang, Z., Li, M., Wang, Q., Qin, Y., Stuard, S. J., Peng, Z., Deng, Y., Ade, H., Ye, L., & Geng, Y. (2020). Optimization Requirements of Efficient Polythiophene:Nonfullerene Organic Solar Cells. *Joule*, *4*(6), 1278–1295. https://doi.org/10.1016/j.joule.2020.04.014

Liao, S. H., Jhuo, H. J., Cheng, Y. S., & Chen, S. A. (2013). Fullerene Derivative-Doped Zinc Oxide Nanofilm as the Cathode of Inverted Polymer Solar Cells with Low-Bandgap Polymer (PTB7-Th) for High Performance. *Advanced Materials*, *25*(34), 4766–4771. https://doi.org/10.1002/ADMA.201301476

lin, yuanbao, Firdaus, Y., Isikgor, F. H., Nugraha, M. I., Yengel, E., Harrison, G. T., Hallani, R., el Labban, A., Faber, H., Ma, C., Zheng, X., Subbiah, A. S., Howells, C. T., Bakr, O. M., McCulloch, I., de Wolf, S., Tsetseris, L., & Anthopoulos, T. D. (2020). Self-assembled Monolayer Enables HTL-free Organic Solar Cells with 18% Efficiency and Improved Operational Stability. *ACS Energy Letters*, acsenergylett.0c01421. https://doi.org/10.1021/acsenergylett.0c01421

Lin, Y., Wang, Y., Wang, J., Hou, J., Li, Y., Zhu, D., & Zhan, X. (2014). A star-shaped perylene diimide electron acceptor for high-performance organic solar cells. *Advanced Materials*. https://doi.org/10.1002/adma.201400525

Liu, Q., Jiang, Y., Jin, K., Qin, J., Xu, J., Li, W., Xiong, J., Liu, J., Xiao, Z., Sun, K., Yang, S., Zhang, X., & Ding, L. (2020). 18% Efficiency organic solar cells. *Science Bulletin*, *65*(4), 272–275. https://doi.org/10.1016/j.scib.2020.01.001

Liu, Q., Romero-Gomez, P., Mantilla-Perez, P., Colodrero, S., Toudert, J., & Martorell, J. (2017). A Two-Resonance Tapping Cavity for an Optimal Light Trapping in Thin-Film Solar Cells. *Advanced Energy Materials*, *7*(18), 1–8. https://doi.org/10.1002/aenm.201700356

Liu, X., Ding, P., Yuan, Z., Tian, H., Jiao, Y., & Agbolaghi, S. (2020). Elevated air stability in PBDT-DTNT:PCBM solar cells by focusing on roles of fibrillar/patterned nanostructures via graphene/polymer constituents. *Solar Energy*, *198*(January), 101–112. https://doi.org/10.1016/j.solener.2020.01.031

Lo, V., Landrock, C., Kaminska, B., & Elicia, M. (2012). Manufacturing cost modeling for flexible organic solar cells. *2012 Proceedings of Technology Management for Emerging Technologies*, 2951–2956. http://ieeexplore.ieee.org/xpls/abs_all.jsp?arnumber=6304313

Ma, W., Yan, H., Zhou, K., & Naveed, H. B. (2019). Nanostructure of Organic Solar Cells. In *Advanced Nanomaterials for Solar Cells and Light Emitting Diodes*. Elsevier Inc. https://doi.org/10.1016/b978-0-12-813647-8.00002-3

Manuscript, A. (2020). *Energy & Environmental Science*. *207890*. https://doi.org/10.1039/b000000x

Mao, P., Wei, Y., Li, H., & Wang, J. (2017). Junction diodes in organic solar cells. *Nano Energy*, *41*, 717–730. https://doi.org/10.1016/j.nanoen.2017.10.027

Marrese, M., Guarino, V., & Ambrosio, L. (2017). Atomic Force Microscopy: A Powerful Tool to Address Scaffold Design in Tissue Engineering. *Journal of Functional Biomaterials*, *8*(1), 7. https://doi.org/10.3390/jfb8010007

Martens, T., Beelen, Z., D'Haen, J., Munters, T., Goris, L., Manca, J., D'Olieslaeger, M., Vanderzande, D., de Schepper, L., & Andriessen, R. (2003). *Morphology of MDMO-PPV:PCBM bulk heterojunction organic solar cells studied by AFM, KFM, and TEM*. https://doi.org/10.1117/12.452453

Martens, T., D'Haen, J., Munters, T., Beelen, Z., Goris, L., Manca, J., D'Olieslaeger, M., Vanderzande, D., de Schepper, L., & Andriessen, R. (2003). Disclosure of the nanostructure of MDMO-PPV:PCBM bulk hetero-junction organic solar cells by a combination of SPM and TEM. *Synthetic Metals*. https://doi.org/10.1016/S0379-6779(02)01311-5

Marzo, A., Beiza, F., Ferrada, P., Alonso, J., & Roman, R. (2017). *Comparison of Atacama Desert Solar Spectrum vs. ASTM G173-03 Reference Spectra for Solar Energy Applications*. 1–13. https://doi.org/10.18086/eurosun.2016.09.01

Mayer, A. C., Scully, S. R., Hardin, B. E., Rowell, M. W., & McGehee, M. D. (2007). Polymer-based solar cells. *Materials Today*, *10*(11), 28–33. https://doi.org/10.1016/S1369-7021(07)70276-6

Mijovic, J. S., & Koutsky, J. A. (2013). *Polymer-Plastics Technology and Engineering Etching of Polymeric Surfaces : A Review*. *January 2013*, 37–41.

*Mismatch Effects | PVEducation*. (2019). https://www.pveducation.org/pvcdrom/modules-and-arrays/mismatch-effects

Misra, A., Kumar, P., Srivastava, R., Dhawan, S. K., Kamalasanan, M. N., & Chandra, S. (2005). Electrochemical and optical studies of conjugated polymers for three primary colours. *IJPAP Vol.43(12) [December 2005]*, *43*, 921–925. http://nopr.niscair.res.in/handle/123456789/8901

Müller-Buschbaum, P. (2014). The active layer morphology of organic solar cells probed with grazing incidence scattering techniques. *Advanced Materials*. https://doi.org/10.1002/adma.201304187

Nalwa, K. S., Kodali, H. K., Ganapathysubramanian, B., & Chaudhary, S. (2011). Dependence of recombination mechanisms and strength on processing conditions in polymer solar cells. *Applied Physics Letters*, *99*(26). https://doi.org/10.1063/1.3671999

Nalwa, K. S., Mahadevapuram, R. C., & Chaudhary, S. (2011). Growth rate dependent trap density in polythiophene-fullerene solar cells and its implications. *Applied Physics Letters*, *98*(9), 093306. https://doi.org/10.1063/1.3560483

Nam, S., Jang, J., Cha, H., Hwang, J., An, T. K., Park, S., & Park, C. E. (2012). Effects of direct solvent exposure on the nanoscale morphologies and electrical characteristics of PCBM-based transistors and photovoltaics. *Journal of Materials Chemistry*, *22*(12), 5543. https://doi.org/10.1039/c2jm15260f

Nave, C. R. (1999). Band Theory for Solids. (n.d.). http://hyperphysics.phy-astr.gsu.edu/hbase/Solids/band.html

Neamen, Donald A. (2003). Semiconductor Physics and Devices: Basic Principles (3rd ed.). *McGraw-Hill Higher Education*. ISBN 0-07-232107-5)

Nelson, J. (2011). Polymer: Fullerene bulk heterojunction solar cells. *Materials Today*, *14*(10), 462–470. https://doi.org/10.1016/S1369-7021(11)70210-3

Nicholson, P. G., & Castro, F. A. (2010). Organic photovoltaics: Principles and techniques for nanometre scale characterization. *Nanotechnology*, *21*(49). https://doi.org/10.1088/0957-4484/21/49/492001

Norrman, K., Ghanbari-Siahkali, A., & Larsen, N. B. (2005). 6 Studies of spin-coated polymer films. *Annual Reports Section "C" (Physical Chemistry)*, *101*, 174. https://doi.org/10.1039/b408857n

NREL. (2021). *Photovoltaic Research | NREL*. https://www.nrel.gov/pv/assets/pdfs/best-research-cell-efficiencies.20200708.pdf

*NREL Developing Improved Tech to Lower Costs for Multi-Junction Solar Cells*. (2018). https://www.solarreviews.com/blog/nrel-developing-tech-lower-cost-multi-junction-solar-cells

Nunzi, J. M. (2002). Organic photovoltaic materials and devices. *Comptes Rendus Physique*, *3*(4), 523–542. https://doi.org/10.1016/S1631-0705(02)01335-X

O. Kasap, S., & Sze, S. M. (2002). Semiconductor Devices: Physics and Technology. In *Technology*. https://doi.org/10.1016/S0026-2692(82)80036-0

Oklobia, O. (2016). *Investigations of Thermally Induced Morphology in P3HT / PCBM Thin Films : Influence of Composition and Thermal Annealing on Photovoltaic Properties Ochai Oklobia A thesis submitted in partial fulfilment of the requirement of Staffordshire University for*. *February*.

Oklobia, O., & Shafai, T. S. (2013a). A quantitative study of the formation of PCBM clusters upon thermal annealing of P3HT/PCBM bulk heterojunction solar cell. *Solar Energy Materials and Solar Cells*, *117*, 1–8. https://doi.org/10.1016/j.solmat.2013.05.011

Oklobia, O., & Shafai, T. S. (2013b). A study of donor/acceptor interfaces in a blend of P3HT/PCBM solar cell: Effects of annealing and PCBM loading on optical and electrical properties. *Solid-State Electronics*, *87*, 64–68. https://doi.org/10.1016/j.sse.2013.05.005

Olivier, Y., Niedzialek, D., Lemaur, V., Pisula, W., Müllen, K., Koldemir, U., Reynolds, J. R., Lazzaroni, R., Cornil, J., & Beljonne, D. (2014). 25th anniversary article: High-mobility hole and electron transport conjugated polymers: How structure defines function. *Advanced Materials*, *26*(14), 2119–2136. https://doi.org/10.1002/adma.201305809

Onsager, L. (1934). Deviations from Ohm's Law in Weak Electrolytes. *The Journal of Chemical Physics*, *2*(9), 599–615. https://doi.org/10.1063/1.1749541

Pan, H., Li, Y., Wu, Y., Liu, P., Ong, B. S., Zhu, S., & Xu, G. (2006). Synthesis and Thin-Film Transistor Performance of Poly(4,8-didodecylbenzo[1,2-b:4,5-b']dithiophene). *Chemistry of Materials*, *18*(14), 3237–3241. https://doi.org/10.1021/cm0602592

Pan, H., Li, Y., Wu, Y., Liu, P., Ong, B. S., Zhu, S., & Xu, G. (2007). Low-Temperature, Solution-Processed, High-Mobility Polymer Semiconductors for Thin-Film Transistors. *Journal of the American Chemical Society*, *129*(14), 4112–4113. https://doi.org/10.1021/ja067879o

Pan, M. A., Lau, T. K., Tang, Y., Wu, Y. C., Liu, T., Li, K., Chen, M. C., Lu, X., Ma, W., & Zhan, C. (2019). 16.7%-efficiency ternary blended organic photovoltaic cells with PCBM as the acceptor additive to increase the open-circuit voltage and phase purity. *Journal of Materials Chemistry A*, *7*(36), 20713–20722. https://doi.org/10.1039/c9ta06929a

Pan, X. (2014). Scholars' Mine Processing and feature analysis of atomic force microscopy images Xiao Pan. 学位論文. http://scholarsmine.mst.edu/masters_theses

Park, C. do, Fleetham, T. A., Li, J., & Vogt, B. D. (2011). High performance bulk-heterojunction organic solar cells fabricated with non-halogenated solvent processing. *Organic Electronics: Physics, Materials, Applications*, *12*(9), 1465–1470. https://doi.org/10.1016/j.orgel.2011.05.020

Park, K. M., Lee, M. B., & Choi, S. Y. (2015). Investigation of surface features for 17.2% efficiency multi-crystalline silicon solar cells. *Solar Energy Materials and Solar Cells*, *132*, 356–362. https://doi.org/10.1016/j.solmat.2014.07.023

Peng, H., Sun, X., Weng, W., & Fang, X. (2017). Synthesis and Design of Conjugated Polymers for Organic Electronics. *Polymer Materials for Energy and Electronic Applications*, 9–61. https://doi.org/10.1016/B978-0-12-811091-1.00002-1

Perez, L. A., Zalar, P., Ying, L., Schmidt, K., Toney, M. F., Nguyen, T. Q., Bazan, G. C., & Kramer, E. J. (2014). Effect of backbone regioregularity on the structure and orientation of a donor-acceptor semiconducting copolymer. *Macromolecules*, *47*(4), 1403–1410. https://doi.org/10.1021/ma4019679

Peterson, E. D., Smith, G. M., Fu, M., Coffin, R. C., Adams, R. D., & Carroll, D. L. (2010). Increased photon absorption and conversion in ternary bulk heterojunction systems of CdSe/CdS core-shell nanoparticles/methyl viologen composites, conjugated polymers, and fullerenes. *2010 35th IEEE Photovoltaic Specialists Conference*, 001643–001647. https://doi.org/10.1109/PVSC.2010.5616546

Petty, M. C. (2008). Molecular Electronics: From Principles to Practice. USA: Wiley.

Peter, S. (2009). Electrical Characterisation of Organic Electronic Materials and Devices, Wiley, New Jersey

Philipp, H. R. (1971). Optical properties of non-crystalline Si, SiO, SiOx and SiO2. *Journal of Physics and Chemistry of Solids*, *32*(8), 1935–1945. https://doi.org/10.1016/S0022-3697(71)80159-2

*Population: one planet, too many people? (report) - Resilience*. (n.d.). Retrieved May 10, 2021, from https://www.resilience.org/stories/2011-01-20/population-one-planet-too-many-people-report-jan-21/

Preis, P., Buchholz, F., Diaz-Perez, P., Glatz-Reichenbach, J., Peter, C., Schmitt, S., Theobald, J., Peter, K., & Søiland, A. K. (2014). Towards 20 % solar cell efficiency using silicon from metallurgical process route. *Energy Procedia*, *55*, 589–595. https://doi.org/10.1016/j.egypro.2014.08.030

Price, S. C., Stuart, A. C., Yang, L., Zhou, H., & You, W. (2011). Fluorine Substituted Conjugated Polymer of Medium Band Gap Yields 7% Efficiency in Polymer−Fullerene Solar Cells. *Journal of the American Chemical Society*, *133*(12), 4625–4631. https://doi.org/10.1021/ja1112595

Qi, B., & Wang, J. (2013). Fill factor in organic solar cells. *Physical Chemistry Chemical Physics*, *15*(23), 8972–8982. https://doi.org/10.1039/c3cp51383a

Qi, B., Zhou, Q., & Wang, J. (2015). Exploring the open-circuit voltage of organic solar cells under low temperature. *Scientific Reports*, *5*, 1–10. https://doi.org/10.1038/srep11363

Razzell-Hollis, J., Wade, J., Tsoi, W. C., Soon, Y., Durrant, J., & Kim, J. S. (2014). Photochemical stability of high efficiency PTB7:PC70BM solar cell blends. *Journal of Materials Chemistry A*, *2*(47), 20189–20195. https://doi.org/10.1039/C4TA05641H

Records, R. C. E. (2015). *Research Cell Efficiency Records | Department of Energy*. Department of Energy. https://www.energy.gov/eere/solar/articles/research-cell-efficiency-records

Reviews, S., & Progress, S. (2016). *Selective etching of polymeric materials*. https://www.jstor.org/stable/43420627?seq=1

Revoju, S. (2018). *Molecular Design , Synthesis and Performance Evaluation of Phenothiazine-based Small Molecules for Organic Solar Cells* (Issue February). https://doi.org/10.13140/RG.2.2.27203.50728

Saitoh, A. (2007). Raman scattering, luminescence, and absorption edge under hydrostatic pressures of layered BiI3 and SbI3. *Journal of Raman Spectroscopy*, *38*(5), 537–542. https://doi.org/10.1002/jrs.1676

Sariciftci, N. S., Braun, D., Zhang, C., Srdanov, V. I., Heeger, A. J., Stucky, G., & Wudl, F. (1993). Semiconducting polymer-buckminsterfullerene heterojunctions: Diodes, photodiodes, and photovoltaic cells. *Applied Physics Letters*, *62*(6), 585–587. https://doi.org/10.1063/1.108863

Sariciftci, N. S., Smilowitz, L., Heeger, A. J., & Wudl, F. (1992). Photoinduced Electron Transfer from a Conducting Polymer to Buckminsterfullerene. *Science*, *258*(5087), 1474–1476. https://doi.org/10.1126/science.258.5087.1474

Scharber, M. C., & Sariciftci, N. S. (2013). Efficiency of bulk-heterojunction organic solar cells. *Progress in Polymer Science*, *38*(12), 1929–1940. https://doi.org/10.1016/j.progpolymsci.2013.05.001

Schoder, T. (2018). *Monocrystalline Cells vs. Polycrystalline Cells: What's the Difference? | CED Greentech*. https://www.cedgreentech.com/article/monocrystalline-cells-vs-polycrystalline-cells-whats-difference

Sendy, A. (2021). *Types of Solar Panels: Which One Is the Best Choice?* https://www.solarreviews.com/blog/pros-and-cons-of-monocrystalline-vs-polycrystalline-solar-panels

Settanni, G., Zhou, J., Suo, T., Schöttler, S., Landfester, K., Schmid, F., & Mailänder, V. (2016). *Protein corona composition of PEGylated nanoparticles correlates strongly with amino acid composition of protein surface*. https://doi.org/10.1039/x0xx00000x

Sharma, R., Lee, H., Gupta, V., Kim, H., Kumar, M., Sharma, C., Chand, S., Yoo, S., & Gupta, D. (2016). Photo-physics of PTB7, PCBM and ICBA based ternary solar cells. *Organic Electronics*, *34*, 111–117. https://doi.org/10.1016/j.orgel.2016.04.022

Shirakawa, H., & Macdiarmid, A. G. (1977). Electrical Conductivity in Doped Polyacetylene. *Physical Review Letters*, *39*(17), 1098–1101.

Shockley, W., & Queisser, H. J. (1961). Detailed balance limit of efficiency of p-n junction solar cells. *Journal of Applied Physics*, *32*(3), 510–519. https://doi.org/10.1063/1.1736034

Shrotriya, V., Yao, Y., Li, G., & Yang, Y. (2006). Effect of self-organization in polymer/fullerene bulk heterojunctions on solar cell performance. *Applied Physics Letters*, *89*(6), 063505. https://doi.org/10.1063/1.2335377

Socrates, G. (2004). *Infrared and Raman Characteristic Group Frequencies: Tables and Charts by Socrates, George: Very Good Spiral-bound (2004) | WeBuyBooks*. https://books.google.com/books/about/Infrared_and_Raman_Characteristic_Group.html?id=LDoAAjMnwEIC

*Solar FAQs*. (n.d.). Retrieved May 10, 2021, from https://old-www.sandia.gov/~jytsao/Solar FAQs.pdf

*Solar PV – Analysis - IEA*. (2021). https://www.iea.org/reports/solar-pv

Søndergaard, R., Hösel, M., Angmo, D., Larsen-Olsen, T. T., & Krebs, F. C. (2012). Roll-to-roll fabrication of polymer solar cells. *Materials Today*, *15*(1–2), 36–49. https://doi.org/10.1016/S1369-7021(12)70019-6

Song, L., Wang, W., Barabino, E., Yang, D., Körstgens, V., Zhang, P., Roth, S. v., & Müller-Buschbaum, P. (2019). Composition-Morphology Correlation in PTB7-Th/PC 71 BM Blend Films for Organic Solar Cells. *ACS Applied Materials and Interfaces*, *11*(3), 3125–3135. https://doi.org/10.1021/acsami.8b20316

Spanggaard, H., & Krebs, F. C. (2004). A brief history of the development of organic and polymeric photovoltaics. *Solar Energy Materials and Solar Cells*, *83*(2–3), 125–146. https://doi.org/10.1016/j.solmat.2004.02.021

Sprau, C., Buss, F., Wagner, M., Landerer, D., Koppitz, M., Schulz, A., Bahro, D., Schabel, W., Scharfer, P., & Colsmann, A. (2015). Highly efficient polymer solar cells cast from non-halogenated xylene/anisaldehyde solution. *Energy and Environmental Science*, *8*(9), 2744–2752. https://doi.org/10.1039/c5ee01917f

Su, M.-S., Kuo, C.-Y., Yuan, M.-C., Jeng, U.-S., Su, C.-J., & Wei, K.-H. (2011). Improving Device Efficiency of Polymer/Fullerene Bulk Heterojunction Solar Cells Through Enhanced Crystallinity and Reduced Grain Boundaries Induced by Solvent Additives. *Advanced Materials*, *23*(29), 3315–3319. https://doi.org/10.1002/adma.201101274

Sun, Q., Zhang, F., Wang, J., An, Q., Zhao, C., Li, L., Teng, F., & Hu, B. (2015). A two-step strategy to clarify the roles of a solution processed PFN interfacial layer in highly efficient polymer solar cells. *Journal of Materials Chemistry A*, *3*(36), 18432–18441. https://doi.org/10.1039/c5ta05117g

Supasai, T., Amornkitbamrung, V., Thanachayanont, C., Tang, I. M., Sutthibutpong, T., & Rujisamphan, N. (2017). Visualizing nanoscale phase morphology for understanding photovoltaic performance of PTB7: PC71BM solar cell. *Applied Surface Science*, *422*, 509–517. https://doi.org/10.1016/j.apsusc.2017.05.205

Tams, C. (2009). The Use of UV/Vis/NIR Spectroscopy in the Development of Photovoltaic Cells | PerkinElmer. *Semantic Scholar*. https://www.perkinelmer.com/uk/libraries/APP_UseofUVVisNIRinDevelopmentPV

Tang, C. W. (1986). Two-layer organic photovoltaic cell. *Applied Physics Letters*, *48*(2), 183–185. https://doi.org/10.1063/1.96937

Technologies, A. (2008). Agilent AFM 5500 Scanning Probe Microscope User ' s Guide. *Agilent Technologies*. http://www.charfac.umn.edu/instruments/5500_Users_Guide.pdf

Tessmer, I., Kaur, P., Lin, J., & Wang, H. (2013). Investigating bioconjugation by atomic force microscopy. *Journal of Nanobiotechnology*, *11*(1), 25. https://doi.org/10.1186/1477-3155-11-25

Tsao, J. U., Lewis, N., & Crabtree Argonne, G. (2006). *Solar FAQs*.

van Veldhoven, E., van der Veer, H., Maas, D., Graat, P., Verheijen, M. A., Galagan, Y., & Andriessen, R. (2018). *Organic Polymer Solar Cell Morphology Characterization with AFM, TEM and Helium Ion Microscopy (HIM)*. https://doi.org/10.1017/S1431927610059751

Wadsworth, A., Moser, M., Marks, A., Little, M. S., Gasparini, N., Brabec, C. J., Baran, D., & McCulloch, I. (2019). Critical review of the molecular design progress in non-fullerene electron acceptors towards commercially viable organic solar cells. *Chemical Society Reviews*, *48*(6), 1596–1625. https://doi.org/10.1039/c7cs00892a

Wallace C. H. Choy. (2013). Organic Solar Cells Materials & Device Physics. In *Green Energy and Technology*. https://doi.org/10.2174/97816080528511120101

Wan, Q., Guo, X., Wang, Z., Li, W., Guo, B., Ma, W., Zhang, M., & Li, Y. (2016). 10.8% Efficiency Polymer Solar Cells Based on PTB7-Th and PC71BM via Binary Solvent Additives Treatment. *Advanced Functional Materials*, *26*(36), 6635–6640. https://doi.org/10.1002/adfm.201602181

Wang, M., Zheng, S., Wan, X., Su, Y., Ke, N., Zhao, N., Wong, K. Y., & Xu, J. (2013). Limit of Vocin polymeric bulk heterojunction solar cells predicted by a double-junction model. *Solar Energy Materials and Solar Cells*, *108*, 17–21. https://doi.org/10.1016/j.solmat.2012.08.005

*World Energy Statistics | Enerdata*. (n.d.). Retrieved May 10, 2021, from https://yearbook.enerdata.net/

Wu, Z. (2004). Transparent, Conductive Carbon Nanotube Films. *Science*, *305*(5688), 1273–1276. https://doi.org/10.1126/science.1101243

wwwMicroChemicalscom. (n.d.). *Chapter 01 MicroChemicals ®-Fundamentals of Microstructuring WET CHEMICAL ETCHING-BASICS*. www.microchemicals.com/downloads/application_notes.html

Yacobi, B. G. (2003). *Semiconductor Materials: An Introduction to Basic Principles*. Kluwer Academic Publishers. https://doi.org/10.1007/B105378

Yamanari, T., Taima, T., Sakai, J., & Saito, K. (2009). Origin of the open-circuit voltage of organic thin-film solar cells based on conjugated polymers. *Solar Energy Materials and Solar Cells*, *93*(6–7), 759–761. https://doi.org/10.1016/j.solmat.2008.09.022

Yang, D., Löhrer, F. C., Körstgens, V., Schreiber, A., Bernstorff, S., Buriak, J. M., & Müller-Buschbaum, P. (2019). In-Operando Study of the Effects of Solvent Additives on the Stability of

Organic Solar Cells Based on PTB7-Th:PC 71 BM. *ACS Energy Letters*, *4*(2), 464–470. https://doi.org/10.1021/acsenergylett.8b02311

Ye, Z., & Zhao, X. (2010). Phase imaging atomic force microscopy in the characterization of biomaterials. *Journal of Microscopy*. https://doi.org/10.1111/j.1365-2818.2009.03282.x

Yin, Z., Wei, J., & Zheng, Q. (2016). Interfacial Materials for Organic Solar Cells: Recent Advances and Perspectives. *Advanced Science*, *3*(8), 1500362. https://doi.org/10.1002/advs.201500362

Yoo, J. J., Balakrishnan, K., Huang, J., Meunier, V., Sumpter, B. G., Srivastava, A., Conway, M., Mohana Reddy, A. L., Yu, J., Vajtai, R., & Ajayan, P. M. (2011). Ultrathin planar graphene supercapacitors. *Nano Letters*, *11*(4), 1423–1427. https://doi.org/10.1021/NL200225J/SUPPL_FILE/NL200225J_SI_001.PDF

Yu, G., Gao, J., Hummelen, J. C., Wudl, F., & Heeger, A. J. (1995). Polymer Photovoltaic Cells: Enhanced Efficiencies via a Network of Internal Donor-Acceptor Heterojunctions. *Science*, *270*(5243), 1789. https://doi.org/10.1126/SCIENCE.270.5243.1789

Yu, G., & Heeger, A. J. (1998). Charge separation and photovoltaic conversion in polymer composites with internal donor/acceptor heterojunctions. *Journal of Applied Physics*, *78*(7), 4510. https://doi.org/10.1063/1.359792

Yuan, J., Guo, W., Xia, Y., Ford, M. J., Jin, F., Liu, D., Zhao, H., Inganäs, O., Bazan, G. C., & Ma, W. (2017). Comparing the device physics, dynamics and morphology of polymer solar cells employing conventional PCBM and non-fullerene polymer acceptor N2200. *Nano Energy*. https://doi.org/10.1016/j.nanoen.2017.03.050

Zang, Y., Li, C. Z., Chueh, C. C., Williams, S. T., Jiang, W., Wang, Z. H., Yu, J. S., & Jen, A. K. Y. (2014). Integrated molecular, interfacial, and device engineering towards high-performance non-fullerene based organic solar cells. *Advanced Materials*, *26*(32), 5708–5714. https://doi.org/10.1002/adma.201401992

Zhang, F., Zhuo, Z., Zhang, J., Wang, X., Xu, X., Wang, Z., Xin, Y., Wang, J., Wang, J., Tang, W., Xu, Z., & Wang, Y. (2012). Influence of PC60BM or PC70BM as electron acceptor on the performance of polymer solar cells. *Solar Energy Materials and Solar Cells*, *97*, 71–77. https://doi.org/10.1016/j.solmat.2011.09.006

Zhang, K., Chen, Z., Armin, A., Dong, S., Xia, R., Yip, H.-L., Shoaee, S., Huang, F., & Cao, Y. (2018a). Efficient Large Area Organic Solar Cells Processed by Blade-Coating With Single-Component Green Solvent. *Solar RRL*. https://doi.org/10.1002/solr.201700169

Zhang, S., Ye, L., Zhang, H., & Hou, J. (2016). Green-solvent-processable organic solar cells. *Materials Today*, *19*(9), 533–543. https://doi.org/10.1016/j.mattod.2016.02.019

Zhang, S., Ye, L., Zhao, W., Liu, D., Yao, H., & Hou, J. (2014). Side Chain Selection for Designing Highly Efficient Photovoltaic Polymers with 2D-Conjugated Structure. *Macromolecules*, *47*(14), 4653–4659. https://doi.org/10.1021/ma500829r

Zhang, X., Fan, P., Han, Y., & Yu, J. (2019). Effect of Crystallinity Modulation between Electron Transport Layer and Photo-Generation Materials on ZnO-Based Polymer Solar Cells. *Energy Technology*, *7*(2), 263–268. https://doi.org/10.1002/ente.201800666

Zhao, L., Zhao, S., Xu, Z., Yang, Q., Huang, D., & Xu, X. (2015). A simple method to adjust the morphology of gradient three-dimensional PTB7-Th:PC $_{71}$ BM polymer solar cells. *Nanoscale*. https://doi.org/10.1039/C5NR00148J

Zhao, W., Ye, L., Zhang, S., Fan, B., Sun, M., & Hou, J. (2014). Ultrathin Polyaniline-based Buffer Layer for Highly Efficient Polymer Solar Cells with Wide Applicability. *Scientific Reports*, *4*, 6570. https://doi.org/10.1038/srep06570

Zhao, W., Ye, L., Zhang, S., Sun, M., & Hou, J. (2015). A universal halogen-free solvent system for highly efficient polymer solar cells. *J. Mater. Chem. A*, *3*(24), 12723–12729. https://doi.org/10.1039/C4TA07029A

Zhou, E., Cong, J., Wei, Q., Tajima, K., Yang, C., & Hashimoto, K. (2011). All-polymer solar cells from perylene diimide based copolymers: Material design and phase separation control. *Angewandte Chemie - International Edition*, *50*(12), 2799–2803. https://doi.org/10.1002/anie.201005408

Zhou, H., Yang, L., Stuart, A. C., Price, S. C., Liu, S., & You, W. (2011). Development of Fluorinated Benzothiadiazole as a Structural Unit for a Polymer Solar Cell of 7 % Efficiency. *Angewandte Chemie International Edition*, *50*(13), 2995–2998. https://doi.org/10.1002/anie.201005451

Zhou, N., Lin, H., Lou, S. J., Yu, X., Guo, P., Manley, E. F., Loser, S., Hartnett, P., Huang, H., Wasielewski, M. R., Chen, L. X., Chang, R. P. H., Facchetti, A., & Marks, T. J. (2014). Morphology-performance relationships in high-efficiency all-polymer solar cells. *Advanced Energy Materials*, *4*(3). https://doi.org/10.1002/aenm.201300785